Development of MRI methods to map cerebral metabolic oxygen consumption in humans

by Alberto Merola, MSc

A Thesis submitted to the School of Graduate Studies
in Partial Fulfilment of the Requirements for the Degree
Doctor of Philosophy
Cardiff University

© Copyright by Alberto Merola, February 2016

Doctor of Philosophy (2016) Cardiff University

(Psychology) Cardiff, Wales

TITLE:	Development of MRI methods to map cerebral metabolic oxygen consumption in humans
AUTHOR:	Alberto Merola
SUPERVISORS:	Prof. Richard G. Wise, Prof. William P. Gray, Dr. Kevin Murphy
PAGES:	xiv, 233

Declaration form

DECLARATION

This work has not been submitted in substance for any other degree or award at this or any other university or place of learning, nor is being submitted concurrently in candidature for any degree or other award.

Signed …… Date ……

STATEMENT 1

This thesis is being submitted in partial fulfilment of the requirements for the degree of PhD.

Signed …… Date ……

STATEMENT 2

This thesis is the result of my own independent work/investigation, except where otherwise stated.

Other sources are acknowledged by explicit references. The views expressed are my own.

Signed …… Date ……

STATEMENT 3

I hereby give consent for my thesis, if accepted, to be available online in the University's Open Access repository and for inter-library loan, and for the title and summary to be made available to outside organisations.

Signed …… Date ……

STATEMENT 4: PREVIOUSLY APPROVED BAR ON ACCESS

I hereby give consent for my thesis, if accepted, to be available online in the University's Open Access repository and for inter-library loans after expiry of a bar on access previously approved by the Academic Standards & Quality Committee.

Signed …… Date ……

Summary

The quantification of brain activity has been one of the main goals of neuroimaging since the earliest applications. In functional magnetic resonance imaging (fMRI) such an aim has been pursued indirectly by studying changes of the blood oxygenation dependent signal triggered by alterations in blood flow following changes in energy metabolism. Such approach is limited because of the complex relationship between the vascular and neural systems in brain tissue. Therefore methods have been proposed to assess oxygen metabolism, which directly underlies energy supply to brain tissue and therefore brain activity.

Investigating existing and novel MRI methods, the thesis aims to improve the assessment of oxygen metabolism for a fully quantitative measurement of this biomarker.

A simulation study has been carried out to optimise one of the mathematical (fMRI calibration) models used to relate the measured signal to the underlying physiology. As a result we are able to define a new model, less complex and more accurate for estimation of oxygen extraction fraction.

Following this, an estimation approach recently developed in our centre is applied to carbon dioxide and oxygen calibrated fMRI data in an experimental setting firstly for a repeatability study and then for a drug study looking at the acute effects of caffeine on brain metabolism and haemodynamics. The precision of the novel approach shows values consistent with previous methods, but with much higher spatial resolution. Exploiting this, acute caffeine effects are characterized with a voxel-wise level of detail, showing results consistent with literature electrophysiological findings.

Finally, an innovative method for estimating oxygen extraction fraction, based on velocity spectral imaging and estimation of transverse relaxation time, is introduced and tested at a proof-of-concept level. The performance and limits are examined through simulation and experimentation, suggesting that it might be a viable alternative to the calibration techniques previously introduced.

Abbreviations

AAT	arterial arrival time
ADP	adenosine diphosphate
ANOVA	analysis of variance
ASE	asymmetric spin echo
ASL	arterial spin labelling
ATP	adenosine triphosphate
BOLD	blood oxygenation level-dependent
CaO2	arterial O_2 content
CASL	continuous ASL
CBF	cerebral blood flow
CBV	cerebral blood volume
$CMRO_2$	cerebral metabolic rate of O_2
CvO_2	venous O_2 content
CVR	cerebrovascular reactivity
dcFMRI	dual calibrated fMRI
ECoG	electrocorticography
EEG	electroencephalography
EPI	echo planar imaging
EPISTAR	EPI and signal targeting with alternating radiofrequency
FAIR	flow-sensitive alternating inversion recovery
FID	free induction decay
fMRI	functional magnetic resonance imaging
G(R)E	gradient (recalled) echo
GESSE	gradient echo sampling of spin echo
GKM	general kinetic model
Hb	haemoglobin
Hct	haematocrit
MEG	magnetoencephalography
MRI	magnetic resonance imaging
mTI	multi inversion time

NIRS	near-infrared spectroscopy
NMR	nuclear magnetic resonance
OEF	O_2 extraction fraction
PaO2	arterial O_2 partial pressure
PASL	pulsed ASL
pCASL	pseudo-continuous ASL
PET	position emission tomography
$PetCO_2$	end-tidal partial pressure of CO_2
$PetO_2$	end-tidal partial pressure of O_2
PICORE	proximal inversion with a control for off-resonance effects
pO_2	partial O_2 pressure
PROM	phase-based regional O_2 metabolism
qBOLD	quantitative BOLD
QUIPSS	QUantitative Imaging of Perfusion using a Single Subtraction
QUIXOTIC	QUantitative Imaging of eXtraction of Oxygen and TIssue Consumption
RF	radio frequency
SE	spin echo
SNR	signal to noise ratio
TAT	tissue arrival time
TE	time echo
TI	inversion time
TR	repetition time
TRUST	T_2-Relaxation-Under-Spin-Tagging
VS-ASL	velocity selective ASL
VSEAN	Velocity Selective Excitation with Arterial Nulling

Acknowledgments

Before beginning my thesis I would like to spend a few lines to thank all the people that made the years of my PhD in CUBRIC special.

Firstly, my supervisors Prof. Richard Wise and Dr. Kevin Murphy who made all this possible. I am grateful for their support as well as the advice and the knowledge they shared with me. They have been great from both a professional and a human point of view, and I hope they feel the trust they granted me during this period has eventually paid off.

I would also like to thank the people I have been working with the most. Alan, who put up with my broken English in the first months; Esther, for always being up for helping (and scanning!); Mike, for the discussions on the experiments and modelling, as well as the weekends spent scanning in the basements of CUBRIC rather than out enjoying Cardiff's rare moments of sunshine. I am also thankful to Sharmila for the support in planning and carrying out the experiments, to Cyril and Spiro who were always as keen on helping me out as they were busy and to John for his great knowledge of MRI (and rugby!).

I would also like to mention some of the people that made CUBRIC such a great place to be, starting with Kacper, Lorenzo and Tobias, with whom I shared many good times and who repeatedly showed me such generous friendship; but also Hannah, Jess, Mark, Joe, Ian, Catherine and all the people from the office for all the lunches, evenings, parties, conferences, dinners and six nations watching. Lastly, I am grateful to anyone who was up for a chat in the kitchen or a pint at the pub, which made even the toughest day happier.

Many people from outside the office deserve to be thanked. Among these Grace, who especially put up with my end-of-PhD struggle, and my family and friends from home: admittedly some of them don't really know what I have been doing here, where Cardiff is, or what an MR scanner does, but they've always been there for me and that's what matters the most.

Publications arising from this thesis:

Journal articles:

1. Measurement of oxygen extraction fraction (OEF): an optimised BOLD signal model for use with hypercapnic and hyperoxic calibration.

Merola, A., Murphy, K., Stone, A. J., Germuska, M. A., Griffeth, V. E. M., Blockley, N. P., Buxton, R. B., Wise, R. G. (2016).

NeuroImage - Epub ahead of print. doi:10.1016/j.neuroimage.2016.01.021

2. The acute effects of caffeine on brain oxygen metabolism: a dual calibrated FMRI study

Merola A, Germuska MA, Warnert EAH, Richmond L, Helme D, Khot S, Murphy K, Rogers P, Hall J and Wise RG

In submission

Index

Thesis outline

Energy metabolism underlies brain activity. As the former is predominantly oxidative, oxygen consumption measurements can be used as a proxy for the latter. Multiple MRI techniques have been developed with this purpose and for providing an effective alternative to other more invasive methods such as PET. In this thesis we aim to develop and evaluate viable means for measuring absolute brain oxygen consumption with MRI by further advancing current approaches and by proposing new applications.

Chapter 1 introduces the main physiological processes underlying brain metabolism, oxygen consumption and gas transportation in blood, relevant to the methods employed in this work. The motivations for pursuing the quantification of oxygen metabolism are presented, along with a brief review of techniques currently available.

Chapter 2 offers an introduction to MRI, from the physical principles to the main applications. All the major methods applied later in the experimental section of the thesis are presented, especially those related to fMRI. The most relevant MRI techniques recently developed for quantifying the absolute brain oxygen consumption are reviewed, with particular attention to those based on hypercapnic and hyperoxic calibration that are used in this thesis.

In **Chapter 3** the physiological model adopted by hypercapnic and hyperoxic calibration methods for estimating absolute oxygen metabolism is investigated. With a simulation study and using innovative metrics of goodness of the estimates we are able to characterise the bias present in the literature models. The process of optimisation leads to the proposal of a new *simplified calibration model* that shows improved performances and more accurate estimates of oxygen extraction fraction.

Chapter 4 assesses the repeatability of the results supplied by a novel estimation framework recently developed in our centre using calibration methods, together with measurements of blood flow and a mathematical model relating them. The resulting estimates are characterised by a level of repeatability comparable to that obtained with previous methods, but with an improved spatial resolution. The information supplied by such maps is of extreme interest for applications aimed at studying brain physiology across grey matter. Metrics of repeatability inform positively on the feasibility of the estimation framework in future applications.

In **Chapter 5** the same estimation framework is applied for a randomised, double-blind, placebo-controlled study on caffeine, enabling us to assess its acute effects on brain metabolism and haemodynamics. Results show a general decrease in oxygen metabolism after caffeine consumption, consistent with a decrease in energetic demand due to an overall inhibitory effect previously reported by electrophysiology studies. With this work we also exemplify the feasibility of our approach, showing its effectiveness in a drug study application.

Chapter 6 introduces and explores a new method for quantifying brain oxygen consumption alternative to techniques based on hypercapnic and hyperoxic calibration and exploiting measurements of relaxation ( ) to estimate venous oxygenation. Background theory, simulations and real case applications are presented, together with an extensive discussion on the main limitations. Estimates of venous blood oxygenation in two subjects are found to increase following a visual task. The proof of concept reported represents a first step towards the proposal of a new promising alternative to current techniques for measuring absolute brain oxygen metabolism.

Finally, an overall discussion of the most relevant results of the experimental section of the thesis (**Chapters 3** to **6**) and the ultimate conclusions are reported in **Chapter 7**.

Chapter 1

Neural activity, blood flow and oxygen metabolism

From the earliest applications, one of the main goals of neuroimaging has been to study brain activity. This can be done directly measuring the electromagnetic signal generated by the cells both with invasive methods, such as electrocorticography (ECoG), or through non-invasive methods, like electro- or magneto-encephalography (EEG and MEG respectively). Other approaches focus instead on mapping and measuring the metabolic and haemodynamic changes due to brain activity. Among these there are invasive techniques, like positron emission tomography (PET), and non-invasive techniques, such as magnetic resonance imaging (MRI).

This chapter firstly includes a brief general introduction to the main physiological mechanisms underlying brain activity, with particular focus on the connection between neural activity, energy metabolism and blood flow. Then an overview of the principal neuroimaging methods for estimating oxygen metabolism is provided.

1.1 Physiology and energetics of neural signalling

The neurons are the cells responsible for generating and transmitting information in the brain in the form of electrical signal. They are composed of a body, where the nucleus is located and the signal is generated, a single axon, carrying outgoing signals and branching to reach several others neurons, and dendrites, which are able, along with the body itself, to exchange information with other neurons in synapses.

The excitability of the neurons, that allows the generation and transmission of these signals, originates from a negative electronic potential (about -70 mV) between the intra- and the extra-cellular space: the membrane potential. The potential is due to a dynamic balance of ions: Na^+, Ca^{2+} and Cl^- have a greater concentration outside than inside the cell, while the opposite is true for K^+. A complex system of channels regulates the ionic flux, with or without energy consumption depending on the direction relative to the chemical and electrical gradients.

The signal is generated by a transient depolarization perturbing the membrane potential (referred to as an action potential or spike) and then propagated along the axon to reach the synapses. Here the signal is transmitted to other neurons through chemical signalling with neurotransmitters: molecules able to affect the ion channels of the receiving neuron altering its potential. A positive alteration is called excitatory and is achieved mostly through glutamate, while a negative alteration is called inhibitory and is achieved mostly through γ–aminobutyric acid (GABA). The signal is then re-generated in the post-synaptic neuron depending on the net alteration of the polarization resulting from the sum of all excitatory and inhibitory contributions.

After transmission, recovery from neuronal signalling takes place at the synaptic level: neurotransmitter molecules are brought back to the pre-synaptic terminal and the membrane potential is restored in both pre- and post- synaptic neuron, requiring the transport of Na^+ ions against the gradient. In particular, the first

process is operated by the astrocytes, a type of glial cell that also interfaces neurons with blood vessels and with them constitutes the neurovascular unit.

Neural signalling has an energetic cost, which is not equally distributed among all the processes described. In fact, it is estimated that about three quarters of the energetic demand is associated with the recovery at the post-synaptic neuron (Buxton, 2009) and the remaining quarter accounts for the other energetic costs, as membrane potential maintenance, spiking, neurotransmitter recycling, etc. This has two main consequences: 1) energy metabolism is closely related to spiking rate (Laughlin and Sejnowski, 2003), even though this is driven by recovery rather than spiking costs; 2) metabolism is mostly localized in the synaptic sites (Raichle and Gusnard, 2002), rather than where the spiking takes action. In particular the first point justifies the approach adopted by some neuroimaging techniques to take into consideration energy metabolism rather than electromagnetic signals as a measure of brain activity.

The large amount of energy required for brain activity is supplied in the form of glucose and oxygen coming through the blood stream. Inside the brain cells, glucose undergoes different chemical processes that result in the production of adenosine triphosphate (ATP), the compound in which free energy is stored. The reversible reaction that transforms ATP into adenosine diphosphate (ADP) is coupled to all the energetic processes in the cell: from ATP to ADP when the process requires energy, from ADP to ATP in case of energy storage.

Glucose is processed into ATP in two steps (see Figure 1-1): from glucose to pyruvate, in a process known as *glycolysis*, and then from pyruvate to waste products (CO_2 and H_2O) undergoing the TCA cycle in the mitochondria. Both steps result in ATP production, but with substantial differences: in fact the TCA cycle requires O_2 consumption, it is slower and supplies 18 times more ATP then glycolysis. Not all the pyruvate produced by glycolysis necessarily enters the TCA cycle. It can also be stored and build up in the cytosol as lactate which is then exchanged between astrocytes and neurons with a mechanism known as *lactate shuttle* (Pelligrino et al., 2012) depending on the energetic demand. Despite different pathways, the close relationship between functional activity and local

glucose metabolism has been also verified in early animal studies (Sokoloff, 1981).

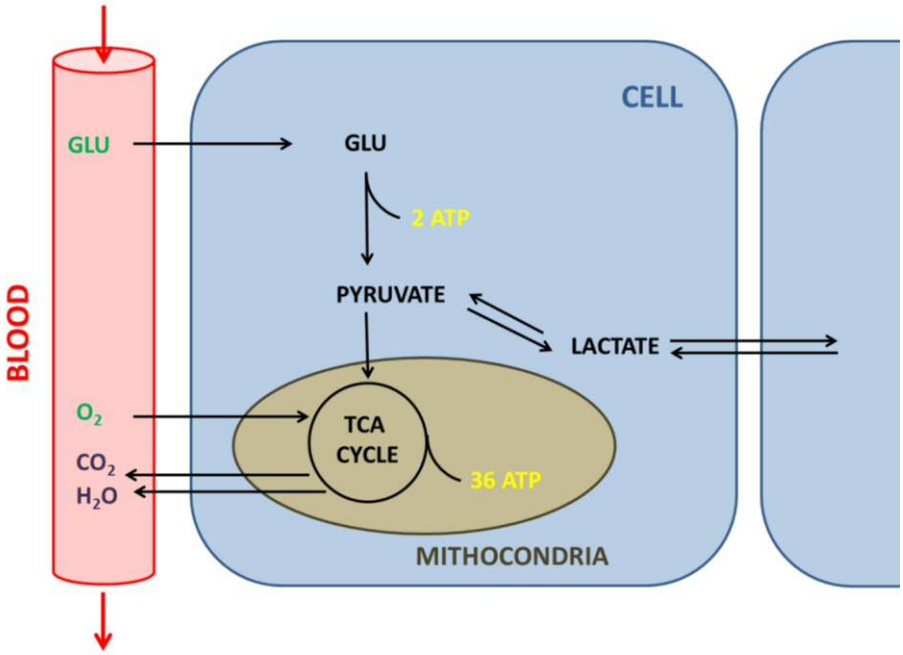

Figure 1-1: Schematic of ATP production in the cell through glucose (GLU) metabolism. The transformation of a molecule of GLU into pyruvate, process called *glycolysis,* results in the production of 2 molecules of ATP. Pyruvate can then be further metabolised into CO_2, H_2O and 36 ATP molecules through oxidative metabolism.

1.2 Blood flow and oxygen metabolism

1.2.1 Cerebral blood flow regulation

Cerebral blood flow (CBF) is the rate of arterial blood delivered to the capillary bed of a certain mass of tissue, typically expressed in units of ml of blood per 100 grams of tissue per minute (ml/100g/min). CBF has a key role in sustaining brain tissue as it supplies glucose and oxygen necessary for metabolism. Whole brain CBF is about 50 ml/100g/min (Rostrup et al., 2005) and it is heterogeneously distributed across the brain, with values in grey matter about twice as much as in white matter. The vascular system supporting CBF is formed by a group of branching vessels in the parenchyma and then draining the blood: from large arteries to small arterioles and capillaries, and then back from small venules to big draining veins. The fraction of tissue volume occupied by blood vessels is referred to as cerebral blood volume (CBV) and it has a typical value of about 4 ml/100g (Buxton, 2009).

One of the most important factors modulating CBF regulation is neural activity. As brain tissue cannot store glucose or O_2 (Siesjo and Plum, 1971), a steady supply of nutrients needs to be maintained both at baseline and after stimulation. The mechanism linking local neuronal activity to increase in CBF is known as neurovascular coupling and it is regulated by the complex relationship between neurons, astrocytes and blood vessels that together form the vascular unit. Evidence from *in vivo* studies on animals shows that CBF changes are likely driven by a feedforward mechanism involving neuronal signalling via neurotransmitters (Attwell and Iadecola, 2002; Lauritzen, 2005). Astrocytes mediate the neurotransmitter activity of both excitatory and inhibitory pathways to vascular response, through their role in glutamate recycling (Pellerin and Magistretti, 2004). This activity triggers the production of vasoactive chemical agents such as K^+ and NO (Lecrux and Hamel, 2011; Raichle and Mintun, 2006), which can alter the membrane potential of the surrounding cells.

In fact, CBF is determined by regulating the vascular resistance, dependent on the internal diameter of the vessels. This resistance is mainly due to the arterial side

of the vascular tree, and in particular the arterioles, by virtue of the smooth muscle layer surrounding the vessels which is able to alter their diameter. Different vasoactive substances can induce an increase or decrease of the vascular resistance with different chemical paths. Although, the mechanism by which relaxation or constriction of the muscle is induced is common and it is regulated by Ca^{2+} concentration in the smooth muscle cells' cytosol. Vasoactive agents can act on ion channels and alter the membrane potential increasing or decreasing cytosolic Ca^{2+} concentration inducing muscle contraction or relaxation respectively.

A well-known vasoactive agent is CO_2, which causes vasodilation and CBF increase. High concentrations of this agent in blood prevent the clearance of CO_2 from tissue, causing a build-up that results in acidification of the environment. This alters the membrane potential and triggers Ca^{2+} depletion. Another vasoactive agent is adenosine, which not only is a fundamental substrate for energy metabolism forming ATP, but is also crucial in the regulation of the neurovascular unit acting both as a neuromodulator, reducing neuronal excitability, and as a powerful vasodilator (Berne et al., 1983). A widely consumed substance that causes vasoconstriction acting as an antagonist of the adenosine receptors is caffeine, discussed in more detail in Chapter 5.

1.3 O_2 and CO_2 in blood

1.3.1 Transportation and physiology

Among all the substances transported by the blood stream, O_2 and CO_2 play a crucial role, with the first being a metabolic reagent and the second a waste product. These gases are exchanged between the external environment and the blood stream in the capillary bed of the alveoli, the functional units of the lungs. Exchange is determined by gradients of gas concentration, with O_2 passively diffusing into blood during inspiration and CO_2 passively diffusing into alveolar space during expiration.

Despite this apparent similarity, the mechanism of transportation is quite different between the two. As CO_2 is highly soluble in water, most of it (about 85%) reacts dissociating into bicarbonate ions ( ) and protons ( ) with the result of reducing the blood pH. The reaction is normally quite slow, but it is accelerated in blood due to the presence of the enzyme carbonic anhydrase. This maximizes the amount that can be transported and exchanged ensuring an effective system of metabolic waste elimination. Of the remaining 15%, about 5% is transported as free CO_2, while about 10% is bound to the protein haemoglobin (Hb). The typical expired pressure at rest is about 40 mmHg.

In contrast, O_2 solubility in water is very low. What makes it highly soluble in blood is the presence of Hb which can bind an O_2 molecule at the iron site of each of its four *haem* groups. The result is that most of the gas is carried in the vessels bound to Hb and only a small percentage in the plasma. The relationship between O_2 arterial partial pressure (PaO_2) and Hb O_2 saturation follows a sigmoidal law (Eq. 1-1): this means that the saturation remains almost constant for PaO_2 values above a certain level (about 160 mmHg), while it is very sensitive to changes below that level. The contribution of oxygen dissolved in plasma to the total arterial content (CaO_2) is only significant when the Hb is almost totally saturated (see Figure 1-2).

The equations describing these effects are:

Eq. 1-1

Also known as Severinghaus equation, and:

Eq. 1-2

Where ε is the coefficient of solubility of oxygen in blood (0.0031 ml O_2/dl_{blood} mm Hg) and φ is the O_2 carrying capacity of haemoglobin (1.34 ml O_2/g_{Hb}).

The typical PaO_2 is around 110mmHg and the difference between inspired and expired pressure is about -50 mmHg, with the saturation dropping from about 98% in large arteries to 70-65% in venous blood. Work on animals suggests that O_2 saturation has an almost continuous decrease, with values of about 75% in small arterioles (Sakadžić et al., 2015).

The most accurate measure of PaO_2 and $PaCO_2$ is direct intermittent arterial sampling, which involves puncture of the vessel and is therefore invasive. A non-invasive alternative consists of measuring the end tidal concentrations ($PetO_2$ and $PetCO_2$). This is based on the consideration that these values reflect the values in the alveoli: partial pressure of gases in the alveolar capillaries rapidly reaches equilibrium with the alveolar space, so that we can assume the two quantities to be the same (Dubois, 1952). This has been tested to hold true during rest in healthy subject, whereas overestimates of arterial partial pressure have been found in conditions like intense exercise or diseases, especially as regards values of CO_2 (Benallal et al., 2002; Robbins et al., 1990; Young et al., 1991). Evidence suggests that the main source of bias is associated with deviation from the normal breathing pattern (Benallal et al., 2002; Jones et al., 1979).

Deviations from normocapnic-normoxia

When the normal concentrations of inspired O_2 and CO_2 (typically 20.9% and 0.04% respectively, condition also referred to as normocapnic-normoxia) are altered, various physiological processes arise aimed at maintaining viable levels of pH and O_2 partial pressure in tissue. For our purpose, these are of particular interest because they can be exploited as mechanisms of contrast to investigate the property of these gases in neuroimaging applications. In fact, experiments involving administration of atypical concentrations of O_2 and CO_2 will be discussed later in Chapter 3, Chapter 4 and Chapter 5.

As previously mentioned, CO_2 is known for its vasodilatory effect on arteries, so that levels higher than normal (hypercapnia) increase blood perfusion, while lower values (hypocapnia) induce a decrease. The ratio between changes in CO_2 and CBF is often referred to as cerebrovascular reactivity (CVR) to CO_2. The relationship between end-tidal values of CO_2 and CBF is generally not linear, but it can be assumed as such for limited changes in CO_2 (Tancredi and Hoge, 2013). O_2 has been found to have a much less pronounced effect on blood perfusion with an opposite direction compared to CO_2, with some studies pointing at a vasoconstrictive action during increased partial pressure (hyperoxia) (Bulte et al., 2007).

Complications to these main effects are related to interaction effects between the two gases, which occur firstly at a biochemical level. In fact the Hb O_2 binding affinity is inversely proportional to CO_2 concentration and therefore proportional to pH (Bohr effect), while O_2 concentration decreases blood ability to carry CO_2 (Haldane effect, a review of both can be found in (Jensen, 2004)). Moreover, both hyperoxia and hypercapnia trigger hyperventilation (Dean et al., 2004; Wise et al., 2007), respectively reducing the end-tidal partial pressure of CO_2 and increasing the end-tidal partial pressure of O_2 ($PetCO_2$ and $PetO_2$).

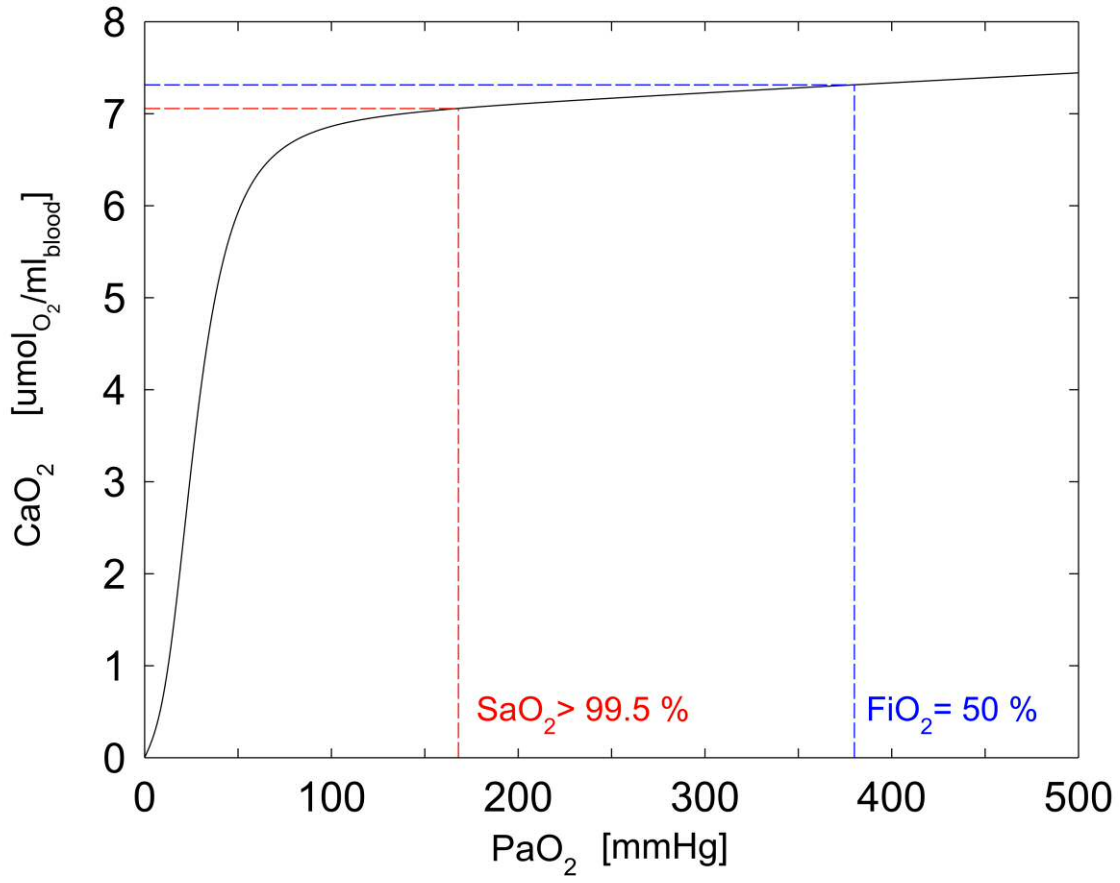

Figure 1-2: Arterial oxygen content (CaO_2) as a function of arterial partial pressure of O_2 (PaO_2) calculated with Eq. 1-1 and 1-2. Highlighted in red the value of O_2 for which Hb reaches 99.5% saturation (SaO_2), where the CaO_2-O_2 relationship starts being dominated by the additional O_2 dissolved in plasma and becomes linear. In blue, values corresponding to a 50% fraction of inspired O_2 (FiO_2), typically used in gas challenges.

1.3.2 OEF and $CMRO_2$ during rest and activation

The percentage of O_2 extracted from the blood stream is referred to as the oxygen extraction fraction (OEF) and it can be calculated from the content in arteries and veins (and) with a mass conservation law as:

Eq. 1-3

Despite heterogeneous distributions of CBF, OEF tends to be constant across the healthy brain at rest, with typical values of about 0.4 (Buxton, 2009).

By combining the information on the blood delivered, the arterial content of O_2 and the proportion of O_2 extracted by the tissue, it is possible to measure the cerebral metabolic rate of O_2 consumption ($CMRO_2$):

Eq. 1-4

Considering a typical value of 8 μmol/ml for , values of $CMRO_2$ are around 160 μmol/100g/min (Buxton, 2009). Eq. 1-3 is also known as Fick's principle and states that the quantity of a O_2 taken up by a tissue per unit of time is equal to the quantity entering it via the arterial blood minus the quantity leaving in the venous blood.

Energy metabolism in the brain is characterized by a high baseline, with local increases due to intense activation typically of about 20-30%. Such increases could be supported simply by altering CBF and OEF, without affecting the underlying mechanisms of energy production. Although, in reality the possibility of uncoupling between the two processes for ATP synthesis – discussed earlier in this chapter - determines different metabolic behaviours during rest and activation. At rest the proportion between glucose and oxygen metabolism has

been found very similar to the one described by the mass equation that regulates the oxidative metabolism (Raichle et al., 1970), suggesting that the energetic supply at resting state is dominated by the more energetically efficient oxidative pathway.

The situation changes with activation, when the time efficiency of glycolysis plays an important role. A breakthrough in the understanding of brain metabolism was made by Fox and Raichle in their studies looking at estimating oxygen metabolism, glucose metabolism and cerebral blood flow in humans (Fox and Raichle, 1986). What they found is that, in activated areas of the somatosensory cortex, CBF and glucose metabolism increases much more than oxygen metabolism, typically with a ratio between 2 and 3 (Buxton, 2009). Moreover later studies have found that during activation, glycolysis increases much more than oxidative metabolism, possibly explaining this effect (Fox et al., 1988; Lin et al., 2010). This seems to suggest that increase in glucose metabolism during activation is driven by glycolysis (due to the time efficient response) triggered by pre-synaptic activity, while $CMRO_2$ reflects the overall energy cost of neural activity (Buxton, 2009). This theme, already partially introduced when introducing the idea of neurovascular coupling, is crucial for the MRI approach to image of the brain activation and will be expanded in Chapter 2.

Due to its strict connection to energy consumption, oxygen metabolism is considered a potentially important biomarker for assessing brain physio/pathology and treatment's effects (Lin et al., 2010). Alterations in both OEF and $CMRO_2$ have been found in conditions and diseases like stroke (Heiss and Herholz, 1994), dementia (Tohgi et al., 1998), Alzheimer's (Ishii et al., 1996), multiple sclerosis (Ge et al., 2012) and tumours (Leenders, 1994; Vlassenko et al., 2015). In cases where there is no metabolic alteration but the perfusion decreases endangering the O_2 supply to the tissue (condition known as ischemia), OEF alone can be used to detect inadequate perfusion. In fact, alterations of OEF are used as markers in head injuries and cerebrovascular diseases (Coles et al., 2004; Diringer et al., 2000; Marchal et al., 1996; Ragan et al., 2012).

1.3.3 Methods for investigating oxygen metabolism

An early attempt to assess oxygen metabolism in vivo was proposed by Kety and Schmidt with tracer kinetic measurements (Kety and Schmidt, 1948). Nitrous oxide (N_2O, a metabolically inert gas) is delivered to a subject until it equilibrates with the brain tissue. Then the rate of disappearance is measured and CBF is calculated on the assumption that this rate is a function of how much of the gas is in the tissue at any time. Combining such information with measurements of blood oxygen content obtained by sampling the carotid artery and jugular vein it is possible to measure bulk $CMRO_2$ with Fick's principle.

In the following decades more sophisticated neuroimaging methods have been developed, able to measure oxygen metabolism exploiting different physical processes and with different degrees of specificity, invasiveness and accuracy. Here we give an overview of the most important ones.

1.3.3.1 Positron emission tomography

Position emission tomography (PET) is one of the earliest neuroimaging methods able to investigate brain physiology and specifically energy metabolism. PET involves the use of radioactive tracers (radionuclides, e.g. ^{18}F, ^{15}O and ^{11}C) formed substituting stable atoms with unstable isotopes in biological molecules. As the radioactive decay takes place a positron is emitted, which annihilates with an electron producing two γ-rays in opposite directions. This activity is measured, producing a map of the spatial distribution of the tracer over time. Arterial or venous samples can also be taken, in order to measure radioactivity in total blood or plasma and allow quantification. What characterizes PET is the possibility of studying a variety of different biological processes with high specificity, due to the high number of different tracers that can be created.

The investigation of oxygen metabolism is performed with a technique called triple oxygen PET, in which the isotope ^{15}O is employed in three compounds delivered sequentially: $C^{15}O$, $H_2{}^{15}O$ and $^{15}O_2$. Inhalation of $C^{15}O$ is used to measure CBV, injection of $H_2{}^{15}O$ is used to measure CBF and finally, from inhalation of $^{15}O_2$, OEF and $CMRO_2$ are measured. This method is the first one allowing the

measurement of the spatial distribution of oxygen metabolism. It has been used in the early seminal studies on metabolism and neurovascular coupling (Fox et al., 1988; Mintun MA, Raichle ME, Martin WR, 1984; Raichle et al., 1983) and it is now considered a gold standard for measuring $CMRO_2$ (Ito et al., 2005).

Nevertheless PET techniques present several issues, such as the cost, the technical complexity, the time constraints imposed by the isotopes' half-life and the technological requirements involved (e.g. an in-site cyclotron). Moreover the invasiveness due to the administration of ionizing radiations limits its use for longitudinal and repeatability studies.

1.3.3.2 Near-infrared spectroscopy

Near-infrared spectroscopy (NIRS) is a technique that exploits the optical properties of tissue to assess total, oxy- and deoxy- haemoglobin (tHb, Hb and dHb respectively) content in the vessels. In fact, while tissue is transparent to near-infrared light, Hb and dHb in small vessels (<1mm diameter, (Ferrari and Quaresima, 2012)) show characteristic spectra of absorption in a range of about 650 to 910 nm (Lloyd-Fox et al., 2010) that can be directly related to their content in the blood stream. Measurements are made with an array or a cap of light emitters and detectors put in direct contact with the skin of the subject, similar to what happens in EEG, leading to the creation of maps. Due to limits on the power of the light emitted, NIRS is only sensitive to vessels within a range of 3-4 cm from the skull surface.

NIRS studies have been typically focusing on measuring the physiological changes due to neural activation discussed in the previous paragraphs. These measurements lead to estimates of relative changes in $CMRO_2$, either alone (Boas et al., 2003) or in combination with other methods able to estimate changes in CBF (Hoge et al., 2005). Although, absolute quantification of $CMRO_2$ is unfeasible due to the necessary assumptions on the baseline value of physiological parameters such as CBV and tHb.

Compared to other methods, NIRS is minimally invasive, not expensive and supplies measurements with high time resolution, but has a poor spatial resolution and only supplies estimates of relative changes in $CMRO_2$.

1.3.3.3 Magnetic resonance imaging

Since its introduction in the 1990s, functional magnetic resonance imaging (fMRI) has relied on alteration in oxygen metabolism and blood flow to explore brain activity. A straightforward MRI technique for measuring $CMRO_2$ is highly desirable, as it would represent a cheaper and less invasive alternative to the PET gold standard, ready to be implemented in hospitals and neuroimaging centres all over the world.

Various methods for measuring firstly relative changes and then absolute $CMRO_2$ have been introduced in recent years and they will be described in detail later in Paragraph 2.2.3. Some MRI techniques allow researchers to obtain accurate and repeatable whole brain estimates. Others have been proposed for voxel-wise estimates, but no one method has emerged yet as the complete and valid alternative to the gold standard PET techniques, so that further research and improvement is still needed. The experimental chapters of this thesis try to address this issue optimizing already available techniques (Chapter 3), testing these developments in different contexts (Chapter 4, Chapter 5) and finally exploring new methods (Chapter 6).

Chapter 2

Introduction to MRI and fMRI

The aim of this chapter is to introduce the basic concepts of magnetic resonance imaging (MRI) and subsequently of functional magnetic resonance imaging (fMRI).

MRI comprises a series of techniques able to interact with the magnetic properties of the matter in our body exploiting strong magnetic fields and radiofrequency pulses. Measuring these interactions we are able to infer about the structure or function of the regions under investigation. In this brief description, the focus is on techniques which are most relevant to the experimental work presented in the rest of the thesis. In particular the chapter includes a comprehensive review of the most relevant MRI methods adopted so far for quantifying oxygen metabolism in human brain.

2.1 Basic MRI concepts

2.1.1 The origins of the signal

Atoms with an odd number of protons or neutrons are characterised by a non-zero spin angular momentum . Associated with their spin, there is a dipolar magnetic moment . The relationship between the two is given by:

Eq. 2-1

where the constant γ is called gyromagnetic ratio. According to the quantum mechanics description, is calculated from the spin angular momentum number as:

Eq. 2-2

Where is quantised and can only take integral or half-integer value and the constant *h* denotes the Planck's constant.

As the human body is largely composed of water, hydrogen (H) is particularly abundant in tissues and represents a good target for imaging. Most MRI applications are tuned to interact with H atoms, whose nuclei are composed of a single proton and therefore have spin. In the following we are therefore focusing on applications with H, which is characterised by $I = ½$ and quantum number $m_I = \pm ½$.

In the absence of relevant magnetic perturbations the magnetic moments of a pool of H nuclei are randomly oriented in tissues and their resulting sum can be assumed null. Instead, when a magnetic field is applied, they tend to align with the field. In particular – according to a process known as Zeeman effect - the

system reaches an equilibrium in which all moments will populate the energy states described by:

— Eq. 2-3.

As for H $m_I = \pm ½$, these states are two: the low energy state (-), with spins aligned parallel to the field or the high energy state (+), with spins aligned anti-parallel. The energy difference between the two states ΔE can therefore be expressed with the following:

Δ — Eq. 2-4

The ratio of the two populations of spins (N+/N-) is finally described by Eq.2.5, where *k* is the Boltzmann constant and *T* is temperature.

— Eq. 2-5

This distribution, known as the Boltzmann distribution, predicts a resulting magnetic dipole (also known as bulk magnetization) aligned with as a result of the majority of spins reaching the lower energy state. Assuming that in a sample all spin at high energy state have magnetic moment – — and all those at low energy state have magnetic moment – —, the magnitude of the resulting magnetic dipole is:

— —— Eq. 2-6

where N is the total number of protons.

Because of the external magnetic field, the alignment of the spinning nuclei is also characterised by the precession of the spins around the field direction. This process is described by Eq. 2.7, where γ equals 42.56 MHz/T for H atoms.

—— Eq. 2-7

The frequency of precession generated by the main magnetic field is denoted with ν_0 and referred to as the Larmor frequency. ν_0 is directly proportional to the magnitude of the main magnetic field, accordingly to Eq. 2.8.

ν Eq. 2-8

So far we have described how spins in a static magnetic field tend to reach an energetic equilibrium and how they behave when approaching the alignment to this field but for our purposes it is important to note that only when is perturbed, altering its alignment to the magnetic field, does precession produce a detectable signal. This signal can then be altered to encode information about the tissue from which it originates.

2.1.2 RF pulses and gradients

In an MRI scanner the main magnetic field is produced with coils of superconductive material. In addition to these, other coils are used for producing radiofrequency pulses ( ) and magnetic gradients ( ) which are exploited to generate, modulate and encode the signal. The magnetic gradients can be created in all directions independently or in combination, with the components along the x, y and z directions denoted as , and respectively. Finally, receiver coils positioned perpendicularly to the x and y axes detect the changing magnetic field

generated by the precessing dipoles when the net equilibrium magnetization is perturbed and produces a component in the xy-plane.

2.1.2.1 RF pulses

The RF pulses, denoted as , have the aim of tipping the magnetization vector , so that a net electric signal is generated in the receiver coils. is usually delivered along the x axis, so that rotates around the same axis, towards the xy-plane. In order for this to happen, must be oscillating at the Larmor frequency ν_0, that is it must be on resonance with the precession frequency: an effect known as nuclear magnetic resonance (NMR). If this is not the case and the pulse is off-resonance, only a smaller portion of the magnetization is measurable by the receiver coils on the xy-plane.

pulses are usually characterised by the angle they produce between the static magnetic field and the magnetization vector, also known as *flip angle*. High flip angles generate higher and components of magnetization in the xy-plane and therefore higher signals. The same flip angle can be obtained increasing the magnitude or the duration of the RF pulse.

The process for which energy is supplied through RF pulses to the protons, so that more of them reach a high energy state perturbing , is called *RF excitation*. During the opposite process energy is dissipated as heating and more protons return to a low energy state, with the longitudinal component of magnetization returning to and the transverse components and return to 0. This last process, called *relaxation*, occurs naturally and will be discussed in more detail later on.

2.1.2.2 Magnetic field gradients

Magnetic field gradients are fundamental for MRI, as they allow encoding information about the magnetization itself. This information is primarily exploited for image reconstruction, but then also for signal selection or contrast purposes, for example in motion sensitizing applications. As the resonant frequency is directly proportional to the magnetic field applied, introducing a

spatial gradient of the magnetic field along one direction imposes a spatial gradient of the Larmor frequency along that same direction. These spatial variations of can be expressed as:

Eq. 2-9

Where , and represent the positions along the three axes.

2.1.3 Longitudinal and transverse relaxation

As mentioned, when an RF pulse is applied it gives rise to a transverse magnetization on the xy-plane and may also leave longitudinal magnetization on the z axis. This is a transient high energy state, from which the system moves towards a low energy state. The less energetic state is reached when the magnetization aligns with , the longitudinal magnetization goes back to equilibrium value aligned on the z axis and the transversal magnetization vanishes.

These two processes are known as longitudinal and transverse relaxation. They occur with an exponential behaviour and can be characterised by two independent time constants: T_1 and T_2 respectively. They are specific for each different component of the human tissue, being therefore fundamental parameters for the contrast in the images, along with proton density and others related to the scan sequence (such as flip angle α, repetition time TR and echo time TE).

Relaxation originates from dynamic fluctuations of the magnetic field due to the fact that the magnetic dipoles are sensitive not only to the main magnetic field, but also to the small magnetic fields generated from the surrounding dipoles and their perturbations. In particular longitudinal relaxation (also referred to as T_1 recovery) is caused by the exchange of energy from nuclei to their surrounding environment (*lattice*). Transverse relaxation (also known as T_2 decay) is caused by the exchange of energy from one nucleus to another. Also, T_2 is determined by

the effect of dephasing in the precession and therefore coherence loss induced by the fluctuations. Typically at 3T values of T_1 are longer than 1s, whereas T_2 is about one order of magnitude smaller. Reported values for grey matter, white matter, arterial blood and cerebrospinal fluid at 3T are about 1.4 s, 1 s, 1.6 s and 4 s respectively (Wansapura, 1999; Stanisz, 2005). We will take a closer look at the transverse relaxation later when discussing the basis of functional MRI.

2.1.4 Free induction decay, gradient echo and spin echo

After the RF excitation pulse has been applied and the desired flip angle achieved, T_1 recovery and T_2 decay take place. In particular the signal induced in the receiver coil oscillates at the Larmor frequency and decreases with a process known as free induction decay (FID). The FID is indeed characterised by a signal decrease, but typically by much more than expected. This enhanced decay is described in terms of an apparent transverse relaxation time, T_2^*, shorter than T_2 and occurring naturally, due to magnetic field inhomogeneity inducing small changes in precession frequencies across the protons and loss in phase coherence.

Mechanisms of signal refocusing are therefore necessary as the dephasing occurs almost immediately after the RF excitation pulse has been applied, making the signal difficult to detect. In MRI two different approaches are exploited for refocusing transverse magnetisation: gradient echo (GE) and spin echo (SE).

During a gradient echo (also known as gradient recalled echo or GRE) the signal is re-phased by applying gradients along the frequency encoding direction. After the RF excitation pulse a dephasing gradient is imposed for a short period of time, followed by a rephasing gradient of opposite sign (typically with negative value). Doing so, after an initial increase in the rate of phase dispersion, the signal recovers some of the phase coherence and is refocused. In particular it reaches its maximum - the refocusing echo - at the characteristic time $t = TE$, when the area under the rephasing gradient equals the one under the dephasing gradient (see pulse diagram in Figure 2-1, top). The signal obtained is sensitive to the

apparent transverse relaxation time T_2* as the gradients are not able to correct the changes in precession frequencies due to field inhomogeneity.

However, given that T_2* results from constant offsets rather than fluctuating fields, it is possible to correct for these inhomogeneity effects and obtain an image with T_2 contrast. This is done by the spin echo, which exploits an additional RF pulse on top of two gradients for refocusing the signal. In this case after the initial RF pulse giving rise to the transverse magnetization, two gradients with same sign (typically positive) are interleaved with a 180° refocusing pulse. The pulse has the effect of rotating the dephasing transverse magnetization around its own axis by 180°, reversing the dephasing process and eventually resulting in the net transverse magnetisation being refocused in an echo (see pulse diagram in Figure 2-1, bottom). Due to the inversion of the dephasing process, the effects of static field inhomogeneity are corrected, while the transverse relaxation due to spin-spin interactions is maintained, resulting in a signal sensitive to T_2 rather than T_2* contrast. It is noteworthy that in an SE imaging approach, there are two echoes occurring simultaneously: one due to the 180° RF pulse and the other due to the read-out gradient pulses. In a conventional SE these two echoes occur at the same time, with the 180° refocusing pulse applied at $t = TE/2$. It is also possible to shift the two echoes, with an approach known as asymmetric spin echo (ASE). As in this case the transverse magnetization phase is only affected by field inhomogeneities for a certain time, the ASE sensitivity to transverse relaxation is in between the ones of SE and GE. More details on the origins of T_2 and T_2* will be presented later on, when considering the interactions between physiology and MRI signal (Paragraph 2.2.1.1).

2.1.5 Image formation

2.1.5.1 Slice selection, frequency encoding and phase encoding

RF pulses and gradients are exploited, among the others, to encode the information about the spatial distribution of the transverse magnetization into the frequency and phase of the signal. In fact, imaging is made possible because the local precession frequency is proportional to the local magnetic field which can be manipulated by applying gradient fields. In conventional applications this is done in three steps: slice selection, frequency encoding and phase encoding.

The slice selection consists of determining the position and geometry of the field of view. This is done applying simultaneously an RF pulse at the Larmor frequency ν_0 and a spatial gradient (typically a gradient, see pulse diagrams in Figure 2-1) in order to excite only a portion of protons included in a thin slice (typically on the xy plane). The spatial gradient generates a spatial distribution of frequencies around ν_0, with ν_0 corresponding to a particular value z_0 of the z coordinate. Doing so, when the RF pulse is applied, only the spins at z_0 are affected producing an component that is detectable.

After this step, the distribution of the transverse magnetization needs to be encoded in the x and y plane. Applying a spatial gradient along the x direction, the precession frequency of the transverse magnetization varies linearly along the x axis. During the continuous application of the gradient , the MR signal is measured at discrete time-points in which it will have a different amount of phase change (see pulse diagrams in Figure 2-1). Therefore the total signal acquired will be the sum of a range of frequencies rather than the only Larmor frequency. In particular the component of the signal at a particular frequency is proportional to the transverse magnetization at a certain value of the x coordinate. In this process, referred to as frequency encoding, the information on the position of the transverse magnetization is encoded in the frequency of the acquired signal.

Similarly for the y axis the spatial information is encoded in the phase of the signal detected. This is done applying a spatial gradient before data

acquisition and causing spins to accumulate a phase difference dependent on their position (see pulse diagrams in Figure 2-1). When the phase encode gradient is switched off this phase difference remains and spins are said to be phase encoded. In this way components of the transverse magnetization will have different phases depending on their position along the y axis, regardless of their precession frequency.

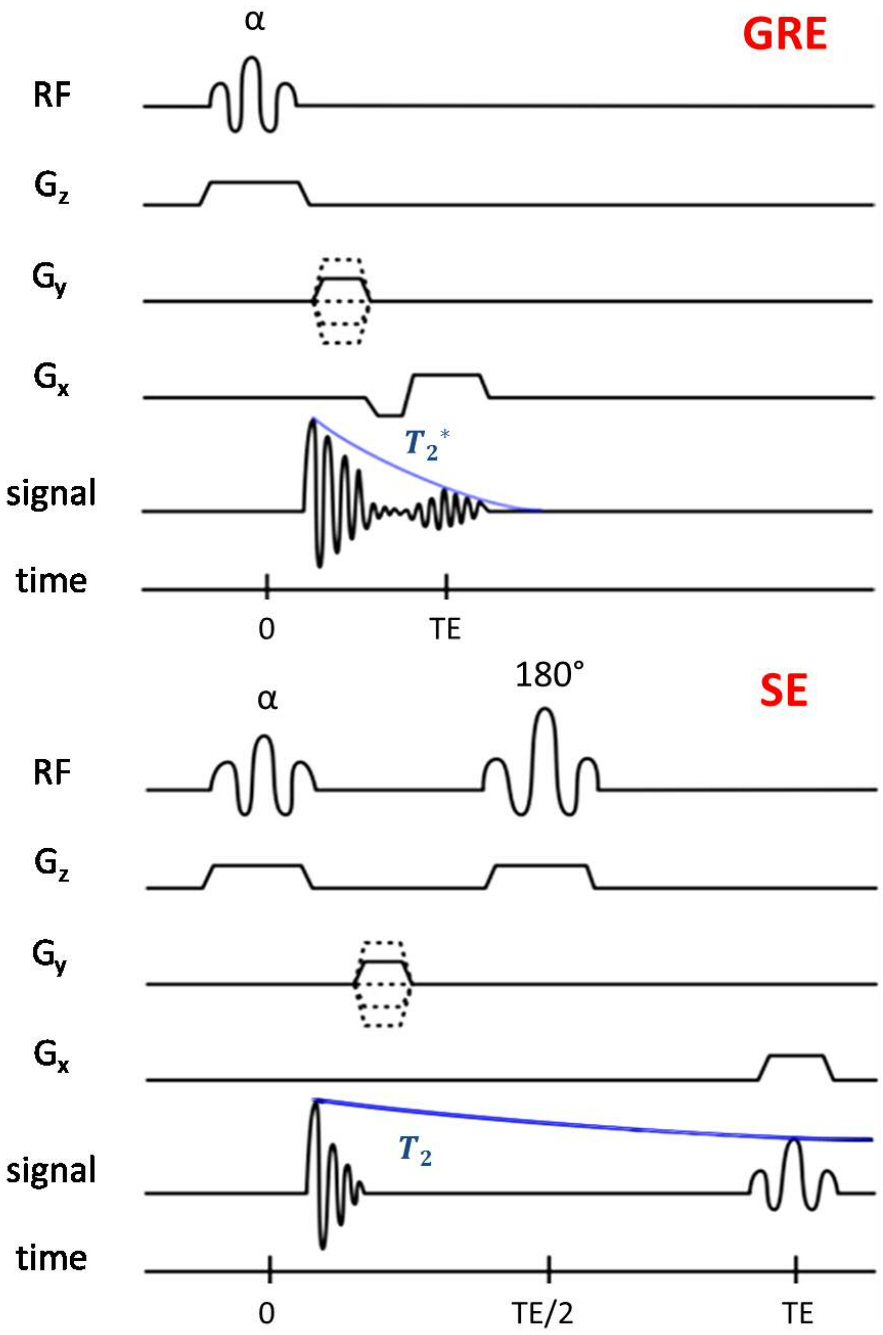

Figure 2-1: pulse sequence diagrams for standard GRE (top) and SE (bottom) sequences with Cartesian navigation of k-space (see Paragraph 2.1.5.2). In both cases, the phase encoding gradient (G_y) has a fixed value for each TR.

2.1.5.2 K-space

Let be the transverse magnetization in a position of the xy plane. If we were to measure the signal due to this magnetization arising from a small area *dA* without any encoding we would have:

Eq. 2-10

Once the encoding has been performed, the information about the spatial distribution of - that is the image of interest - is encoded in the frequency and phase of the signal S(t) detected by the coils. Considering the rotating frame of reference, the phase acquired over time due to the gradient vector can be expressed as:

Eq. 2-11

Therefore the oscillating signal measured by the coils during a short period of readout can be expressed as:

Eq. 2-12

At this point it is useful to introduce the vector = (k_x, k_y) defined as $\frac{\gamma}{}$, so that the measured signal can be expressed in terms of its dependence on as:

Eq. 2-13

This formalism allows us to think about as a spatial frequency (Hz/cm). Also, as the expression in Eq. 2.12 equals an inverse Fourier transform, the space of the image of interest and the k-space can be considered as Fourier transform conjugate spaces. It is then possible to retrieve from the measured signal in k-space through a 2D Fourier transformation:

Eq. 2-14

where $\mathcal{F}$ denotes the Fourier transform operator. In fact, the process of image readout consists of navigating and sampling k-space with the phase encoding and frequency encoding gradients. The amplitude of a voxel S(*) of this image represents the amplitude of a 2D sinusoidal wave with spatial frequency on x and y across the all image defined respectively by k^*_x and k^*_y.

Values of k close to 0 define low frequencies of the image of interest and are mainly responsible for the contrast, whereas high values define sharp transitions and details. The spatial resolution of will depend on the range of values measured, following the Nyquist criterion. So resolution in x depends on the magnitude of the read-out gradient and on the extent of the data collection time, while resolution in y depends on the magnitude of the maximum phase-encoding gradient.

2.1.5.3 K-space sampling trajectories

By k-space trajectory, what is meant is the trajectory traced in the readout phase and frequency to sample k-space. What allows us to traverse through the k-space is, as previously mentioned, the application of phase and frequency encode gradients. The k-space trajectory chosen determines both the acquisition strategy and the image reconstruction algorithm to be employed. In particular different trajectories have different acquisition times and are affected by different types of artefacts.

One of the most popular approaches is the Cartesian navigation, that consists of a raster in which each line of k-space (along the k_x axis) corresponds to the frequency-encoding readout at a fixed value of the phase-encoding gradient (k^*_y). All lines in the raster are parallel and separated by equal distance in k-space. This trajectory is typically more robust than others to artefacts due to resonance offset, eddy currents, and other imperfections. In its classic implementation each line of k-space is acquired after an RF pulse, that is after each repetition time TR, leading to long scan times.

A faster implementation instead exploits echo trains that allow sampling of the whole (or portions of) k-space with just one (or few) RF pulses. In this application the gradients change dynamically, allowing sampling almost continuous in space, with an alternating direction of the trajectory along the k_x coordinate (see Figure 2-2,A). This also leads to increase the sensitivity to several artefacts such as geometric distortions.

The spiral trajectory instead navigates the k-space describing a spiral, either starting from the origin of k-space outward (spiral-out) or vice versa (spiral-in). This is done exploiting oscillatory phase and frequency encoding gradients with amplitude increasing during time (or decreasing, in the case of spiral-in). The simultaneous use of both gradients shortens the readout time, leading to the acquisition of the whole k-space in a single TR (see Figure 2-2,B). However, it can be more demanding for the gradient generating hardware and has different artefacts when compared to the previously presented approaches. Also, given that the sampling of the k-space is not evenly distributed, the reconstruction process through the Fourier transform is more complicated.

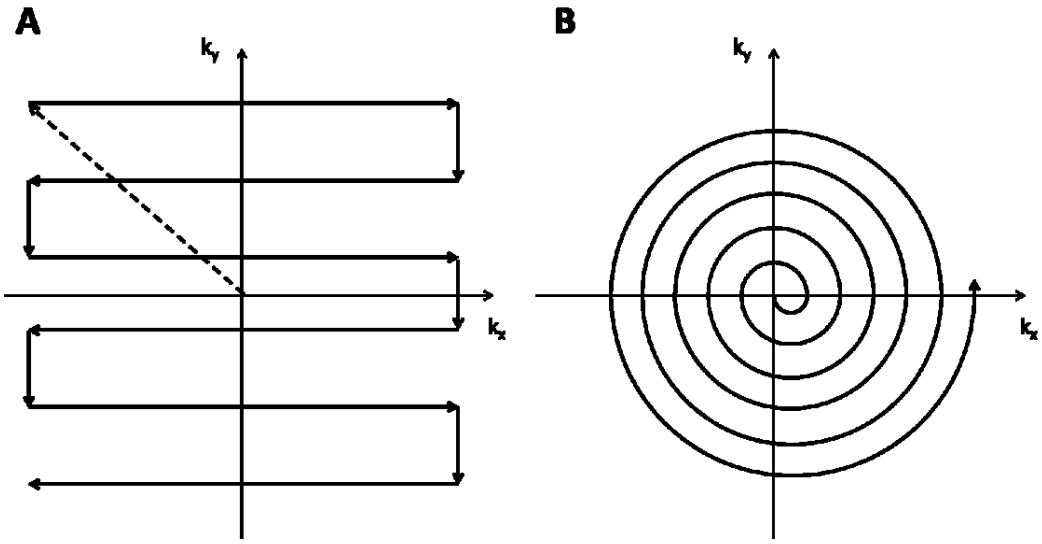

Figure 2-2: k-space sampling trajectories. In panel A the Cartesian trajectory for a train of phase encoding gradients allowing sampling of the entire space in a single TR. In panel B a spiral (out) trajectory.

2.1.6 Motion encoding, q-space and Fourier velocity imaging

2.1.6.1 Motion encoding

So far the MR signal has been considered in terms of a static spatial distribution. However, the MR signal shows sensitivity to movement, random or coherent, and many methods have been developed for quantifying this phenomenon. The techniques can be divided into two broad groups: those that encode the information in the phase of the signal (*phase contrast* techniques) and those that encode it in its magnitude (*time-of-flight* techniques). Here we focus on the former, as a novel application of this group will be presented in Chapter 6.

As previously seen, the local precession frequency of protons is proportional to the local magnetic field. The phase dependency of a pool of moving spins resonating at the same frequency (also referred to as isochromat) can be derived from its precession frequency. In fact the phase of an isochromat at position and time *t* can be expressed as:

Eq. 2-15

where the first terms - - take account of the static magnetic field and its inhomogeneity , whereas the last term expresses the dependency on the local gradient (spatially dependent and time varying). Considering now the rotating frame of reference and disregarding for simplicity the effect of , the phase acquired over time *t* can be expressed as per Eq. 2.11. It is always possible to express the component of an isochromat's position (t) along the direction of applied gradient as the sum of its temporal derivatives at t = 0. Let's take, for ease, the 1D case of direction x:

– — Eq. 2-16

Substituting Eq. 2.16 in the 1D version of Eq. 2.15 it is possible to give a general expression for the phase shift acquired relative to a stationary spin at position $x_0 = 0$. In practice, depending on the specific application, high order temporal derivatives can be considered not significant and the equation simplifies into a dependency on the only position (x_0) and local velocity (v_{x0}) of the isochromat:

Eq. 2-17

Where the n^{th} moment M_n is defined as

Eq. 2-18

Therefore it is possible to adjust the moments of the gradient so that the phase acquired by the signal encodes information about spin position or velocity. In particular by setting M_0 to 0 and M_1 to a value different from 0 the signal becomes velocity but not position sensitive, allowing velocity imaging.

The requirement on the moments' value is typically achieved exploiting pulsed field gradients (PFG), that is rectangular gradient pulses of duration δ and separation Δ with equal and opposite amplitudes $\pm G$ in the case of a GE sequence or with equal amplitudes but separated by a 180° RF pulse in a SE sequence. In fact for a PFG the magnitudes of the moment are $M_0 = 0$ and $M_1 = G\Delta\delta$, where G is the amplitude of the gradient in the direction considered (see Figure 2-3). This leads to an accumulated phase ϕ for movements in a fixed direction *x* that we can calculate with Eq. 2.16-17 as: .

The amount of phase encoding which is possible to apply is limited, as the maximum phase difference distinguishable between images obtained with two different values of the gradient is $\pm\pi$. Therefore a boundary is also introduced on the maximum value of velocity detectable without aliasing:

Δ , were ΔM_1 represents the first moment difference between two PFG applied.

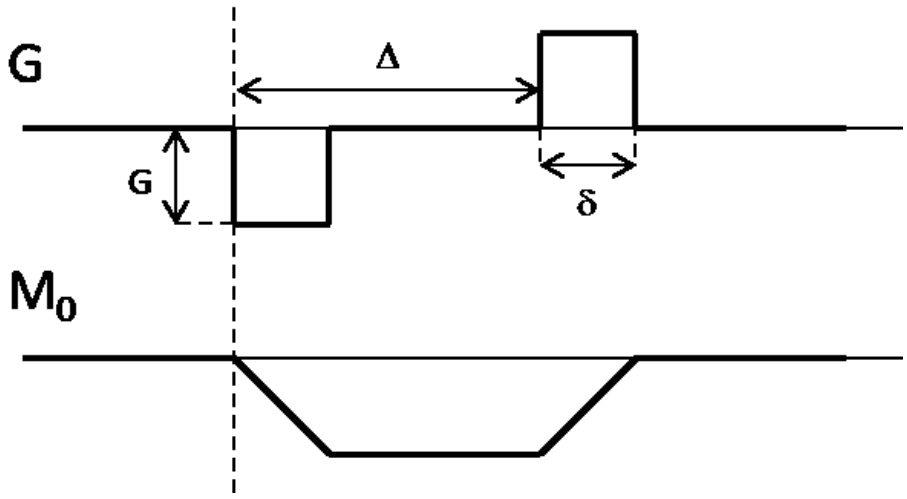

Figure 2-3: Gradient applied (G) and correspondent 0-moment (M_0) for a PFG applied in a gradient echo sequence. The resulting M_0 is nulled while $M_1 = G\Delta\delta$

2.1.6.2 Fourier velocity imaging

There are several ways to exploit the information given by the obtained phase maps. In particular Fourier velocity imaging consists of collecting several phase images sampling different values of the gradient . To explore this approach it is possible to introduce the formalism of the q-space with the q variable defined as:

— . This allows to exploit a reciprocal displacement space, the q-space, described as the motion encoding domain, similarly to what happens with the k-space for position encoding. The sampling of the q-space is carried out stepping through different amplitudes of PFGs.

With the variable introduced, the MR signal can be expressed combining spatial and velocity imaging:

Eq. 2-19

Where is the signal arising from nuclei with position and velocity . It is worth noting that this last equation expresses the relationship of duality between the -space and the space of position and velocity (-space). It's therefore possible to use the Fourier transform to investigate rather than extending the equation presented in the previous paragraph (Eq. 2.14) in order to include .

Finally the sampling of the q-space has to obey the rule on phase encoding imposed by the Nyquist criterion. Therefore the maximum velocity detectable without aliasing (max_v_{enc}) is defined by the v_{enc} associated with the minimum value of the gradient applied (G_{step}) and the resolution in velocity is determined by the number of samples acquired.

2.2 Functional MRI

Functional MRI (fMRI) is the group of MRI methods aimed at measuring brain activity. This is only done indirectly, measuring the regional effects of the haemodynamics and relying on the assumption that local cerebral blood flow (CBF) is coupled to neuronal activity. The motivations for this – already discussed in Chapter 1 - are rooted in evidence found, since early modern physiological experiments, of changes in local CBF triggered by alterations in neural activity (James, 1890).

The first method introduced relies on the venous blood oxygenation level-dependent (BOLD) effect. The differential MR signal due to the BOLD effect (hence BOLD signal) is triggered by changes in deoxyhaemoglobin (dHb) content, which acts as an endogenous contrast agent. Given that the BOLD signal is nonlinearly dependent on various physiological and biophysical factors, it only supplies a qualitative or semi-quantitative measure of brain activity.

Another group of methods have been developed, focused on directly measuring changes in blood perfusion. This group is based on the arterial spin labelling (ASL) technique, which exploits magnetized water in the blood stream as an endogenous tracer. Using some mathematical models is possible to relate the ASL signal to CBF, a measure that has a straightforward physiological meaning.

2.2.1 Blood Oxygen Level Dependent Signal

2.2.1.1 Origin of the signal

The BOLD signal originates from a combination of two different phenomena that occur in the brain: one biophysical and the other physiological.

The first is due to the different magnetic properties of haemoglobin (Hb), which is diamagnetic when bound to O_2 molecules but is paramagnetic when not bound (Pauling and Coryell, 1936), therefore disrupting the surrounding magnetic field. In particular the relationship between blood magnetic susceptibility (χ_{blood}) and haematocrit (Hct) is described by Weisskof and Kiihne (Weisskoff and Kiihne, 1992) as:

$$\chi \qquad \pi \quad \Delta\chi \qquad \text{Eq. 2-20}$$

where $\Delta\chi_{do}$ (0.264 ppm) is the difference in susceptibility between fully oxygenated and fully deoxygenated red blood cells and Y is the fractional haemoglobin saturation, which expresses the percentage of red blood cells bound to oxygen. As Hct is proportional to the haemoglobin concentration ([Hb]≅Hct/0.03), there is a linear relationship between blood susceptibility and fractional haemoglobin saturation.

Blood susceptibility affects the magnetic signal inducing frequency shifts and signal dephasing and ultimately shortening the transverse relaxation time T_2*. In particular defining R_2*=1/T_2*, it is possible to express R_2* as:

Eq. 2-21

The second component - R_2' - accounts for the reversible relaxation rate which depends on χ_{blood} and therefore on [dHb], while R_2 denotes the irreversible

transverse relaxation rate ($R_2=1/T_2$), which is dependent on intrinsic tissue susceptibility and field inhomogeneities not caused by dHb (Davis et al., 1998).

These properties of Hb are coupled to another characteristic physiological effect taking place: when an area of brain is activated in response to a stimulus, the blood flow to the tissue increases to such an extent that the oxygen delivered exceeds the metabolic need, as discussed in Chapter 1 (see Figure 2-4). This seems to support the idea that CBF and $CMRO_2$ are driven by neural activity in parallel: CBF as a feedforward response to synaptic activity, $CMRO_2$ as a feedback response to overall energy cost (Buxton, 2009). The result is a decrease in OEF and dHb content, resulting therefore in an increased MR signal (Buxton et al., 2004). This modulation of the amount and local concentration of dHb affecting the MR signal (S) was first found by Ogawa (Ogawa et al., 1993) and referred to as the blood oxygen level dependent (BOLD) effect. The signal arising, called BOLD signal, can be expressed as:

$$\frac{\Delta}{} \qquad \Delta \qquad \text{Eq. 2-22}$$

The relationship between neural activity and BOLD signal is intrinsically nonlinear as it is mediated by the previously mentioned cascade of events and it is modulated by the baseline physiological state of the brain tissue, such as baseline CBV and dHb. For this reason the BOLD signal can only provide a semi-quantitative tool for mapping brain activity.

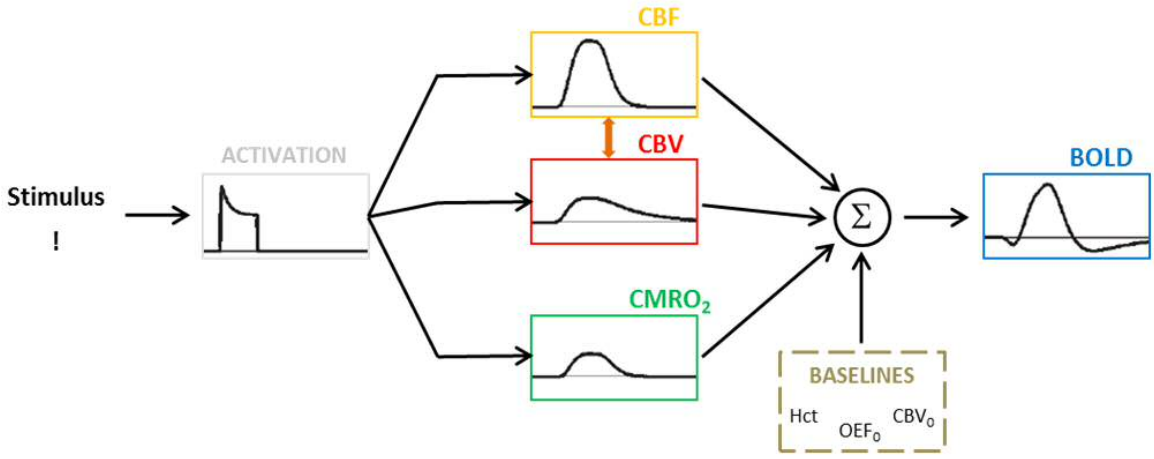

Figure 2-4: Schematic of the chain of events triggered by a stimulus in brain tissue. The interaction between the different physiological parameters involved determines the dynamics of the BOLD signal. Adapted from Blockley et al. (Blockley et al., 2012b).

2.2.1.2 BOLD signal modelling

A simplified model for describing the BOLD signal was firstly introduced by Davis (Davis et al., 1998) and then Hoge (Hoge et al., 1999a) based on modelling studies carried out by Boxerman (Boxerman et al., 1995a) Ogawa (Ogawa et al., 1993) and Weisskoff (Weisskoff et al., 1994). This model allows us to express the relationship between BOLD signal and changes in magnetic susceptibility of blood due to changes in dHb content with physiological parameters of interest, such as CBF, CBV and $CMRO_2$.

As previously seen, the exponential decay of the MR signal in a GRE experiment is characterized by the parameter R_2^*, which is the sum of an irreversible and a reversible component (R_2 and R'_2 respectively). The latter can be described as (Ogawa et al., 1993; Yablonskiy and Haacke, 1994):

β Eq. 2-23

with k being a proportionality constant depending on magnetic field strength and β expressing the nonlinear dependence of the MR signal on venous oxygenation (Boxerman et al., 1995b). In particular the value of β has been originally fixed to 1.5 at 1.5 T as a compromise between the values of 1 and 2, which would more accurately describe the relationship for large and small vessels respectively. It is therefore possible to express the change in R2* due to an alteration from a baseline state (denoted with subscript 0) as:

$$\Delta \qquad \beta \qquad \beta \qquad \text{Eq. 2-24}$$

Considering the expression for BOLD signal in Eq. 2.22 and assuming small values of ΔR_2^* is possible to obtain the following approximated equation:

$$\cong \qquad \Delta \qquad \text{——} \quad \text{——} \qquad \text{Eq. 2-25}$$

With the scaling parameter M lumping together physical scanning parameters and geometrical factors and the effect of baseline dHb content on susceptibility, defined as:

Eq. 2-26

Eq. 2.25 can be rearranged to express the relationship of the BOLD signal with two different parameters of interest: $CMRO_2$ and CBF. In fact, due to Fick's principle of mass conservation, we have:

$$\text{——} \qquad \text{———} \quad \text{——} \qquad \text{Eq. 2-27}$$

This allows one to directly relate the BOLD signal with the underlying metabolism. Then it is possible to express the CBV ratio, with a power law relationship in terms of CBF ratio, that is:

Eq. 2-28

with the parameter α=0.38 known as Grubb's parameter (Grubb et al., 1974). Finally, substituting the values in Eq. 2.27 and Eq. 2.28, Eq. 2.25 can be expressed again as:

Eq. 2-29

This model, although simplified and only considering the extravascular origin of the signal, has been successfully used in experiments to model the BOLD signal in both simulations and real world experiments (Buxton et al., 2004; Obata et al., 2004). Moreover it has been possible to adjust its application to a field strength of 3 T, just by tuning the parameters α and β : (α,β)=(0.2,1.3) as found by Bulte and colleagues (Bulte et al., 2012), or (α,β)= (0.14,0.91) as suggested by Griffeth and Buxton (Griffeth and Buxton, 2011). In particular this model will be studied and applied in the next chapters of this thesis for baseline $CMRO_2$ assessment.

2.2.2 Arterial Spin Labelling and CBF quantification

2.2.2.1 General principles

The principle of ASL is to label water in the arterial blood stream to exploit the blood itself as an endogenous tracer. The perfusion of this tracer in the tissue is then measured, giving an estimate of the water exchanged at the capillary level in brain tissue.

This operation can be conceptualized in three steps: 1) labelling of arterial blood: the magnetic characteristics of blood are altered at the arteries level by inverting or saturating its longitudinal magnetization; 2) post labelling delay: time delay to allow the labelled bolus of blood to reach and perfuse the tissue of interest; 3) signal acquisition: once all the blood is expected to be in the tissue. As the labelling results in a relative attenuation of the MR signal, the acquisition is typically carried out with a *tag-control* scheme: images are acquired with the labelling being (tag) or not (control) applied alternately. The ASL signal is then obtained by the subtraction of control images, in which the magnetization is relaxed, and tag images, in which the longitudinal magnetization of arterial blood is inverted. The obtained difference in magnetization (ΔM) is therefore proportional to CBF, but also to other underlying physiological parameters. In order to have a quantitative measurement of CBF, further processing of the signal is need, which we will discuss in details later on when describing the ASL signal modelling for CBF quantification (Paragraph 2.2.2.3).

It is important to consider that the contrast given by the tag is negative and it only applies to the water in the blood which we expect to exchange with tissue water. In grey matter, considering typical values of perfusion (approximatively 60 ml/100g/min, equivalent a rate of 0.01/s) and labelled blood bolus duration (up to about 2s), ASL measurements perturb approximately 2% of the total MR signal. Considering then the label efficacy and signal decay, this limits the difference between label and control images to about 1%. Signal fluctuations, mainly due to subject motion, are proportional to the signal intensity in the un-subtracted images, which is dominated by static tissue. For this reason ASL is a

noisy signal, with values of SNR typically between 3 and 5 times lower than BOLD.

Several approaches have been proposed to address this issue and improve SNR. They typically rely on decreasing the intensity of the signal from static tissue without a proportional decrease in the ASL difference signal. One of them, widely used for research and clinical ASL but not exploited in the experimental part of this work, is referred to as background suppression and aims at nulling the signal from the static tissue prior to readout using a combination of spatially selective saturation and inversion pulses (Alsop et al., 2014). For other methods, oriented on the post-labelling and readout phase we refer to the next paragraphs.

2.2.2.2 Signal encoding

Depending on the strategy adopted for labelling arterial blood and therefore encoding the signal of interest, ASL techniques can be divided into three broad groups: continuous ASL (or CASL), pulsed ASL (or PASL) and velocity selective ASL (VS-ASL). In the following we are going to give a general description of all of them, with more details supplied for the PASL case as it is the approach adopted in the experimental chapters of this thesis.

CASL

In this case the labelling is operated with a continuous inverting RF pulse (typical duration between 1 and 3 s) in conjunction with a slice selective gradient targeted at a certain distance from the region to be imaged on the arterial side (usually in the neck). This is often referred to as an inversion plane, crossing which the blood is labelled. This technique is characterized by high SNR, but also high specific absorption rate (SAR) and magnetization transfer effects. Due to the long labelling pulse and post labelling delay CASL is also characterized by long TR. An alternative CASL approach is the pseudo-CASL (or pCASL), that exploits for the same purpose, a train of short pulses rather that a single long RF pulse, reducing SAR and being more practical to implement on most MR systems, while maintaining the same SNR.

PASL

With PASL the tag is performed by applying a short spatially selective pulse (typically between 5 and 20 ms) on the arterial blood contained in a whole slab, or tagging volume, proximal to the imaging region. PASL techniques are characterized by lower SAR and short TR thanks to the nature of the labelling pulse, on the other hand they are affected by the quality of the tagging volume produced, in terms of spatial homogeneity and SNR lower than in CASL (Wong et al., 1998a). With PASL it is usually possible to position the tagging volume closer to the imaging volume compared to CASL, due to the reduced magnetization transfer, resulting in a shorter post labelling delay. Nevertheless the technique is affected by off-resonance effects, in which some inversion is induced outside the tagging volume.

Several methods have been proposed for addressing the issue of how to minimize changes in the static tissue contribution between the tag and control condition in order to enhance SNR. This is particularly important for PASL due to the proximity of the tagging volume to the imaging region. In the method known as echo planar imaging and signal targeting with alternating radiofrequency (or EPISTAR, (Edelman et al., 1994)), during the control image formation a tagging volume is positioned above the imaging region to induce the same off-resonance effect as in the tag and therefore a null contribution after the tag-control subtraction. Due to the close proximity of the tagging volume, a common artefact produced is the tagging of venous blood flowing downwards that confounds the dependency of the final ASL on CBF. More recently a new scheme was introduced in order to avoid magnetization transfer effects (Edelman, 1998). This exploits a 360° adiabatic pulse for the label, while two 180° adiabatic pulses for control are applied sequentially at the same location as the labelling pulse. Doing so, the magnetization transfer effects are the same as for the labelling pulse and cancel with image subtraction for all slices.

With another method, known as flow-sensitive alternating inversion recovery (or FAIR, (Kim, 1995)), the tag image is acquired with a non-selective inversion pulse, and the control image is acquired with a slice-selective inversion pulse on the image slice. In this way, the signal in the imaged region in the tag originates from the recovery of both arterial blood and tissue, while from the recovery of tissue alone in the control. As this last contribution from tissue in the image slice is ideally identical in both experiments, it cancels out. In FAIR a common artefact is represented by venous blood being tagged, leading to biases similar to the one found in EPISTAR (but with opposite direction). Finally a third method known as proximal inversion with a control for off-resonance effects (or PICORE, (Wong et al., 1997)), exploits a tag-control scheme similar to that of EPISTAR. While the tag remains the same, in the control image an RF inversion pulse with shifted frequency is applied without field gradients, so that the same off-resonance effect is produced on the image plane in both images. In this way the contribution from the venous blood to the total signal affecting EPISTAR and FAIR is nulled.

Another issue that has been addressed is the duration of the labelled bolus. In fact while in CASL bolus duration is a well-known parameter (and equals the labelling pulse duration), in PASL it is not and it depends on the heterogeneous mixture of velocity profiles of the different arteries included in the tagging volume. This represents a major limit when it comes to modelling the ASL signal and estimation of CBF. A method known as QUantitative Imaging of Perfusion using a Single Subtraction, type II (or QUIPSS II, (Wong et al., 1998b)) overcomes this difficulty creating a bolus with well-defined duration. This is done by applying a saturation pulse to the tagging volume at a time $t = TI_1$ after the RF tagging pulse ($t = 0$). Doing so, even the tagged arterial blood still present in the tagging volume is saturated, ensuring a bolus of duration TI_1. The time between tag and imaging is then $t = TI_2$ and, for the technique to be applied successfully, two conditions must be satisfied: i) the saturation pulse has to be applied before all the bolus has left the tagging volume and ii) TI_2 must be long enough to allow the entire bolus to reach the imaging region.

The PASL approach was developed after CASL and is nowadays very popular in research, despite the lower SNR, due to its rapidity and flexibility. In particular it is possible to use it in combination with another imaging module and obtain a simultaneous BOLD-ASL acquisition (see Paragraph 2.2.2.4).

VS-ASL

This kind of method is a sub-group of PASL which only tags the blood flowing slower than a fixed velocity (typically 1 cm/s), therefore targeting the blood contained in very small vessels. This is done by a non-selective RF saturation pulse in conjunction with a series of pulse gradients able to de-phase the signal originating from fast-flowing blood while maintaining the one from the targeted blood (see Paragraph 2.1.6.1 for more details). VS-ASL applications are more recent (Wong et al., 2006) and less widely used than CASL and PASL, due to their technical complexity and reduced SNR, and they are often used in combination with other imaging modules, as the ones reported later in paragraph 2.2.3.2.

2.2.2.3 ASL modelling for CBF quantification

ASL signal is only proportional to CBF and for absolute quantification it is necessary to introduce a mathematical model that describes the evolution of the signal taking into account the contribution of physiological parameters other than just CBF.

The most popular models in use derive from the general kinetic model (GKM, (Buxton et al., 1998)) which is based on tracer kinetics principles. This applies to both the CASL and PASL approach, with only the details of the mathematical implementation being different between the two. The tracer considered is the magnetisation difference ΔM, which has a dynamic over time expressed in terms of:

- delivery function, c(t) : normalized tagged blood arriving in the voxel

- residue function, r(t) : normalized tagged blood left in the voxel

- magnetisation relaxation function, m(t): describes the amount of remaining longitudinal magnetisation of the tagged blood after relaxing.

It is possible to express $\Delta M(t)$ as a convolution of the previous, in the form:

Eq. 2-30

Where M_{0B} is the equilibrium magnetization of the arterial blood and CBF is a scaling factor.

The delivery function is defined taking into account its dependency on the tagging duration τ (well defined in CASL, $\tau = TI_2$ in PASL with QUIPSS II), the transit time delay occurring for the tagged blood to reach the voxel of interest (Δt) and the relaxation undergone by the labelled water:

Eq. 2-31

Where α is the tagging efficiency and T_{1B} is the longitudinal relaxation of blood.

The residue function describes the dynamic of the tagged blood according to a mono-compartmental model as:

Eq. 2-32

Where λ is the blood/tissue partition coefficient. Finally in the original description the magnetisation relaxation function describes the evolution of magnetized water that, after been exchanged at the capillary level, is characterized by the longitudinal relaxation of tissue T_{1T}:

Eq. 2-33

Substituting the expression in Eq. 2.31, Eq. 2.32, Eq. 2.33 into Eq. 2.30 and integrating over time is possible to obtain the following equations.

PASL

Eq. 2-34

with

Eq. 2-35

and

Eq. 2-36

CASL

Eq. 2-37

with

Eq. 2-38

and

Eq. 2-39

This model makes the assumption of instantaneous exchange of labelled water between blood and tissue, so that the ratio of $\Delta M(t)$ to the venous concentration is constant and equal to λ. Although this can be considered true in most cases, in voxels where there is a substantial microvasculature component with blood that

does not perfuse in the tissue but flows to reach more distal areas, the Buxton model leads to CBF overestimates. Other models able to take into account such effect are based on two-compartment models (Chappell et al., 2010; Parkes and Tofts, 2002) which separate the contribution of the voxel magnetization in terms of intra- and extravascular compartments. In the model proposed by Chappell and colleagues (Chappell et al., 2010) the total magnetization is expressed as the sum of the ones arising from tissue (*tis*) and arteries (*art*):

Eq. 2-40

Where has the form reported in Eq. 2.34, while is expressed as:

Eq. 2-41

Where aCBV is the arterial blood volume. In this case Δt_a is the transit time delay occurring for the tagged blood to reach the intravascular compartment of the voxel, henceforth called arterial arrival time (AAT), whereas the Δt use in the expression for is referred to as tissue arrival time (TAT).

Both the one and the two compartment models are described using several parameters other than CBF. These need to be either estimated or fixed to literature values based on the information content of the data available. In the rest of the thesis we will use Buxton model to fit the data for which $\Delta M(t)$ is measured at a single t = TI, referred to as "single TI" data. The Chappell model will be used instead to fit data in which the magnetization is measured at different TI ("multi TI" or mTI) leading to estimates of aCBV, TAT and CBF.

One parameter that needs to be measured in both models independently from the fitting is the equilibrium magnetization of blood M_{0B}. This is done with an EPI scan equivalent to the ASL control acquisition with an infinite TR (Çavuşoğlu et al., 2009) exploiting the relationship:

Eq. 2-42

Where M_{0CSF} is the equilibrium magnetization of CSF (easily localized), R is the ratio of the proton density of blood in the sagittal sinus to CSF (fixed to 0.87, (Çavuşoğlu et al., 2009)), $T^*_{2,B}$ and $T^*_{2,CSF}$ are the relaxation times for CSF and arterial blood which are 43.6 ms and 74.9 ms respectively at 3T (Çavuşoğlu et al., 2009; Zhao et al., 2007).

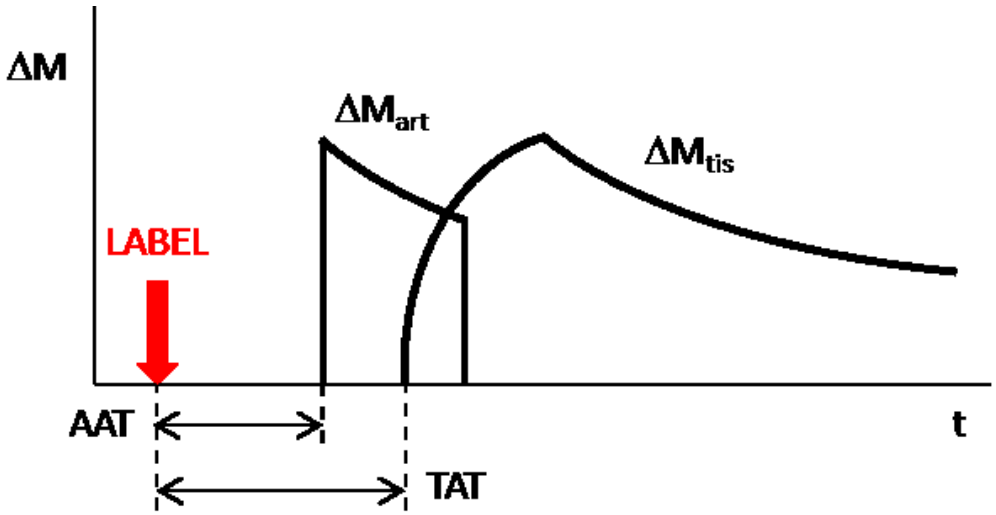

Figure 2-5: Evolution of magnetization difference as expressed by Chappell's model for a PASL experiment (Chappell et al., 2010). The GKM follows the same description but ignoring the contribution of the arterial component ( )

2.2.2.4 Simultaneous BOLD-CBF acquisition

ASL sequences typically consist of the repetition of interleaved acquisitions following the tag-control scheme previously described. As discussed, the signal obtained as difference of magnetization ΔM can be used to estimate CBF in a steady state or in its evolution over time. Given that these images are typically acquired with GRE-EPI readout sequence, they are also sensitive to T_2^* effects. If this can be considered a source of nuisance for estimating perfusion, on the other hand it can be exploited to simultaneously estimate BOLD signal.

This sensitivity to both ASL and BOLD contrast is subject to a trade-off determined by the value of TE chosen: in fact while the ASL signal is greater for short TE (Liu et al., 2001), the BOLD signal is optimized for specific values of TE (about 30 ms at 3T, (Clare et al., 2001)).

Historically, in the first applications that aimed at a simultaneous acquisition of BOLD and ASL data this interdependency between the two contrasts was not considered and data were acquired in an interleaved fashion (Hoge et al., 1999b). Then a single echo was used with a TE selected as a trade-off between the two optimal ones (Chen and Parrish, 2009a). Finally a more efficient approach was developed, exploiting a dual echo GRE acquisition in which at each TR a first image with ASL weighting is acquired at a short TE and a second one later for BOLD contrast (Yongbi et al., 2001). In particular the spiral readout, thanks to the rapidity of k-space navigation, enables to use a particularly short TE for the first echo, benefitting the CBF measurement and optimizing the dual echo approach. For this reason dual echo acquisitions with spiral readout will be used in Chapter 4 and Chapter 5 for simultaneous BOLD-ASL acquisition.

In order to separate the two contributions to the signal some processing is required. As regards ASL, one approach that has shown increased performance, compared to a pairwise subtraction, is the surround subtraction of the tag-control images from the first echo (Liu and Wong, 2005). This consists of subtracting from each image the average of the previous image and the next image, giving a difference signal that is insensitive to low frequency fluctuations in the overall signal. Similarly BOLD signal is obtained with an operation of

surround averaging (Liu and Wong, 2005) by adding to each tag-control image from the second echo the average of the previous and next images, resulting in a signal that is insensitive to flow.

2.2.3 Methods for measuring $CMRO_2$ and OEF

Various methods for absolute $CMRO_2$ measurement have been proposed in recent years, confirming the increased interest among the MR community in finding an alternative to invasive methods for the study of oxygen metabolism. Despite the research in the field so far, no particular method emerged as the optimal and PET is still considered the gold standard method for such measurements.

2.2.3.1 Susceptibility methods

These methods aim at estimating the venous oxygen saturation by measuring the susceptibility difference between venous blood vessels and surrounding brain parenchyma. The information can then be combined to independent estimates of CBF to assess $CMRO_2$ exploiting Fick's principle. Susceptibility measurements ($\Delta\chi$) are practically done acquiring phase images ($\Delta\phi$) with a GRE experiment and assuming some knowledge on the angle (θ) between the vessels under investigation and the magnetic field (B_0) with the following:

$$\Delta \quad \pi \quad \Delta\chi \qquad \text{Eq. 2-43}$$

Where the hypothesis of vessels being analogue to infinite cylinders - that is much more extended in one dimension than the other two - is made.

Such methods were originally proposed for investigating the saturation of major vessels, supplying bulk $CMRO_2$ estimates (Haacke et al., 1997) and then developed for regional applications (such as PROM, (Fan et al., 2012)), leading to more details on the spatial distribution of oxygen metabolism. The principal limitation of this group of techniques is the spatial resolution. In fact, in case of

bulk measurements, the O_2 saturation measurement represents an integration of the information relative to a large region drained by the selected vessel. On the other hand, in case of a ROI measurement in a region rich of pial veins, partial volume effects affect the accuracy of the estimates.

2.2.3.2 T_2 methods

These methods aim at estimating the value of T_2 within the veins, from which it is possible to assess S_vO_2 through a calibration curve. Blood is typically isolated with tag-control labelling techniques analogous to those employed in ASL but targeted on inflowing venous rather than arterial blood. The T_2 signal is then acquired at different TEs to quantify the signal loss due to dHb. Combining this with a measure of CBF it is then possible to estimate $CMRO_2$.

The first of these methods is known as T_2-Relaxation-Under-Spin-Tagging (TRUST) and was introduced by Lu and colleagues (Lu and Ge, 2008). The main limitation of this technique is the difficulty of isolating pure venous blood and then the sensitivity to partial volumes effects. Practically, this restricts its employment to large venous vessels, such as the sagittal sinus. Therefore TRUST just provides a global measurement of venous oxygenation and, when CBF is acquired, $CMRO_2$. Another source of nuisance in the estimate is represented by fast flowing blood in large vessel, whose effect are minimized with a using a series of non-slice-selective T2-preparation pulses rather than the conventional spin-echo sequence.

Developments of this first approach were introduced with methods known as QUantitative Imaging of eXtraction of Oxygen and TIssue Consumption (QUIXOTIC, (Bolar and Rosen, 2011)) and then Velocity Selective Excitation with Arterial Nulling (VSEAN, (Guo and Wong, 2012)). They both exploit velocity selective ASL techniques in order to isolate the signal exclusively from post-capillary blood. On top of that, VSEAN adopts phase encoding modules to maximise the separation between the static and moving components of the signal, representing a substantial improvement to QUIXOTIC. These methods offer a single slice acquisition therefore allowing to calculate maps of S_vO_2, rather than just bulk measurements as in TRUST. Although promising, they have

limitations that challenge their application, especially related to the characterization of the velocity selective modules and to SNR, as the proportion of signal they base their estimate on is inherently small.

2.2.3.3 R_2' methods

This group of methods quantifies S_vO_2 based on the signal loss in extravascular tissue due to dHb, that is on the reversible relaxation rate R_2'. R_2' sensitive images are obtained either from combination of T_2 and T_2* images (typically GESSE), or with sequences like asymmetric spin echoe (ASE), providing specific sensitivity to R_2'.

Two such approaches exploit an MRI signal model that directly relates S_vO_2 to the magnetic signal. The first one, originally developed by An and colleagues (An and Lin, 2000), uses a single compartment tissue model to produce venous CBV, S_vO_2 and OEF maps. He and Yablonskiy, with their quantitative BOLD method (qBOLD, (He and Yablonskiy, 2007)), have developed this approach, introducing a multiple-compartment model and accounts for tissue, blood and CSF signal. Both allow to obtain voxel-wise estimates of the parameters of interest. The main drawbacks of these models are that some sources of signal dephasing are ignored, such as proton diffusion and local susceptibility differences due to other that dHb.

2.2.3.4 Calibrated BOLD methods

Due to the complex dependence of the BOLD signal on various underlying physiological parameters – summarized in Figure 2-4 – BOLD signal changes alone do not supply enough information to quantify brain tissue metabolic activity.

The calibrated BOLD techniques address this issue by characterising the signal at a certain physiological baseline state (a process known as calibration) and then estimating relative metabolic changes from that baseline. This is typically done by performing gas challenges and exploiting mathematical models that relate the BOLD signal to underlying physiological parameters, such as the Davis model in Eq. 2.28.

Practically, this is done by estimating at a first stage the maximum BOLD signal change (M) for the current state through isometabolic alterations of the venous deoxyhaemoglobin content (in the case of hypercapnic and hyperoxic calibration) or through specific acquisitions (in the case of R_2` calibration). Then relative changes in $CMRO_2$ triggered by stimuli can be measured having fixed the parameter M in the considered mathematical model.

Hypercapnic calibration

In its original form, this calibration is performed increasing the concentration of inspired CO_2, typically up to about 5%, with normal concentration of O_2. Mild hypercapnia is known to elicit an increase in CBF through vasodilation (Poulin et al., 1996) and the assumption is made that the metabolism is unaltered. Therefore measuring the triggered BOLD signal and the change in CBF it is possible to estimate M with the Davis model as:

Eq. 2-44

A variant induces hypercapnia in the subject with a breath-hold rather than gas challenge. This might be subject to more sources of nuisance, such as reduction in arterial pO_2 and SNR issues due to the limits on the breath-hold duration (Bulte et al., 2009).

Hyperoxic calibration

Similarly to the previous method, hyperoxic calibration is performed increasing the concentration of inspired O_2, typically to about 50 or 100%. Hypercapnia has the effect of changing the proportion of deoxy- to oxy- haemoglobin in the venous side of the vascular tree, while supposedly maintaining CBF and metabolism unaltered. In order to relate the triggered BOLD signal to the changes in deoxy- to oxy-haemoglobin, more sophisticated mathematical models were developed,

taking into account the mechanism of transport of oxygen in blood (Chiarelli et al., 2007). Again, with this new formulation is possible to estimate the maximum BOLD signal change as:

Eq. 2-45

Where the expression for $\Delta[dHb]/[dHb]_0$ requires one to measure the arterial pO_2 and to assume a value of the baseline oxygen extraction fraction OEF_0.

R'$_2$ calibration

A different approach adopted by Blockley and colleagues (Blockley et al., 2012a) integrates the information given by R_2` in the BOLD-calibration framework. This is based on the consideration that if all the effect related to BOLD are reversed with a spin echo, then the measured relaxation would be accounted for by $R_2$`, as per Eq. 2.18. Therefore M can be estimated at baseline with the equation:

Eq. 2-46

Where R_2` is measured with sequences like ASE or GESSE (gradient echo sampling of spin echo). This kind of calibration does not rely on assumptions on the underlying physiology (such as isometabolism), but it is sensitive to macroscopic field inhomogeneity.

Limitations of calibrated BOLD methods

The main limitation of the calibrated BOLD techniques stems from the physiological assumption made, that mild hypercapnia and hyperoxia change respectively CBF and arterial O_2 content, but not $CMRO_2$. In fact simulation studies addressing this issue have highlighted that changes in $CMRO_2$ during

hypercapnia and even more during hyperoxia would strongly affect the estimated changes in metabolism (Blockley et al., 2015).

These assumptions are still the subject of discussion and the dependence of $CMRO_2$ on altered arterial CO_2 and O_2 levels have been reported with variable results. Hyperoxia has been found to cause an increase (Rockswold et al., 2010)), decrease (Richards et al., 2007; Xu et al., 2012) and no change (Diringer et al., 2007) in oxygen metabolism. Similarly hypercapnia has been observed to cause an increase (Horvath et al., 1994; Jones et al., 2005; Yang and Krasney, 1995), decrease (Sicard and Duong, 2005; Xu et al., 2011) and no change (Barzilay et al., 1985; Kety and Schmidt, 1948; Novack et al., 1953) in oxygen metabolism.

The most relevant studies suggest hypometabolism resulting from both hypercapnia and hyperoxia with a relative decrease in $CMRO_2$ respectively up to 13% (for a +10 mmHg increase in end tidal CO_2, (Xu et al., 2011)) and 10% (for a 50% fraction of inspired O_2, (Xu et al., 2012)). Although, given the successful literature reports of the calibrated fMRI approaches to estimating OEF and $CMRO_2$, it seems unlikely that they are affected by violation of assumptions of isometabolism to such an extent. Moreover, if these metabolic changes where quantified, they could be included in the Davis model for a more accurate calibration. Further investigation of the circumstances in which $CMRO_2$ is altered is therefore desirable.

Another source of nuisance might be represented by changes in CBF with hyperoxia, due to the vasoconstrictive properties of O_2 (Bulte et al., 2007). Recent evidence suggests that this is more specifically due to the hyperoxia-induced changes in CO_2 (Croal et al., 2015). This effect can be addressed either with a fine regulation of the gas challenging imposing isocapnia during hyperoxia or taking it into account in the estimation models.

A more fundamental limitation of these methods is represented by the relative nature of the calculated change in metabolism. This means that comparisons of estimated values of percentage change in $CMRO_2$ between subjects, and even within subjects in different conditions, might be confounded by changes in the baseline metabolism. In fact several factors, such as drugs (Brown et al., 2003),

are known to alter the baseline physiological state of the subject, causing changes in BOLD signal and artificial variations in $CMRO_2$ changes estimated.

2.2.3.5 Dual calibrated BOLD methods

Recently, extensions of the approaches of Davis (Davis et al., 1998) and Hoge (Hoge et al., 1999b) have been developed, using both hypercapnia and hyperoxia induced CBF and BOLD signal changes within the same experiment, hence the name of dual calibrated BOLD methods or dual calibrated fMRI (dcFMRI). The novelty of the dcFMRI methods is that they allow us to estimate venous deoxyhaemoglobin concentration and thus OEF and absolute $CMRO_2$ (Bulte et al., 2012; Gauthier and Hoge, 2012; Wise et al., 2013) rather than just relative changes as in the previous calibrated techniques.

The first version of dcFMRI technique, proposed by Bulte and colleagues (Bulte et al., 2012), adopts a two-stage approach: a first hypercapnic respiratory challenge is performed to calculate the parameter M, which is then used to fit the signal to the Davis model in a following hyperoxic challenge, allowing the estimate of the only unknown venous oxygen saturation (S_vO_2).

Both the developments proposed by Gauthier and Hoge (Gauthier and Hoge, 2012) and Wise and colleagues (Wise et al., 2013) introduce expansions to the Davis model accounting for simultaneous changes in CBF and C_aO_2 due to the hypercapnic and hyperoxic task respectively. These developments rely on a novel expression for the $[dHb]/[dHb]_0$ ratio to substitute in Eq. 2.25, that is respectively:

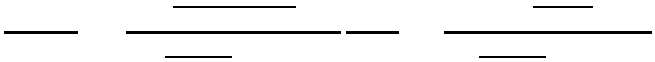

Eq. 2-47

And

Eq. 2-48

Where [(d-)Hb] indicates the (de-)oxyhaemoglobin concentration, CBF is the cerebral blood flow, OEF the oxygen extraction fraction, CaO_2 the arterial content of oxygen, φ the O_2 carrying capacity of Hb and the subscript 0 denotes the baseline condition.

The two versions of the expanded model are found to be mathematically equivalent (as shown by Blockley and colleagues (Blockley et al., 2015)). While these methods address the issue of estimating absolute rather than relative $CMRO_2$, they are still affected by the potential uncertainty upon the assumptions of isometabolism during hyperoxia and hypercapnia.

Other aspects of the dcFMRI methods will be discussed in Chapter 3, when an optimization of the Wise model (Wise et al., 2013) will be proposed, and in Chapter 4 and Chapter 5, when double calibrated BOLD measurements for assessing $CMRO_2$ will be presented.

Chapter 3

Measurement of oxygen extraction fraction (OEF): an optimised BOLD signal model for use with hypercapnic and hyperoxic calibration

In this chapter we investigate the physiological models adopted by hypercapnic and hyperoxic calibration methods for estimating absolute oxygen metabolism. With a simulation study and using innovative metrics of goodness of the estimates we are able to characterise the bias present in the literature models and the dependency of the estimates on different respiratory designs, in the ideal noiseless condition. The process of optimisation focuses in particular on the values of two biophysical parameters of the *original calibration model*: and β. This leads to the proposal of a new *simplified calibration model* characterised by a single fitting parameter (θ), that more accurately estimates oxygen extraction fraction and has higher performances in an error propagation analysis.

3.1 Introduction

BOLD fMRI is a common tool for basic neuroscientific and clinical research. However, relating changes in BOLD signal to local brain activity is complicated by its dependence on various physiological parameters, in particular CBF, $CMRO_2$ and CBV.

As seen in Paragraph 2.2.3 of Chapter 2, mathematical models and MRI-based methods have been proposed to unfold this dependence (Davis et al., 1998; Hoge et al., 1999a; Wise et al., 2013) and to measure $CMRO_2$ changes. In particular, recent extensions of the original approaches of Davis (Davis et al., 1998) and Hoge (Hoge et al., 1999b) have been developed allowing the use of both hypercapnia and hyperoxia induced CBF and BOLD signal changes within the same experiment, to estimate venous deoxyhaemoglobin concentration and thus OEF and absolute $CMRO_2$ (Bulte et al., 2012; Gauthier and Hoge, 2012; Wise et al., 2013).

It is this last approach that we investigate with this chapter, focusing on improving the calibration model previously defined for describing BOLD signal behaviour by Wise et al. (2013) (see Figure 3-1). The aim of this simulation study is to empirically modify the original calibration model to optimise the integration of information carried by BOLD and CBF signals, modulated through hypercapnic and hyperoxic respiratory challenges, in order to provide the best estimates of OEF_0 and therefore absolute $CMRO_2$ from the analysis of a set of synthetic BOLD signals generated with a detailed BOLD signal model (Griffeth and Buxton, 2011) in the ideal noiseless condition. Accurate estimates of OEF_0 are crucial for the assessment of absolute $CMRO_2$, therefore it is necessary to optimize the calibration model (Wise et al., 2013) to best explain BOLD signal behaviour across a range of potential underlying physiological states to apply the model in practice in the healthy and diseased brain.

The focus in this work is on optimising the values of two parameters of the calibration model: and β (see models summary, Figure 3-1). In the original implementations – as reported in Paragraph 2.2.3.4 - these parameters represented the Grubb's parameter (Grubb et al., 1974) and the exponent of a

nonlinear dependence of the MR signal on venous oxygenation (Boxerman et al., 1995b) respectively. Here instead, following the scheme adopted by Griffeth and Buxton (Griffeth and Buxton, 2011), they are simply recast as fitting factors, removing the previous strict connection to the biophysical origin of the signal.

However, other assumptions underlying the original calibration model are still made, in particular that mild hypercapnia and hyperoxia change respectively CBF and arterial O_2 content (CaO_2), but not $CMRO_2$ (Jain et al., 2011). The validity of physiological assumptions is still controversial and is examined in detail in a recent paper by Blockley and colleagues (Blockley et al., 2015) that investigates sources of systematic error in dual calibrated BOLD approaches to $CMRO_2$ estimation.

The simulations in this study (a flowchart of the analysis framework is shown in Figure 3-2) provide a detailed analysis of the biases present in estimating OEF_0 from the original calibration model assuming previously reported values of and β. The simulations allow us to define a *simplified calibration model*, with fewer parameters and improved performances.

This model is similar to others recently proposed to simplify the original Davis model (Blockley et al., 2015; Griffeth et al., 2013) by linearizing the relationship between BOLD signal and changes in deoxyhaemoglobin. What distinguishes the simplified calibration model is the subsequent process of optimization of the parameters, which eventually leads to improved performance in estimating OEF_0.

Finally, an analysis on the effects of input errors was carried out comparing the simplified calibration model with the original one. This provided a first evaluation of the behaviour of this model when dealing with errors in measurements and also a further understanding of its limits.

3.2 Methods

3.2.1 Dataset generation

3.2.1.1 Generation of physiological states

A set of BOLD signals was created to simulate experiments at 3 Tesla, using the detailed model employed by Griffeth and Buxton (Griffeth and Buxton, 2011), developing an approach taken by Uludağ et al. (Uludağ et al., 2009) and adapted here to simulate experiments in which arterial oxygen and carbon dioxide tensions are modulated for the measurement of OEF_0 and $CMRO_2$. The model relates the BOLD signal to the echo time TE, taking into account the contribution of four different compartments: one extravascular and three intravascular, i.e. arterial, venous and capillary. The signal is therefore computed as a sum of the different sources weighted for their respective volumes (see models summary, Figure 3-1 and parameters value Figure 3-2).

This model was chosen because of its sensitivity to different aspects of the signal, in particular the introduction of the capillary compartment, which represents an improvement in accuracy of signal description compared to previous models. Moreover it allows the variation of underlying physical and physiological factors, allowing to simulate a wide set of different experimental conditions.

The simulated different physiological states where created by picking 1000 quartets of values of baseline cerebral blood volume (CBV_0), baseline cerebral blood flow (CBF_0), baseline oxygen extraction fraction (OEF_0) and haematocrit (Hct). These parameters were designed to span wide ranges of plausible physiological values with assumed Gaussian distributions ($N \sim (\mu,\sigma)$) centred on typically previously reported values.

CBV_0 was chosen from a distribution with mean $\mu = 5.5$ ml/100g and standard deviation $\sigma = 1.5$ ml/100g (spanning the range [0.5,10.5] ml/100g), CBF_0 with $\mu = 50$ ml/100g/min and $\sigma = 8.3$ ml/100g/min (spanning the range [23,83] ml/100g/min), OEF_0 with $\mu = 0.5$ and $\sigma = 0.133$ (spanning the range [0.1, 0.9])

and Hct with $\mu = 0.415$ and $\sigma = 0.0284$ (spanning the range [0.31,0.53]). The remaining physical and physiological parameters required by the detailed model, were set to the values proposed by Griffeth and Buxton (Griffeth and Buxton, 2011) at 3T (see Figure 3-2).

3.2.1.2 BOLD signal generation

Different sets of BOLD signals were created from the detailed model by combining these physiological inputs with the expected CBF changes produced by different combinations of respiratory gas challenges. Both hyperoxic and hypercapnic conditions were simulated and considered (see gas designs summary, Figure 3-4) following the practical work developed in our centre using similar designs (Wise et al., 2013).

The effects of hypercapnic stimuli were directly related to CBF changes through an assumed linear cerebrovascular reactivity to CO_2 (fixed to 3 % ΔCBF/mmHg accordingly to reports from Bulte et al. (Bulte et al., 2012) and Mark et al. (Mark et al., 2010)). It is noteworthy that for the values of CBF_0 and the mild levels of hypercapnia considered we expect an approximately linear relationship between end tidal CO_2 and CBF (as per Tancredi and Hoge (Tancredi and Hoge, 2013) and Reivich (Reivich, 1964)).

In order to reflect BOLD signal changes with hyperoxia, the detailed model has been integrated with well-known physiological descriptions of carriage of oxygen in the blood, under the assumption of isometabolism in hyperoxia. Eq. 1-1 and Eq. 1-2 have been adopted to take account of the arterial oxygen saturation and content, incorporating in hyperoxia the important component of oxygen carried in solution in the blood plasma.

Then venous oxygen saturation (SvO_2) has been calculated as :

Eq. 3-1

considering negligible the role of O_2 dissolved in venous plasma (as in Chiarelli et al. (Chiarelli et al., 2007)).

Each simulated respiratory experiment and therefore each BOLD signal simulated, consisted of 13 equally spaced samples, each representing a block of experimental data. This approach aimed to simulate studies in which data time series (BOLD, CBF, pO_2, pCO_2) are averaged over blocks of time (as in Bulte et al., (Bulte et al., 2007); Chiarelli et al., (Chiarelli et al., 2007); Wise et al., (Wise et al., 2010)). Levels of end-tidal CO_2 and O_2 partial pressure modulation were chosen to represent those typically used in previous calibrated fMRI studies.

The simulated respiratory experiments (see gas designs summary, Figure 3-4) were chosen to be of two main types: simultaneous or interleaved modulation of the O_2 and CO_2 supply. For the simultaneous experiment, a single instance being considered (design A), hypercapnia and hyperoxia were applied simultaneously as previously experimented in our centre (Wise et al., 2013). For the interleaved experiments either hypercapnia or hyperoxia is applied, but not both together. Typically a single level of hypercapnia and hyperoxia is chosen, alternated with normocapnia and normoxia as used by Bulte et al. (Bulte et al., 2007) for their $CMRO_2$ calibration study and also in our previously presented work (Wise et al., 2013).

In addition, three new interleaved designs are proposed, for which more than one level of hypercapnia ("interleaved modulated in CO_2"), hyperoxia ("interleaved modulated in O_2") or hypercapnia and hyperoxia ("interleaved modulated") is employed (see Figure 3-4). These additional designs are included to explore the information that they can yield for the original calibration model, discussed further below. These new designs are aimed at simplifying the experiment compared to the simultaneous design while possibly allowing the extraction of the same amount of information as available from that design.

3.2.2 Criteria for optimising and β values

Estimates of OEF_0 using the original calibration model (Figure 3-1) were obtained by setting literature values of the and β parameters: (0.2,1.3) as used by Bulte et al (Bulte et al., 2012), and (0.14,0.91) as suggested by Griffeth and Buxton (Griffeth and Buxton, 2011). The resulting values, for both the simultaneous and interleaved gas challenge designs, were considered as "standard" results against which others are referenced. The aim of the optimisation process was to establish values of and β that minimise the error and bias in OEF_0 estimated across the range of physiological states using the original calibration model.

The first part of the optimisation process fitted the original calibration model to the generated BOLD signals. We estimated the values of the parameters M and $[dHb_0]$, defined in Wise et al. (Wise et al., 2013), with Matlab (Mathworks, Natick, MA) function lsqnonlin for different pairs of the and β parameters: 2500 combinations of parameters in which ranged from 0 to 1 in steps of 0.0204 and β from 0.5 to 3 in steps of 0.051. Two different approaches were chosen and compared for assessing the best (β) pairs: (1) the (β) parameters were chosen to minimize the residual sum of squares (RSS) fit to the BOLD signal, and (2) they were chosen to minimize the difference between the OEF_0 estimate from the original calibration model and the true OEF_0 entered into the detailed model (dOEF).

The first approach optimised and β by minimizing the RSS index among all combinations of physiological states. This was obtained as the sum of the squared differences between the fitted and simulated BOLD signal. However it must be remembered that a good fit of the model to the signal is not a guarantee for good OEF_0 estimate; in fact the relationship between the BOLD signal and OEF_0 is non-linearly regulated through the original calibration model. and β are regarded simply as parameters to be fit: the search space is extended broadly beyond the literature values and no constraint is imposed on their value.

Computing the RSS over the entire search space leads to the definition of characteristic surfaces, whose minimum points represent the pairs of (,β) which give the best fit for the specific physiological states considered. The surfaces of all the physiological states were studied and the respective minima found. Also the median surface was calculated from all the physiological states and the results compared to those of the single states in order to understand if common and representative patterns of minima could be detected across all physiological states. These common surface shapes would suggest that a single (,β) combination would optimise the fit of all the physiological states. Otherwise, if the single surfaces present patterns so greatly different among each other that the median surface is not representative of the whole set, the choice of an optimum (,β) pair may not be possible.

The second approach optimised and β by minimizing the absolute difference between the estimated OEF_0 from the original calibration model and the true OEF_0 used as an input to the detailed model (dOEF). The analysis was carried out calculating difference index surfaces for all physiological states and also the median surface. This is of course a theoretical exercise given that experimentally the information about the real value of OEF_0 is not available as it is the goal of the measurement. Nevertheless, as in the case of the signal RSS indices, it is useful in the context of simulations to assess whether a common representative pattern can be found in the calculated surfaces and what kind of information may be extracted in experiments. In contrast to the first approach, this second approach was introduced to specifically address the minimisation of errors in OEF_0 estimate without aiming at a good fit to the simulated BOLD data.

We further addressed the need to find a single representative value of (,β) that optimises OEF_0 estimates when only the BOLD and CBF information are available and OEF_0 is unknown, reflecting the real world situation. The search for the best combination was performed by combining, for the simulations, the information given by both the RSS and dOEF indices. The resulting values of (,β) would be a trade-off between a good fit to the real data and accurate estimates of OEF_0,

therefore matching the criteria for an optimum model which provides reliable estimates of $CMRO_2$ consumption in a real world case.

3.2.3 Development of the original calibration model and proposal of the simplified model

We also investigated the nature of the relationship between and β and its dependence on the respiratory challenge design. In fact, the results from the analysis above may be influenced by the interaction of the two parameters for the particular task considered rather than reflect their general behaviour. The aim was, therefore, to find reliable optimum and β values with reduced dependence on the choice of experimental design, making the model applicable over a wide range of potential experiments.

In particular, we studied the RSS and dOEF indices having fixed β, so that its relationship with is disentangled. We tested different literature values of β and the results were compared to investigate the relationship between these two parameters. On the basis of the results of these analyses we introduced a new optimal model, the simplified calibration model (Eq.3-2, also see models summary, Figure 3-1), that aims to offer a single estimation framework for all different respiratory designs.

This new model removes the β parameter, reducing the complexity from 4 to 3 parameters: M, dHb_0 and θ (Eq.3-2). For M and dHb_0 we refer to the previous study from our laboratory (Wise et al., 2013), while θ may be considered an empirical parameter lumping together different sources of physiological information expressed by and β in the original calibration model. The single optimum value of θ was selected as a representative value across all the designs considered.

— —— ——— Eq.3-2

The choice to remove the β parameter, equivalent to setting β = 1, rather than fixing was a pragmatic one in order to reduce the model complexity. In addition there is a historical trend to increasing field strength in MRI. At higher field β tends closer to 1 as a larger proportion of the BOLD signal contribution is extravascular. The form of this simplified model therefore becomes physically more representative at higher field strengths.

3.2.4 Approaching the real-world case

Having proposed the simplified model we returned our focus to the initial practical goal of the study, namely obtaining the best estimates of OEF_0 from the analysis of a set of BOLD signals, with no information of the real OEF_0 itself, that is, without calculation of the dOEF index. At the same time, the respiratory challenge designs showing the lowest bias and variability in estimated OEF_0 were identified. This was done with the intention of providing practical advice for experimental designs.

We further investigated the situation in which θ was fixed to the optimum value found, considering both the whole dataset and a subset including only the physiological states for which the value of each input parameter (i.e. CBF_0, CBV_0, Hct and OEF_0) lay within the μ±σ range. This set (270 cases) is more similar to an ideal "average dataset", excluding outliers while including physiological states which should be more frequently found in real data, at least in the healthy brain. The results for all designs are reported and compared to those previously found with the original calibrated model and literature values of and β.

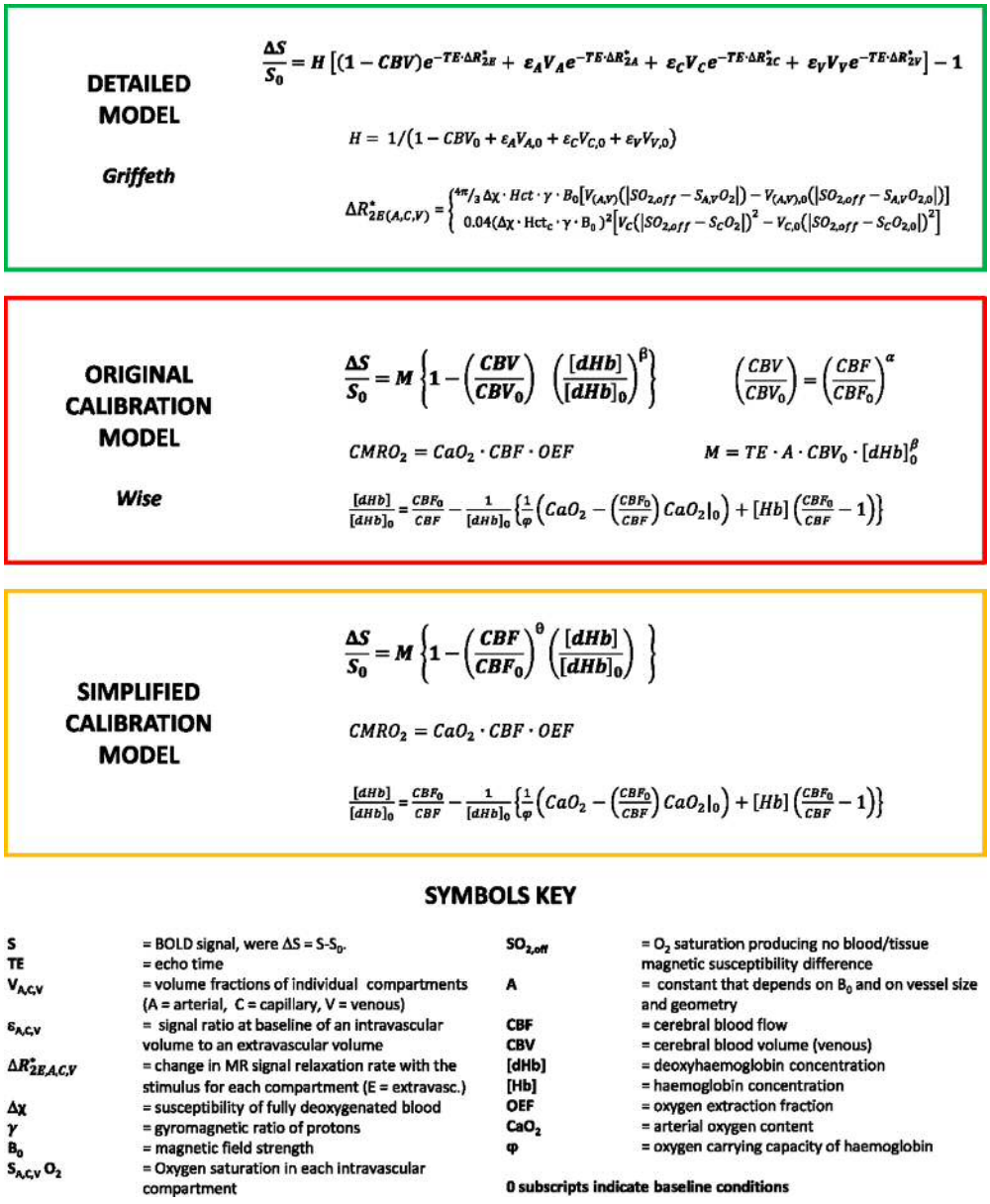

Figure 3-1: From the top to the bottom, in the green box the detailed model proposed by Griffeth and Buxton (Griffeth and Buxton, 2011), used for the data simulation. In red the calibration model defined in the previous paper (Wise et al., 2013), used in the estimates and for the calculation of RSS index and OEF_0 discrepancy. In yellow the newly proposed simplified model. For details please refer to the respective papers.

Parameters quoted in model summary		Parameters not quoted in model summary	
TE	= 32 ms	**λ**	= intra to extravascular spin density ratio : 1.15
$V_{A,C,V}$	= 0.2·CBV, 0.4·CBV, 0.4·CBV	$\varphi_{t,C,V}$	= exponent relating CBF to total, capillary, venous CBV: 0.38, 0.1, 0.2
$\varepsilon_{A,C,V}$	= 1.3, 1.02, 0.5	**k**	= fraction of capillary blood considered arterial: 0.4
$\Delta R^*_{2\,E,A,C,V}$	= -0.4, 0, -3.1, -10.2 s^{-1}	$\Delta R^*_{2E,A,C,V}(0)$	= resting extravascular arterial, capillary, venous rate of signal decay: 25.1, 21.3, 28.9, 50.9 s^{-1}
$\Delta\chi$	= $2.64\cdot10^{-7}$	$\omega_{A,C,V}$	= arterial, capillary, venous fraction of total CBV_0: 0.2, 0.4, 0.4
γ	= $2.68\cdot10^{8}$		
B_0	= 3 T		
$S_{A,C,V}O_2$	= 0.98, 0.74, 0.59		
$SO_{2,off}$	= 0.95		
Hct	= 0.44		
Hct_c	= 0.33		
Hb	= 15 g/dl		

Figure 3-2: Values of the parameters used in the detailed model for the generation of the synthetic datasets

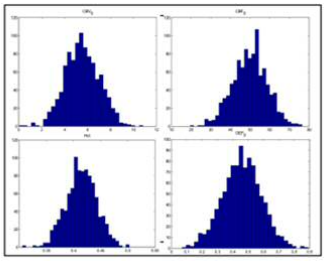

1000 physiological states generated picking Gaussian distributed values of :

CBV_0 with μ =5.5, σ =1.5 ml/100g/min
CBF_0 with μ =50, σ =8.3 ml/100g
OEF_0 with μ =0.5, σ = 0.133
Hct with μ =0.415, σ =0.0284

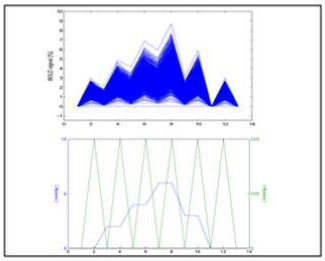

Physiological states and gas delivery data are used to generate a set of 1000 BOLD signals and a single CBF signal for each gas challenge design considered.

Synthetic BOLD and CBF signals are then the inputs of our estimation framework.

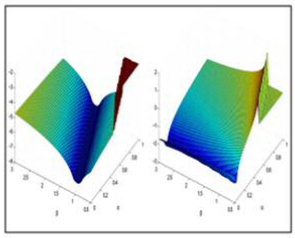

Criteria for optimizing (α,β) values are investigated:

- **RSS values**
- **Discrepancy in OEF_0**

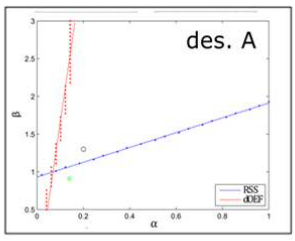

The issue of collinearity between the two (α,β) parameters is analysed, leading to:

- **optimization of the calibration model**
- **definition of simplified model**

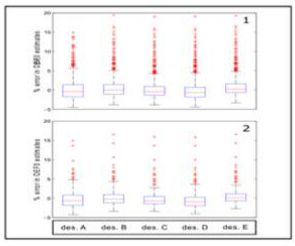

The approach to real case study is proposed and its results analysed.

Figure 3-3: flowchart of the analysis process

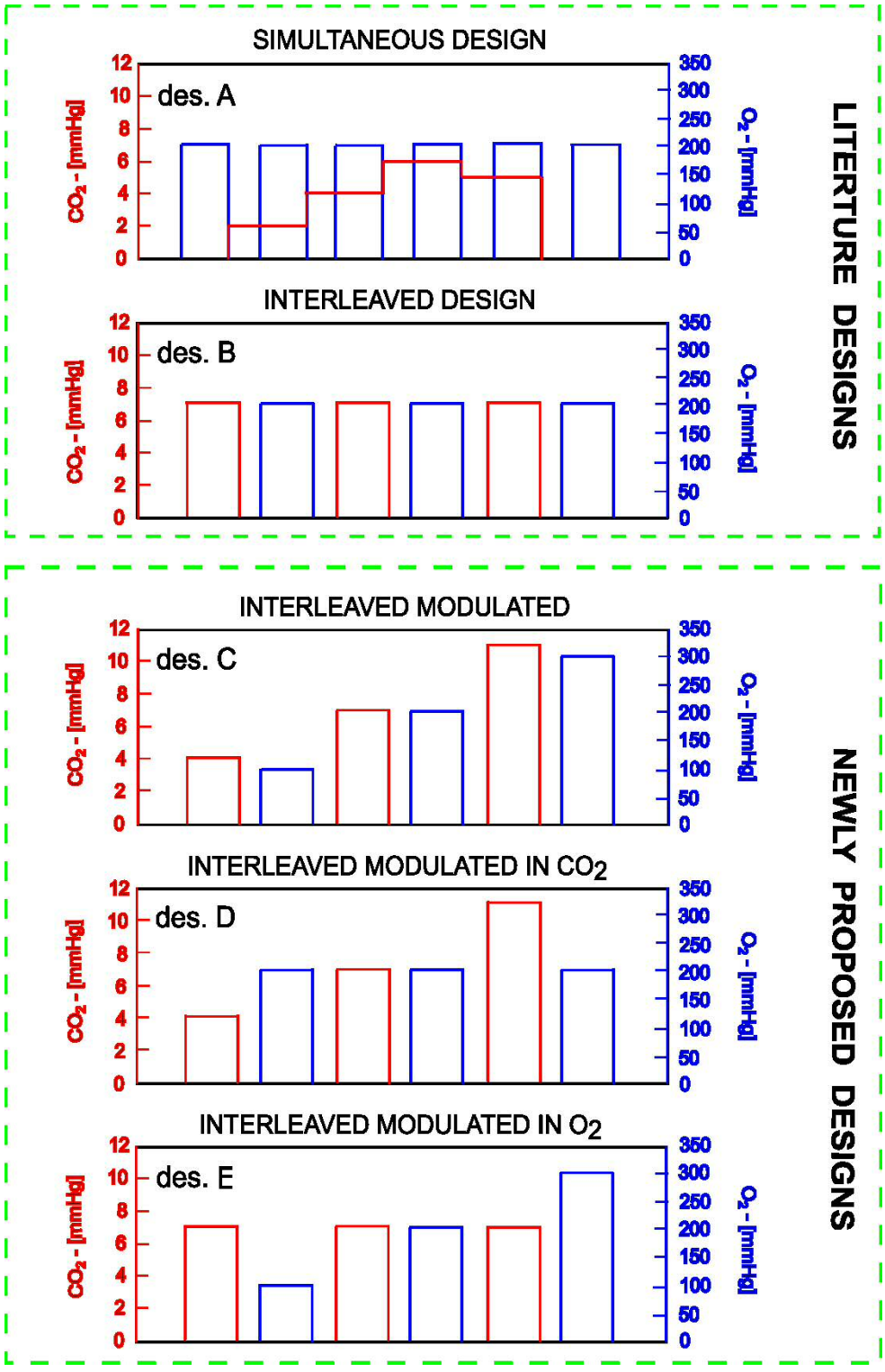

Figure 3-4: respiratory challenge designs considered for the simulations

3.2.5 Error propagation analysis

We performed a targeted error analysis of the original and simplified calibration models to demonstrate the effect, on OEF estimation, of errors in the measurement of key elements of the brain's responses to hypercapnia and hyperoxia. Only the interleaved design (des. B, Figure 3-4) was considered at this stage, as one of the more common types of respiratory experimental designs employed in calibrated fMRI studies. In particular, five sources of error were tested independently of one another: (1) error in the measurement of the CBF response to CO_2, which we express as error in cerebrovascular reactivity (change in CBF per mmHg change in partial pressure of end-tidal CO_2), (2) error in the measurement of the BOLD signal response to CO_2, (% BOLD signal change per mmHg change in partial pressure of end-tidal CO_2), (3) error in the measurement of the BOLD signal response to O_2, (% BOLD signal change per mmHg change in partial pressure of end-tidal O_2), (4) change in $CMRO_2$ with hypercapnia and (5) change in $CMRO_2$ with hyperoxia.

Error in the measurement of the CBF response to CO_2 was introduced as an additive factor on the assumed value of cerebrovascular reactivity in the model (fixed to 3% ΔCBF/mmHg, see *BOLD signal generation* section in Methods). The simulated measured values of cerebrovascular reactivity considered were, therefore, between 2 and 4% ΔCBF/mmHg, (an error from -33 to +33%). The same rationale was applied to introduce error in BOLD signal measurement during hypercapnia and hyperoxia, with measurement errors ranging from -33 to +33% of the true value of BOLD signal response. In these three cases the resulting erroneous simulated traces of CBF and BOLD signal were input to the nonlinear estimate framework for OEF_0 estimation.

The final two sources of error introduce the effects of the violation of the assumption of isometabolism during hypercapnia and hyperoxia that have been suggested in some previous investigations (as reported in Paragraph 2.2.3.4 in Chapter 2). The $CMRO_2$ changes with hypercapnia and hyperoxia were introduced during the BOLD signal generation with the detailed model. The ranges of changes in oxygen consumption were fixed below extreme values found

in literature: 1% change in $CMRO_2$ for 1 mmHg change in end-tidal CO_2 (against 1.5%/mmHg found by Xu et al., (Xu et al., 2012)) and 1% change in $CMRO_2$ for 40mmHg change in end-tidal O_2 (against between 1.86%/40mmHg and 1.16%/40mmHg found by Xu et al., (Xu et al., 2011) for hyperoxia with a fraction of inspired O_2 of respectively 50 and 98%). These values therefore led to errors spanning between -7 and +7% change in $CMRO_2$ during hypercapnia and -5 and +5% change in $CMRO_2$ during hyperoxia, for the chosen respiratory design (des. B, Figure 3-4).

Performance in estimating OEF_0 in the simplified calibration model was compared to the original calibration model. The nature of the difference between these models was further investigated by analysing the role of the balance between the fractions of capillary and venous baseline CBV (respectively ω_C and ω_V) and the exponents relating CBF to total, capillary and venous CBV (respectively $_t$, $_C$ and $_V$, in Griffeth and Buxton (Griffeth and Buxton, 2011), see Figure 3-2). In particular, estimates of OEF_0 were calculated for the interleaved design (des. B, Figure 3-4) where, on top of the four varying input baseline physiological parameters, different values of ω_C and ω_V, $_t$, $_C$ and $_V$ have been considered. The values considered matched the ones used in (Griffeth and Buxton, (Griffeth and Buxton, 2011), that is: [0.6 – 0.2] and [0.2 – 0.6] for ω_C and ω_V while maintaining the arterial blood volume fraction equal to 0.2, [0.3 – 0.65] for $_t$, [0 – 0.33] for $_C$ and [0 – 0.65] for $_V$.

Finally the robustness of the simplified model has been tested against variations of two experimental parameters: the echo time TE and the static magnetic field B_0. This was done to assess the sensitivity of the optimization process to such parameters and the degree of error introduced in the estimates of OEF_0 when using the simplified model in applications other than the one it has been optimized for (i.e. TE = 32 ms and B_0 = 3 T).

We firstly repeated the process of optimization of α and β on datasets of synthetic BOLD signals created for TE of 22, 27, 32, 37 and 42 ms at both 3 and 7 T. Only the simultaneous design (des. A, Figure 3-4) was considered in this case, as the interleaved design (des. B) is shown not to carry enough information for

the optimization both of α and β. Then, exploiting the same approach adopted for the rest of the error propagation analysis, we estimated OEF_0 with the simplified calibration model considering the different values of TE and B_0 as sources of systematic error. In this case only the interleaved design (des. B, Figure 3-4) was considered for consistency with the error propagation analysis. For the application at 7 T, the detailed model, optimized for 3 T experiments, had to be modified in order to take account of the field dependency of the baseline extravascular signal decay rate and of the baseline intravascular signal decay rate. The former was fixed at 35 ms (Griffeth et al., 2013), while for the latter a quadratic model has been used to extrapolate its dependency on haematocrit, based on data available in literature for experiments at 1.5 and 4.7 T (Silvennoinen et al., 2003), 3 T (Zhao et al., 2007) and 7 T (Blockley et al., 2008).

3.3 Results

3.3.1 The original calibration model

The results of using literature values for the parameters (,β) and fitting the original calibration model to the simulated BOLD signal at 3T using the nonlinear RSS estimates are shown in Figure 3-5. The percentage errors in OEF_0 estimates for values of (0.14, 0.91) and (0.2, 1.3) in both the simultaneous and interleaved gas challenge designs are shown as compared to OEF_0, the input into the detailed model. An overestimate of OEF_0 is observed in all cases, with mean and median values of 11.63 %, and 11.17 % respectively for the simultaneous design with (,β) = (0.2, 1.3) (Figure 3-5,1); 10.46 % and 9.89 % for the simultaneous design with (,β) = (0.14, 0.91) (Figure 3-5,2); 10.54 % and 10.11 % for the interleaved design with (,β) = (0.2, 1.3) (Figure 3-5,3); 10.66 % and 10.14 % for the interleaved design with (,β) = (0.14, 0.91) (Figure 3-5,4). These results provided us with the motivation to optimise the and β parameters in order to minimise this bias.

Figure 3-6 shows the RSS surfaces in the (,β) space for a single mean state (OEF_0 = 0.4, CBF_0 = 55 ml/100g/min, CBV_0 = 5 ml/100g and Hct = 0.44 – top row) and the median across all physiological states (bottom row). A reliable and representative minimum point cannot be found for either type of experimental design; a minimum for each physiological state can be found but not consistently across states, i.e. it is not possible to select a single pair of (,β) values which minimizes the discrepancy between the data generated with the detailed model and the signal fitted with the original calibration model. In the interleaved case this is due to the extreme irregularity of the surfaces in a single physiological state (Figure 3-,2). Then in the median over all physiological states and in the simultaneous cases those surfaces assume a characteristic “valley shape”, whose minima are ill-defined (Figure 3-6,1,3,4). The minima lie in a wide region at the bottom of the valley which appears to broaden once the boundaries of the (,β) space are extended (data not shown). This suggests a difficulty with fitting the

original calibration model, namely, the collinear nature of the relationship between the two parameters and β.

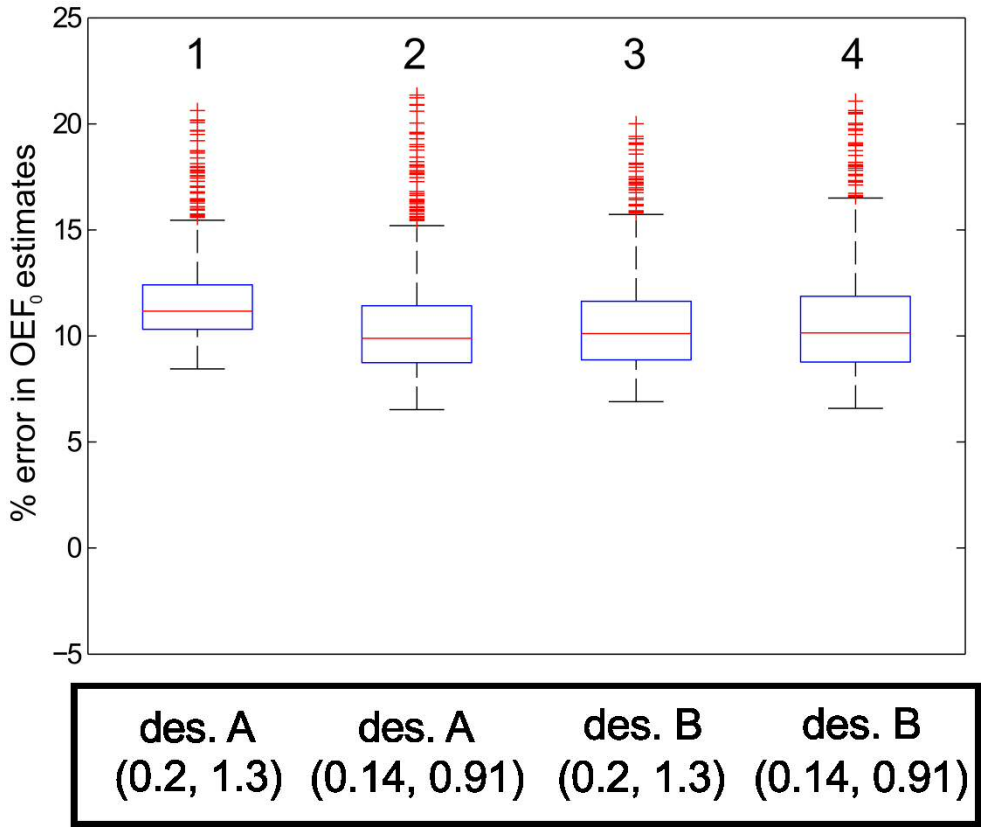

Figure 3-5: Percentage errors in OEF_0 estimates from fitting (residual sum of squares) the calibration model for different literature values of (α,β) parameters and gas challenge design (design A: simultaneous design, design B: interleaved design, referred to Figure 3-2).

Figure 3-7 plots the surfaces for the discrepancy between true OEF_0 and that estimated from the original calibration model over (,β) space. In contrast with the RSS surfaces, similar patterns are observed for the two respiratory challenge designs, but large differences exist between the single mean physiological state and the average one. In all cases, similarly to what has been shown for the RSS analysis, it is possible to find a minimum for each physiological state, but not one representative for all states, demonstrating that an optimal and β combination cannot be prescribed when considering only the minimisation of the error in measured OEF_0.

3.3.2 Collinearity in the original calibration model

Figure 3-8 shows the lines extrapolated from the points of minimum of the RSS and dOEF median curves for the five different gas challenge designs considered. The intersection for the simultaneous design (des. A) is (0.07,1), whereas for the interleaved modulated (des. C) is (0.06,0.7) and for the interleaved modulated in CO2 (des. D) is (0.06,0.85). An optimum combination was found also for the interleaved design modulated in CO2 (des. E) but laying outside the space of the (,β) considered for our analyses (0.08,0.4). For the interleaved design (des. B), the distribution of the minima is such that it is not informative to calculate a line of best fit. Figure 3-8 also shows how the intersection for designs A, C and D differ from the optimum values of (,β) previously proposed in literature and here marked with a black circle and a green star (respectively (0.3,1.2) and (0.14,0.91)).

Figure 3-9 illustrates statistics on the logarithm values of the two indices, RSS and dOEF. Three values of fixed (,β) were tested in order to remove the effect of collinearity between parameters and β. These values were 0.91, 1.3 and 1: the first two taken from the literature, while the last chosen as the value that effectively removes the effect of β from the model. The minima of the median curves reflect the behaviour of the whole set of physiological states for the simultaneous design (des. A) and for respiratory designs when CO_2 delivery modulation is exploited in interleaved designs (des. C, D). By comparison, in the

interleaved design (des. B) there is more variability across physiological states, suggesting that the choice of a minimum would be far less representative of the general behaviour of the curves. Also the magnitude of the RSS index is so low that it becomes uninformative (note the change of scale in Figure 3-9, des. B compared to the others). Finally the result for the interleaved design modulated in O_2 (des. E) is noteworthy as the calculated RSS index seems to be insensitive to the considered values of and therefore a significant minimum cannot be identified.

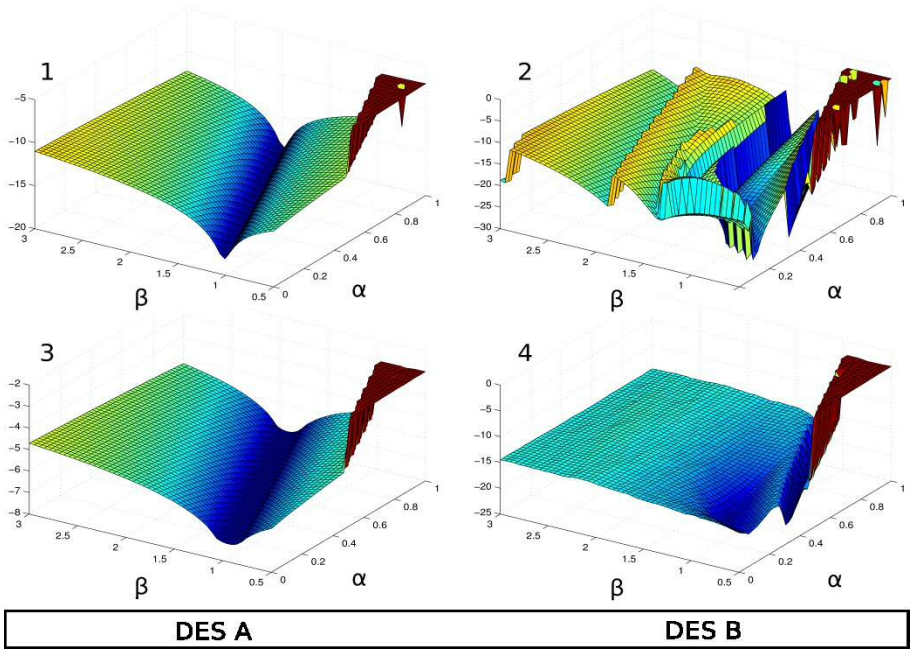

Figure 3-6: Logarithm of the RSS surface in the (α,β) space for simultaneous (des. A) and interleaved (des. B) designs. (1) and (2) show surfaces for a single mean physiological state (OEF_0 = 0.4, CBF_0 = 55 ml/100g/min, CBV_0 = 5 ml/100g and Hct = 0.44). (3) and (4) show surfaces for the median calculated on all 1000 states. In both cases a reliable minimum cannot be found and the collinearity between the two parameters α and β is highlighted.

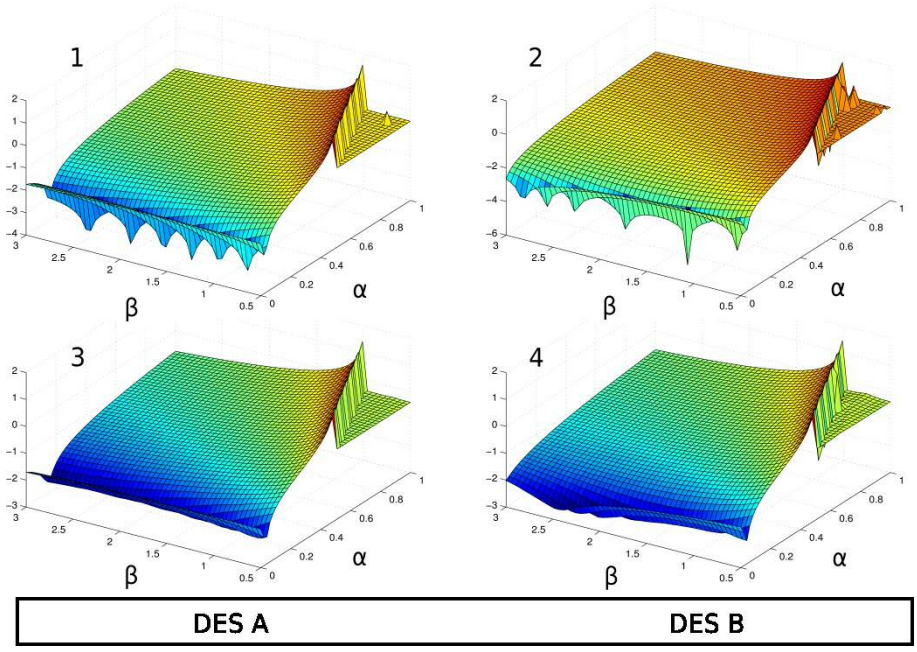

Figure 3-7: Logarithm of the absolute error in OEF_0 estimate surface in the (α,β) space for simultaneous (des. A) and interleaved (des. B) designs. (1) and (2) show surfaces for a single mean physiological state (OEF_0 = 0.4, CBF_0 = 55 ml/100mg/min, CBV_0 = 5 ml/100g and Hct = 0.44). (3) and (4) show surfaces for the median calculated on all 1000 states. In both cases reliable minima cannot be found.

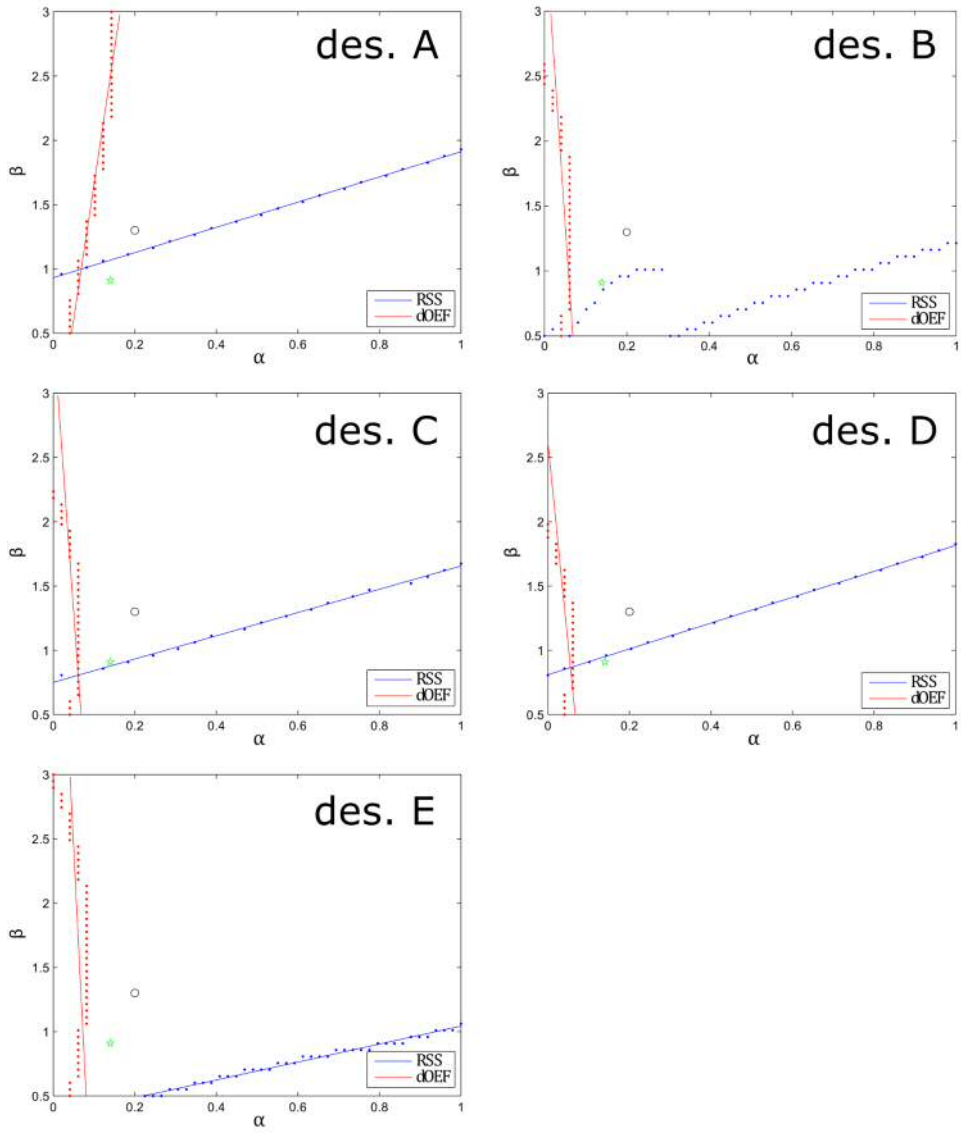

Figure 3-8: Lines extrapolated from the minimal points of the median curves for the residual sum of square (RSS) and absolute discrepancy in OEF_0 (dOEF) indices in all different designs. The combinations of (α,β) for which minima coincide are (0.07,1.00) in design A, (0.06,0.07) in design C, (0.06,0.85) in design D. The combination is outside the search space for design E (0.08,0.4), whereas a line of best fit was not calculated for the RSS index in design B. Literature combinations of (α,β) are shown with a black circle (0.2,1.3) and a green star (0.14,0.91) for comparison.

3.3.3 The simplified model

For the simplified model, i.e. the original calibration model in which the β parameter is fixed to 1 and the new parameter θ substitutes for , the single optimum value of β has been selected that gives the minimum of the median dOEF curves across the dataset. This value is β = 0.06 for each design (apart from the interleaved one, des. B) as reported in the middle column of Figure 3-9. Strictly, this is a suboptimal solution, given that the minima of RSS and dOEF median curves do not coincide. Nevertheless this choice matches the value of for the intersections found in Figure 3-8. Also, the consistency across designs of selecting this single representative value of the θ parameter for the simplified model offers a practical benefit justified by the results below.

The percentage errors in OEF_0 estimates fitting the simulated signal through minimisation of RSS only using the simplified model are reported in Figure 3-10. The biases in the distributions of estimates from the set of underlying physiological states are only slight, with mean and median values lower that those reported in Figure 3-5: 2.45 %, and -0.35 % respectively for the simultaneous design (Figure 3-10,1 , des. A); 2.83 %, and 0.05 % for the interleaved design (Figure 3-10,1 , des. B); 2.44 % and -0.39 % for the interleaved modulated design (Figure 3-10,1 , des. C); 2.15 % and -0.69 % for the interleaved modulated in CO_2 design (Figure 3-10,1 , des. D); and 3.13 % and 0.33 % for the interleaved modulated in O_2 design (Figure 3-10,1 , des. E). In summary all respiratory designs show similar results with this simplified calibration model. The small value of θ found led us to consider the effect of fixing its value to 0. Results (not reported in figures) showed mean errors in OEF_0 estimates about -6 %, with distributions mainly within the range -10 – 5 %.

Finally in Figure 3-10, 2 the percentage errors in OEF_0 estimates are shown for the simplified model but considering only the physiological states in which the value of each input variable is included in the respective μ±σ range. For all, as expected, the boxplots are tighter than those comprising the wider range of physiological states.

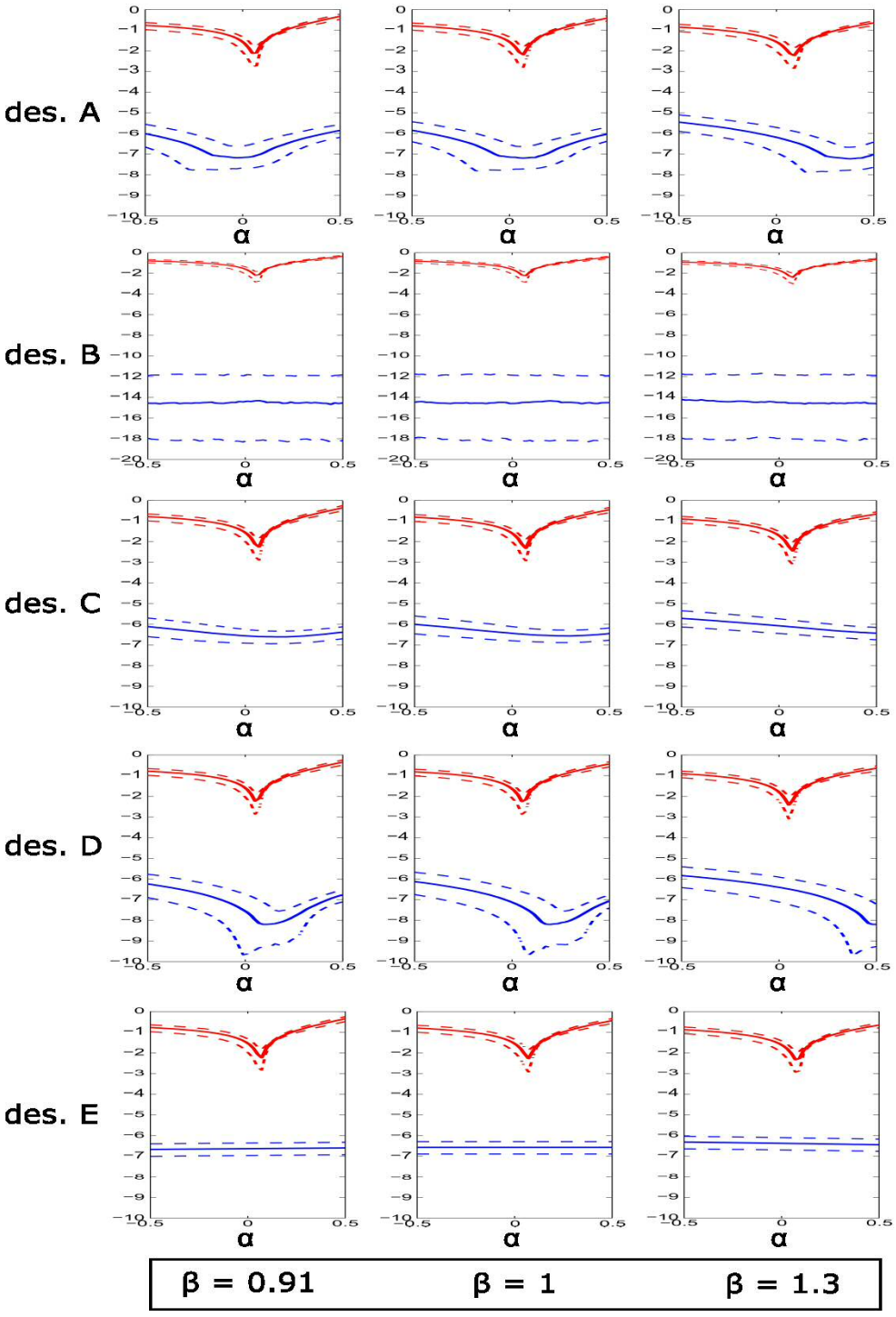

Figure 3-9: Curves of the logarithm of the RSS index (blue) and dOEF index (red) for the calibration model with β fixed to different values. All the designs are considered. The median curves are shown in solid lines, while the boundaries containing the central 75% of the distributions are shown in dotted lines.

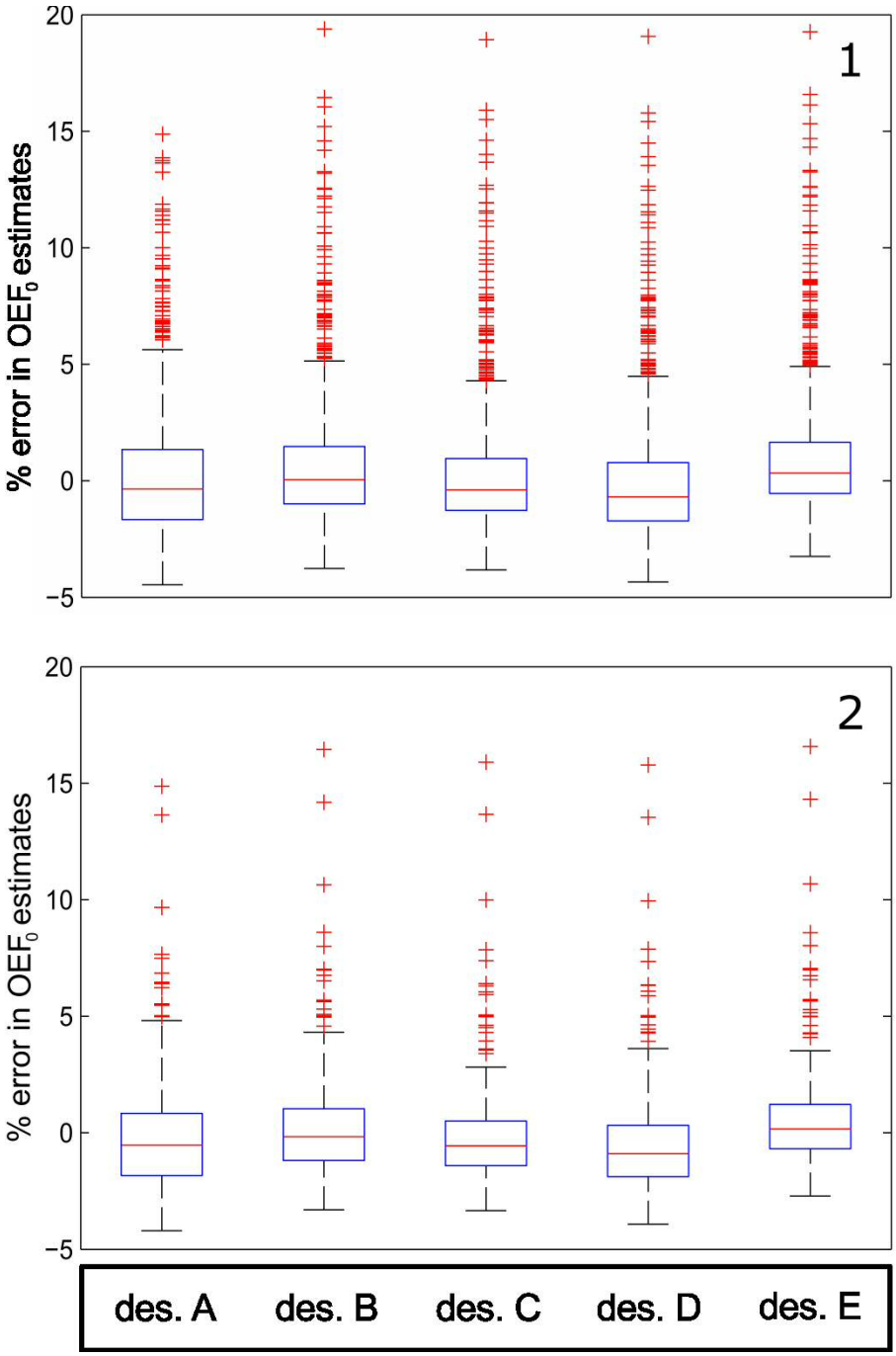

Figure 3-10: Percentage errors resulting from the estimate of OEF_0 using only a nonlinear RSS minimization, simulating the experimental situation. (1) shows results achieved from implementing the simplified model (θ=0.06) on all physiological states. (2) presents results using the simplified model (θ=0.06) with ranges of physiological states considered narrowed to $\mu\pm\sigma$.

3.3.4 Error propagation

Figure 3-11 summarises the results of the error propagation analysis. The upper row (A) reports results from the original calibration model, whereas the lower row (B) reports results from the simplified calibration model. The columns report the effect of the different errors considered. For both models and for all sources of error considered, the performance in estimating OEF_0 worsens as the error increases, and worsens at higher values of true underlying OEF_0. Furthermore, the degree of error affects both the offset and the slope of the scatterplot lines in each of the five cases of error. Of particular note is the effect of altered oxygen metabolism with hyperoxia (Figure 3-11-5 A and B). The relationship between true and estimated values of OEF_0 is non-linear and larger changes in oxygen metabolism lead to a huge increase of error in OEF_0 estimates (some of the results not shown in the figure).

The direction of the effect on OEF_0 is different depending on the error. For both models a positive error in CBF estimation to CO_2 (Figure 3-11-1 A,B), BOLD estimation due to O_2 (Figure 3-11, 3 A,B) and $CMRO_2$ increases due to CO_2 (Figure 3-11,4 A,B), cause an underestimate of OEF_0 while a negative error causes an overestimate of OEF_0 , In the other cases (Error in BOLD estimation to CO_2, Figure 3-11-2 A,B and $CMRO_2$ increase due to O_2, Figure 3-11,5 A,B) the opposite is true.

The principal difference between the original calibration and the simplified model, highlighted in Figure 3-11, is the offset and slope of the lines, most clear in the error-free condition (blue crosses, corresponding to noiseless condition in all panels). The original calibration model shows a slope very close to the unity but also a significant offset that shifts the relationship between true and estimated OEF_0 away from the identity line (plotted as a black line), leading to consistent overestimation of OEF_0. In comparison, for the simplified model, the offset is minimized and the slope is close to unity such that the discrepancy between true and estimated OEF_0 is particularly small over the middle range of OEF_0 values.

Figure 3-12 illustrates the influence of the balance between the fractions of capillary and venous baseline CBV and the effects of altered exponents relating CBF to total, capillary and venous CBV. The estimates of OEF_0 show relatively little sensitivity to changes in all parameters apart from $_V$ (the exponent relating fractional changes in venous blood volume to blood flow, Figure 3-12,4 A,B) and venous blood volume fraction ω_V at lower values of OEF_0. Similarly to Figure 3-11, the main difference between the two models is the offset in the estimate of OEF_0.The biased in the results introduced by altering the blood volume parameters change little between the models and appear independent of offset between the two models.

Figure 3-13 illustrates the sensitivity to changes in TE and B_0 of the optimization approach presented and of the simplified calibration model proposed. In Figure 13-A are shown lines extrapolated from the points of minimum of the RSS and dOEF median curves for the simultaneous design (des. A) at different combinations of TE and B_0. This figure is analogous to Figure 8, where only the case of TE = 32 ms and B_0 = 3 T is reported. Results show that the optimum combinations found are sensitive to both parameters, TE and B_0. However, while for 3 T (Figure 3-13,A, solid lines) the combinations gravitate around the optimum one selected for the simplified model, for 7 T (Figure 3-13,A, broken lines) they are shifted towards values of approximately (0.19,1.2).

Furthermore, while in the first case TE mostly affects the optimal value of β, at 7 T it affects more the optimum α. The scatterplot in Figure 3-13,B reports the error introduced estimating values of OEF_0 with the simplified model from the BOLD signals created at different values of TE and B_0. Similar values are obtained for the other respiratory experiments considered (data not shown). Results highlight that the estimates are only slightly sensitive to variations in TE, with the introduced error being negligibly small when considering 3 T experiments, but showing a larger offset when using the 3 T optimised simplified model at 7 T

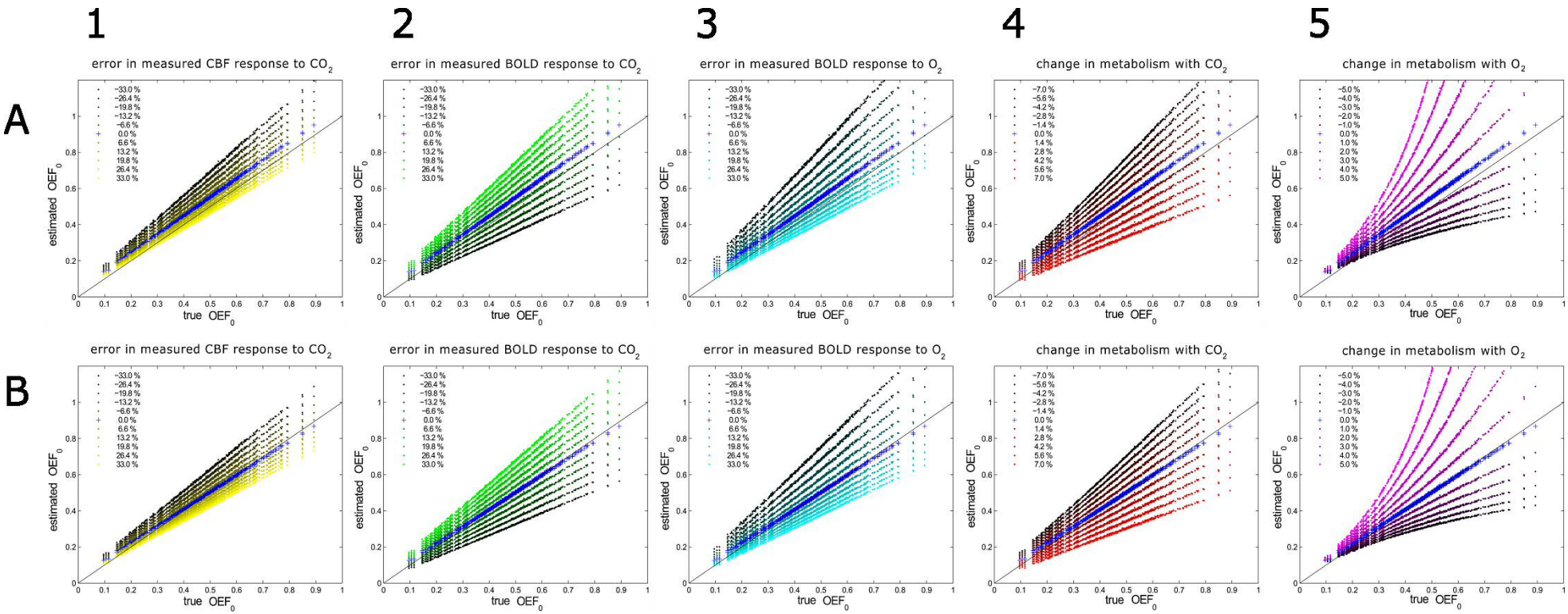

Figure 3-11: Estimated vs true OEF_0 values of the dataset for two different models (A original calibration model, B simplified calibration model) for different sources of error: (1) percentage error in measured CBF response to CO_2, (2) percentage error in measured BOLD response to CO_2, (3) percentage error in measured BOLD response to O_2, (4) change in oxygen metabolism due to +7mmHg change in end-tidal CO_2 and (5) change in oxygen metabolism due to +200mmHg change in end-tidal O_2.

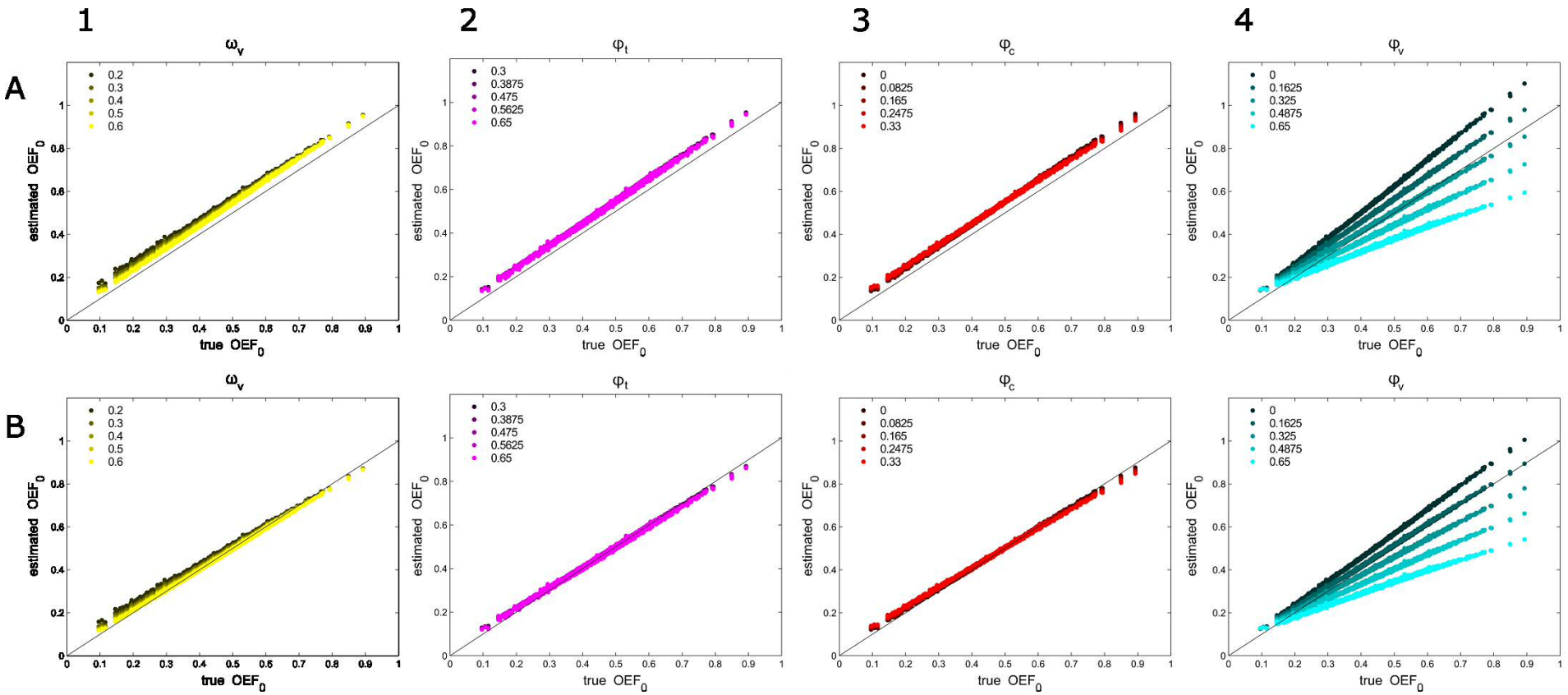

Figure 3-12: Estimated vs true OEF_0 values of the dataset for two different models (A, top row, original calibration model and B, bottom row, simplified calibration model) and different values of: (1) fractions of venous baseline CBV (ω_v, with capillary baseline CBV=0.8-ω_v), exponents relating CBF to (2) total CBV (φ_t), (3) capillary CBV (φ_c) and (4) venous CBV (φ_v).

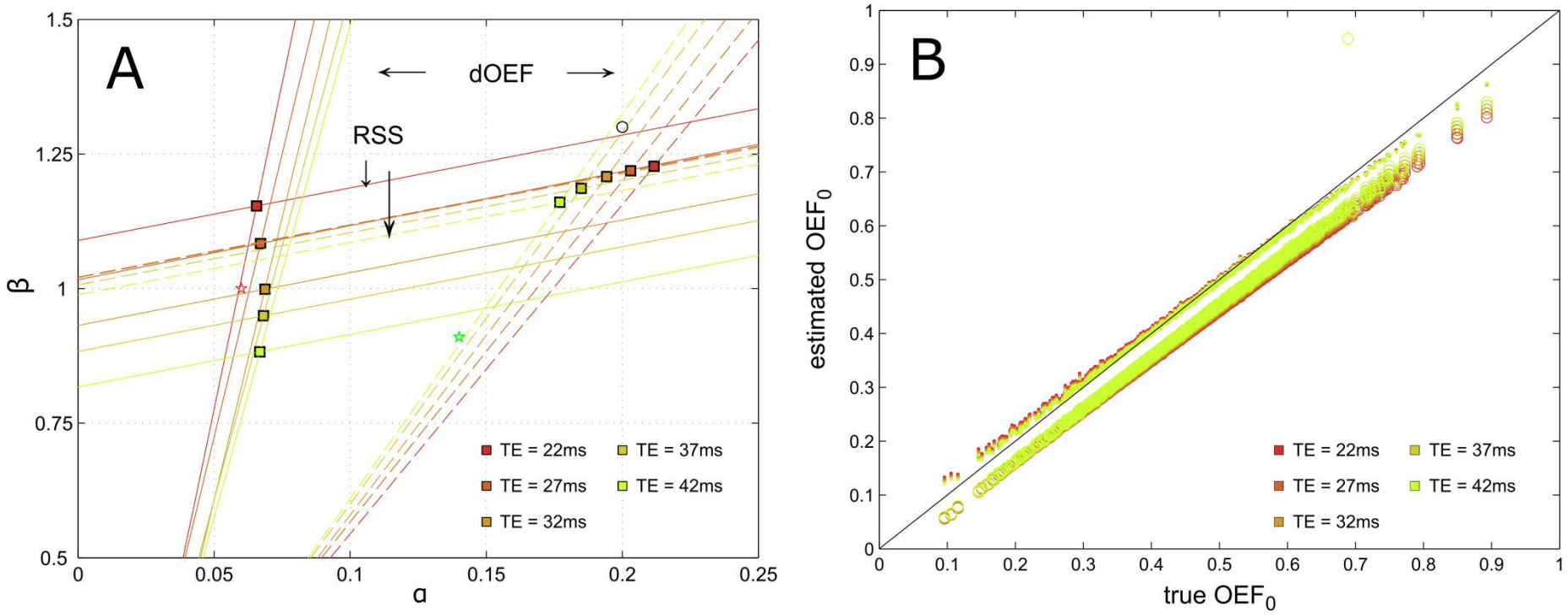

Figure 3-13: A) optimal (α,β) combinations found for different TE and B_0. Shown are extrapolated lines of minimal values of RSS and dOEF indices (solid lines: 3 T, broken lines: 7 T) and combinations previously considered (black circle = (0.2,1.3), green star = (0.14,0.91) and red star = (1,0.06)). In this case only the simultaneous design (des. A) is analysed. B) Values estimated with the simplified model against true values of OEF_0 for different TE and B_0 (dots: 3 T, open circles: 7 T). In this case only the interleaved design (des. B) is considered.

3.4 Discussion

The process that led to the optimization of the original calibration model is summarized in Figure 3-3. Our simulated data was a set of BOLD signals created using the detailed signal model (Griffeth and Buxton, 2011) with Gaussian distributed values of physiological parameters (CBV_0, CBF_0, OEF_0 and Hct) and five different specific respiratory experimental designs employing hypercapnia and hyperoxia, some previously published and some new. Estimates of OEF_0 obtained using the original calibration model (Wise et al., 2013) and literature combinations of α and β using residual sum of squares (RSS) proved unsatisfactory. We therefore considered an index based on the magnitude of the discrepancy between the real and estimated OEF_0 (dOEF) in addition to the RSS. The consequent minimisation led to values of α and β that are a good trade-off between the experimental necessity to fit to the BOLD signal and the capacity to estimate OEF_0 in an unbiased manner.

We demonstrate substantial collinearity between the parameters of the original calibration model when estimating OEF_0, a feature that leads to erroneous results illustrated by the valleys in Figure 3-6 and Figure 3-7, in which we have almost the same value of the RSS and dOEF indices for very different combinations of α and β which therefore produce broad distributions of potential OEF_0 estimates. The collinearity suggests that for practical applications using the respiratory challenges here analysed, values of α and β need to be fixed. We overcame the collinearity, in a practical sense, by the analysis of the relationship between the two indices for fixed values of β and fixing the α and β parameters to those values where minima of both RSS and absolute discrepancy in OEF_0 estimate curves coincided, providing optimised OEF_0 estimates and BOLD signal fits. Figure 3-8 shows that this is not achieved using the literature values of α and β and explains the bias in the results in Figure 3-5.

The consequence of our practical optimisation in this work is that we take α and β parameters to have no specific physiological meaning compared to those

introduced in the original models by Davis (Davis et al., 1998) and Hoge (Hoge et al., 1999a). Figure 3-9 shows that once alpha is fixed to the value minimizing the dOEF index, the sensitivity of the model to the chosen β is only small. In fact the values of β considered mostly affect the behaviour of the RSS index, which is orders of magnitude lower than the dOEF one. This therefore allows us to fix β to 1 and thus to introduce the simplified model. Note that the approach we take is similar to others recently taken (Blockley et al., 2015; Griffeth et al., 2013), in which β has been fixed to 1. Differences arise when considering that in those cases α has been chosen as Grubb's parameter (Grubb et al., 1974), instead of an optimized fitting parameter, as in the present case. The one we propose is of course, strictly speaking, a suboptimal model, in which, for the purpose of simplicity and generality of the model, the best possible fit to the data is compromised in favour of a better estimate of OEF. This model overcomes the difficulty of defining an optimum value for α and β in the interleaved gas challenge designs (des. B, Figure 3-5) and of needing to consider a different pair of parameters, α and β, for each different respiratory experiment. For all the designs considered, the distributions of percentage errors in OEF_0 estimates lay almost exclusively within the ±5% range, with rare outliers. This same accuracy, assuming good estimates of CBF, would be directly translated into $CMRO_2$ estimates through the defining relationship ($CMRO_2 = CBF \cdot OEF \cdot CaO_2$). The simplified model shows good performance for all interleaved modulated designs, which mimic more closely the behaviour of a real experiment in which end tidal values will vary over time and between hypercapnic and hyperoxic blocks. The simplified model offers, therefore, a reliable and adaptable tool for estimating OEF_0, and therefore absolute $CMRO_2$, across a range of respiratory experiment designs. Indeed, the simulation framework that we have presented could be applied to any arbitrary respiratory experimental design.

Given the substantial equivalence between experimental designs in their ability to estimate OEF_0 once the model parameters are fixed, we may substitute the more sophisticated experimental designs, in which both CO_2 and O_2 are elevated simultaneously, with simpler interleaved designs (as in Bulte et al., (Bulte et al., 2012)). The simplification achieved would be significant firstly in terms of

instrumentation and control of the experiment, as this requires only one gas to be delivered at any given time. Moreover the BOLD signal behaviour itself is likely to be simplified in an interleaved block sequence, less affected for instance by transients between different levels of hypercapnia and hyperoxia. Both of these improvements may also lead to more rapid data acquisition.

Our simulated results also help to explain the estimates of OEF_0 in our previous study (Wise et al., 2013). Figure 3-5 reports overestimates of OEF_0 when using the original calibration model with two pairs of literature (α,β) parameters, leading directly to overestimates in $CMRO_2$. In our previous study (Wise et al., 2013) experimental data were fitted with literature values of α and β. This may help to explain the higher values of $CMRO_2$ reported in Table 1 of the Wise and colleagues study (Wise et al., 2013), compared to previous MRI and PET studies (Bulte et al., 2012; Gauthier and Hoge, 2012; Ito et al., 2004). From the current work, similar biases in OEF_0 estimates from other groups' work using similar respiratory challenges and literature (α,β) values would also be expected.

The limitations of the present study lie mainly in the synthetic nature of the data. In the BOLD signal generation process no noise was added to the resulting time series. We made this choice because our focus was on the analysis of the model properties and in particular on its bias in OEF_o estimation, with an approach similar to that of Griffeth and Buxton (Griffeth and Buxton, 2011). The simulation environment was necessary to study and optimise the behaviour of the original calibration model, in particular for the analysis of the discrepancy in OEF_0 estimates, which leads to the identification of the optimum parameters α and β and to the definition of a simplified model with an optimum parameter θ. Even though synthetic, the set of simulated BOLD signals was designed to span a wide range of physiological states defined by CBF_0, CBV_0, OEF_0 and Hct. The results show the distributions of errors in OEF_0 estimates to be narrow with median values close to 0, demonstrating a substantial insensitivity to differences in the underlying physiological state for both the original calibrated model and the simplified one. In particular these models to estimate OEF are robust to variations in haematocrit that is considered to be an unknown variable, and therefore a source of uncertainty.

Using the simplified model, the analysis of a subset of physiological states in which the value of each input parameter was included in the narrower mean ± one standard deviation range, that is, a more realistic range for the healthy brain, led to even more accurate final results in OEF_0 estimates (Figure 3-10,2). This suggests that the outliers found using the wider range of physiological states may be due to particular combinations of unusual physiological states rather than possible critical issues with the simplified model.

The error propagation analysis illustrated the differences between the original and simplified calibration models and their likely practical limitations. Figure 3-11 shows the offset in OEF_0 estimates in the application of the original model, eliminated by the new simplified model. Both models are susceptible to errors in the measurement of the CBF and BOLD responses to the respiratory challenges. Performance in terms of absolute error in estimated OEF_0 tended to be worse at higher OEF values, although fractional errors were largely independent of true OEF_0. In practice, the accurate estimation of CBF responses to CO_2 is more challenging, and carries greater uncertainty, than the estimation of BOLD signal responses to CO_2 and O_2, largely as a result of the low contrast-to-noise of arterial spin labelling. The errors represented in Figure 3-11,1 (CBF response to CO_2) are likely to be of a realistic order of magnitude, depending on a number of experimental factors, while the uncertainty of BOLD responses is likely to be smaller and contribute less to OEF_0 estimate error in practice.

Changes in $CMRO_2$ during hypercapnia and even more during hyperoxia would strongly affect the estimated OEF_0. This is to be expected, as the assumptions of isometabolism in hypercapnia and hyperoxia, although still object of discussion, are commonly assumed as hypotheses for BOLD calibrated methods (see Paragraph 2.2.3.4).

The most relevant studies suggesting deviation from isometabolism during respiratory tasks report hypometabolism resulting from both hypercapnia and hyperoxia with relative decrease in $CMRO_2$ respectively up to 13% (for a +10 mmHg increase in end tidal CO_2, (Xu et al., 2011)) and 10% (for a 50% fraction of inspired O_2, (Xu et al., 2012)). These, according to our results, would translate in

very severe errors in OEF_0 estimates even for average values of OEF_0: 50% overestimate in hypercapnia and 42% underestimate in hyperoxia (for the simplified calibrated model with OEF_0 = 0.4 and $CMRO_2$ changes scaled to match the variations in end tidal CO_2 and O_2 of our interleaved design, des. B, Figure 3-5). This indicate the failure of both the original and the newly proposed model in accordance with results from Blockley and colleagues (Blockley et al., 2015) when testing the effect of changes in metabolism during hypercapnia on OEF estimates for calibrated BOLD methods.

Further investigation of the circumstances in which $CMRO_2$ is altered needs to be performed. It is possible that, with mild respiratory challenges that limit the violation of the assumption of isometabolism, the errors in OEF_0 suggested by Figure 3-11,4 and Figure 3-11,5 can be maintained within practically acceptable levels. However, we must be cautious in future assumptions of isometabolism in studies of cerebral pathology.

Finally it has been demonstrated that the better estimates of OEF_0 obtained with the simplified model, and more specifically the absence of the offset affecting the estimates of the calibration model, are not dependent on the particular balance between the fractions of capillary and venous baseline CBV or the exponents relating CBF to CBV used in the detailed model for creating the synthetic BOLD signal. This suggests that the optimization carried out and the performance of the simplified model is not significantly dependent on the characteristic features of the detailed model when considering the blood volumes of the venous and capillary compartments. The effects of different blood volumes will be partly absorbed into the parameter M in the original and simplified calibration models. While this is often considered in studies using the original calibration model as the maximum achievable BOLD response, in the current framework where the focus is the unbiased estimation of OEF, we do not interpret its biological significance and consider it simply as a fitting parameter of no particular interest. In fact, the role of M in our approach is drastically different from other early approaches to calibrated fMRI. In those cases it is used to calibrate changes in BOLD signal and therefore accurate estimates of M are crucial for accurate assessment of changes in oxygen metabolism. In our approach instead, thanks to

a model in which hypercapnia- and hyperoxia- induced changes are both accounted for simultaneously, M, although still estimated, is just a by-product of an estimation of OEF_0 and has therefore been put into the background. Finally, given the different form of the simplified calibration model, we expect the estimate of M obtained to be different to those reported in literature as they are representative of different information.

Effects of considering different values of TE and B_0 are investigated showing that the optimal combination of α and β is sensitive to TE at both 3 and 7 T. However, at 3T the error introduced in the estimates of OEF_0 over a practical range of TE is negligible. Conversely, the effect of B_0 cannot be ignored as results at 7 T show that using the simplified calibration model would lead to a significant bias in the estimates of OEF_0 and therefore another (α,β) combination should be used. Considering a characteristic TE of 25 ms for a GRE experiment at 7 T, the optimal combination found is about (0.21,1.245). Our analysis, therefore, not only supplies a complete picture of the influence of TE and B_0 on the newly proposed model, but also demonstrates how our optimization approach can conveniently be adapted by other groups to different research settings, such as 7 T experiments.

3.5 Conclusions

In conclusion, we have demonstrated our simulation framework as a useful means of testing calibration models for respiratory experiments aimed at measuring OEF_0. We have shown that the proposed simplified model is a potentially valuable tool for the unbiased evaluation of OEF_0 and therefore absolute $CMRO_2$ in studies using respiratory challenges. In particular, we would recommend the simplified calibration model as it offers accurate results along with reduced complexity and enhanced flexibility with respect to the respiratory design of the experiment.

As the model has been found to be particularly affected by errors in measurements for high values of OEF_0, its application for absolute estimates of $CMRO_2$ may not be optimal in those pathological conditions where extreme values of OEF_0 might be expected. In considering practical experimentation, since similar accuracy is achieved across different respiratory challenge designs when θ is fixed to its optimal value in the simplified model, the least complex interleaved designs may be used with that model with no detriment to the OEF_0 estimates.

These guidelines will be applied for the studies in Chapter 4 and Chapter 5, where an interleaved design is used for the respiratory tasks and the simplified calibration model is integrated in the estimation framework used.

Chapter 4

Repeatability study on a dual calibrated fMRI method for estimating brain oxygen metabolism

In this study we assess the repeatability of a novel estimation framework recently developed in our centre. Dual-echo GRE data from a dcFMRI experiment are related to the underlying physiology through a forward model. With a Bayesian estimate we are then able to measure five parameters: CBF, OEF_0, CVR, CBV and $CMRO_2$. Measurements of correlation, ICC and CV are exploited to show that the results are characterised by a level of repeatability comparable to that obtained with previous techniques (both MRI and PET), but with an improved spatial resolution. The information supplied by such maps is of extreme interest for applications aimed at studying brain physiology across grey matter.

4.1 Introduction

In this study, we want to assess the repeatability of the estimates of brain haemodynamics and metabolism obtained from dual calibrated BOLD experiments with a novel forward model developed in our lab (Germuska et al., 2015). We do this with a test-retest repeatability experiment on ten healthy volunteers in the resting state. In particular, our aim is to evaluate the precision and reliability of the estimates and to collect reference data in order to determine the viability of the estimation framework adopted for future studies. Results will be compared to recent similar repeatability studies on brain metabolism with PET (Bremmer et al., 2011) and MRI (Barhoum et al., 2014; Liu et al., 2013) techniques.

As mentioned, the estimates presented are based on a newly developed forward model that describes analytically the contributions of BOLD signal, ASL signal and of the measured end-tidal partial pressures of CO_2 and O_2 ($PetCO_2$, $PetO_2$ respectively) to the measured dual echo GRE signal in a dual calibrated BOLD approach. We are then able to estimate quantitative maps of five main physiological parameters involved in brain metabolism across grey matter: OEF_0, CBF, perfusion-induced CVR, venous CBV and $CMRO_2$. In parallel to these, another set of measures of brain haemodynamics is provided for comparison by an already validated multi-inversion time ASL technique (mTI-ASL), developed by Chappell and colleagues (Chappell et al., 2010).

4.2 Materials and methods

4.2.1 Participants and experimental design

Ten healthy volunteers (4 females, age = 27±10) were recruited for this study. Exclusion criteria were introduced with special attention to possible difficulties in complying with respiratory tasks (asthma, smoking, cold/flu, etc.). Volunteers' tolerance of hypercapnic periods and prolonged breathing through a facial mask was tested with a benching session held in the days before the scanning session. The study was approved by the local ethics committee and written informed consent was obtained from each participant prior to each session.

Each participant was scanned at resting state (eyes open) on a single scan session and fMRI acquisitions were repeated twice for a total duration of about 60 min. A multi inversion time dual echo scan (mTI scans, 10 min) was acquired, followed by a dual calibrated fMRI scan (dcFMRI scan, 18 min). These same scans were then repeated. During each of the dcFMRI scans an 18 min respiratory task was performed, with interleaved levels of hypercapnia, hyperoxia and medical air being delivered to the subjects. An anatomical scan was also acquired for segmentation and registration to anatomical space when not already available.

4.2.2 Gas delivery, breathing circuit and respiratory task

The respiratory task design we adopt is similar to interleaved paradigms previously presented in literature (Bulte et al., 2012; Wise et al., 2013) and was optimized according to results from modelling with real noise carried out in our centre in collaboration with Dr. Germuska. The design includes three periods of hypercapnia interleaved with two periods of hyperoxia, for a total duration of 18 minutes (see Figure 4-2,B). In order to achieve hypercapnia, fixed values of 5% CO_2 (balance air) were administered. Instead, as regards O_2, the levels of administered gas were modified with positive and negative emphasis. This meant delivering short periods of respectively 100% O_2 (14s) and 10% O_2 (40s) in order to accelerate the process of reaching the hyperoxic state and then return to

normoxia. It is noteworthy that although hypoxic mixtures were administered, the short duration did not induce arterial blood hypoxia. Inspired fractions of 50% O_2 (balance air) were delivered during plateau periods. Supplies of 5% CO_2 (balance air), 10% O_2 (balance N_2), 100% O_2 and medical air were delivered at a flow rate of 25 l/min to the gas mixing chamber which was placed in the MR control room. The mixing chamber was then connected to the breathing circuit through a humidifier. An independent O_2 backup cylinder was also connected directly to the breathing circuit for safety reasons. The gas delivery system consisted of a laptop personal computer using in-house Matlab software (Mathworks, Natick, MA, USA) to control the voltage output from a NI-DAQ AD converter (National Instruments, Austin, TX). The output voltages were then fed into four mass flow controllers (MKS Instruments, Wilmington, MA, USA) that allowed us to administer the fixed flow of selected gas. The respiratory circuit adopted was similar to the one proposed by Tancredi and colleagues (Tancredi et al., 2014). This circuit includes a system of one-way valves that minimizes re-breathing and an open reservoir that allows the subject to breath room air in case of failure of the delivery system (see Figure 4-1). Gas levels were sampled from the volunteers' facemask and tidal partial pressures of O_2 and CO_2 were measured and recorded using rapidly responding gas analysers (AEI Technologies, Pittsburgh, PA, USA).

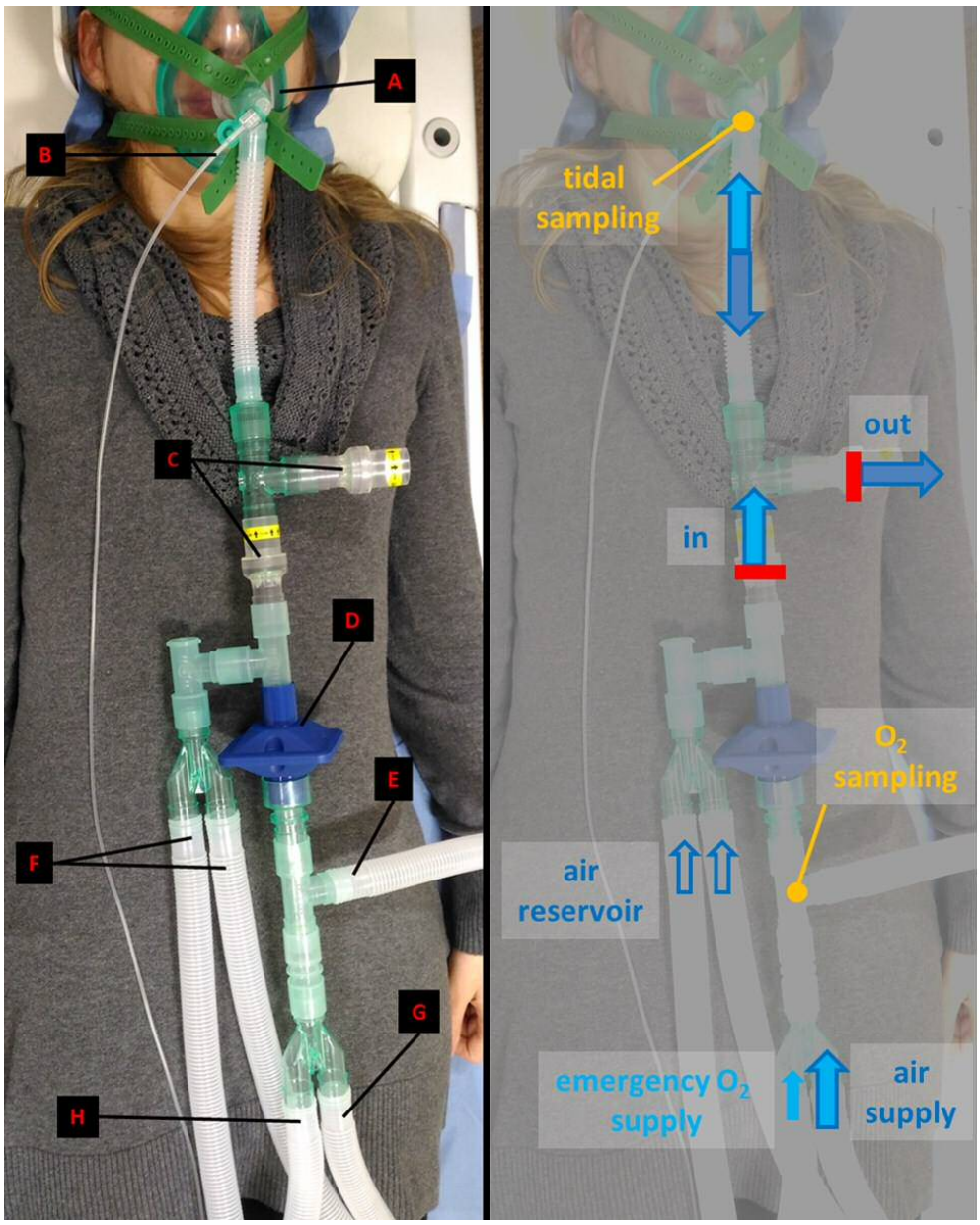

Figure 4-1: The breathing circuit in use, based on the one proposed by Tancredi and colleagues [19].

A – fitted mask; B – tidal gases sampling line; C – one-way valves; D – bacterial filter; E – supplementary O_2 sampling line; F – reservoir limbs (~1.3 l, open end); G – air mixture supply; H – emergency O_2 supply.

4.2.3 fMRI data acquisitions

Scanning was performed on a 3T GE HDx MRI (GE Healthcare, Milwaukee WI) with a body transmit coil and 8-channel head receive coil. All participants underwent (or had available) whole brain T1-weighted structural scans (3D FSPGR, 1x1x1 mm voxels, TI/TR/TE = 450/7.8/3 ms).

As regards the mTI PASL, dual-gradient echo (GRE) readout and spiral k-space acquisition imaging was used with the following acquisition parameters: TE1 = 2.7 ms, TE2 = 29 ms, matrix = 64x64, voxel size = 3x3x7mm^3, slice gap = 1 mm, 12 slices. Automated linear shimming with the built-in software (GE HDx) was performed. Perfusion weighting on the two scans included four equally spaced inversion times each: 150, 300, 450, 600 ms and 1000, 1400, 1800, 2200 ms. Proximal inversion and control for off-resonance effects (PICORE) tagging scheme was used with a quantitative imaging of perfusion using a single subtraction (QUIPSS II) cut-off at 700ms for TI>700 ms. Label thickness was 200mm with a 10-mm gap between the distal end of the labelling slab and the most proximal imaging slice. In both cases a variable TR increasing with the value of TI was used, so that TR-TI was fixed to 0.85 s for TI<0.7 s, while was fixed to 0.7 s for TI>0.7 s. This resulted in minimization of imaging time. Twenty control–tag pairs were acquired for each TI and each TI was repeated separately, resulting in a total of 160 repetitions and a final acquisition time of about 3.5 and 6 minutes respectively.

During the dcFMRI acquisition, simultaneous perfusion and BOLD imaging data was collected using a PASL PICORE, QUIPSS II imaging sequence with a dual-gradient echo (GRE) readout and spiral k-space acquisition with the same prescription as the mTI scans: TE_1 = 2.7 ms, TE_2 = 29 ms, TR = 2.2 s, Flip Angle = 90°, FOV = 22 cm, Matrix = 64 x 64, 12 slices of 7 mm thickness with an inter-slice gap of 1 mm acquired in ascending order, TI_1 = 700 ms, TI_2 = 1500 ms for the most proximal slice and was incremented for the subsequent slices, tag thickness = 20 cm, 10 mm gap between labelling slab and bottom slice, 10 cm QUIPSS II saturation band thickness. This resulted in a 490-volume acquisition (245 tag-control pairs) for each of the dcFMRI acquisitions.

All mTI and dcFMRI scans were preceded by two calibration scans. The first consisted in a single shot EPI scan to estimate the equilibrium magnetization of brain tissue (M_0), used for perfusion quantification (Çavuşoğlu et al., 2009), with the same acquisition parameters as for the perfusion-weighted scans, except for being acquired with fully relaxed magnetization and no labelling. The second was a low resolution, minimal contrast image used for coil sensitivity correction in GE scanners (Wu et al., 2011), with the same acquisition parameters as for the equilibrium magnetization scan, except for TE = 11 ms and TR = 2 s.

4.2.4 dcFMRI signal modelling

The forward model (Germuska et al., 2015) used in this work and later in Chapter 5 is based on a signal model constructed by combining a detailed description of the arterial spin labelling (ASL) signal developed by Woolrich and colleagues (Woolrich et al., 2006) and a model of the BOLD model developed in our centre in collaboration with Dr Mike Germuska. The proposed method simultaneously estimates signal changes from a dual-echo acquisition to find the physiological parameters that provide a best fit to the acquired data.

The analytical description of the model allows us to adopt two different estimation approaches: one exploiting least-mean-square (LME) analysis and the other - adopted in this work - exploiting a Bayesian approach. Computationally, this is done with a *Matlab* toolbox for variational Bayesian approaches (VBA) developed and made available by Daunizeau and colleagues (Daunizeau et al., 2014).

In this paragraph we firstly report the equations defining the forward model and then supply a quick overview of the VBA approach. A more detailed description is to be found in the original papers (Daunizeau et al., 2014; Germuska et al., 2015).

4.2.4.1 The forward model

The total MR signal S_{TOT} resulting from a dual-gradient echo (GRE) imaging sequence with a PASL PICORE, QUIPSS II scheme for ASL signal can be expressed as:

Eq. 4-1

Where S_{ASL} is the ASL signal and the BOLD contribution is accounted for by changes in transverse relaxation rate R_2^*. Practically these two contributions to the overall signal S_{TOT} are considered separately, with the measured TE_1 time series used to calculate the ASL signal, and the TE_2 used to calculate the BOLD signal. This is acceptable assuming changes being fairly slow (compared to TR) and therefore lack of cross-contamination of the two signal signals. Despite this, given that all the model parameters are estimated in a single forward model, information from the one signal is used to infer on the other.

As regards the latter, it can be expressed following the model first proposed by Wise and colleagues (Wise et al., 2013) and then simplified in Chapter 3 as:

Eq. 4-2

and Eq. 4-3

Where A is a scaling factor depending on field magnitude and geometry fixed to 3.7, [dHb] is the deoxy-haemoglobin concentration, $PaCO_2$ is the arterial partial pressure of O_2 and CVR is the cerebrovascular reactivity (in $\%\Delta CBF/mmHg_{CO2}$). Then OEF_0 can be calculated from the expression for $[dHb]/[dHb]_0$ (Wise et al., 2013):

Eq. 4-4

Prior to analysis and during the fitting process, the T_2^* signal is high-pass filtered with a cut-off value of 340 s to remove any significant baseline drift.

The ASL contribution S_{ASL} can also be expressed, following the Woolrich model (Woolrich et al., 2006), as a sum of a static component (S_s) and a component due to perfusion (S_b):

Eq. 4-5

Where the static component is expressed in terms of changes in voxel magnetization M:

Eq. 4-6

So that changes in M_0 are assumed to derive from a change in blood volume and water exchange and can therefore be used to calculate venous CBV. M_0 is estimated by the model, while a fixed value of 5 ml/100g was instead used for tissue CBV.

The perfusion component is then expressed in terms of changes of CBF and the kinetic PASL model:

Eq. 4-7

Where $M_{0,blood}$ and T_{1b} are respectively the baseline magnetization and the longitudinal relaxation time of blood, R_{pn} is 1 for tag and -1 for control and finally TI_1, TI_2 and δt are the times time to saturation, time to imaging and transit time defined by the QUIPSS II tagging scheme. For T_1 signal the high-pass filter is operated by the surrounding subtraction process. Although the mean signal for each echo time is preserved so that $R_{2,0}^*$ and $M_{0,blood}$ can still be estimated.

The relationship between PaO_2 and arterial T_{1b} is taken to be linear (as per Ma and colleagues, (Ma et al., 2014)) and described by:

Eq. 4-8

The unknown parameters were fixed to literature values, with b = $-6.14x10^{-4}$ (extrapolated from Ma and colleagues, (Ma et al., 2014)) and c = 1.793 (from Lu and colleagues, (Lu et al., 2004)). As regards the contribution of $PetO_2$ and to $PetCO_2$ to calculated CaO_2 and $\Delta PaCO_2$ respectively, local variation of the haemodynamic response (*hr(t)*) was allowed modelling each of them separately as gamma-variate functions:

$$\eta \qquad \eta \qquad \eta \qquad \eta$$ Eq. 4-9

with t_{max} (fixed to 0.2 s) denoting the time of peak and η_i free parameter determining the rise and fall times of the response (with i = CO_2, O_2). Finally $CMRO_2$ is calculated as:

Eq. 4-10

4.2.4.2 The Bayesian estimation framework

Bayesian inference is an approach to statistical inference that allows us to estimate parameters of a stochastic model based on the contribution of both evidence from measurements and prior knowledge on the parameters and the model themselves. At the basis of Bayesian inference is Bayes' theorem, which expresses the relationship between the probability of a group of unknown parameters θ of a model given and a set of measurements X as:

Eq. 4-11

Where $p(X|\theta)$ is the probability of the measurements given the parameters, $p(\theta)$ is the *a priori* knowledge on the parameters and p(X) is the is the probability of the measurements. $p(\theta|X)$ is also known as posterior distribution, while $p(X|\theta)$ and $p(\theta)$ are respectively the likelihood and the prior on the parameters θ.

What makes the problem of determining the posterior distribution challenging is the fact that in general the form for $p(X|\theta)$ is unknown and therefore there might be no analytically exact solution to the problem. In these cases then the posterior distribution has to be estimated. This can be done with approaches like Markov Chain Monte Carlo (MCMC) techniques, in which a numerical approximation to the exact posterior is provided, typically with long computational times. Other approaches instead – such as the VBA one adopted by Danizeau and colleagues in their software (Daunizeau et al., 2014) – only supply an approximation to the posterior distribution, allowing to calculate locally optimal estimates of the parameters under investigation through variational analysis. This is done approximating the posterior $p(\theta|X)$ with a distribution $q(\theta)$, whose analytic form is well known (usually - and in this case - gaussian). The goodness of approximation is measured in terms of a dissimilarity function $d(q(\theta);p(\theta|X),p(X))$, so that the inference is performed by estimating the $q(\theta)$ that minimizes the dissimilarity function. In particular, thanks to the defined analytic form of $q(\theta)$, this is achieved with a regularized Gauss-Newton optimization scheme, drastically decreasing the computational load.

In our case the forward model of the signal y is defined as:

Eq. 4-12

Where $g(\cdot)$ is non-linear and expressed as per Eq. A-1, θ is the vector of unknown parameters, X are the input measurements and e is the error. θ includes eight parameters: four physiological parameters reported in the study (OEF_0, CBF, CVR and CBV), then the baseline static magnetisation (M_0) and relaxation rate ( ) and finally the parameters determining the shape of the haemodynamic responses for CO_2 and O_2 (η_{CO2} and η_{O2} respectively).

4.2.5 Data analysis

4.2.5.1 dcFMRI data and end-tidal traces

dcFMRI data were pre-processed with motion correction (MCFLIRT, (Jenkinson et al., 2002)) and brain extraction (BET, (S. M. Smith, 2002)) and spatially smoothed with a Gaussian kernel of 6 mm with SUSAN (Smith and Brady, 1997), separately for echo 1 and echo 2. Estimation of physiological parameters of interest was performed with the forward model previously developed in our lab (Germuska et al., 2015) adapted for a Bayesian approach, whose defining equations have been reported in the previous paragraph for reference. This model was adopted because it allows us to take into account different aspects of physiology contributing to the measured BOLD and ASL signals in a simultaneous optimization and also because it is less prone to estimation failure compared to previous calibrated BOLD methods. The priors on estimates were defined specifying means and standard deviations (mean,std.) as OEF_0 = (0.35,0.1), CBF = (60,Inf) ml/100g/min, CVR = (3,0.774) %mmHg, CBV = (1.9,2.34) ml/100g, where by "Inf" we mean a non-informative prior. These values were fixed in agreement with reported physiological ranges and consistently with those used in the original study on the Bayesian framework for the forward model (Germuska et al., 2015). Non-informative priors are used to initialize the estimate without carrying information, therefore they can be thought about as uniform distributions of probability. No prior is defined on the estimates of $CMRO_2$ as this is calculated as $CMRO_2 = CBF \cdot OEF \cdot CaO_2$, where CaO_2 is the arterial content of oxygen. As regards other parameters, they were kept the same as those adopted in the original work (Germuska et al., 2015).

The inputs to the framework are dual echo GRE images and $PetO_2$-$PetCO_2$ traces, then analytic models describing the magnetization decay occurring at the first and second TE were used to estimate grey matter maps of OEF_0, CBF, CVR, venous CBV and $CMRO_2$. Prior to analysis, the end-tidal responses were visually aligned with the MR data to remove the influence of any bulk delay between the recorded end-tidal traces and the fMRI data. The resulting maps were registered

into anatomical space and finally to MNI space (using FSL FLIRT (Jenkinson et al., 2002) and then FNIRT (Andersson et al., 2007)) for second level analysis.

Mean whole grey matter values of each estimated parameter were calculated for the scans and masked subsequently for I) partial volume grey matter values (based on MNI space priors) greater than 30% and II) estimated values of CBF within the range [0 200] ml/100g/min. The first criterion was imposed as an empirical threshold to avoid values affected by poor SNR of the signal in white matter, while the second was used as a sanity check on the estimates to exclude non-physiological values.

4.2.5.2 mTI ASL CBF data

Data were analysed using a two-compartment model developed by Chappell and colleagues (Chappell et al., 2010) which attenuates the error in CBF estimates due to signal arising from intravascular blood by modelling its effect on the ASL signal. In particular, the *oxford_asl* program – included in the FSL BASIL toolkit – was used, allowing to obtain unscaled CBF maps, along with estimated arterial blood volume (aCBV, only if found to significantly contribute to the signal) and tissue arrival time (TAT). CBF quantification and coil sensitivity correction were then performed as for the dcFMRI data.

Mean whole grey matter values of each estimated parameter were calculated for the three scans and masked following the same criteria adopted for the dcFMRI data. Finally estimates of cerebral perfusion were also used to probe the quality of the corresponding estimated values of CBF obtained with the dcFMRI model (with single inverstion time) through a correlation analysis.

4.2.5.3 Repeatability analysis

Indices quantifying the repeatability of the estimates were calculated for each parameter at a bulk grey matter level. Firstly those resulting from a correlation analysis between the estimates in the two time points, aiming at quantifying to what extent the two set of measurements covariate: coefficient of determination (R^2), effect size (β) and statistical significance (p).

Then the intraclass correlation coefficient (ICC, (McGraw and Wong, 1996; Shrout and Fleiss, 1979)) was used as a measure of absolute agreement between the bulk estimates. The ICC has previously been applied to fMRI data to quantify the ratio between the total data variance of interest and the one under investigation (Bright and Murphy, 2013; Lipp et al., 2015). In particular, it can be applied in a voxel-wise fashion in order to obtain estimates of spatial repeatability of the signal (Lipp et al., 2014). Two different ICC indices were therefore considered: one calculated on whole grey matter values of the parameters across subjects (corresponding to ICC(3,k) in [16] or ICC(A,k) in [17]) and another considering voxel-wise comparisons between the two scans for each participant separately (corresponding to ICC(3,1) in [16] or ICC(A,1) in [17], also referred to as "spatial ICC" in (Lipp et al., 2014)). These are hence referred to as inter-subjects ICC (ICC_{inter}) and intra-subjects ICC (ICC_{intra}) respectively. Both are interpreted according to commonly used guidelines that classify values ICC as "poor", values between 0.41 and 0.59 as "fair", values between 0.60–0.74 as "good" and values > 0.74 as "excellent" (Cicchetti, 2001).

In order to evaluate the precision and spread of the bulk results, coefficient of variance (CV) of the estimates were also calculated. Similarly to the case of ICC estimates, two CV indices were considered: one taking account of the differences between the subjects of the cohort (CV_{inter}) and the other considering the variability occurring in each subject separately (CV_{intra}). CV_{inter} was calculated as the average between the values of the standard deviation divided by the mean of all participants' estimates calculated in the two sessions. CV_{intra} was calculated for each person by dividing the standard deviation of the two measures by their mean. These CV indices were visually integrated with Bland-Altman plots, scatterplots in which the differences between two set of measurements are plotted against their means. Calculating the mean (m) and standard deviation (sd) across the differences, it is then possible to characterise as outliers the values lying beyond the interval of $m \pm 1.96*sd$.

CV indices were also calculated at a voxel-wise level, enabling to evaluate the precision of the estimates across grey matter. As for the bulk case, CV_{inter} was calculated as the average between the values of the standard deviation divided

by the mean of all participants' estimates calculated in the two sessions. Differently from the bulk estimates, CV_{intra} was calculated as the mean across subjects of the ratios between the standard deviation and the mean of the two measurements. This allowed us to calculate a unique map for comparison with the relative CV_{inter} map.

4.3 Results

4.3.1 dcFMRI data and respiratory traces

As shown in the averaged end-tidal traces reported in Figure 4-2-A, subjects' O_2 increased during periods of hyperoxia, while CO_2 increased during hypercapnia. The average baseline $PetO_2$ value was 113 mmHg, while it was 42 mmHg for $PetCO_2$. Plateau levels of hyperoxia caused an average increase of approximately 230 mmHg in $PetO_2$ and the average increase in $PetCO_2$ from baseline with hypercapnia was 11.5 mmHg. Moreover, periods of hyperoxia appear to produce a reduction $PetCO_2$ of about 2 mmHg, while periods of hypercapnia correspond with an increase in $PetO_2$ of approximately 10 mmHg, consistently with literature findings (Floyd et al., 2003; Tancredi et al., 2014) and in agreement with the mechanisms of gas transportation in brain tissue introduced in Paragraph 1.3 (in particular Haldane and Bohr effects, (Jensen, 2004)). The corresponding inspired gas fractions are reported in Figure 4-2-B. In one subject, the respiratory task run included hyperoxic periods 10s shorter than for the rest of the subjects (excluded from the average in Figure 4-2).

Figure 4-3 and Figure 4-4 show the raw images of a single acquisition of echo 1 and echo 2 for one representative subject and the relative perfusion signal obtained as the average of surround subtracted echo 1 signal from the same subject.

Figure 4-5 shows an axial view of the maps of all the estimated parameters registered to MNI space in the two time points for a single representative subject. In these maps it is also possible to see areas where the algorithm fails its estimates (indicated by arrows). All the maps estimated for all subjects are reported for reference in the Supplementary material paragraph (Figure 4-14 and Figure 4-15).

.

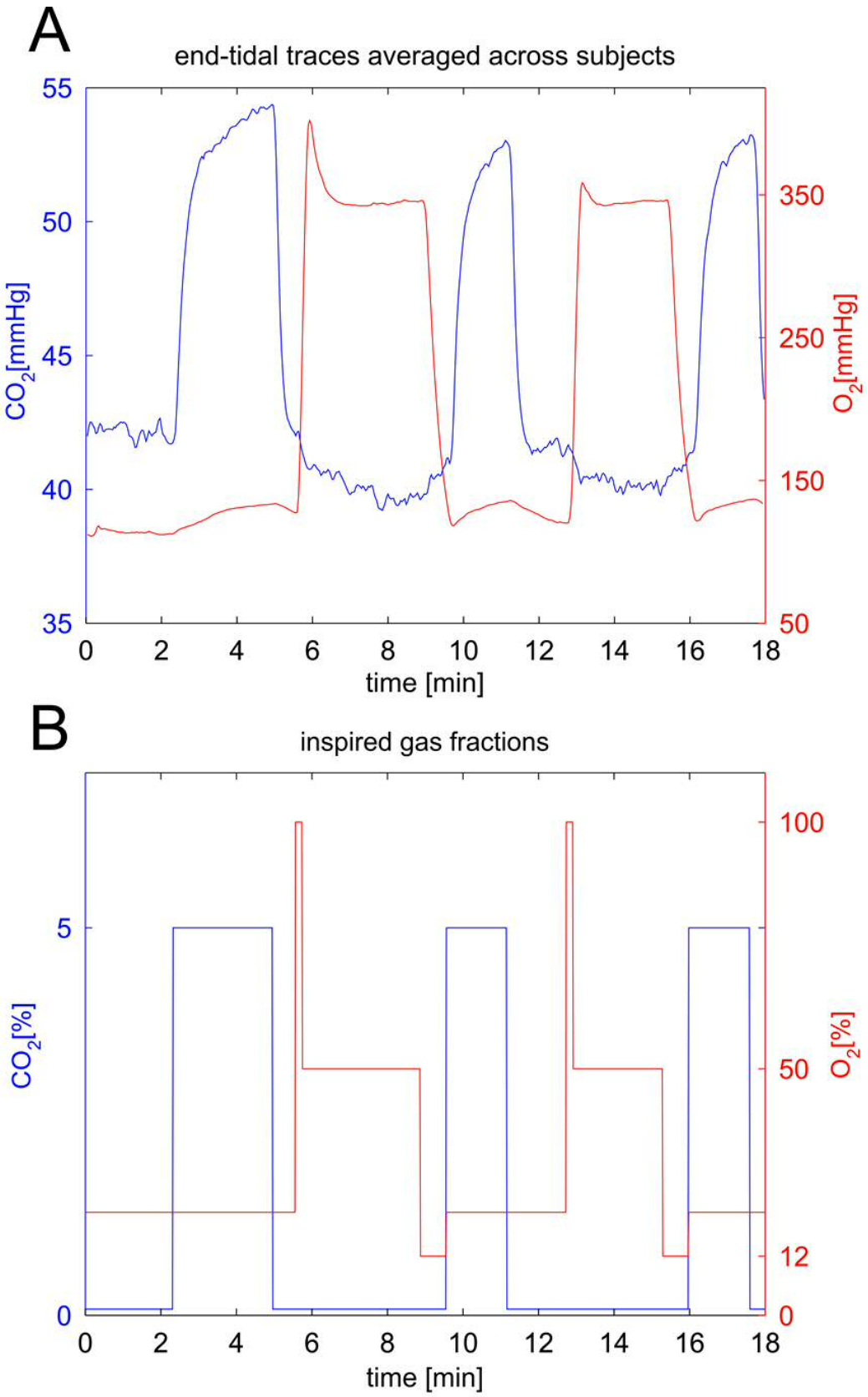

Figure 4-2: A - end-tidal values of partial O_2 and CO_2 pressure averaged across N=9 subjects. B – inspired gas fractions for the respiratory task.

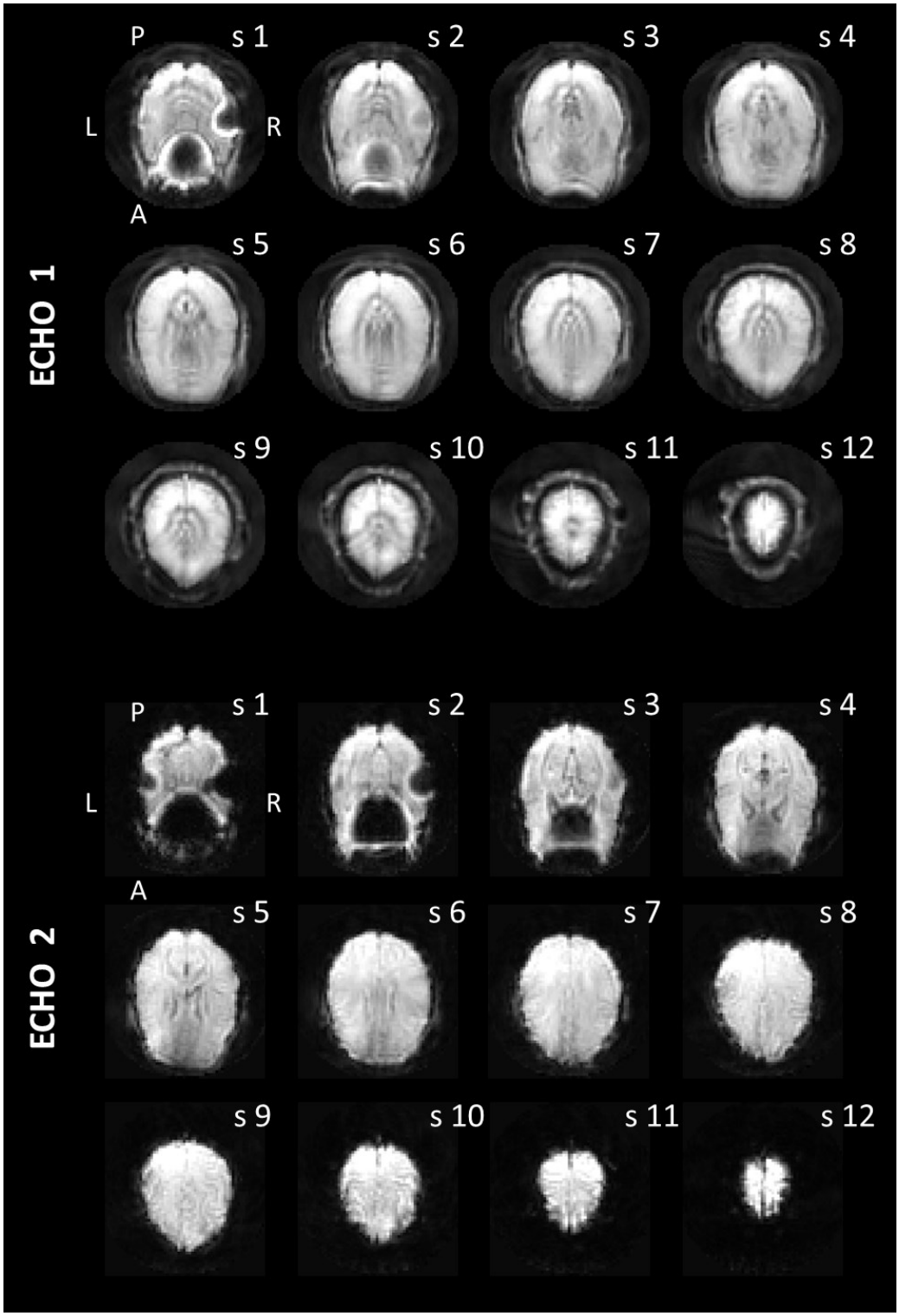

Figure 4-3: Raw images of a single acquisition of echo 1 (top) and echo 2 (bottom) for a single subject. In both cases slices are presented from the bottom (s1) to the top (s12).

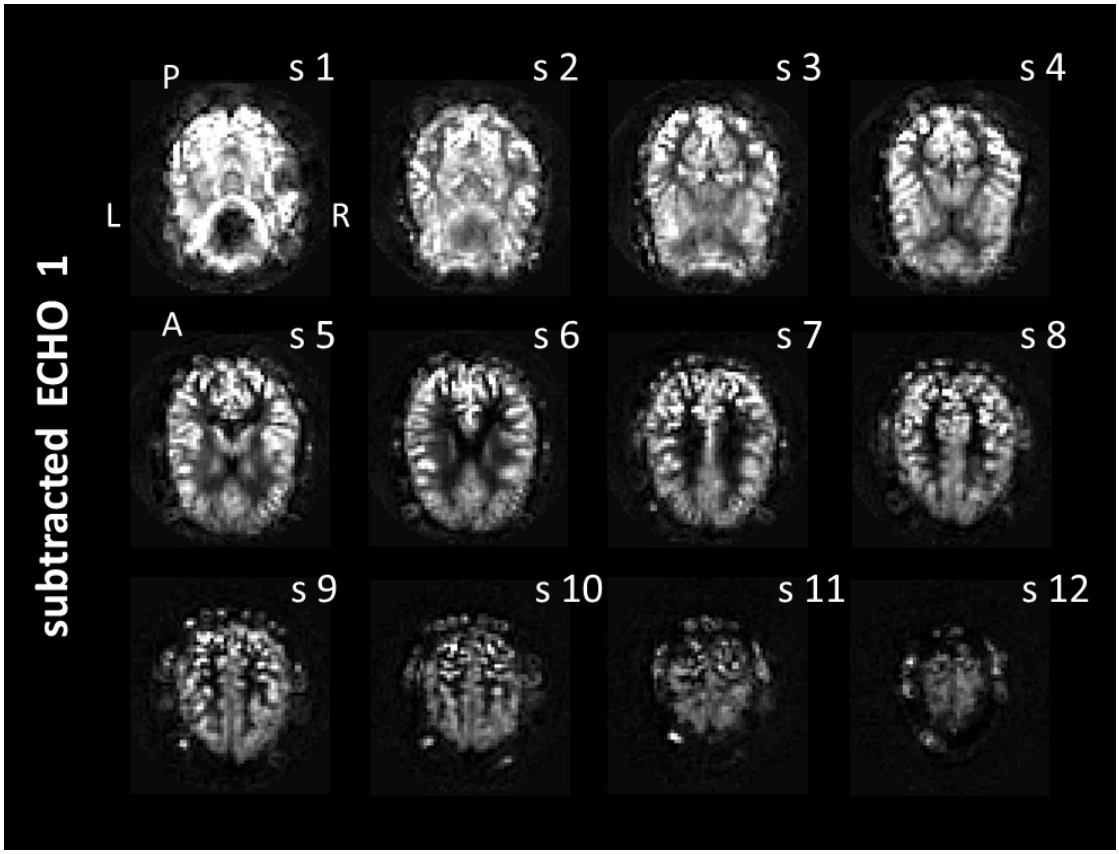

Figure 4-4: Images obtained from the averaging over time of surround subtracted echo 1 acquisitions for a single subject. The contrast shown is proportional to blood perfusion (arbitrary units). Slices are presented from the bottom (s1) to the top (s12).

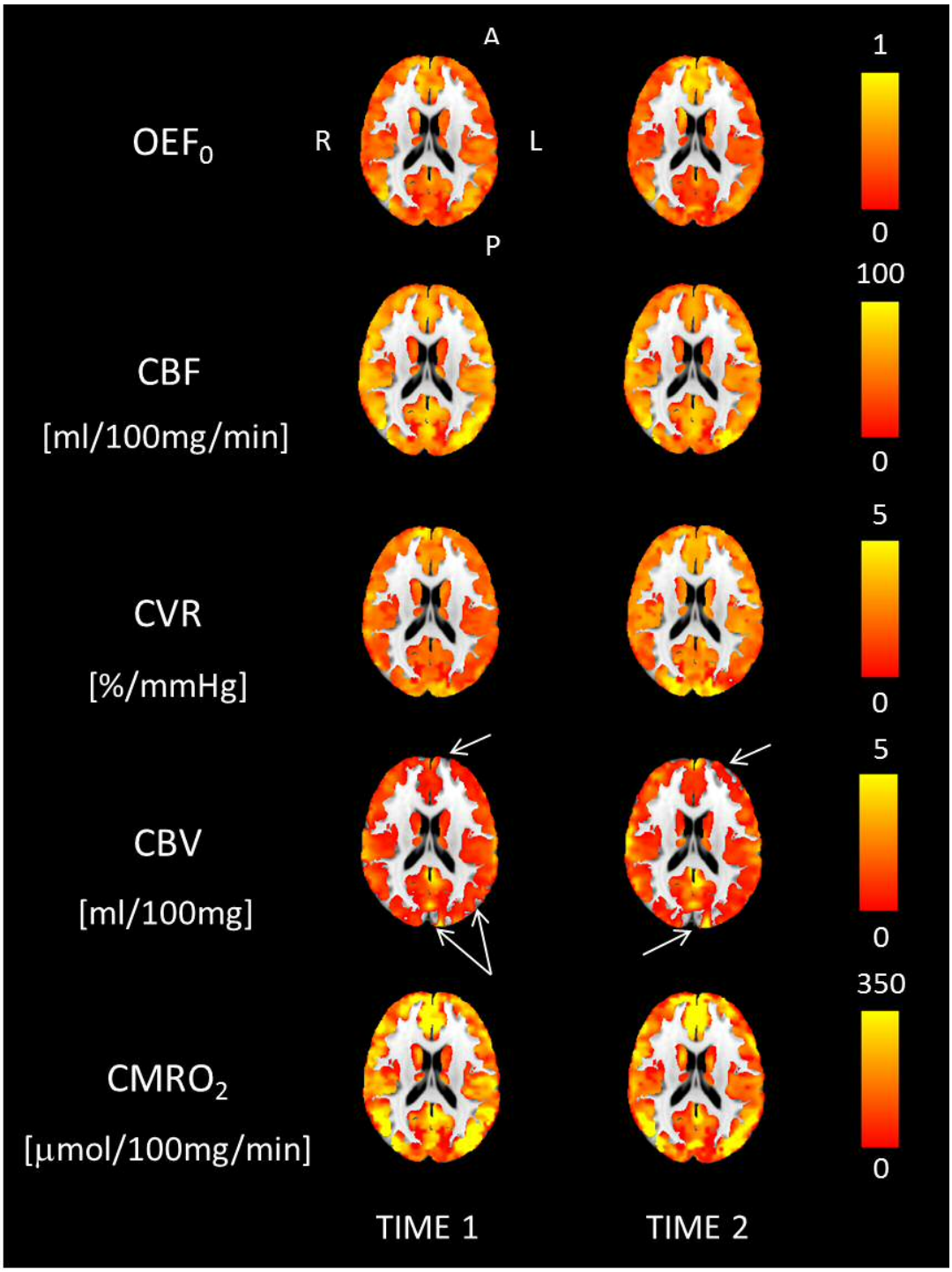

Figure 4-5: Axial view of the estimated maps of the physiological parameters for a representative subject in the two time points. White arrows point at areas where the algorithm fails to output valid values.

Grey matter values of the five physiological parameters for both sets of measurements are reported in Figure 4-6. Averages across subjects show only slight and not significant changes between the two time points, with pooled mean values of 0.38±0.076 for OEF_0, 56±11.7 [ml/100mg/min] for CBF, 2.6±0.47 [%/mmHg] for CVR, 1.9±0.35 [ml/100g] for CBV and 183±49 [μmol/100mg/min] for $CMRO_2$.

Results of the correlation analysis are reported for all parameters in Figure 4-7. In this case the goodness of fit is mixed: while OEF_0, CBF and CBV show relatively high values of the coefficient of determination (R^2>0.5) and good values of the effect size (β>0.75), CVR and $CMRO_2$ only present a mediocre agreement between the two measurements, with relatively high values of R^2, but effect size away from the ideal (0.449 and 0.659 respectively).

As regards the ICC indices, ICC_{inter} is found to be "excellent" for all five parameters, with particularly high performances for OEF_0 and CBF (>0.9, Figure 4-8, top). Results are more varied for the voxel-wise analysis, with values of ICC_{intra} remarkably high for CBF, mostly "excellent" for CVR, CBV and $CMRO_2$, while mostly "good" for OEF_0.

Figure 4-8 (bottom) shows the CV indices calculated for the precision analysis. Values of CV_{inter} are generally high, ranging between 17.5% for CVR to 26.9% for $CMRO_2$. CV_{intra} indices have similar distributions across parameters, with a value of 6.7±6.6% for OEF_0, 6.9±5.9% for CBF, 9.6±8.8% for CVR, 8.4±6.3% for CBV and 12±9.6% for $CMRO_2$. In only three cases (not corresponding to the same subject) CV_{intra} is higher than CV_{inter}.

Bland-Altman plots are reported for all parameters in Figure 4-9. Results show most of the values clustering around the pool averages for OEF_0, CVR and CBV, with bias in the differences of 4.9%, 2.6% and -9.4% respectively compared to the relative mean. For these parameters it is also possible to find an outlier (not always corresponding to the same subject). Distributions for CBF and $CMRO_2$ are instead broader, with bias in the differences of just -0.4% and 4.6% respectively and no outliers.

Maps of the CV indices calculated at a voxel-wise level for each parameter are reported in Figure 4-10. As for the bulk estimates, values of intra-subjects CV are generally lower than values of inter-subjects CV. Notably, for all physiological parameters areas of interface between grey matter and different structures (white matter, ventricles and skull) present higher CV values. For both CV_{intra} and CV_{inter}, CBF shows the lowest variability, with values mostly homogeneous across parameters apart from few focal areas. A similar situation is shown by OEF_0 and CVR, but with higher estimates. CBV and $CMRO_2$ show instead high CV_{intra} and CV_{inter} indices with highly irregular distributions in space.

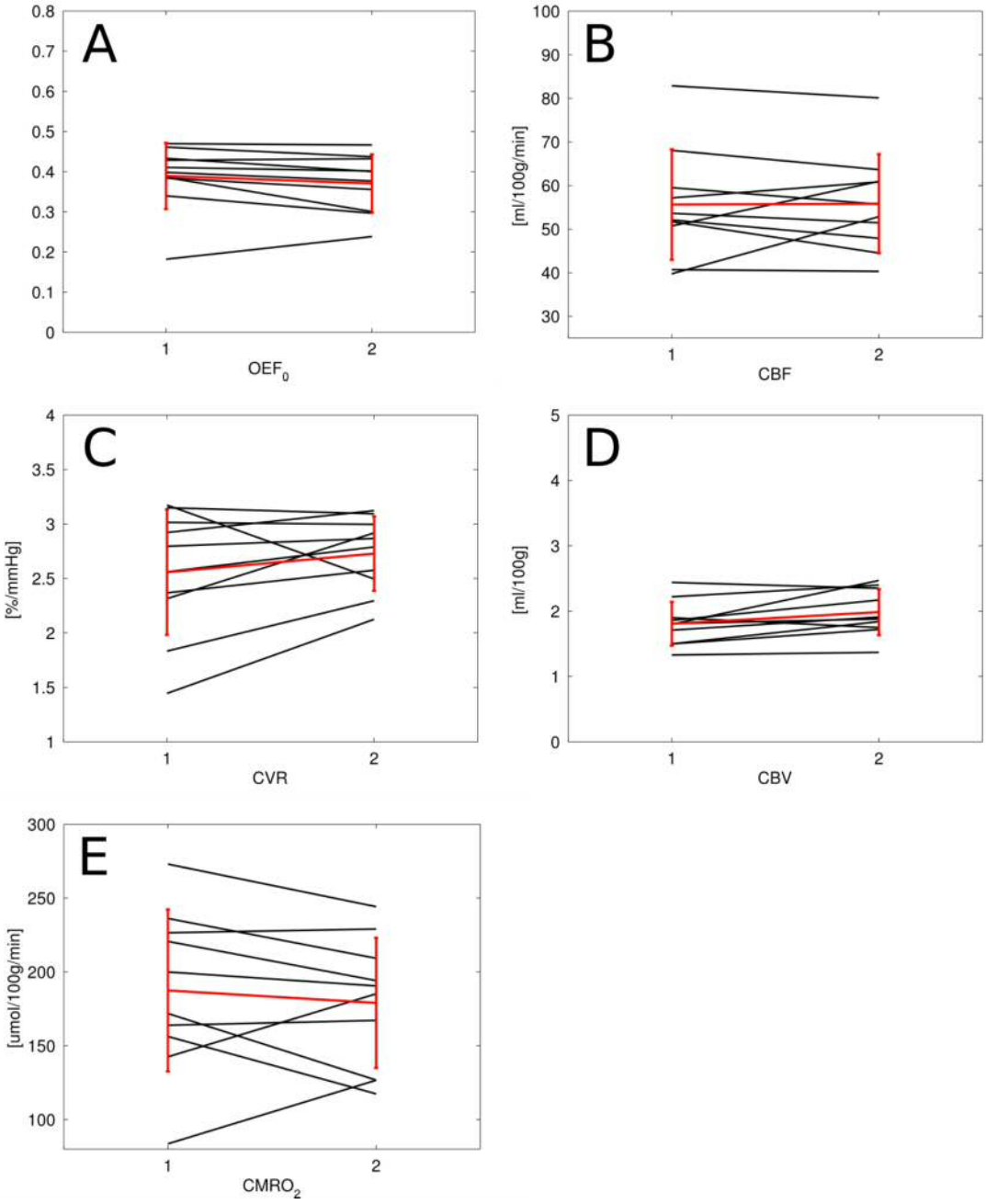

Figure 4-6: Grey matter values of the five physiological parameters for all subjects for the two time points. In red, average values with bars representing standard deviations.

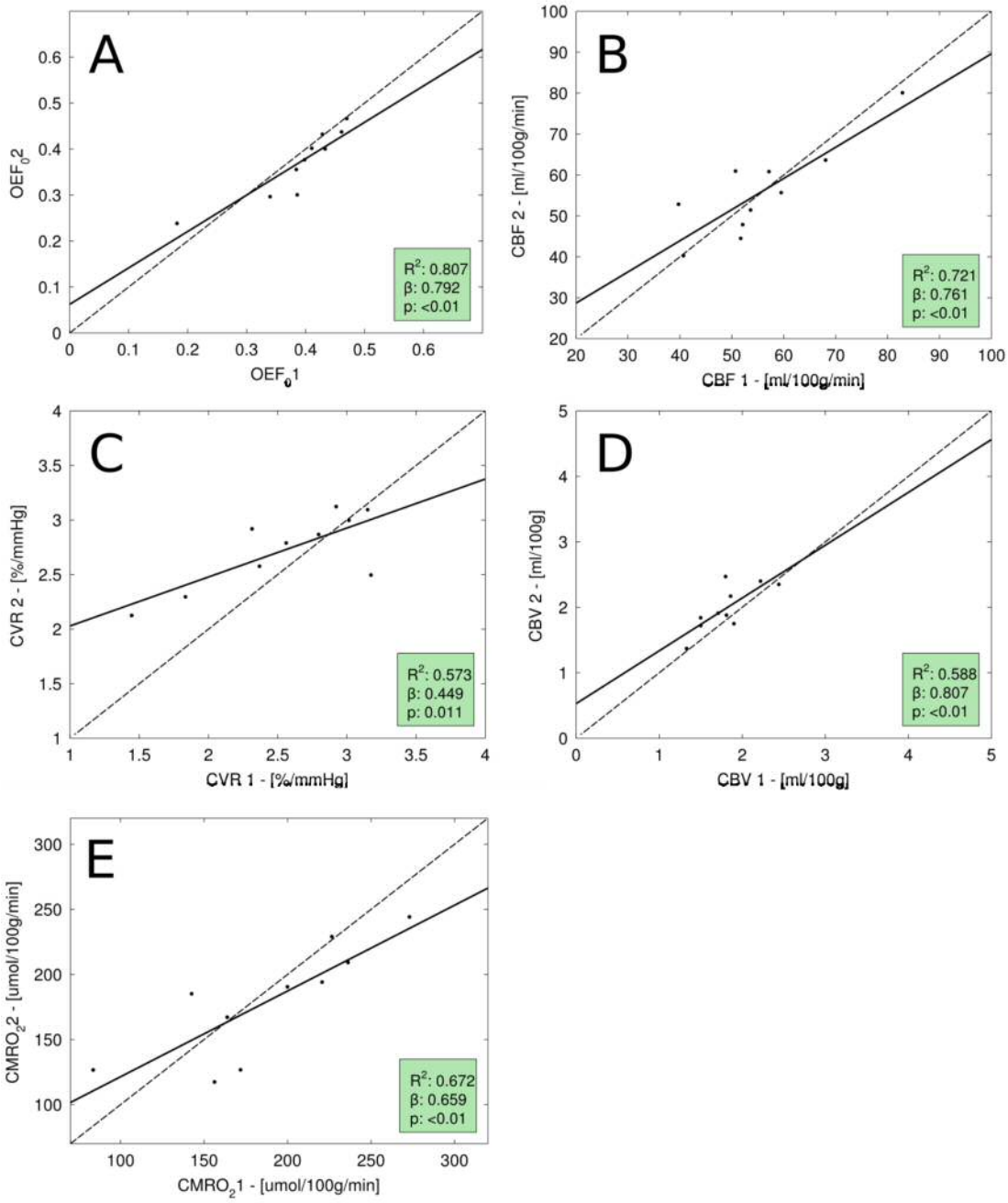

Figure 4-7: results of correlation analysis between the two set of measurements (1 and 2) for the five parameters. Solid lines show the best fit and displayed are the coefficient of determination (R^2), effect size (β) and statistical significance (p).

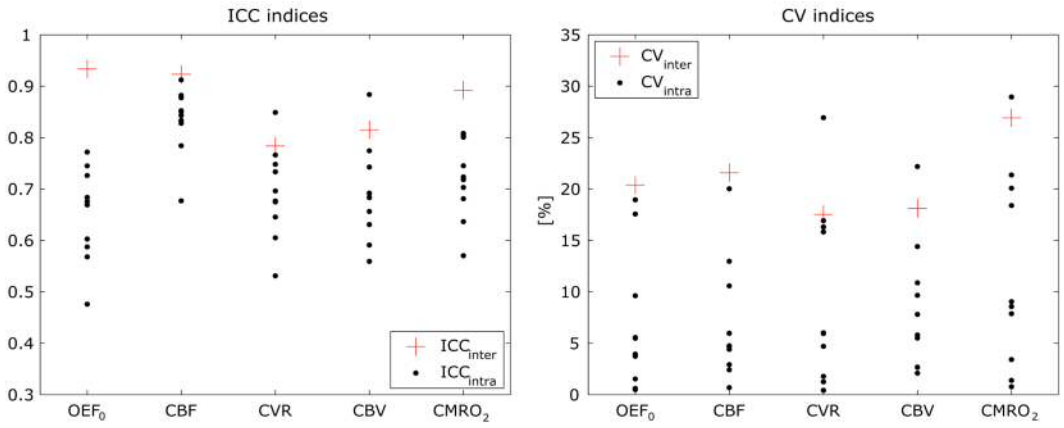

Figure 4-8: ICC and CV indices for all parameters considered.

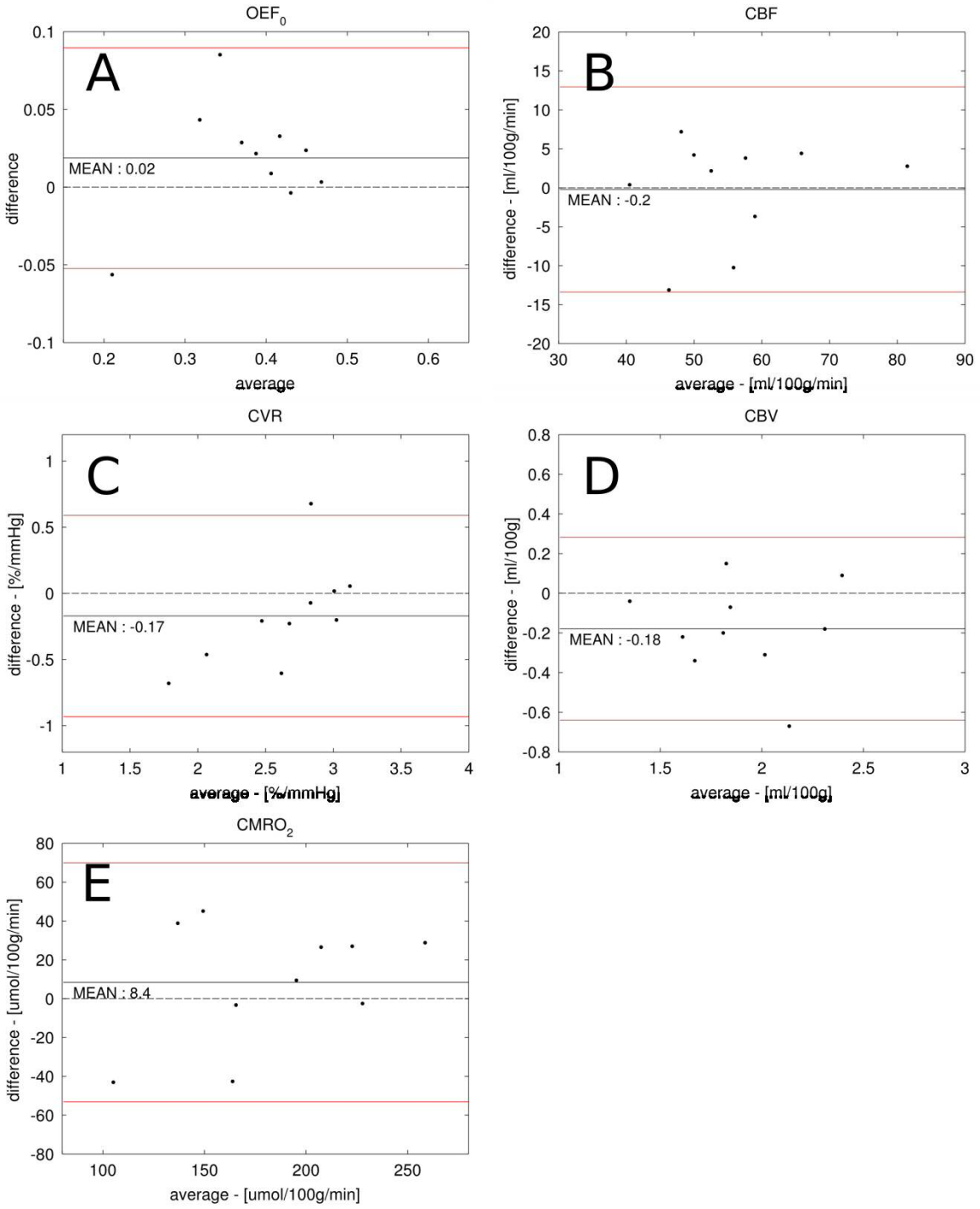

Figure 4-9: Bland-Altman plots for each physiological parameters. In black solid lines the mean between measures difference in the two time points, while red lines denote intervals of mean $\pm$ 1.96*standard deviation.

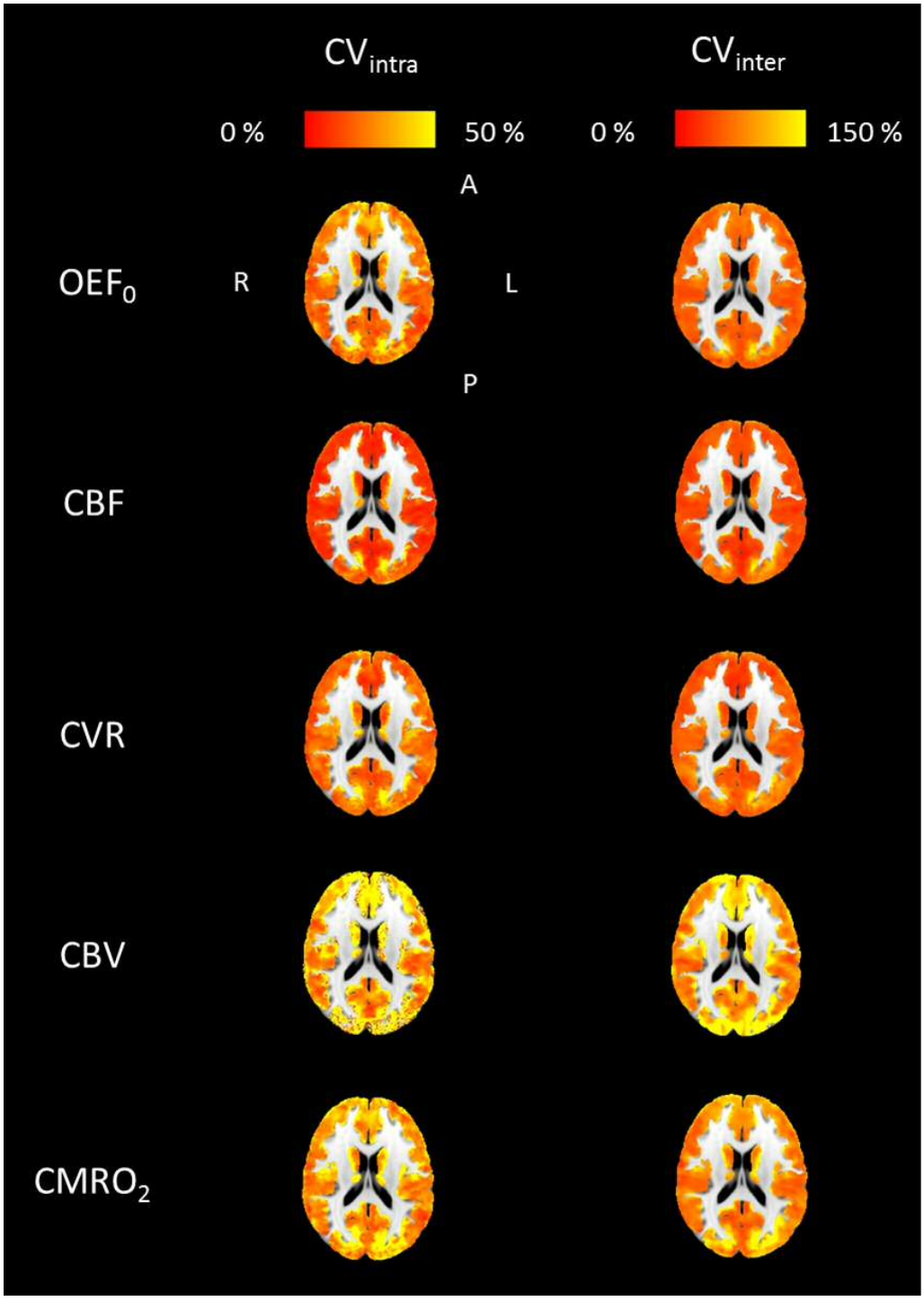

Figure 4-10: Axial view of the maps of intra- and inter-subjects CV calculated for each estimated parameter.

4.3.2 mTI data

Figure 4-11 shows the relative perfusion signal obtained as the subtracted image (tag-control) for a representative subject at different values of inversion time (TI) and relative evolution of the signal arising from a particular region. The effect of perfusing labelled blood over time is evident, highlighting a good quality of the signal.

In Figure 4-12 axial views of the CBF and TAT maps registered to MNI space in the two time points are reported for a single representative subject. As expected, maps of TAT seem less homogeneous than the CBF ones.

Grey matter estimates of CBF and TAT for both set of measurements are reported in Figure 4-13,A,B. As for the dcFMRI data, averages across subjects show only slight and not significant changes between the two time points, with pooled mean values of 36±9 ml/100mg/min for CBF and 0.76±0.061 s for TAT. In Figure 4-13,C,D results of the correlation analysis on CBF are reported: panel C shows the relationship between estimates of CBF calculated from mTI data from the two time points, while in panel D these are correlated with estimates of CBF obtained with the forward model from dcFMRI data. While in the former case the correlation shows strong repeatability, in the latter the high value of the coefficient of determination (R^2=0.796) and an effect size not far from ideal (β=1.17) is coupled to the presence of an offset of about 20 ml/100mg/min between the two measurements, with the proposed forward model consistently supplying higher estimates. Bland-Altman plots (Figure 4-13,E,F) show measurements spreading along the means (y axis), while clustering quite tightly around the difference (x axis), the only exception being a single subject for both CBF and TAT. As regards the ICC indices (Figure 4-13,G), they are found to be mostly excellent for both parameters, with ICC_{intra} of 0.94 and 0.82 for CBF and TAT respectively and poor values of ICC_{intra} found just in a single subject. Figure 4-13,H shows the calculated CV indices: CV_{inter} are 24.5% for CBF and 8.1% for TAT, while CV_{intra} means are 6.1±6.8% and 2.7±3.7% respectively.

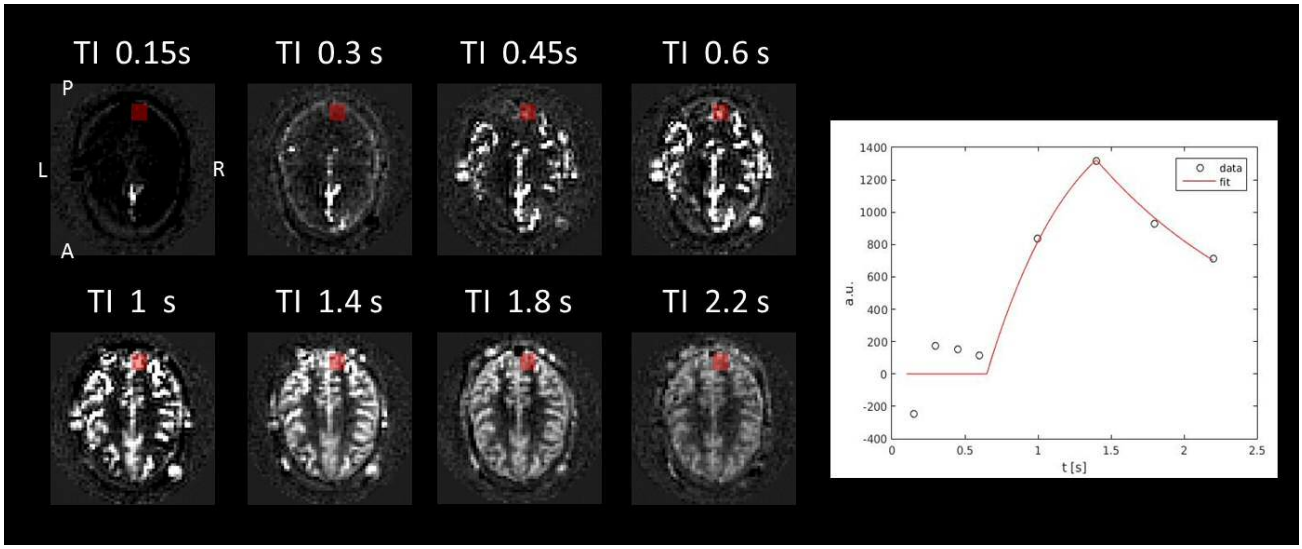

Figure 4-11: On the left: single slice acquisitions on the subtracted signal (tag-control) for a representative subject at different values of inversion time (TI). On the right: example of evolution in time (circles) and best fit (GKM) of the signal from a ROI in the right visual cortex (red in the raw data).

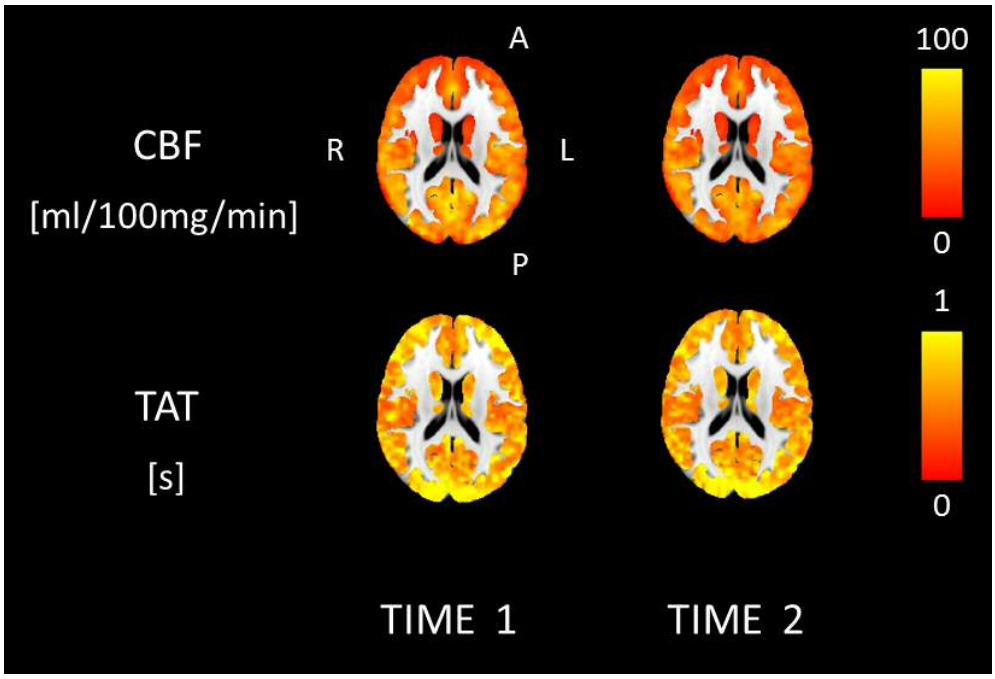

Figure 4-12: Axial view of the estimated maps of the physiological parameters for a representative subject in the two time points.

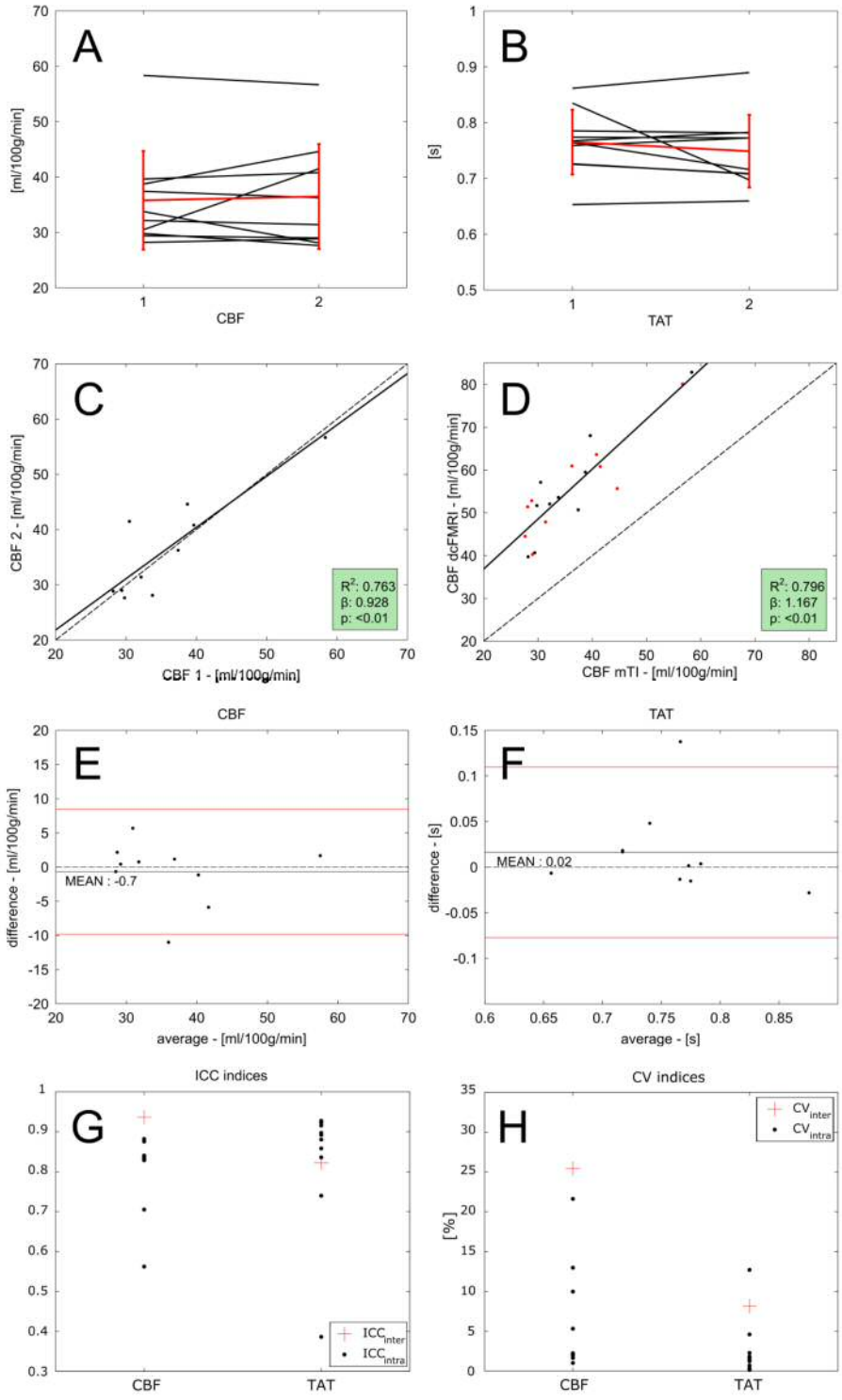

Figure 4-13: Summary of the calculated statistics for the mTI data. A,B – mean grey matter values (in read the averages across subjects); C – correlation scatterplot for CBF; D - correlation scatterplot between CBF values estimated from dcFMRI vs mTI data (in black dot values from session 1, in red from session 2); E,F – Bland-Altman plots; G,H – ICC and CV indices.

4.4 Discussion

Grey matter values estimated with the forward model show an overall consistency of the results between the sets of measurements taken in two time points, with t-tests revealing no significant changes at a group level. Measured values of 0.38±0.076 for OEF_0 are in agreement with what reported from previous studies in our lab (0.42±0.12, (Wise et al., 2013)) or from other centres, with typical values for other MR methods ranging between 0.26 (Bolar and Rosen, 2011) and 0.395 (Guo and Wong, 2012). Global grey matter measures of CBF (56 ml/100mg/min) tend to be higher than what typically reported for MRI and PET studies (41 ml/100mg/min (Bulte et al., 2012), 42 ml/100g/min (Ibaraki et al., 2010)), but they are consistent with those from our previous study and similar ones, especially when considering young cohorts (56 ml/100mg/min (Wise et al., 2013), 52 ml/100mg/min (Gauthier and Hoge, 2012) and 63 ml/100g/min (Ances et al., 2009)). Estimates of 2.6±0.47 %/mmHg for CVR lie on the lower side of the typical range of values obtained for comparable CO_2 challenges in most of the MRI literature (between 5.15±1.1 %/mmHg (Bulte et al., 2012) and 2.82±1.21 %/mmHg (Heijtel et al., 2014)). Values of 1.9±0.35 ml/100g for CBV are similar to those reported in literature and obtained with other MRI methods (2.18±0.41 ml/100g (Blockley et al., 2013), 2.46±0.28 ml/100g (An and Lin, 2002) and 1.75±0.13 ml/100g (He and Yablonskiy, 2007)). Finally average $CMRO_2$ values of 183±49 μmol/100g/min are comparable to reported values obtained with the dual calibrated BOLD method previously presented by our lab (184±45 μmol/100g/min (Wise et al., 2013)), other calibrated BOLD methods (145±30 μmol/100g/min (Gauthier and Hoge, 2012) and 155±39 μmol/100g/min (Bulte et al., 2012)) and values of 182±12 μmol/100g/min (Liu et al., 2013), 158±18 μmol/100g/min (Fan et al., 2012) and 157.4±19.7 μmol/100g/min (Roland et al., 1987) obtained with different MR methods and PET. Nevertheless a few subjects show substantial changes between the two time points or outlying values, highlighting a degree of noise in the estimates, especially as regards CVR and $CMRO_2$.

High resolution maps in Figure 4-3 show the overall consistency of the two set of measurements and also supply a representative example of the variability of the estimates across the brain, with generally spatially smooth results for OEF_0 as opposed to more irregular estimates for CBV and CVR.

The correlation analysis shows an overall elevated level of correlation between the estimates, although highlights less than optimal performances in the cases of CVR and $CMRO_2$. In particular, in Figure 4-5,C,E different subjects appear as outliers. The main cause can be found considering the nature of the measurements, as both are derived from other estimates: CVR as the ratio between percent change in CBF and absolute changes in $PetCO_2$ while $CMRO_2$ as the product of OEF_0 and CBF. This means that they are particularly sensitive to cumulative effects of noise on the original measurements.

ICC indices give a further quantification of the absolute agreement between the estimates: high values for the ICC_{inter} index support what found in the correlation analysis, while calculated ICC_{intra} indices inform about consistency at a voxel-wise level. As expected, ICC_{intra} is generally lower than ICC_{inter} because averaging the estimate across grey matter allows some of the noise contributions to be reduced. In fact it might be argued that the good agreement of the estimates at a grey matter level is simply due to the averaging operated on a possibly wide range of noisy and non-informative estimates. Our analysis gives evidence that this is not the case: in fact ICC_{intra} indices show that estimates are generally consistent also at a voxel-wise level. Results are especially good for values of CBF, while they tend to be less in agreement for OEF_0.

A further understanding of the variability in the data is given by the calculated CV indices. CV_{inter} and CV_{intra} indices measure the proportion of the variability in the estimates originating from inter-subjects differences (such as normal distribution of physiological parameters in the cohort) and intra-subject differences (more related to accuracy and precision of the measures). As values of CV_{intra} are found to be generally lower than CV_{inter}, this means that the method applied is accurate enough to capture the single subject's physiology. Moreover, grey matter CV_{intra} values of 6.7±6.6% for OEF_0, 6.9±5.9% for CBF and 12±9.6%

for $CMRO_2$ are comparable with those reported in PET literature for other methods aiming at estimating brain metabolism and haemodynamics across brain (5.7±4.4%, 8.4±7.6% and 5.3±3.9% respectively, (Coles et al., 2006)). They appear instead higher than those reported from MRI methods for bulk estimates (3.2±1.2%, 2.8±0.8% and 3.8±1.4% respectively with TRUST, (Liu et al., 2013)).

Voxel-wise CV indices are higher than those reported for bulk estimates, typically by a factor of 2 and 3 for the intra- and inter-subjects case respectively. This is expected due to the high spatial resolution but it allows us to inform about the spatial distribution of the variability in the estimates. In particular they show that the low CV indices calculated at a bulk level for OEF_0 and CBF are representative of the voxel-wise distribution of these indices. This does not seem to be the case for estimates of CBV, which present the highest degree of variability. Maps of $CMRO_2$ further support the notion that the precision of the estimates is degraded by the contribution of both OEF_0 and CBF variability.

The Bland-Altman plots visualize the relationship between the inter-subject and intra-subject variability or measurement precision, where the first is here given by the spread along the x axis, while the second is the spread along the y axis. Results for the latter confirm what also found calculating ICC and CV indices, that is a generally good agreement of the estimates in the two time points with a few outliers lowering the performance. As regards instead the inter-subject variability, the plots are consistent with what found in physiology, that is values of OEF_0 mostly clustered around the mean, with more varied values of CBF and $CMRO_2$.

The analysis of the estimates obtained from the mTI data can firstly be used to compare the estimate of CBF with measurements using a single inversion time. Results show a good correlation between the measurements but also a consistent offset, with the forward model supplying values typically 20 ml/100g/min higher than the mTI data. This can be explained mostly considering that estimates from single TI measures - as in the case of the forward model – tend to overestimate CBF, compared to those from mTI measures. This is due both to assumed constant timings of the labelled bolus (Van Osch et al., 2007) and spurious

arterial contributes to the ASL signal (Chappell et al., 2010). For example the inter-subject variability of TAT estimated using Chappell's model (Chappell et al., 2010) is not accounted for in the forward model and therefore introduces some error in the estimates.

Three main issues are raised by the application of the newly proposed forward model in this study: one regarding the hypothesis underlying its application and two highlighted by the analysis of the results. As regards the first, it relates to the assumption of isometabolism during hypercapnia and hyperoxia when performing respiratory tasks. Studies on the dependence of $CMRO_2$ on altered arterial CO_2 and O_2 levels have found variable results (as discussed in Paragraph 2.2.3.4), with some of the more relevant ones pointing at a decrease in metabolism with both hyperoxia and hypercapnia (Xu et al., 2012, 2011). An eventual deviation from isometabolism during these conditions would translate into great bias on the estimates from calibrated BOLD models, as explored in Paragraph 3.3.4 and as reported by other groups (Blockley et al., 2015). Although still the object of discussion in the field, this is a commonly adopted assumption for BOLD calibrated methods and to investigate it goes beyond the scope of the data of this study.

Another limitation arises from the precision of the estimates obtained with the forward model. As previously discussed, grey matter values reported are generally consistent with those found in literature, with the exception of few outliers. Repeatability of the measurement, quantified with correlation analysis and ICC calculations, has been shown to be overall satisfactory, both at a bulk and voxel-wise level, the worst performances being related to the inherently noisiest derived parameters, i.e. CVR and $CMRO_2$. CV indices are instead higher than those reported in literature and for the mTI calculations, especially when measuring intra-subject variability. Although it does not represent a major limitation as in most cases values of CV_{intra} are lower than CV_{inter}. This indicates that the estimation precision of a subject's parameters is still good enough not to be confounded in the cohort's variability. In fact we should note that the estimates of five physiological parameters presented here have a voxel-wise resolution. Therefore, a trade-off between repeatability and spatial resolution has to be

considered when comparing them to other methods only allowing bulk estimates of fewer parameters.

The final issue originates from the Bayesian approach adopted for the estimates. In fact the use of priors could potentially bias the estimates towards pre-determined values (the priors themselves) rather than the real ones. This would translate into good repeatability and decreased variability in the data, but ultimately resulting in a loss in sensitivity to individual physiology. This argument, however, is contradicted by the evidence of a substantial inter-subjects variability in the estimates, the presence of outlying values, the physiological spread of estimates and relative CV indices across the grey matter. Nevertheless it might be argued that the use of priors, combined with the reported values of repeatability, would make the method under investigation not effective in detecting physiological changes between different conditions, such as the activation due to a task or the response to a drug.

Finally, this study helps us informing about the feasibility of future studies based on the same estimation framework. Considering the distributions of estimates reported, a significance level of 5% and a statistical power of 80%, the sample size (N) needed to detect size effects of 15%, 20% and 25% in a study between independent groups would be of N = 46, 28 and 18 respectively for OEF_0, N = 50, 30 and 20 respectively for CBF and N = 79, 46 and 30 respectively for $CMRO_2$. Similarly, the sample size needed in for matched groups would be of N = 30, 18 and 13 respectively for OEF_0, N = 33, 20 and 14 respectively for CBF and N = 51, 30 and 20 respectively for $CMRO_2$. Finally, the sample size needed in a crossover study such as the one reported in Chapter 5 would be of N = 23, 14 and 10 respectively for OEF_0, N = 25, 16 and 11 respectively for CBF and N = 39, 23 and 16 respectively for $CMRO_2$. These calculations, supported by the repeatability analysis previously presented, suggest that our approach can be applied proficiently for size effects and magnitudes of sample size typically found in fMRI studies. In order to avoid large cohorts, experimental designs characterized by reduced variability in the data should be preferred (e.g. repeated measurements, longitudinal, crossover).

4.5 Conclusions

In this study we have quantified the repeatability of a newly proposed method for estimating brain haemodynamics and metabolism with a dual calibrated BOLD approach in a test-retest experiment on ten healthy subjects in the resting state.

Results show an overall consistency of the estimated parameters with literature reports and a good level of repeatability, with varied performances depending on the specific parameter under analysis and on the spatial resolution considered. In particular the information supplied by grey matter maps is of extreme interest for studies focused on the spatial distribution of brain physiology, despite some reliability limitations compared to methods supplying bulk measurements. The level of variability in the data suggest that our approach can be applied proficiently for appropriate experimental designs with magnitudes of sample size typically found in MRI studies.

More work can be done to further explore the possibilities of this method, such as to test its effectiveness in detecting physiological changes between different conditions. This is the aim of the study presented in Chapter 5, where the same method will be applied to investigate the acute effects of caffeine in a drug study.

4.6 Supplementary material

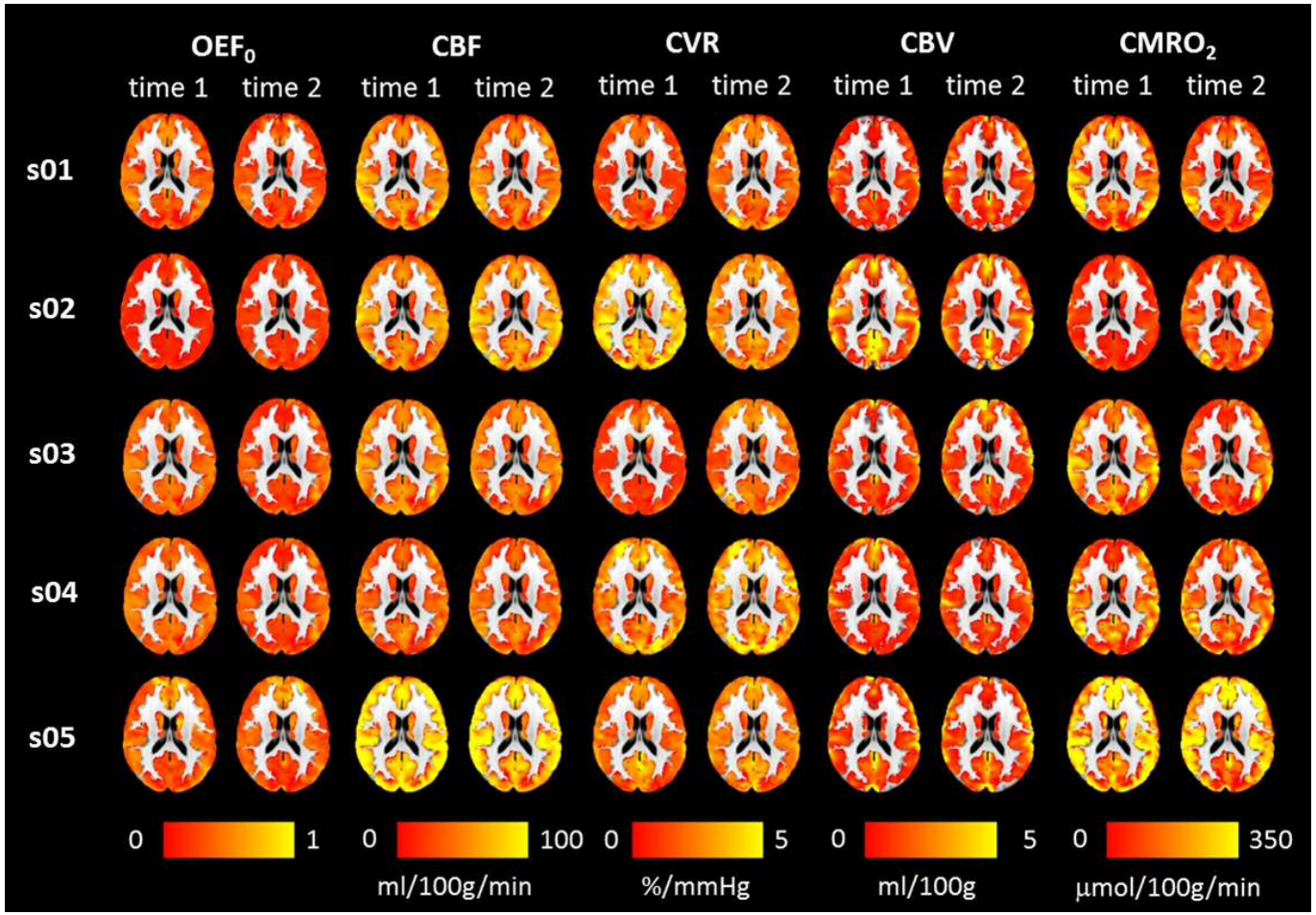

Figure 4-14: Maps of the estimated parameters at each time point for subjects 1 to 5.

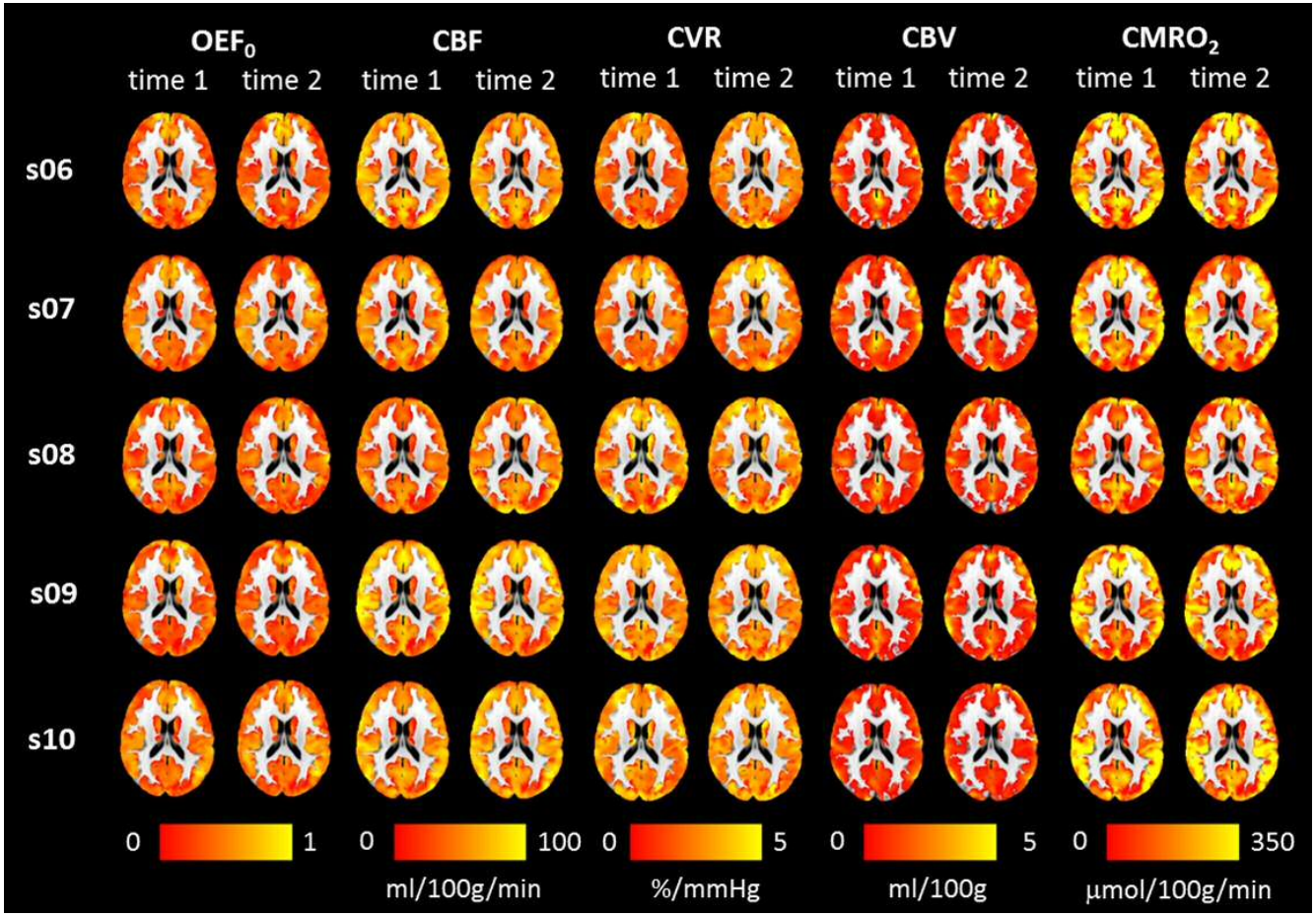

Figure 4-15: Maps of the estimated parameters at each time point for subjects 6 to 10.

Chapter 5

The acute effects of caffeine on brain oxygen metabolism: a dual calibrated fMRI study

In the following study the same estimate framework introduced in the previous chapter is applied for a randomised, double-blind, placebo-controlled study on caffeine. 16 low to moderate consumers were recruited and scanned before and after consumption of a capsule of powdered caffeine (or placebo) with the aim of assessing its acute effects on brain metabolism and haemodynamics. Results show a general decrease in oxygen metabolism after caffeine consumption, consistent with a decrease in energetic demand due to an overall inhibitory effect previously reported by electrophysiology studies. With this work we also exemplify the feasibility of the estimate framework, showing its effectiveness in a drug study application.

5.1 Introduction

In this work we aim to show how the combination of the dual calibrated experimental methodology and the forward modelling estimation approach presented in Chapter 4 can be used to assess the effects of a drug on the brain. We utilise a randomised, double-blind, placebo-controlled study design to demonstrate the acute effects of caffeine ingestion in low to average caffeine consumers. In particular, our aim is to characterize the changes in brain metabolism and haemodynamics following caffeine consumption with a high spatial resolution, quantifying the main underlying physiological parameters of interest.

Caffeine is a methylxanthine and is one of the most frequently and widely consumed psycho-active substances. It is known as a non-selective antagonist of the adenosine receptors, especially types A1 and A2 (both A2A and A2B) (Fredholm et al., 1999; Pelligrino et al., 2012), inhibiting the release of excitatory neurotransmitters. This has two independent consequences on neural activity and blood flow. On one hand, by inhibiting the A1 receptors, it increases the neuronal firing rate (Fredholm et al., 1999). On the other hand, acting on the A2A and A2B receptors located on blood vessels, it promotes vasoconstriction and therefore leads to reduction in CBF (Pelligrino et al., 2012). Due to the non-specific binding of caffeine to both types of receptors (A1 and A2), these effects may vary depending on the proportional expression of the two receptors in specific areas of the brain (Laurienti et al., 2003). In particular, studies with autoradiography (Svenningsson et al., 1997) and PET (Fukumitsu et al., 2003; Ishiwata et al., 2005) found both receptors to be heterogeneously distributed across tissue, with the A1 type more abundant in nucleus caudatus, striatum and superficial cortical areas, while A2 in putamen, nucleus caudatus and thalamus.

Caffeine has also been reported to elicit other effects of psycho-physical nature, such as increased anxiety, alertness and raising blood pressure (Einöther and Giesbrecht, 2013; a Smith, 2002). Caffeine plasma concentration peaks between 30 and 45 min after ingestion followed by a plateau of approximately 60 to 80 min (Fredholm et al., 1999; Nehlig and Boyet, 2000) and is then characterized by

a wide half-life range typically between 2.5 and 10 hours depending mainly on age, gender and weight (Fredholm et al., 1999; Magkos and Kavouras, 2005).

Due to the parallel effect on both the neural and vascular systems, caffeine can alter the coupling between CBF and $CMRO_2$. Converging evidence has been found with PET and MR techniques, indicating a reduction in baseline CBF (Cameron et al., 1990; Field et al., 2003), with an increased task related CBF change (Chen and Parrish, 2009b; Griffeth et al., 2011). Both CBF and BOLD induced cerebrovascular CO_2 reactivity (CVR) changes are reported not to be significant (Chen and Parrish, 2009a; Vidyasagar et al., 2013). Contrasting results have been found for the effects on oxygen consumption. In fact, the most relevant MR studies find decreases in relative stimulus-induced changes in $CMRO_2$ (Chen and Parrish, 2009b; Griffeth et al., 2011), which then translates in increased (Chen and Parrish, 2009) or unchanged (Griffeth et al., 2011) measured BOLD signal. Regarding absolute oxygen metabolism, there is an insufficient body of research to support any specific direction of the effect, with both increase (Griffeth et al., 2011), a tendency to decreasing (not significantly different from placebo, Yang et al., 2015) and no change (Xu et al., 2015) in $CMRO_2$ being reported.

Finally, to our knowledge no MR study has been published supplying grey matter maps of OEF_0 and absolute value $CMRO_2$ after caffeine assumption, motivating the need for a more detailed description of the acute effects on brain metabolism and haemodynamics to be provided.

5.2 Materials and methods

5.2.1 Participants and caffeine administration

Sixteen healthy caffeine consumers (8 males, age = 24.7±5.1) were recruited to the study. Exclusion criteria were introduced with special attention to possible difficulties in complying with respiratory tasks (asthma, smoking, cold/flu) and to spurious interactions with caffeine effects (drug dependency, regular medications altering systemic haemodynamics, negative reaction to caffeine). Volunteers' tolerability to hypercapnic periods and breathing through a face-mask was tested with a benching session held in the days before the first scanning session. Caffeine intake was assessed with a self-reported retrospective log of weekly caffeine consumption that quantified the use of coffee, tea, cola, chocolate and other caffeine-containing drinks, dietary supplements and over the counter medications (Addicott et al., 2009). Volunteers that were low to moderate caffeine consumers (between 51 and 298 mg/day, mean 154.1±76.2 mg/day), did not match exclusion criteria and successfully undertook the benching session were included in the study.

The caffeine dosage administered was 250 mg (roughly equivalent to the caffeine present in 2 cups of ground coffee), chosen not to exceed the recommended daily limit to avoid adverse effects in low to moderate users (300 mg, Fredholm et al., 1999). This is consistent with quantities used in previous studies, typically ranging between 200 and 300 mg (Perthen et al., 2008; Vidyasagar et al., 2013; Yang et al., 2015). The choice of excluding high consumers and caffeine-naïve volunteers was made to maximize the chance of avoiding strong withdrawal effects and unexpected reactions to caffeine respectively.

Participants were asked to abstain from caffeine containing drinks, food, pharmaceuticals and alcohol from the evening before the scanning day (9 pm) and to have a light meal not later than one hour before the visits to our lab. The study was approved by the local ethics committee. Written informed consent was obtained from each participant.

5.2.2 Experimental design

Figure 5-1 illustrates the experimental design. Each participant was scanned on two different days (30.1±18.8 days apart, same time of the day), each day including the same protocol with a pre-dose scan session followed by the delivery of the capsule of drug or placebo (randomized order for males and females) and finally a post-dose scan session.

The pre-dose sessions included an anatomical scan (when not already available for the participant) then a multi inversion time dual echo scan (mTI scans) and a dual calibrated fMRI scan (dcFMRI scan), for the duration of about 40 min. The post-dose sessions instead included a mTI scan followed by a dcFMRI scan and finally another mTI scan, for a total time of about 50 min.

Each dcFMRI scan contained an 18 min respiratory task, with interleaved levels of hypercapnia, hyperoxia and medical air being delivered to the subjects as for the experiment presented in Chapter 4.

At the end of the first scan session the subjects were removed from the MRI scanner and given a capsule containing either 250 mg of powdered caffeine or placebo (cornflour). Caffeine was administered in a double-blind, crossover, placebo-controlled, randomised manner. This was followed by a 30 min pause for the caffeine absorption, during which the subjects were allowed to relax and consumed nothing other than water. After this time, they were led back to the MR suite for the post-dose scanning session. Based on the reported drug kinetics (Fredholm et al., 1999), we expected the plasma levels of caffeine to stay stable for the duration of the second dcFMRI acquisition, that started about 45 minutes after the capsule administration.

At the beginning and end of each scanning day, volunteers were asked to fill in a Mood and Physical Sensations Scale form (MAPSS), in order to evaluate their mental and physical state (Rogers et al., 2010). At the end of the second scanning day participants were also asked to guess on which day they received caffeine or placebo and to explain their choice.

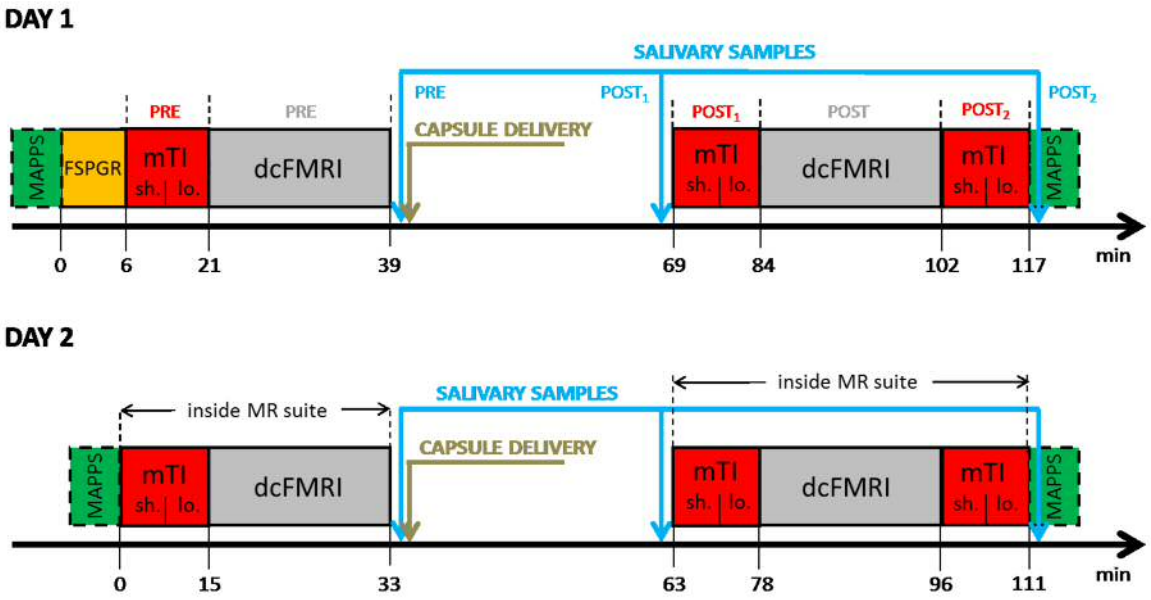

Figure 5-1: Diagram of the experimental design. Capsule delivery consists of caffeine or placebo (order randomized with gender).

5.2.3 Salivary samples

A total of 6 salivary samples (3 for each day) was taken from each volunteer in order to assess the caffeine content in saliva over time. The sample consisted on a swab (Salivette®) the participants had to chew on for a minute.

Before the first sample, subjects were asked to rinse their mouth in order to reduce contamination. In each scanning day one samples were taken pre-dose and approximately 30 and 60 minutes post-dose ("pre", "$post_1$" and "$post_2$" respectively, see Figure 5-1).

As saliva concentration of caffeine is an index of plasma caffeine level (Fredholm et al., 1999), the second and third samples of the day in which caffeine was delivered were used to reveal the stability of the post-dose plasma caffeine levels. Compliance to the request of abstaining from caffeine containing drinks and food was assessed with the first saliva sample of each scanning day.

5.2.4 Respiratory task

As for the study in Chapter 4, the respiratory task design we adopted follows the optimized design defined in our lab according to results from modelling, with three periods of hypercapnia interleaved with two periods of hyperoxia, for a total duration of 18 minutes (Figure 5-3 C). In order to achieve hypercapnia, fixed values of CO_2 (5%) were administered. For O_2, the levels of administered gas were modified with positive and negative pre-emphasis. These meant delivering short periods of respectively 100% O_2 (14s) and 10% O_2 (40s) in order to accelerate the process of reaching the hyperoxic state and then return to normoxia. It is noteworthy that although hypoxic mixtures were administered, the short duration did not induce arterial hypoxia. Supplies of 5% CO_2 (balance air), 10% O_2 (balance N_2), 100% O_2 and medical air were delivered at a total flow rate of 25 l/min to the gas mixing chamber which was placed in the MR control room and connected to the breathing circuit through a humidifier. An

independent O_2 backup cylinder was also connected directly to the breathing circuit for safety reasons.

The gas delivery system consisted of a laptop personal computer using in-house Matlab software (Mathworks, Natick, MA, USA) to control the voltage output from a NI-DAQ AD converter (National Instruments, Austin, TX). The output voltages were then fed into four mass flow controllers (MKS Instruments, Wilmington, MA, USA) that administered the gas at the required flow rate. The respiratory circuit adopted was designed based on that of Tancredi and colleagues (Tancredi et al., 2014). This circuit includes a system of one-way valves that minimizes re-breathing and a reservoir on the expired limb that allows the subject to breath room air in case of failure of the delivery system (see Figure 4-1 in Chapter 4). Gas levels were sampled from the volunteer's facemask and tidal partial pressures of O_2 and CO_2 were measured and recorded using rapidly responding gas analysers (AEI Technologies, Pittsburgh, PA, USA).

5.2.5 fMRI data acquisitions

Scanning was performed on a 3T GE HDx MRI (GE Healthcare, Milwaukee WI) with a body transmit coil and 8-channel head receive coil. All participants underwent (or had available) whole brain T1-weighted structural scans (3D FSPGR, 1x1x1 mm voxels, TI/TR/TE = 450/7.8/3 ms).

As regards the mTI PASL, dual-gradient echo (GRE) readout and spiral k-space acquisition imaging was used with the following acquisition parameters: TE1 = 2.7 ms, TE2 = 29 ms, matrix = 64x64, voxel size = 3x3x7mm^3, slice gap = 1 mm, 12 slices. Automated linear shimming with the built-in software (GE HDx) was performed. Perfusion weighting on the two scans included four equally spaced inversion times each: 150, 300, 450, 600 ms (sh. mTI in Figure 5-1) and 1000, 1400, 1800, 2200 ms (lo. mTI in Figure 5-1). Proximal inversion and control for off-resonance effects (PICORE) tagging scheme was used with a quantitative imaging of perfusion using a single subtraction (QUIPSS II) cut-off at 700ms for TI>700 ms. Label thickness was 200mm with a 10-mm gap between the distal end of the labelling slab and the most proximal imaging slice. As for the

acquisitions in Chapter 4, variable repetition time was used in both cases, such that imaging time was minimized (see Pargraph 4.2.3). Twenty control–tag pairs were acquired for each inversion time, resulting in a total acquisition time of about 3.5 and 6 minutes respectively.

During the dcFMRI acquisition, simultaneous perfusion and BOLD imaging data was collected using a PASL PICORE, QUIPSS II imaging sequence with a dual-gradient echo (GRE) readout and spiral k-space acquisition with the same acquisition parameters as the mTI scans, except for the use of a single inversion time (TI2 = 1500 ms), a set repetition time (TR = 2.2s) and acquiring 490-volumes (245 tag-control pairs).

All mTI and dcFMRI scans were preceded by two calibration scans. The first consisted in a single shot EPI scan to estimate the equilibrium magnetization of brain tissue (M_0), used for perfusion quantification (Çavuşoğlu et al., 2009), with the same acquisition parameters as for the perfusion-weighted scans, except for being acquired with fully relaxed magnetization and no labelling. The second was a low resolution, minimal contrast image used for coil sensitivity correction (Wu et al., 2011), with the same acquisition parameters as for the equilibrium magnetization scan, except for TE = 11 ms and TR = 2 s.

5.2.6 Behavioural data acquisition

Mood, Alertness and Physical Sensations Scales (MAPSS) was used to measure anxiety, alertness, and headache (Rogers et al., 2010). The scale comprised 15 questions to which participants were instructed to rate mood and physical sensation states according to how they were feeling "at the moment" using an eight-point unipolar scale, where 1 represented 'not at all' and 8 represented 'extremely'. Participants were instructed: 'There are no right or wrong answers. Do not spend too much time on any one statement but give the rating which seems to best describe your present feeling'. Three aspects of mood were rated on unipolar scales: energetic mood (sleepy–energetic), tense mood (tense–relaxed) and hedonic tone (sad/gloomy–happy/cheerful). One item assessed

mental alertness. The physical sensation descriptors were clear-headed–muzzy/dazed, light-headed/ feeling faint, jittery/shaky, and headache.

5.2.7 Data analysis

5.2.7.1 dcFMRI data and end-tidal traces

dcFMRI data were pre-processed with motion correction (MCFLIRT (Jenkinson et al., 2002)) and brain extraction (Smith, 2002) and spatially smoothed with a Gaussian kernel of 6 mm with SUSAN (Smith and Brady, 1997), separately for echo 1 and echo 2. Calculation of physiological parameters of interest was performed with a Bayesian framework of analysis applied to the forward model previously developed in our lab (Germuska et al., 2015), whose defining equations were introduced in the previous Chapter (see Paragraph 4.2.4.1 and original papers for reference). The Gaussian priors on estimates were defined specifying means and standard deviations (mean,std.) as OEF_0 = (0.35,0.1), CBF = (60,Inf) ml/100g/min, CVR = (3,0.774) %/mmHg, CBV = (1.9,2.34) ml/100g, where by "Inf" we mean a non-informative prior. Non-informative priors are used to initialize the estimate without carrying information, therefore they can be thought about as uniform distributions of probability. No prior is defined on the estimates of $CMRO_2$ as this is calculated as $CMRO_2 = CBF \cdot OEF \cdot CaO_2$. As regards other parameters, they were kept the same as those reported in the original work (Germuska et al., 2015) and are reported in the Paragraph 4.2.4.1 for reference. The inputs to the framework are dual echo GRE images and $PetO_2$-$PetCO_2$ traces, then analytic models describing the magnetization decay occurring at the first and second TE were used to estimate grey matter maps of OEF_0, CBF, CVR, venous CBV and $CMRO_2$. Prior to analysis, the end-tidal responses were visually aligned with the MR data to remove the influence of any bulk delay between the recorded end-tidal traces and the fMRI data. The resulting maps were registered into anatomical space and finally to MNI space (using FSL FLIRT, (Jenkinson et al., 2002)) for second level analysis.

Mean grey matter values of each estimated parameter were calculated for the four scans and masked for I) partial volume grey matter values (based on MNI

space priors) greater than 30% and then II) estimated values of CBF within the range [0 200] ml/100g/min. The first criterion was imposed as an empirical threshold to avoid values affected by poor SNR of the signal in white matter, while the second was used to exclude non-physiological values. Moreover results from one subject (s16) were excluded for their poor quality in a single acquisition, with abnormally unsteady end-tidal values due to the very irregular breathing pattern that made estimation unfeasible. Therefore the subsequent statistical analyses were carried out on N=15 subjects.

Two-way ANOVA tests were then performed for each parameter estimated to test for differences on the effect of the two factors considered, that is 1) "drug" (i.e. caffeine or placebo) and 2) "dosing" (i.e. pre or post dose). T-tests were also performed to test the significance of differences between changes from pre to post condition with caffeine and placebo.

Group-level voxel-wise analysis were then performed. For each parameter the differences from pre to post condition with placebo were tested against those obtained with caffeine with a paired t-test. In order to do this, anatomical T_1-weighted images were first registered to the MNI152 standard space with the FSL program *FNIRT* (Andersson et al., 2007) and the obtained transformations were then applied to the estimated maps. T statistics were then calculated on the map in MNI 152 standard space with the AFNI program *3dttest++* (Cox, 1996) and thresholded with a voxel-wise significance level of $\alpha_v = 0.01$ and a cluster-wise level of $\alpha_c = 0.05$ with minimum size of 246 mm^3, as estimated with the AFNI program *cdf* (Cox, 1996).

In addition, a ROI analysis was carried out to further investigate the spatial distribution of the estimated parameters at a group level. Mean changes from pre to post condition in caffeine and placebo are reported for seven different ROIs: caudate nucleus, frontal lobe, insula, occipital lobe, parietal lobe, putamen and thalamus (see Figure 5-8, F). These regions were chosen in order to subdivide grey matter into approximately structurally homogeneous areas with the purpose of testing whether changes in haemodynamics and metabolism can be considered consistent across tissue. Note that these regions are characterised by

different volumes: higher for the lobes, while lower for the others. Segmentation was based on the Harvard-Oxford cortical and subcortical structural atlases (threshold 50 %).

5.2.7.2 mTI CBF ASL data

Data was analysed using a two-compartment model developed by Chappell and colleagues (Chappell et al., 2010) which attenuates the error in CBF estimates due to signal arising from intravascular blood by modelling its effect on the ASL signal. In particular, the *oxford_asl* program – included in the FSL BASIL toolkit – was used, allowing us to obtain unscaled CBF maps, along with estimated arterial blood volume (aCBV, if found to significantly contribute to the signal) and tissue arrival time (TAT). CBF quantification and coil sensitivity correction were then performed as for the dcFMRI data.

Mean grey matter values of CBF and TAT were calculated for the six scans and masked following the same criteria adopted for the dcFMRI data. Note that in this case the factor "dosing" has three levels ("pre", "$post_1$" and "$post_2$"). Similarly to the dcFMRI data, two-way ANOVA tests were performed for each parameter to test for the effects of the two factors considered.

Finally t-tests were performed voxel-wise for CBF and TAT to localise possible spatial distributions of the effects as per the dcFMRI data. The registration of the maps from subject space to MNI152 standard space was carried out with *FNIRT* (Andersson et al., 2007), while t statistics were calculated with the AFNI program *3dttest++* (Cox, 1996) and thresholded with a voxel-wise significance level of α_v = 0.01 and a cluster-wise level of α_c = 0.05 with minimum volume size of 246 mm^3. For ease of comparison with the results obtained from dcFMRI data, t-tests were only performed with differences between the pre and $post_2$ condition.

5.2.7.3 Behavioural data

A two-way ANOVA was performed for each of the 15 items of the MAPPS, followed by t-tests on the changes within session due to caffeine or placebo in order to evaluate the effect of the factor considered on the mental state of the subjects.

5.3 Results

5.3.1 Salivary sample data

Concentrations of caffeine from the salivary samples are reported for all subjects in Figure 5-2. These show that the levels of caffeine in saliva are significantly different from baseline ("pre" condition) at thirty minutes post caffeine ingestion and continue to rise from a mean of 2.08 mg/l to a significantly higher mean value of 4.1 mg/l between post-caffeine 1 and post-caffeine 2 samples. In contrast, concentrations remain constantly low for placebo, with one subject showing consistently high concentrations (about 1 mg/l), while for another subject values increased with time.

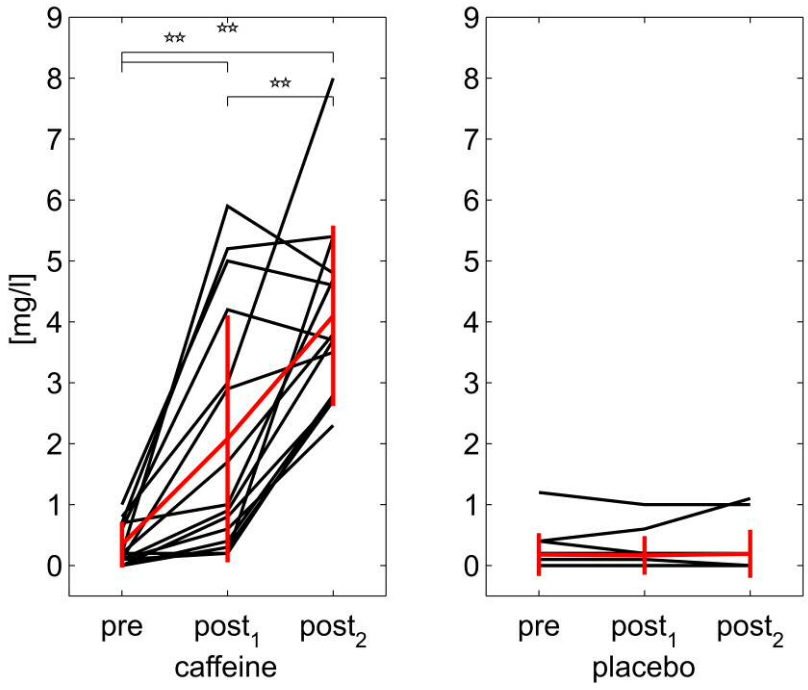

Figure 5-2: values of caffeine salivary concentration for the three samples in each day ("caffeine" or "placebo"). Significance of t-tests reported (**p<.01).

5.3.2 dcFMRI data and respiratory traces

The average baseline $PetCO_2$ value was 113 mmHg, while it was 39 mmHg for $PetCO_2$. The average change in $PetCO_2$ from baseline was 12 mmHg, while plateau levels of hyperoxia caused an average increase of approximately 211 mmHg in $PetO_2$ (see Figure 5-3-B). Periods of hyperoxia appear to produce a reduction in $PetCO_2$ and periods of hypercapnia are associated with slight increases in $PetO_2$. Results of an ANOVA carried out on average increases in end-tidal values did not show any significant effect of drug, dosing or their combination (data not shown).

The end-tidal traces for a single representative subject (s12), the end-tidal traces averaged across all subjects and the respiratory task are reported in Figure 5-3. Reasonably steady values of $PetCO_2$ are maintained during hypercapnia and of $PetO_2$ during hyperoxia, the latter preceded and followed by short perturbations due to periods of 100% O_2 hyperoxia and 10% O_2 hypoxia respectively. The excluded subject (s16) was excluded because of abnormally unsteady values during hypercapnia, hyperoxia and also normocapnia-normoxia, due to the very irregular breathing pattern (data not shown).

Grey matter values of all the estimated parameters for the four conditions considered are reported in Figure 5-4. Changes from "pre" to "post" conditions are not found to vary significantly for any parameters with placebo (when considered separately). Instead, with caffeine a significant increase is found for OEF_0 and CVR, with values changing form 0.42±0.067 to 0.48±0.066 (Figure 5-4,A) and from 2.2± 0.50 to 2.5±0.4 (Figure 5-4, D) respectively. Also, with caffeine significant decreases are found for CBF, CBV and $CMRO_2$, with values changing from 65±12 to 45±6 (Figure 5-4, B) ml/100g/min, from 2±0.4 to 1.3±0.2 (Figure 5-4, E) ml/100g and from 233±48 to 188±36 (Figure 5-4, F) µmol/100g/min respectively.

Results of ANOVA performed on whole grey matter values for each parameter are reported in Table 5-1. Statistics are significant for all effects (drug, dosing and interaction) for CBF and CBV, whereas they are not significant for OEF_0 and CVR.

As regards $CMRO_2$, the effect is significant for both drug and dosing, whereas it is not for their interaction.

Figure 5-5 shows the mean grey matter percent change from the pre to post condition for all parameters with caffeine and placebo. No significant changes are found for any parameters with placebo, whereas they are significant with caffeine for several parameters, with OEF_0 showing an increase of 15.6% (±18.9%, $p < 0.05$), while CBF, CBV and $CMRO_2$ showing a decrease of -30.4% (±6.1%, $p < 0.01$), -31% (±13.8%, $p < 0.01$) and -18.6% (±11.1%, $p < 0.01$) respectively.

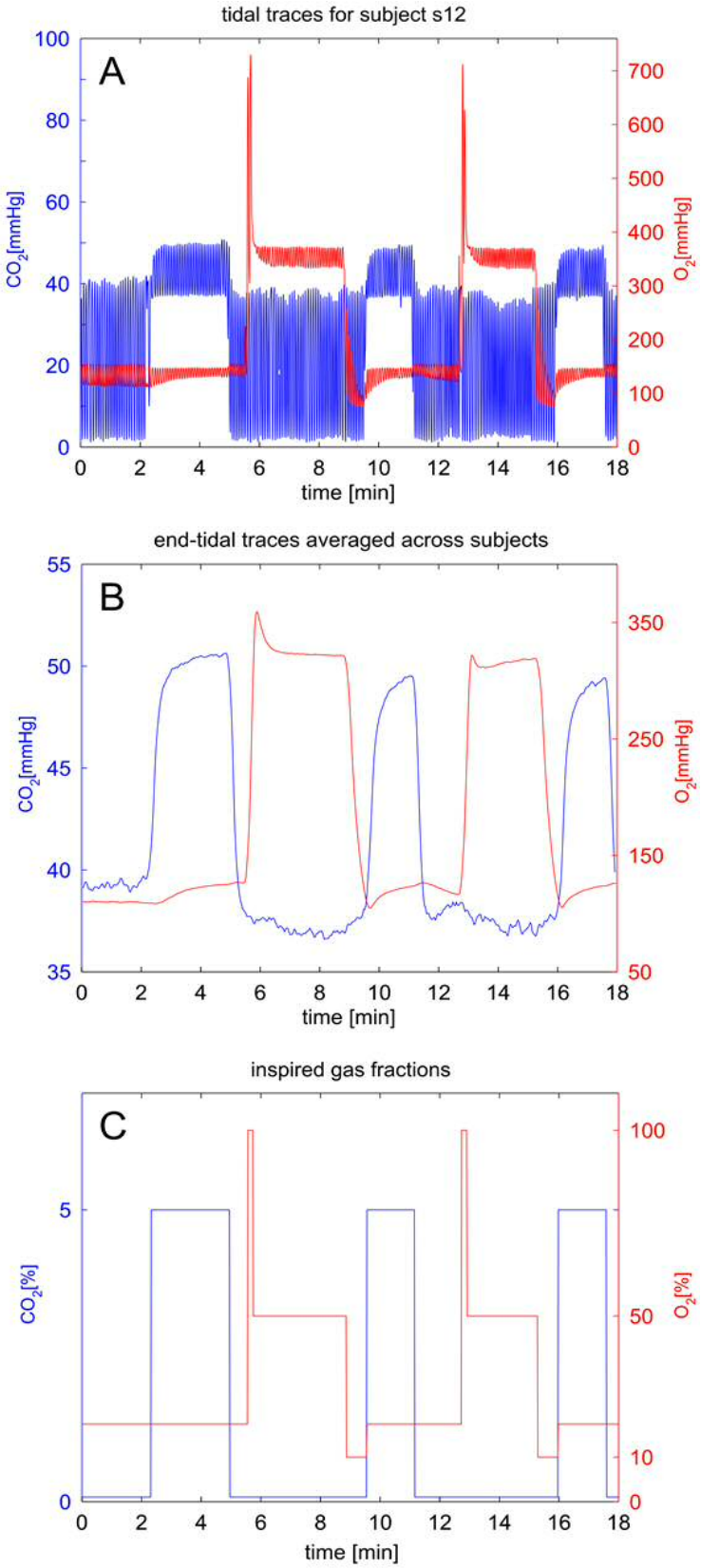

Figure 5-3: A – Tidal traces of a single representative subject (s12). B - End-tidal traces averaged across all subjects. C – inspired gas fractions. In both A and B three periods of hypercapnia and two of hyperoxia are clearly visible, interleaved with short periods of normocapnia-normoxia. Positive and negative emphases can be distinguished before and after the plateau hyperoxic periods, respectively.

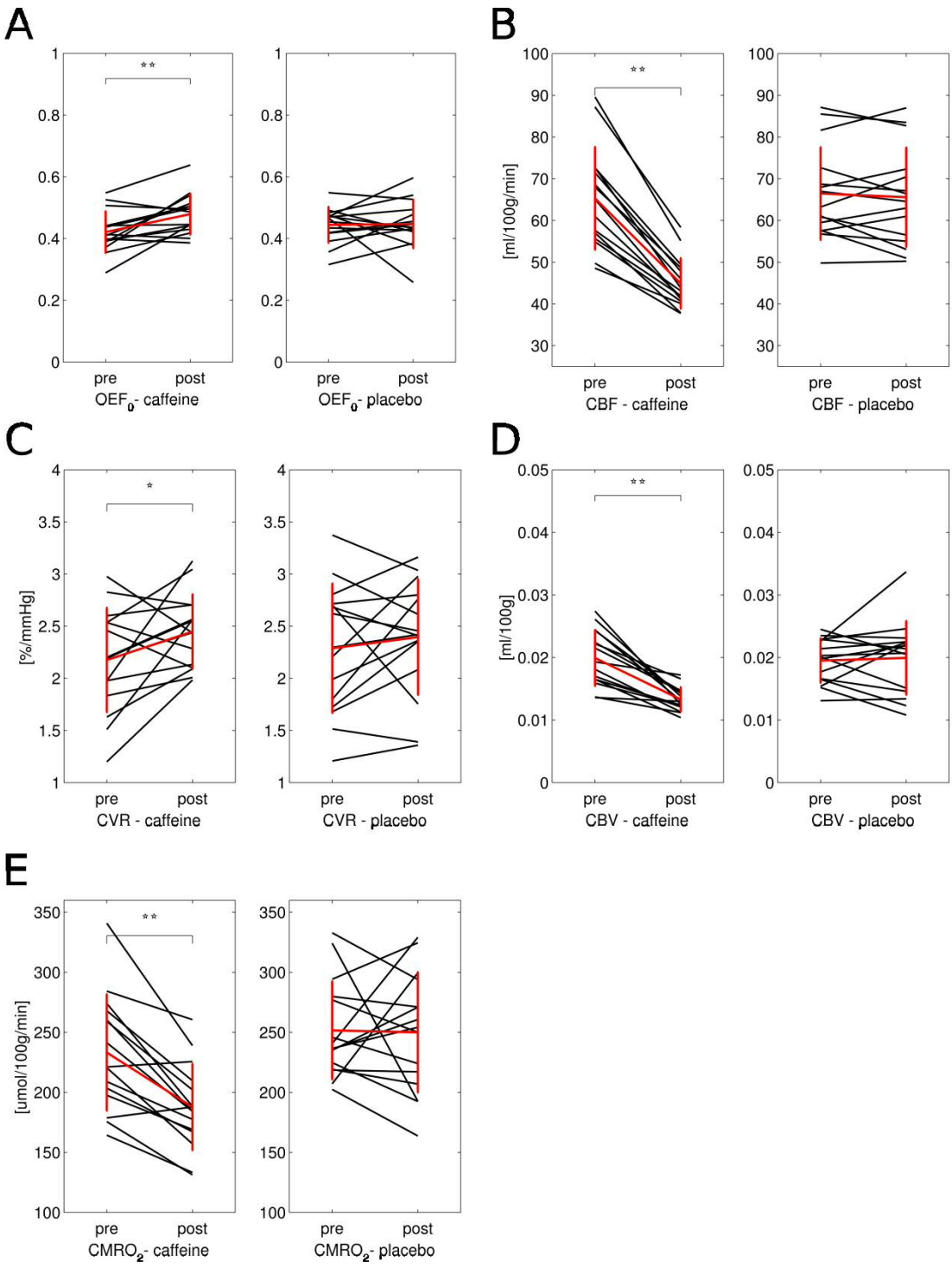

Figure 5-4: mean grey matter values of the five estimated parameters for N=15 subjects. In red the calculated means with bars representing the standard deviations. Significance of t-tests between pre and post condition denoted with asterisks (*p<.05, **p<.01)

	OEF_0		CBF		CVR		CBV		$CMRO_2$	
	F	p val.	F	p val.	F	p val.	F	p val.	F	p val.
DRUG	0.06	0.814	15.88	<0.001	0.05	0.824	8.22	<0.01	12.56	<0.001
DOSING	3.07	0.085	15.07	<0.001	2.04	0.158	8.15	<0.01	4.26	<0.05
INTERACTION	2.51	0.119	12.70	<0.001	0.39	0.536	10.63	<0.01	3.71	0.059

Table 5-1: results of ANOVA performed on GM averaged values of the maps estimated with the dcFMRI model. Statistics (F and p value) for main effects (DRUG, DOSING) and interaction effect (INTERACTION) reported for each of the six parameters considered.

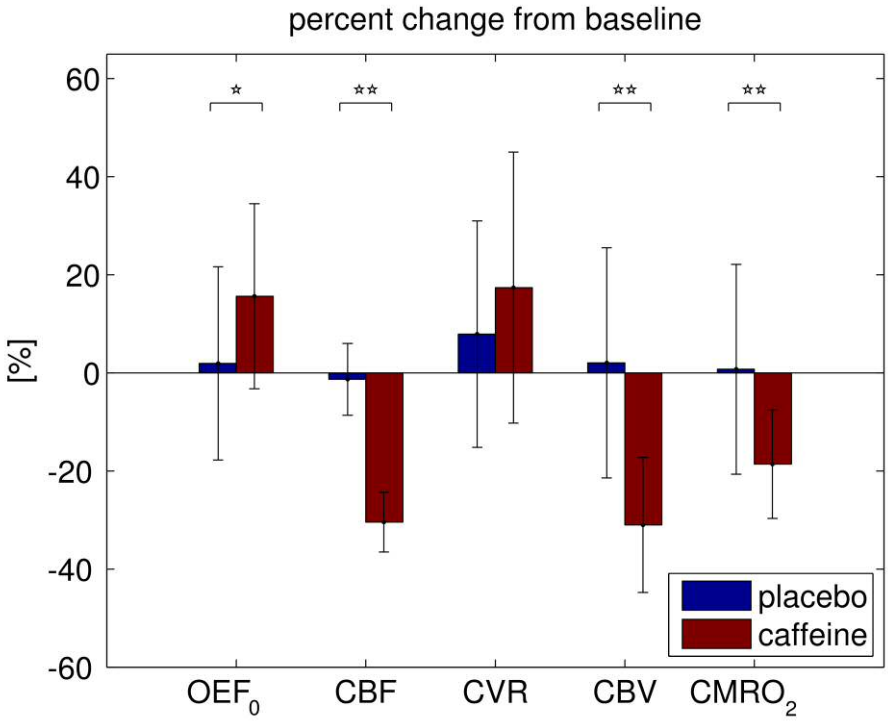

Figure 5-5: mean grey matter values of percent change between pre and post condition for the five estimated parameters (N=15, bars representing the standard deviations). Significance of t-tests are denoted with asterisks (*<.05, **<.01)

Figures 5-6 and 5-7 show results from voxel-wise analysis of the estimated maps. In Figure 5-6 examples of grey matter values of estimated maps registered to MNI152 standard space for a single representative subject (s12) before and after caffeine assumption ("pre" and "post" condition respectively). These maps are consistent with the mean trend, with values of CBF, CBV and $CMRO_2$ generally decreasing while values of OEF_0 and CVR increasing. Besides they are representative of the variability of the result, with generally spatially smooth results for OEF_0 as opposed less smooth estimates for CBV and CVR. In these maps it is also possible to see areas where the algorithm fails its estimates (indicated by arrows in Figure 5-6).

Figure 5-7 displays thresholded t values from the group t-test performed between the differences from pre to post condition with caffeine and placebo. Areas of significant change are found for all parameters. More information on the size and coordinates of these for OEF_0 and $CMRO_2$ can be found in the Supplementary material section at Paragraph 5.5 (Table S-5.1 and S-5.2). CBF and CBV show widespread and highly significant decrease in change due to caffeine. $CMRO_2$ also shows areas of significant decrease, but they are more localized. Conversely, results from OEF_0 and CVR indicate areas of increase due to caffeine, with the latter being confined to only few significant areas. None of the parameters showed a mixed direction of the effect.

Finally Figure 5-8 shows the results of a ROI analysis to further investigate the spatial distribution of the estimated parameters at a group level. Mean changes from pre to post condition in caffeine and placebo are reported for seven different ROIs. These show the effect of caffeine being consistently significant for CBF (Figure 5-8 B), while being more varied for the others. CBV changes (Figure 5-8 D) are only significant in the frontal lobe, occipital lobe, parietal lobe and thalamus (ROIs 2, 4, 5 and 7), while they are not for the other regions. OEF_0 (Figure 5-8 A) changes are significant in the caudate nucleus, putamen and thalamus (ROIs 1, 6 and 7). CVR does not show significant effects, with measurements characterized by high variance across regions. Finally, decreases in $CMRO_2$ (Figure 5-8 E) are only significant in occipital lobe and parietal lobe (ROIs 4 and 5).

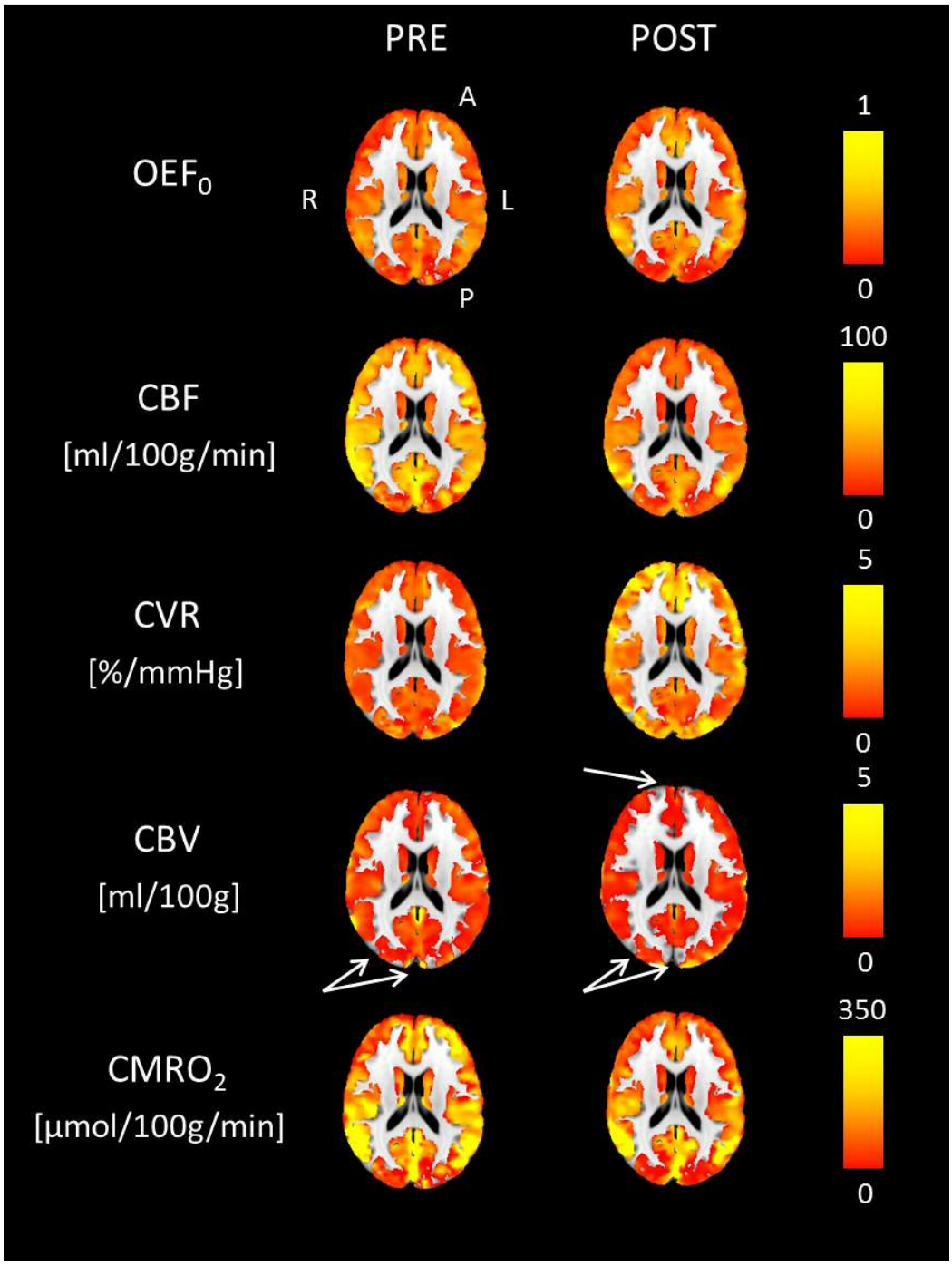

Figure 5-6: Estimated GM maps in MNI space for a single representative subject (s12). Results displayed before and after caffeine assumption (pre and post condition respectively). White arrows point at areas where the estimate failed in CBV and OEF_0 (and therefore $CMRO_2$).

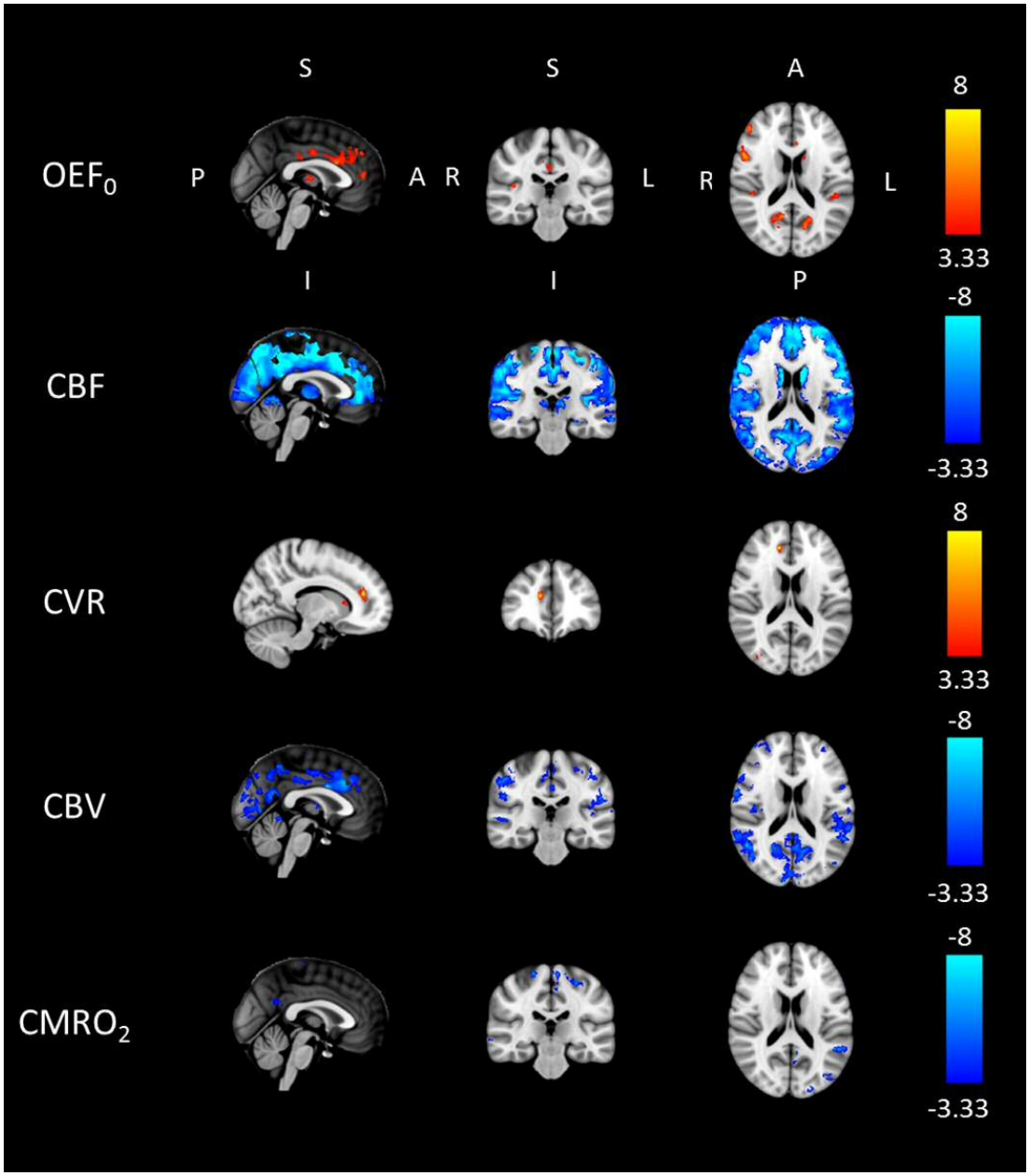

Figure 5-7: Results of a group t-test performed between differences from pre to post condition in caffeine and placebo. Each map shows values of the t statistic for which $p<0.01$ either in negative or positive direction ($t>3.33$ and $t<-3.33$ respectively, 14 dof), and thresholded for cluster size with significance level $\alpha_c=0.05$.

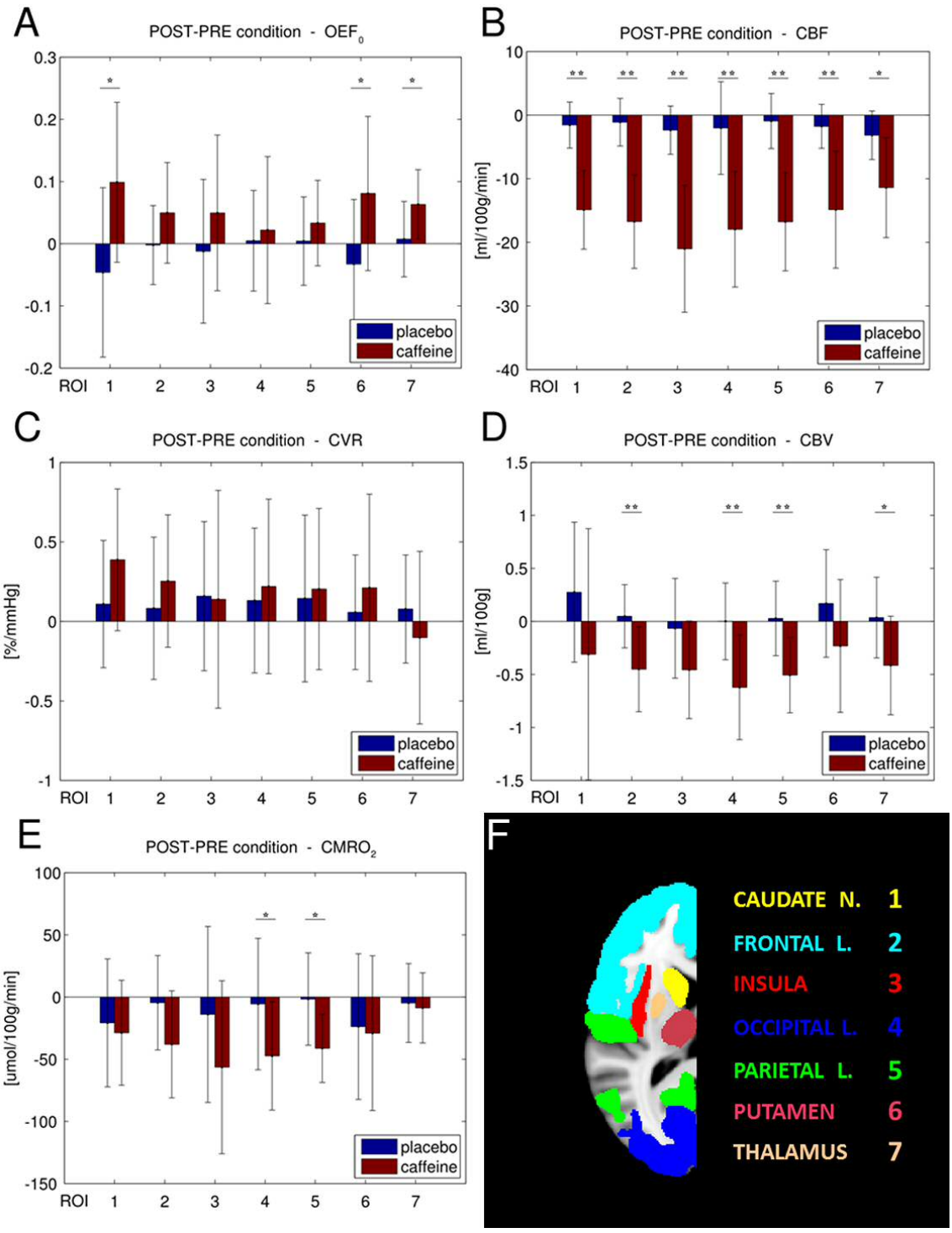

Figure 5-8: Mean differences from pre to post condition in caffeine and placebo for each parameter in different ROIs. Bars represent standard deviations. Significance of t-tests is denoted with asterisks (*<.05, **<.01, fdr corrected).

In panel F key for the ROIs considered: 1 - caudate nucleus; 2 - frontal lobe; 3 - insula; 4 - occipital lobe; 5 - parietal lobe; 6 - putamen; 7 - thalamus.

5.3.3 mTI data

Mean grey matter values of all the estimated CBF and TAT for the six conditions considered are reported in Figure 5-9. Changes from baseline are not found significant for placebo. Instead, in caffeine a significant decrease ($p<.01$) is found for CBF form 49±8.9 ml/100g/min before caffeine delivery to 34±5.6 ml/100g/min after thirty minutes and then to 32±5.2 ml/100g/min after sixty minutes. Also the last two show significant difference, even though less strong ($0.01<p<0.05$). As regards TAT, values for caffeine show significant increase form 0.71±0.038 s in the pre to 0.74±0.029 s at $post_1$ and then to 0.74±0.028 s at $post_2$.

Results of ANOVA performed on whole grey matter values for both parameters are reported in Table 5-2. Statistics are significant for all effects (drug, dosing and interaction) whereas for TAT, the effect is significant for both drug and dosing but it is not for their interaction.

Finally in Figure 5-10 t statistics resulting from a group-level test performed between differences from pre to $post_2$ condition in caffeine and placebo are reported. CBF shows a general significant decrease across grey matter. TAT shows more confined areas of significance, with both a positive and negative direction of the effect (red-yellow and blue-light blue respectively in Figure 5-10).

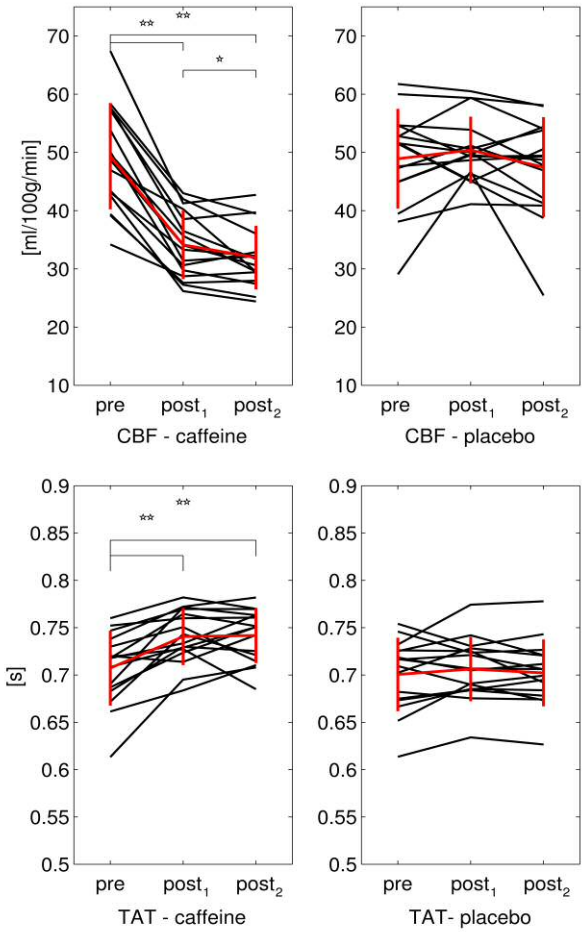

Figure 5-9: mean grey matter values of the two estimated parameters (N=16). In red the calculated means with bars representing the standard deviations. Significance of t-tests between pre, $post_1$ and $post_2$ condition are denoted with asterisks (*p<.05, **p<.01)

	CBF		TAT	
	F	p val.	F	p val.
DRUG	14.59	<0.001	4.22	<0.05
DOSING	39.47	<0.001	10.11	<0.001
INTERACTION	15.86	<0.001	2.48	0.089

Table 5-2: results of a two-way ANOVA performed on values of the maps estimated with the mTI model averaged across grey matter. Statistics (F and p value) for main effects (DRUG: dof (1,60), DOSING dof (2,60)) and interaction effect (INTERACTION) reported for CBF and TAT.

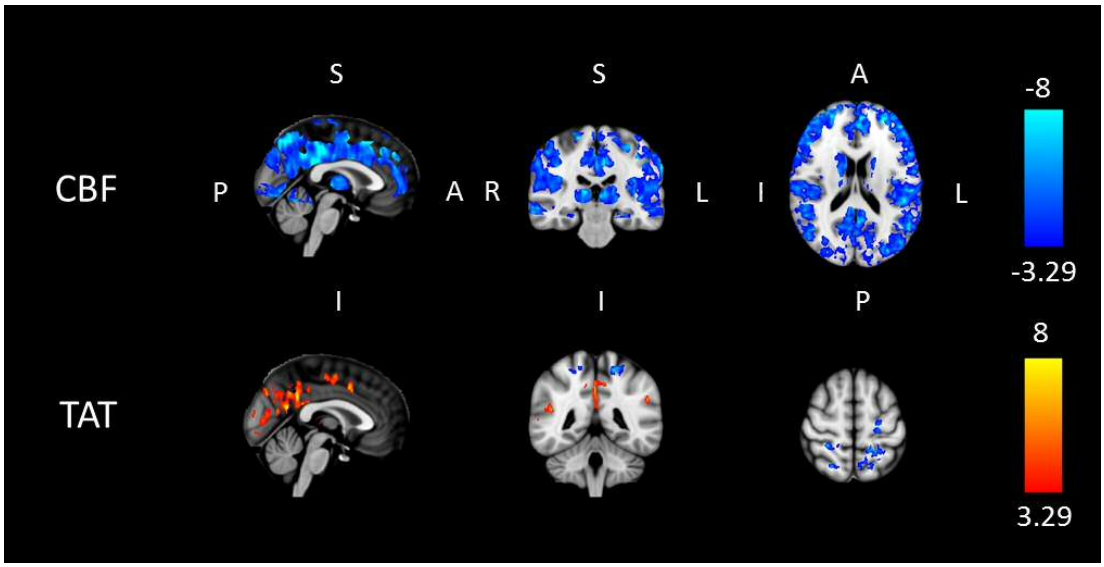

Figure 5-10: Results of group-level t-test performed between differences from pre to post$_2$ condition in caffeine and placebo. Each map shows values of the t statistic for which p<0.01 either in positive or negative direction (t>3.29 and t<-3.29 respectively, 15 dof), and thresholded for cluster size with significance level α_c=0.05.

5.3.4 Behavioural data

The analysis of behavioural data does not show any significant result, with the highest F value relative to a main effect of dosing on the relax-ness feeling (p value not significant when corrected for multiple comparisons). Mean changes from pre to post condition show a not statistically significant trend of caffeine reducing sleepiness, fatigue and headache while increasing energetic mood and jitteriness compared to placebo. These results are shown in the Supplementary material section at Paragraph 5.5 (Table S-5.3).

5.4 Discussion

The grey matter analysis of estimates from the forward model shows CBF and CBV decreasing by about 30% due to caffeine ingestion, while they remain constant with placebo. OEF_0 increases by about 16%, partially offsetting the CBF reduction in oxygen delivery, leading to an overall 18.6% decrease in $CMRO_2$.

All changes are found to be significant when tested for two-way ANOVA and post-hoc t-tests, highlighting a clear effect of caffeine. Despite the variability in the bulk estimates reported in Figure 5.4, all changes from baseline due to caffeine ingestion are found to be significant. The effect is particularly high for CBF, while less pronounced for OEF_0, resulting in a wider range of changes in $CMRO_2$. Based on the power calculations supplied in the Discussion section of Chapter 4, the accuracy of our method seems appropriate to detect the effect size of caffeine on CBF and OEF_0 with a statistical power of 80%.

Our haemodynamics findings confirm what has already been reported (Cameron et al., 1990; Field et al., 2003). The reduction in oxygen metabolism contrasts what is reported by some other MRI studies that show both increases (Griffeth et al., 2011) and no change (Xu et al., 2015) in $CMRO_2$, while is consistent with recent findings using simultaneous near-infrared spectroscopy and transcranial Doppler ultrasound (Yang et al., 2015). Our results are also consistent with an hypothesis of decrease in energetic demand due to an overall inhibitory effect mediated by two distinct mechanisms triggered by caffeine as an antagonist of adenosine receptors: pre-synaptic inhibition of neurotransmitter release and prevention of post-synaptic depression (Pelligrino et al., 2012). The result of the two would be decrease in synaptic activity accompanied by increase in spiking activity. As the metabolic demand of the first is predominant in the total energetic balance of neural activity (Raichle and Gusnard, 2002), a decrease in oxygen metabolism might be expected. This hypothesis is also partially supported by previous electrophysiology studies finding reductions in spectral power with EEG (Dimpfel et al., 1993) and connectivity with MEG (Tal et al., 2013) in the resting state following caffeine ingestion.

As regards CBF, our estimates obtained with dcFMRI acquisitions are also supported by the analyses carried out on data from mTI-ASL acquisitions. In fact, a similar decrease of 30 and 35 % is found when comparing the value in pre to $post_1$ and $post_2$ conditions respectively (Figure 5-9) and a good correlation is found between the two set of measurements obtained with different modality. Results also highlight a seemingly constant offset between the two estimates, with the ones obtained from our forward model being about 15 ml/100g/min higher than the ones obtained with the mTI model. This can be explained considering that estimates from single TI measures - as in the case of the forward model – tend to overestimate CBF compared to those from multi TI measures, due to both assumed constant timings of the labelled bolus (Van Osch et al., 2007) and spurious arterial contributes to the ASL signal (Chappell et al., 2010).

Results for group mean grey matter seem to be overestimating $CMRO_2$ when compared to literature, with a resting state value of 242.4±38.4 μmol/100g/min (averaging the results from pre condition in each day) opposed to reported values of 145±30 (Gauthier and Hoge, 2012) and 155±39 μmol/100g/min (Bulte et al., 2012) obtained with calibrated BOLD methods and values of 182±12 (Liu et al., 2013), 158±18 (Fan et al., 2012) and 125±15 μmol/100g/min (Bolar and Rosen, 2011) obtained with other MR methods and of 157.4±19.7 (Roland et al., 1987) and 120±17.7 μmol/100g/min (Ibaraki et al., 2010) with PET. This overestimate can in part be explained by the young cohort analysed, but can be mostly attributed to the propagation of systematic bias in estimates of CBF and OEF_0. In fact our baseline grey matter CBF estimates are 65.8±11.7 ml/100g/min (averaging the results from pre condition in each day), similar to values of 63 ml/100g/min reported in other studies (Ances et al., 2009), whereas typical literature values range between 41 ml/100g/min (Bulte et al., 2012) and 52 ml/100g/min (Gauthier and Hoge, 2012). Similarly, measured values of 0.433±0.063 for OEF_0 are above those reported by others, with typical values for MR methods ranging between 0.26 (Bolar and Rosen, 2011) and 0.395 (Guo and Wong, 2012). Nevertheless whole brain grey matter estimates appear to be more similar to those found in a previous study from our lab with OEF_0 of 0.42 ± 0.12 and $CMRO_2$ of 184±45 μmol/100 g/min given a CBF of about 56 ml/100g/min

(Wise et al., 2013). Also, the overestimated values reported here suggest that the regularization introduced with the forward model proposed does not bias the results towards the priors.

As grey matter maps were estimated for all parameters, we were able to carry out voxel- and ROI-wise analyses at a group level in order to investigate the spatial distribution of the caffeine effect. All five parameters showed areas of significant differences in the same directions reported for the mean difference across grey matter. These areas were widespread for CBF (as also found for the analysis of mTI-ASL data, Figure 5-10) and CBV, as expected due to adenosine receptors being spread all over the grey matter. Areas of significant change were instead more restricted for OEF_0, $CMRO_2$ and CVR. An analogue spatial distribution of the response to caffeine surfaces from the analysis of changes between pre and post condition due to caffeine for estimated values averaged across seven ROIs. Notably, at a ROI level significant changes in OEF_0 were mostly localized in the putamen, caudate nucleus and thalamus, where the highest concentrations of A1 and especially A2 receptors have been reported to be (Svenningsson et al., 1997; Fukumitsu et al., 2003; Ishiwata et al., 2005). Nevertheless, the first two regions appear to be the one with the most variability in the estimates (see Figure 5.8), possibly due to their size. As a consequence, caution must be taken when considering the implication of such results.

Interestingly, putamen, caudate nucleus and thalamus also show the least difference in $CMRO_2$ between pre and post dose, with values not significantly different between pre and post dose. This could be explained by the maintenance of a higher oxygen supply to the local metabolic need while perfusion is dropping. This behaviour, confined to few small subcortical structures, seems in contrast with the general grey matter tendency and needs further investigation. Surely the findings suggest a complex and spatially distributed effect across grey matter that can be characterised with our novel approach, while cannot be properly captured with standard bulk analyses.

Caffeine salivary concentrations measured suggest that subjects complied with the request of abstaining from caffeine consumption previous the experiments,

with only one dubious case. Although, given that this has outlying values less than half the mean value found thirty minutes after caffeine consumption, it is reasonable to assume that they are not concerning sources of nuisance for the study. The data also show that in most cases salivary samples were taken before peak caffeine concentration, as values increase significantly from $post_1$ to $post_2$. The three samples showing instead a mean decrease in concentration could possibly be due to a faster drug kinetic for those subjects and therefore measures taken closer in time to peak concentration. This is not unexpected, given that time to peak values are reported to be between 30 and 45 minutes (Fredholm et al., 1999). This means that $post_1$ mTI acquisitions might be measuring a changing haemodynamic state of brain tissue, leading to noisier estimates of CBF and also values of CBF significantly different between $post_1$ and $post_2$ conditions (as seen in Figure 5-9). On the other hand we do not expect the haemodynamic state to change significantly for the subsequent post dcFMRI acquisitions thanks to the chosen timing. Also, the values for subjects showing decrease in concentration suggest a good stability of the levels during the time in between the two samples as expected, with a difference of only about 0.67 mg/l.

Data from MAPPS reports did not show significant effects of drug or dosing on the psycho-physic state of the participants. Nevertheless there were non-significant trends indicating that caffeine reduce sleepiness, fatigue and headache and increased energetic mood and jitteriness compared to placebo, which is consistent with effects reported in literature for larger groups of participants (Rogers et al., 2010; Smith et al., 2012). Importantly, values measured with MAPSS and feedbacks from subjects did not indicate significant adverse reactions to caffeine consumption that could have caused discomfort to the subjects and therefore behaviour capable of degrading the quality of the data (e.g. movements into the scanner). In the case of the excluded subject, the unusual pattern of respiratory traces only occurred on the second scanning day and was not related to any particular discomfort experienced (as no negative feedback was reported and the subject was willing to carry on with the "post" acquisition) nor was it repeated in any of the remaining dcFMRI acquisitions from the same or other participants.

The analysis and results presented in this work have three main limitations. The first relates to the assumptions we make on metabolism. We assume isometabolism during hypercapnia and hyperoxia when performing respiratory tasks, as already discussed for the experiment in Chapter 3 and Chapter 4. We also assume that metabolism does not change during the length of the dcFMRI acquisitions. This may not be the case in the post condition of the caffeine day due to possible changes of drug plasma concentration, although evidence suggests that the concentration plateaus by the time the acquisition starts (Fredholm et al., 1999).

A second limitation might be represented by the reliability of individual results. In fact, while values of the parameters averaged across grey matter lie within physiological ranges and show generally sensible trends (as seen in Figure 5-4), individual maps include several outliers (Figure 5-6). Results, together with the repeatability performances reported in Chapter 4, suggest that this is mainly due to low SNR of the MR signal and variability of the respiratory traces, which tend to bias or even prevent the estimates. If this represents a shortcoming on one hand, on the other hand it demonstrates that the estimates are not driven by Bayesian priors as also suggested by the existence of limited areas were the method fails to output valid values (highlighted in Figure 5-6). This limits the use of the technique to group analysis, for which it is still possible to detect distributions of areas of significant effects both in a voxel-wise or ROI-wise calculations.

Furthermore, the levels of variability found together with lack of standard methods for retrospective physiological noise removal (e.g. RETROICOR, Glover, 2000) suggest that care must be taken when trying to apply this method to other conditions, such as functional tasks. More work is therefore needed to evaluate the performance of our method in such approaches.

A third set of limitations is more specifically related to the caffeine effects we are characterizing with a Bayesian estimate framework. A first issue is that, as previously discussed, the CBF values are overestimated compared to those obtained from the mTI model, leading directly to overestimated values of $CMRO_2$

(as by definition $CMRO_2 = CBF \cdot OEF \cdot CaO_2$). If we were to correct the latter using CBF values obtained from the mTI model and keeping OEF constant, we would obtain mean values for $CMRO_2$ in the pre condition of about 155 μmol/100g/min, which is more similar to values reported in literature. Nevertheless, as changes in CBF are consistent between the two techniques, our method still enables to account for this variability and detect these changes. Another issue is specifically related to estimates of $CMRO_2$. In fact, as $CMRO_2 = CBF \cdot OEF \cdot CaO_2$, detection of changes in $CMRO_2$ might simply be triggered by decreases in CBF with little or no change in OEF_0. This could be the case, for example, if the model was highly sensitive to changes in CBF but less so to changes in OEF_0. However, the fact that areas where significant changes in CBF and OEF_0 occurring at the same time show no significant change in $CMRO_2$ (see caudate nucleus, putamen and thalamus in Figure 5-8) argues against this suggestion.

5.5 Conclusions

In conclusion, we have characterised acute effects of caffeine on brain haemodynamics and metabolism in a drug study with the novel forward model and a dual calibrated BOLD experiment. The effects measured are consistent with those known from neural physiology and in agreement with electrophysiology studies. New information is provided in terms of spatial distribution of the estimated maps allowing us to identify particular areas where the significant effects are localized. This represents a major step forward in the understanding of the acute effects of caffeine and it also demonstrates that such method could be applied to assess grey matter haemodynamics, OEF_0 and $CMRO_2$ at a voxel-wise resolution for other pharmacological agents.

5.6 Supplementary material

Volume (mm^3)	t max	COG x (mm)	COG y (mm)	COG z (mm)	Position
4604	6.74	0.298	25.4	30.8	Anterior cingulate and paracingulate g. (R)
1872	8.71	16.5	-63.6	21.9	Precuneous c. (L)
1343	6.97	52.4	10.1	19.7	Inferior frontal g. and precentral g. (R)
1170	6.07	59.3	-2.62	6.61	Central opercular c. (L)
888	10.4	47.9	38.8	21.6	Frontal pole (L)
653	5.84	55.6	-6.43	35.5	Pre- and postcentral g. (R)
564	5.9	35.6	44.8	33.4	Precuneous c. (L)
548	5.96	-15.4	-64.9	18.8	Precuneous c. (L)
418	6.04	41.6	-8.53	9.89	Insular c. (L)
377	5.44	5.19	23.8	58.3	Superior frontal g. (L)
352	5.72	-9.3	14.6	8.11	Caudate nucleus (L)
341	4.71	4.78	-28.5	35.3	Posterior cingulate g. (L)
299	6.26	-46.6	-14.8	41.6	Pre- and postcentral g. (R)
273	4.54	-47.3	-34.9	18.6	Parietal opercular c. (R)
262	4.85	0.925	-13.4	7.61	Thalamus (L and R)
255	6.64	21.3	39.2	39.9	Frontal pole (R)
247	5.22	-24.1	12.1	1.21	Putamen (L)

Table S-5.1: Regions showing significant increase in OEF_0 ordered by size. Reported are the volume, the maximum value of the t statistic (t max) the coordinates of the centre of gravity in MNI152 space (COG x,y,z). In the further right column the position of the regions according to the Harvard-Oxford cortical and subcortical structural atlases ("R/L" = right/left, "c." = cortex, "g." = gyrus).

Volume (mm^3)	t min	COG x (mm)	COG y (mm)	COG z (mm)	position
3532	-7.58	-30.4	-41.1	53.6	Postcentral g. and sup. parietal globule (L)
1525	-7	27.7	-65.9	48.2	Sup. lateral occipital c. (R)
1396	-5.98	-42.9	12.8	30.5	Middle and inf. frontal g. (L)
1157	-6.24	-6.54	-17.4	58.6	Precentral g. (L)
1031	-8.13	50.8	32.8	-3.92	Frontal pole and inferior frontal g. (R)
880	-6.05	-6.67	-54.1	52.1	Precuneous c. (L)
786	-6.74	-54.3	-47	19.9	Post. supramarginal g. (L)
775	-4.85	-3.75	-54.8	24.5	Post. cingulate g. & precuneous c. (L)
611	-4.97	-39.2	-7.82	-2.5	Insular c. (L)
606	-6.28	22.6	-51	58.9	Sup. parietal lobule (R)
601	-6.02	-51.4	25.3	-0.494	Inferior frontal g. (L)
575	-5.59	17	67.5	7.68	Frontal pole (R)
525	-6.64	61	-35.5	-5.15	Middle temporal g. (R)
519	-5.54	-26.3	-0.007	50.5	Sup. & middle frontal g. (L)
483	-5.62	34.6	-75	24.7	Sup. lateral occipital c. (R)
451	-4.97	-8.25	5.89	61.7	Juxtapositional lobule c. (L)
422	-6.27	-22.3	-84.2	29	Sup. lateral occipital c. (L)
390	-5.46	11.2	-46.6	41	Precuneous c. (R)
364	-5.29	-9.12	-40.6	61.6	Postcentral g. (L)
345	-5.27	-33.5	-14.4	63	Precentral g. (L)
323	-6.44	40.2	19.3	29	Middle frontal g. (R)
322	-5.98	-40	-78.9	16.8	Sup. lateral occipital c. (L)
294	-6.15	18.9	-26.7	66.6	Pre- & postcentral g. (R)
254	-6.22	-22.3	-92.8	17.3	Sup. lateral occipital c. (L)

Table S-5.2: Regions showing significant decrease in $CMRO_2$ ordered by size. Reported are the volume, the minimum value of the t statistic (t max) the coordinates of the centre of gravity in MNI152 space (COG x,y,z). In the further right column the position of the regions according to the Harvard-Oxford cortical and subcortical structural atlases ("R/L" = right/left, "c." = cortex, "g." = gyrus).

	DRUG		DOSING		INTERACTION		ch. CAFFEINE	ch. PLACEBO	
FEELING / SENSATION	F	p val.	F	p val.	F	p val.	m±std	m±std	p val.
Clear headed	1.15	> 0.1	0.01	> 0.1	0.01	> 0.1	-0.06 ± 1.29	0 ± 1.37	> 0.1
Muzzy	0.14	> 0.1	0.45	> 0.1	0.67	> 0.1	0.63 ± 1.26	-0.63 ± 1.61	> 0.1
Relaxed	0.34	> 0.1	6.22	0.015	0.19	> 0.1	-0.88 ± 2.55	-1.25 ± 2.08	> 0.1
Tense	0.37	> 0.1	0.42	> 0.1	0.42	> 0.1	-0.73 ± 0.44	-0.31 ± 1.49	> 0.1
Happy	0.64	> 0.1	0.04	> 0.1	0.04	> 0.1	0 ± 0.82	0.13 ± 0.62	> 0.1
Depressed	1.09	> 0.1	0.49	> 0.1	0.12	> 0.1	-0.19 ± 0.54	-0.06 ± 0.68	> 0.1
Energetic	0.03	> 0.1	0	> 0.1	0.23	> 0.1	0.19 ± 1.42	-0.19 ± 1.56	> 0.1
Sleepy	0.58	> 0.1	0.72	> 0.1	0.42	> 0.1	-0.56 ± 1.82	0.22 ± 2.36	> 0.1
Scared	0.70	> 0.1	0.25	> 0.1	0.25	> 0.1	0 ± 0.37	-0.19 ± 0.54	0.083
Stressed	1.43	> 0.1	2.55	> 0.1	0.36	> 0.1	-0.69 ± 1.20	-0.31 ± 0.79	> 0.1
Mentally alert	0.21	> 0.1	0.01	> 0.1	0.07	> 0.1	-0.06 ± 1.24	-0.13 ± 1.36	> 0.1
Fatigued	0.37	> 0.1	0.46	> 0.1	0.37	> 0.1	-0.69 ± 1.25	0.06 ± 1.81	0.054
Jittery	0.07	> 0.1	1.05	> 0.1	1.64	> 0.1	0.56 ± 1.32	-0.06 ± 1.34	> 0.1
Headachy	0.15	> 0.1	0.01	> 0.1	1.04	> 0.1	-0.48 ± 1.36	0.38 ± 1.96	> 0.1
Pounding heart	0.39	> 0.1	0.39	> 0.1	0.78	> 0.1	-0.06 ± 0.57	-0.13 ± 0.34	> 0.1

Table S-5.3: results of statistical analysis performed on MAPPS data. Statistics from two-way ANOVA (F and p value) looking at main effects (DRUG, DOSING) and interaction effect (INTERACTION) reported for all the questions considered. In the furthest right columns values of post-pre changes with caffeine and placebo and the p-value from a t-test testing the difference between the two. Statistics reported not corrected for multiple comparisons.

Chapter 6

Measurement of blood O_2 saturation via estimates with Fourier velocity imaging

This chapter introduces and explores a new method for quantifying brain oxygen consumption not based on hypercapnic and hyperoxic calibration. Multi-echo GRE acquisitions are exploited together with -S_vO_2 calibration curves in order to measure venous blood saturation. Background theory, simulations and real case applications are presented, together with an extensive discussion on the main limitations. Analysis of the synthetic dataset allows us to characterise the effect of noise in the signal and estimates of venous blood oxygenation in two subjects are found to increase following a visual task. This proof of concept represents a first step towards the assessment of a new promising alternative to current techniques for measuring brain oxygen metabolism.

6.1 Introduction

In the previous chapters we have explored in detail calibrated fMRI approaches for estimating OEF and ultimately $CMRO_2$. In this chapter we are focusing on quantifying the venous oxygen saturation (S_vO_2) by estimating and then exploiting -S_vO_2 calibration curves. This, joint with measurements of CBF, is an alternative way of estimating oxygen metabolism.

As discussed in Paragraph 2.2.3.2 similar methods have been proposed in the past years (Bolar and Rosen, 2011; Guo and Wong, 2012) typically exploiting velocity selective pulses with multi-echo acquisitions for estimating and finally S_vO_2. The main novelties of our technique are two: the approach used for isolating the signal from venous vessels and the measurement of to estimate S_vO_2. In fact, in this work we are investigating a new approach that exploits Fourier velocity imaging to encode the MR signal from moving blood, allowing the identification of compartments of the same voxel characterized by different velocities. Then, exploiting a multi-echo acquisition, the decay of signals' spectra with time is calculated and values of are estimated for the velocity range of interest. Finally S_vO_2 and therefore OEF can be assessed through -S_vO_2 calibration curves specifically targeted on values calculated for the venous side of the vascular tree.

The aim of this work is to explore the feasibility of the proposed method. Our approach is twofold: to design a simulation model and to run pilot acquisitions. The model let us create datasets of synthetic MR signals taking account of different aspects of the physiology from which the signal arises and the sources of nuisance that are likely to corrupt it. More specifically, metrics of the proportion of the signal in the data (named spectral signal fraction or SSF) are used to characterize the noise in both simulated and acquired data, giving a quantitative indication on its effects and on the feasibility of the novel technique. Finally the effectiveness of the method is tested in the real case scenario in grey matter regions and by estimating the changes in S_vO_2 triggered by a visual stimulus in the superior sagittal sinus (sSS).

6.2 Methods

6.2.1 Signal analysis pipeline

A flowchart showing the steps undergone by the signal from its origin to the estimates of blood oxygen saturation is reported in Figure 6-2. This paragraph briefly summarises the theoretical description of the signal underpinning the process and already partially introduced in Paragraph 2.1.6.

In the first instance the GRE signal at time *t* after excitation can be described in the form . This can be modelled as a weighted sum of different contributions arising from three different compartments of the voxel considered, characterised by different : tissue, arterial vessels and venous vessels (S_T, S_A and S_V respectively).

The velocity encoding module introduces a dependency of the phase of S on via the application of pulsed field gradients (PFGs) of varying magnitude. Therefore, compartments characterised by different velocities will contribute differently to the evolution of the phase, as described by equation Eq. 2.14 in Chapter 2 and here simplified as:

Eq. 6-1

In particular, it is possible to express the signal arising from a single compartment of a voxel characterised by and transverse relaxation time T_2* at the n-th echo time TE_n as:

Eq. 6-2

Where the first term ( ) is not dependent on or and represents a weighting term accounting for the dependence on the relaxation process.

Applying a Fourier transformation is then possible to express the dependency of S on . The linearity of the Fourier transform operator preserves the weighting term, so that the spectra obtained for each voxel show an exponential decay with time. In particular each point of the v-space will be representative of a certain component of the voxel under analysis.

Finally, with a multi-echo acquisition is possible to estimate the relaxation constant of the moving components of brain tissue at each value of . These values are then used to quantify the oxygenation content exploiting - S_vO_2 calibration curves, that is analytic expressions of the relationship between and S_vO_2 for fixed haematocrit and magnetic field (Hct = 0.44 and B_0 = 3 T respectively in our case).

6.2.2 Synthetic data creation

6.2.2.1 Generation of MR signal

The modelling of the signal starts from the description of a GRE signal at time TE after excitation introducing different levels of complexity.
We have paid particular attention to two aspects: the origin of the signal, in terms of physiology and biophysics underlying the signal itself, and the effect of two sources of noise.

As regards the first aspect, we wanted to take into account the main characteristics of a single grey matter tissue voxel and the variability among different such voxels across brain. This aims to supply our analysis pipeline with realistic signals, in order to enhance the robustness of the results and to better estimate the possible translation of the technique into application to real subjects.

We considered a 3 compartment model with tissue, arteries and veins. Each one has a different weight on the signal based on its volume (95% tissue, 2% arteries,

3% veins, as from Griffeth at al. (Griffeth and Buxton, 2011)) and is characterised by a different depending on the magnetic susceptibility modulated by the specific O_2 saturation. In particular we fixed these to 54 ms and 21 ms for arterial and venous compartment respectively (corresponding to S_aO_2 = 0.98 and S_vO_2 = 0.6 for a fixed Hct of 0.44, as for Zhao and colleagues (Zhao et al., 2007)), while tissue was fixed to 47 ms (as measured at 3 T in resting state extravascular visual cortex by Lu and Van Zijl, (Lu and Van Zijl, 2005)). Note that the compartment labelled as "tissue" groups heterogeneous types, characterized by an approximately static behaviour and of secondary interest (specifically mainly grey matter but also white matter). No cerebrospinal fluid (CSF) compartment has been considered. We therefore assume to model signal relative to tissue in which the CSF partial volume is negligible. This assumption can be considered valid for most grey matter tissue, apart from that localised in proximity to the cortical surface and the ventricles. The implications of this simplification and of the issues due to CSF in real case applications will be further examined later in the Discussion session.

Then the effect of moving blood was simulated, which is the main interest for our purposes. The signal arising from the tissue compartment has been modelled as static. Moving blood instead affects the signal through changes in phase introduced accordingly to the Fourier velocity encoding approach used and then exploited for estimating the oxygen saturation. We assume that the distributions of velocities of the arterial and venous compartments are different in terms of magnitude and direction. The absolute value of velocity is modelled with a linear dependence on vessel size as proposed by Kobari et al. (Kobari et al., 1984). The range of vessels diameters was fixed to span from 5 to 200 μm, to which corresponds a maximum velocity of 6.8 cm/s for the arteries and of 2 cm/s for the veins. The spread of directions of the flowing blood is incorporated, because the only contribution to the phase of the signal arises from the component of the velocity parallel to the direction of the encoding gradient. Moreover, for the sake of simplicity, we have modelled a signal arising from a non-isotropic distribution of vessels and considering a single axial velocity component (z). The probability of a vessel being parallel to the axis of the encoding gradient was considered

maximal and then decreasing following a Gaussian distribution, reaching its minimum for a perpendicular orientation. Then, accordingly for a simplified description of blood flow in the brain, the flow direction has been considered positive for arterial blood (bottom-up direction), while negative for the veins (top-down direction).

6.2.2.2 Noise in the synthetic MR signal

Two different noise sources have been considered. One is referred to as "background noise", to indicate that kind of noise naturally arising from the signal measured in the scanner and due to thermal noise and fluctuations of biophysical parameters underlying the signal. Following the description proposed by Kruger et al. (Kruger and Glover, 2001), this has been modelled as the sum of two different components: one TE-independent (denoted as TE_i component) and the other TE-dependent (denoted as TE_d component). The first is constant in time, whilst the second is proportional to the signal and decays with an exponential law. We fixed the relationship between the two accordingly to experimental results presented by Kruger et al. (Kruger and Glover, 2001) that showed a relationship between the standard deviations of the two components (σ_{TEi} and σ_{TEd} respectively) at the first TE: $\sigma_{TEi} = 2.7 \cdot \sigma_{TEd|TE1}$. This source of nuisance is therefore modulated by fixing σ_{TEi} (from which σ_{TEd} is derived) as a percentage of the absolute value of the noiseless signal at the TE = TE_1. The noise has been added to the MR signal separately for the real and imaginary part of the signal, mimicking the process of acquisition of the signal in the scanner.

The second source of nuisance considered is referred to as "physiological noise" and models the noise due to the slight movement of the tissue compartment. This is primarily due to the effect of the heart beats generating pressure waves causing slight motion (especially in the bottom part of the brain) and imposing therefore to the tissue displacements of about 0.1– 0.13 mm and velocities of the order of magnitude of 1 mm/s (Greitz et al., 1992; Nunes et al., 2005). In practice this phenomenon has been modelled assigning to the tissue compartment a non-zero velocity, whose value has been picked randomly sampling a sine function spanning the range [$-v_{max}$ v_{max}], where v_{max} is the control parameter. We model

the situation in which the phase of the cardiac cycle is randomized with respect to the q-space sampling and for each TE.

Therefore σ_{TEi} and v_{max} are the two parameters we are manipulating in order to modulate the effect of noise on the signal in the simulation, aiming to determine what values cause a failure of the estimation technique. We considered values of σ_{TEi} of 0, 1, 2, 3, 4 and 5 % and v_{max} of 0, 0.5, 1, 1.5, 2 mm/s.

Finally, we explored the effect of summing signals from multiple voxels or from multiple acquisitions of the same voxel. The first has been implemented for reproducing what happens when multiple signals are clustered and summed (e.g. in ROI approaches) and groups of 1, 10, 25, 50, 100 signals were considered. The second feature has been implemented for taking into account repeated acquisitions of the same voxel, as possible in real case acquisitions. The difference between the two is that while in the first case the signal is the sum of contributions from slightly different physiological characteristics but with a varying contribution of noise, in the second the underlying physiology is the same.

6.2.2.3 Velocity encoding and multi-echo acquisition

Velocity encoding is performed via a velocity dependent phase encoding which samples q-space, that is stepping through different values of the PFGs. Considering the magnitude of the velocities involved, the accuracy and resolution needed and the feasibility of eventual application as regards timing and gradient strength, we have sampled q-space in 128 equally spaced bins, fixing the maximum velocity encoding to max_v_{enc} = 20 cm/s, δ = 9 ms, Δ = 13.4 ms (see Paragraph 2.1.6), for which the gradient step is G_{step} = 0.487 mT/m. As mentioned, for simplicity we considered only one direction of the gradient (z axis), stepping through magnitudes from $-G_{max}$ = -31.2 mT/m to G_{max}- G_{step} = 30.7 mT/m, encoding a range of velocities spanning from -20 to 19.6875 cm/s, with a resolution of 0.3125 cm/s.

In order to allow estimates of the relaxation decay constant , it was necessary to generate an array of MR signals, corresponding to a multi-echo acquisition. In

order to match the specifics of the simulation with those of the pilot acquisitions (see below), we modelled a 6-echo acquisition with TE = 11, 20, 29, 38, 47 and 56 ms (see Figure 6-1).

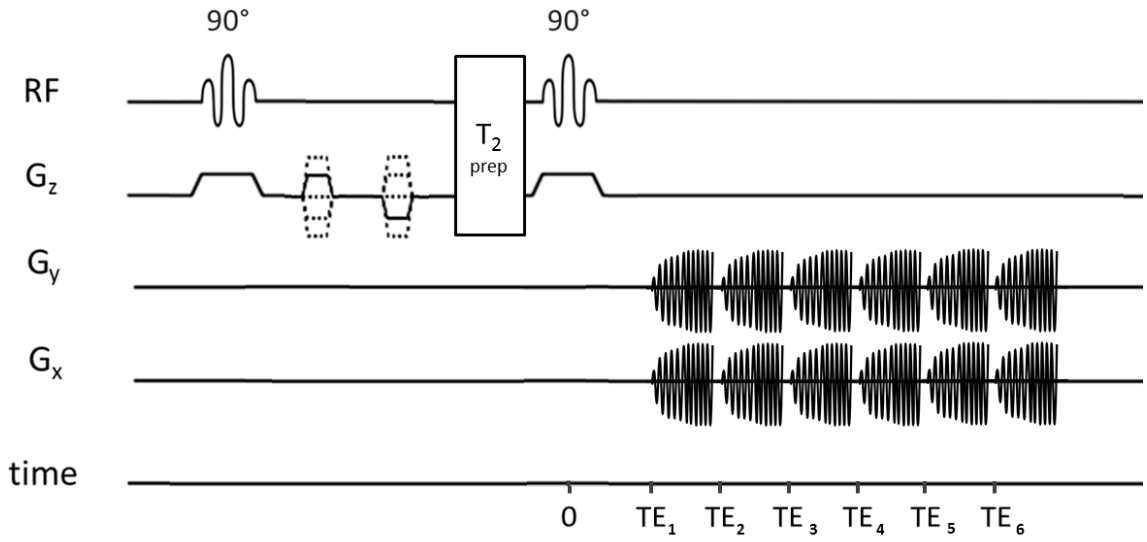

Figure 6-1: Pulse sequence diagram. Following the slice-selective application of a 90° RF pulse, the motion encoding along the z axis is operated via PFGs. the T2* signal is then measured at six different TEs after a T_2 magnetization preparation sequence.

6.2.3 Pilot data acquisition

6.2.3.1 Scanning protocols

Provisional data were acquired for one phantom and two subjects. For all three cases, scanning was performed in a 3T GE HDx MRI (GE Healthcare, Milwaukee WI) with a body transmit coil and 8-channel head receive coil. Data were collected with a six-gradient echo (GRE, TE = 11, 20, 29, 38, 47, 56 ms) readout and spiral k-space acquisition (5 repetitions, TR = 3 s, Flip Angle = 90°, FOV = 22.4 cm, Matrix = 64 x 64, resolution 3.5x3.5x6.9 mm). 10 slices with an inter-slice gap of 1 mm were acquired in ascending order.

The flow velocity encoding module for the Fourier velocity imaging consisted of two series of 65 PFGs: one spacing the positive (from 0 to G_{max}) and the other the negative (from 0 to $-G_{max}$) direction of the q-space along the z axis. This was made necessary because the scanner in use do not allow us to sample the q-space directly from $-G_{max}$ to G_{max}. The parameters used were the same described for the simulation: max_v_{enc} = 20 cm/s, δ = 9 ms, Δ = 13.4 ms, G_{step} = 0.487 mT/m and $-G_{max}$ = -31.2 mT/m.

For the subjects, two consecutive acquisitions were made with the same scanner parameters: one at rest (eyes open, black screen) and one with a visual stimulus (movie), for a total duration of 22 minutes. For the phantom a single acquisition was performed. Acquisitions were limited to such small numbers with the idea of privileging the signal processing aspect of the new technique over the statistical power of calculations achievable through a multitude of subjects.

The two participants had available whole brain T1-weighted structural scans (3D FSPGR, 1x1x1 mm voxels, TI/TR/TE = 450/7.8/3 ms).

6.2.3.2 Signal pre-processing

Four pre-processing steps are made sequentially in order to make the signal from the scanner suitable for analysis. First it is necessary to combine the complex data obtained for each of the eight receiver coils and this has been done with a complex sum. The obtained signal for each acquisition consisted in two series

uniformly spanning the positive and negative values of the gradient in 65 steps each. In order to obtain a single array of 128 items, the phase images were subtracted in order to match in the two acquisitions at G = 0 and then one of the values corresponding to G = 0 and G_{max} were discarded (because matched to the other one and equal to $-G_{max}$ for aliasing, respectively), leading eventually to samplings of the q-space of 128 bins.

Secondly, in case of subjects' acquisitions, motion correction is performed on 4D matrices with the AFNI function *3dvolreg* for each TE separately in order to correct for head movements.

Then phase unwrapping is performed to correct possible artefactual phase differences due to oscillations across $0/2\pi$. This was done with a Matlab toolbox developed for QSM applications and made available by Bilgic and colleagues (Bilgic et al., 2014).

Finally low frequency spatial phase inhomogeneity and drifts are removed with a linear filter, with an approach similar to the one proposed by Langham and colleagues for susceptometry applications (Langham et al., 2009).

Registration of the structural scans from high resolution anatomical space to the native low-resolution phase space was performed with FSL FLIRT (Jenkinson et al., 2002) for the localization of regions of interest.

6.2.4 Analysis

6.2.4.1 Noise characterization

Levels of noise on both simulated and real data have been estimated calculating indices of spectral signal fraction (SSF). SSF has been computed as the fraction of the spectrum corresponding to velocities where we expect to have signal. In data relative to phantom acquisitions (real or simulated), SSF has therefore been computed as the ratio between the energy of the spectrum at v = 0 and the rest, while for data relative to tissue acquisitions (real or simulated) as the ratio between the expected velocities ([-2 6.8] cm/s) and the rest.

This index of SSF is suboptimal, due to the fact that both the portions of the spectrum contain noise. Although it has been chosen to satisfy four criteria based on a pragmatic idea of signal to noise ratio: i) values calculated on synthetic data are inversely proportional to magnitudes of background and physiological noise; ii) they are inversely proportional to the number of voxels considered (in both real and synthetic data); iii) they allow to compare both real and synthetic data without the need for scaling; iv) values decrease with TE.

In order to evaluate the effect of the noise on the synthetic data, realistic SSF indices were estimated from the acquired data. A representative SSF value was estimated as the median of a distribution of indices calculated on 1000 permutated ROIs for each number of voxels (1, 10, 25, 50 and 100). For the two subjects, only signal arising from grey matter was considered, to be consistent without assumptions made in our simulation. Also in this case the obtained SSF values were averaged across the two subjects.

We therefore expect the SSF indices to represent only background noise in the phantom acquisitions and both sources of noise in the subjects' acquisitions. In particular comparing SSF indices obtained from real and synthetic data we want to understand the likelihood of different combinations of simulated (σ_{TEi} , v_{max}) values, the different effect of the two sources of noise considered and ultimately an indication on the levels of noise for which the method fails.

6.2.4.2 T_2 and S_vO_2 estimates*

The data generated either from the simulation or from MR scanner acquisitions have a dependency on and TE. Estimates of are obtained from signal summed over portions of the velocity range. This assumes that, in a simplified description of the vascular tree, contiguous regions of the velocity spectrum are assumed to originate from the same moving compartments, characterized therefore by the same value of . We consider the three compartments of interest (tissue, arterial and venous blood), based on their expected velocity ranges, with the effect of enhancing the signal to noise ratio of the analysis.

For a proof-of-principle of the method, we tested its effectiveness with an application on grey matter ROIs and bulk estimates of and S_vO_2. This has been done in the first case selecting regions of increasing size (size $N_{1,2,..,5}$ = 1, 10, 25, 50 and 100 voxels, where the region of size N_i is a subset of the region of size N_{i+1}) from the grey matter of one subject. In the other case studying the signal relative from the superior sagittal sinus (sSS), similarly to what done by other techniques for whole brain S_vO_2 estimates (e.g. TRUST (Lu and Ge, 2008)). Manually drawn sSS masks were then defined on pre-processed phase images overlaid to low resolution anatomical scans for each subject.
In both cases the signal of interest was obtained as the complex sum of all signals identified as arising from the defined ROI. Finally values of and S_vO_2 were estimated as described in Paragraph 6.2.1 and depicted in Figure 6-2.

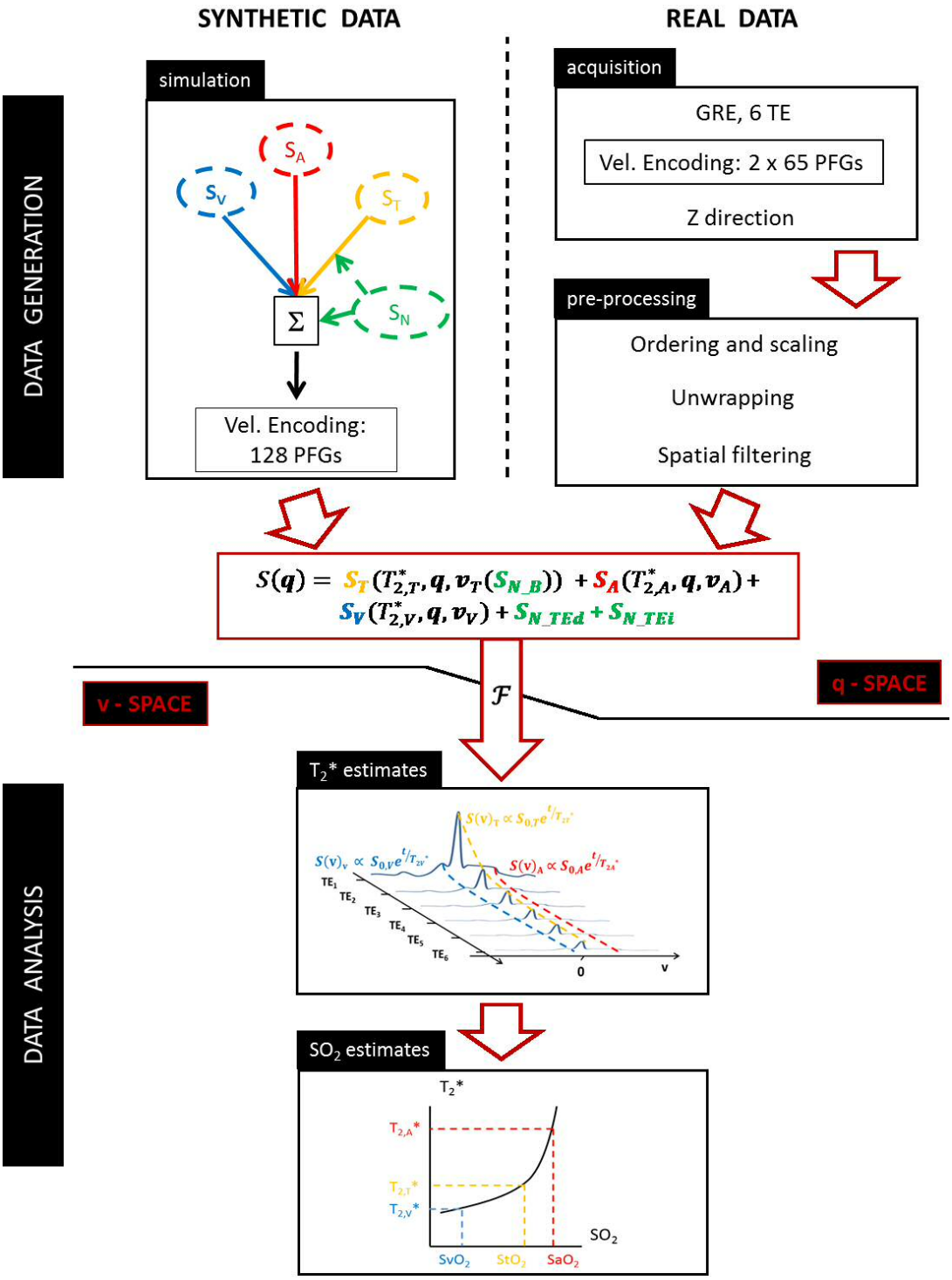

Figure 6-2: data flowchart from generation to the estimates of blood oxygen saturation.

6.3 Results

6.3.1 Resulting synthetic signal

The resulting simulated signals are reported in Figure 6-3. The logarithm of the absolute value of the spectrum for TE = TE_1 is shown as a function of velocity for different combinations of noise. Panels A to D include results from a single voxel, while panels E and F show sums of 10 and 100 voxels respectively.

In Figure 6-3,A the ideal noiseless condition is reported. The signal has a peak corresponding to the static component at v=0 and two lobes corresponding to the components moving with positive and negative direction (arterial and venous respectively). Figure 6-3,B reports the spectrum due to the only physiological noise being set to v_{max} = 1 mm/s, according to typical peak velocities values reported in literature (Nunes et al., 2005). This has the main effects of spreading the peak in the signal due to the static component, so that both the signal due to arterial and venous compartment will be partially corrupted, and introducing oscillations in the spectrum.

Figure 6-3,C shows the spectrum due to the reciprocal situation, in which the physiological noise is null, whilst the background noise is set to σ_{TEi} = 1%. This confounding factor has two main effects on the spectrum: it increases its magnitude, especially in those velocity ranges where there is no signal from moving components, and makes it more irregular. Finally in Figure 6-3,D is reported the spectrum of a signal with the combination of the two effects, that is with σ_{TEi} = 1% and v_{max} = 1 mm/s. In results obtained as sums of multiple voxels (Figure 6-3 E,F), the spectra appear more regular and the signals arising from the three different compartments are more distinguishable at equal levels of noise introduced (σ_{TEi} = 1% and v_{max} = 1 mm/s).

Figure 6-4 shows the fit of the spectral decay of the synthetic signal resulting from the combinations of noise and sums presented in Figure 6-3. As our focus is centred on estimating S_vO_2, only the venous portion of the spectra is considered. Analysis of signal from a single voxel in the noiseless condition (Figure 6-4,A)

show a perfect estimate of = 21 ms excluding the possibility of bias being introduced by the simulation in this scenario. The situation changes quickly with the introduction of one (Figure 6-4,B,C) or both sources of noise (Figure 6-4,D), with overestimates of . For fixed values of σ_{TEi} = 1 % and v_{max} = 1 mm/s the operation of summing increases the regularity of the decays progressively enhancing the quality of the fit (Figure 6-4,D,E,F). Despite this, the accuracy of the estimates remains low, with errors in estimating above 100% even for 100 sums (Figure 6-4,F).

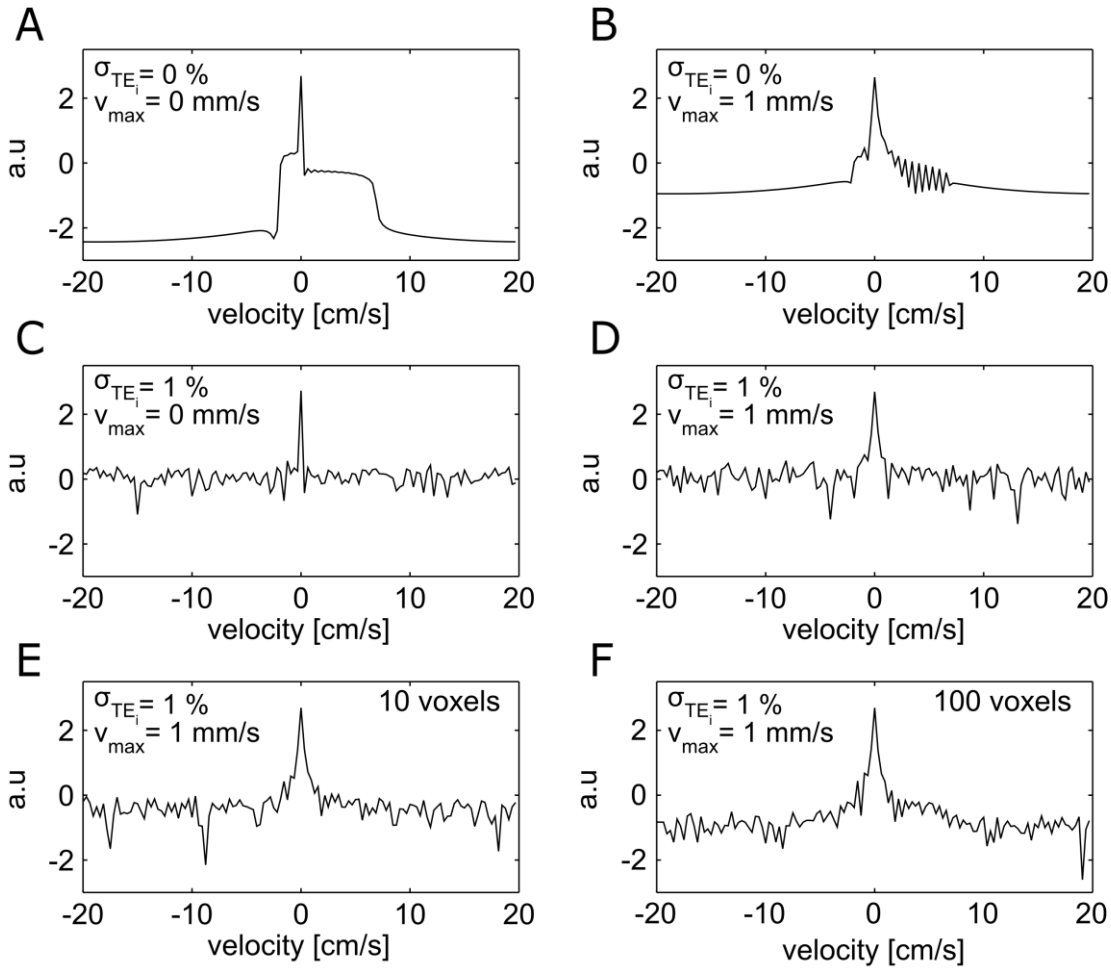

Figure 6-3: logarithm of spectra of simulated signals for different combinations of noise. Panels A to D are relative to signal from a single voxel, while panels E and F show spectra from sums of 10 and 100 voxels respectively.

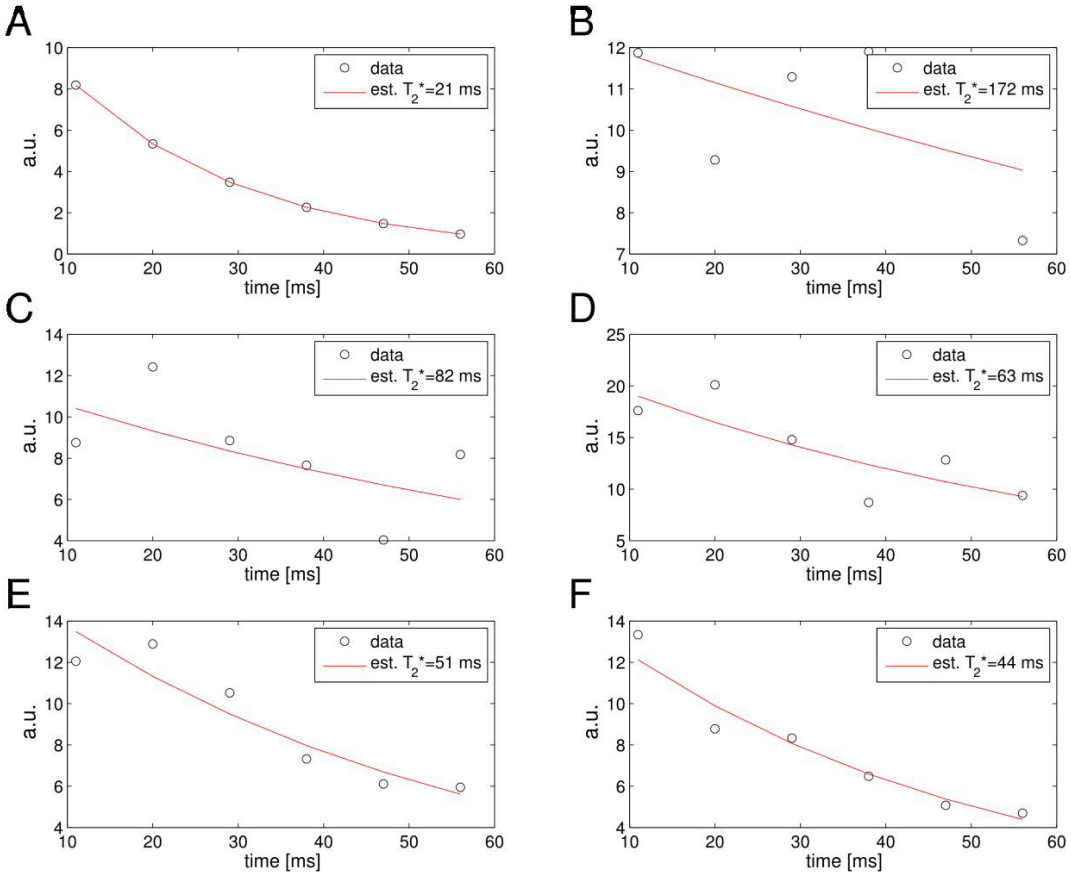

Figure 6-4: fit of the decay of the venous component of the spectra for signals with different combinations of noise and averaging, as in Figure 6-2. Panels A, B, C and D are relative to signal from a single voxel with (σ_{TEi} , v_{max}) values of (0 %, 0 mm/s), (0 %, 1 mm/s), (1 %, 0 mm/s) and (1 %, 1 mm/s) respectively. Panels E and F are relative to spectra obtained from sums of 10 and 100 voxels respectively.

6.3.2 Noise characterization

Statistics of SSF from data acquired on two subjects (rows 1 and 2) and a phantom (row 3) are shown in Figure 6-5. The histograms show the distributions obtained calculating the SSF on the signal arising from 1000 randomly sampled regions of varying extent (1, 10, 25, 50, 100 voxels) and the red lines highlight the median values. These are 0.896, 0.8979, 0.8989, 0.9045 and 0.9185 for subject 1; 0.8677, 0.8685, 0.8685, 0.8686 and 0.8687 for subject two; 0.9434, 0.9440, 0.9440, 0.9440 and 0.9442 for the phantom. In all cases considered the median values of SSF are not decreasing with the size of the regions. Values calculated for the phantom are higher than those calculated for the subjects, which show some inter-subjects variability and negatively skewed distributions especially for low number of voxels.

Figure 6-6 and Figure 6-7 report the values of SSF calculated for different levels of noise and voxels when simulating data from a phantom and a subject respectively. In both cases the values of SSF resulting which are lower than the median ones estimated from the statistics in Figure 6-5 are marked with black dots.

In results from both, SSF is inversely proportional to the amount of noise introduced and to the number of voxels considered. For the phantom values of SSF from the synthetic data compatible with those from the real data seem proportional to the number of voxels considered, meanwhile for the subject estimated SSF becomes quickly higher than that found in the real acquisition for increasing number of voxels.

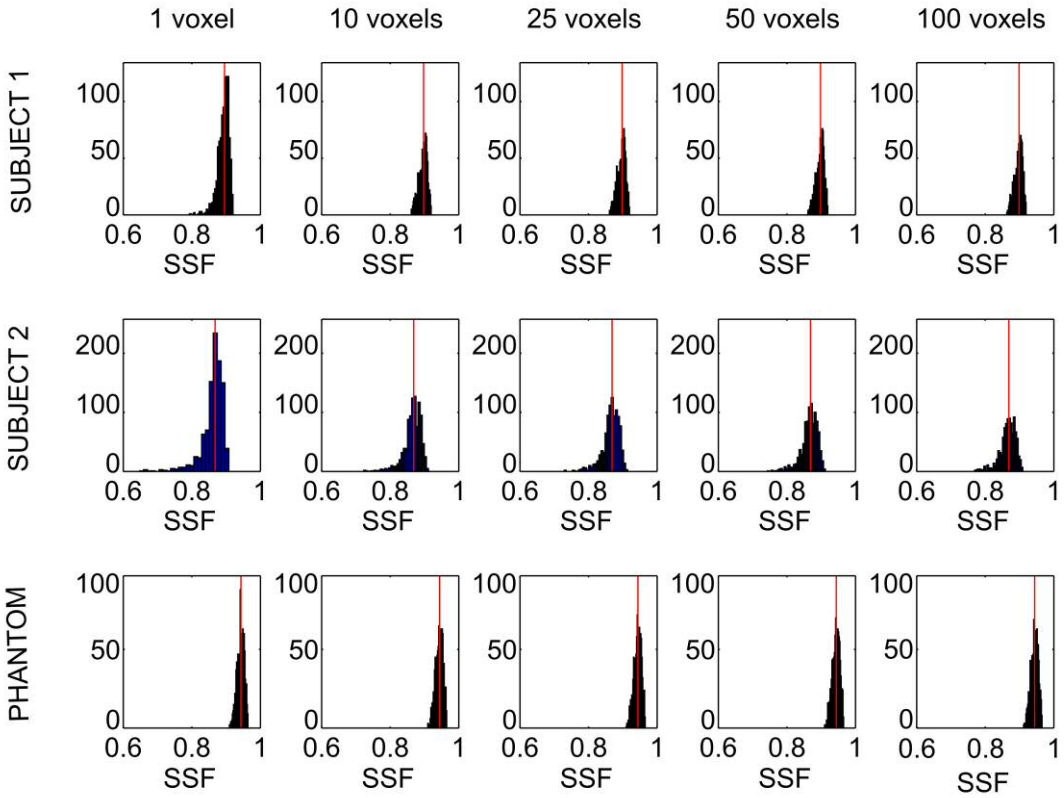

Figure 6-5: SSF distributions for combinatorial selection of 1000 regions of increasing size. For the subjects only grey matter voxels were considered. The median values are indicated in red.

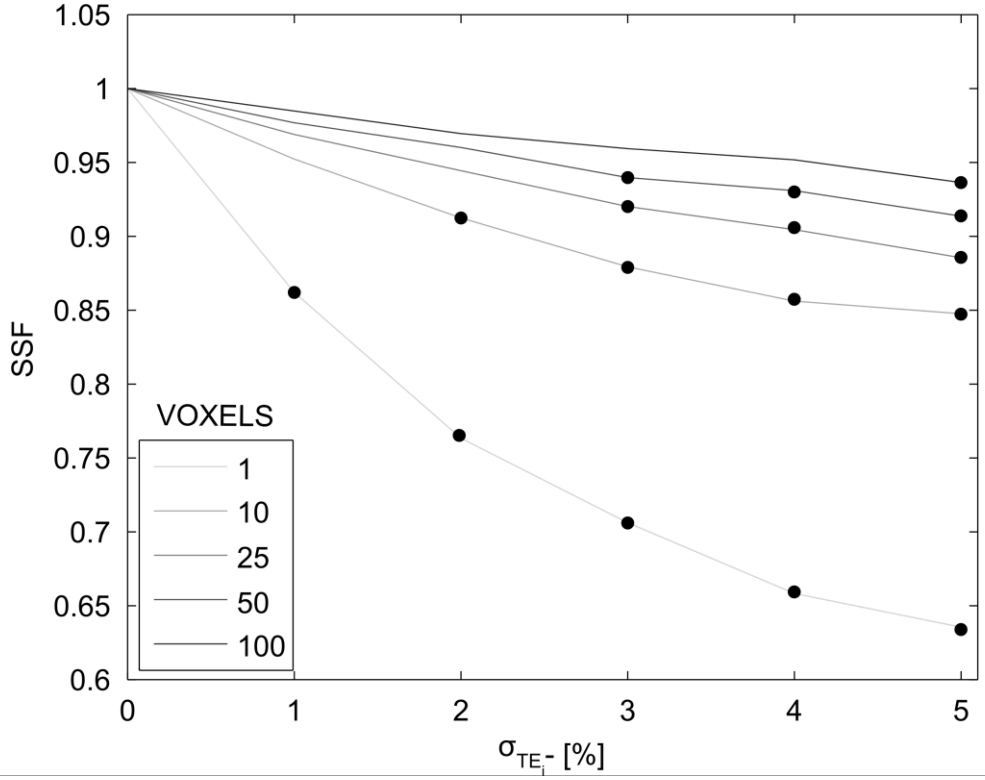

Figure 6-6: SSF values calculated from the synthetic data of a phantom as function of the background noise for different ROI sizes. Black dots indicate SSF values for which SSF is lower than the median value calculated in real data at each ROI size.

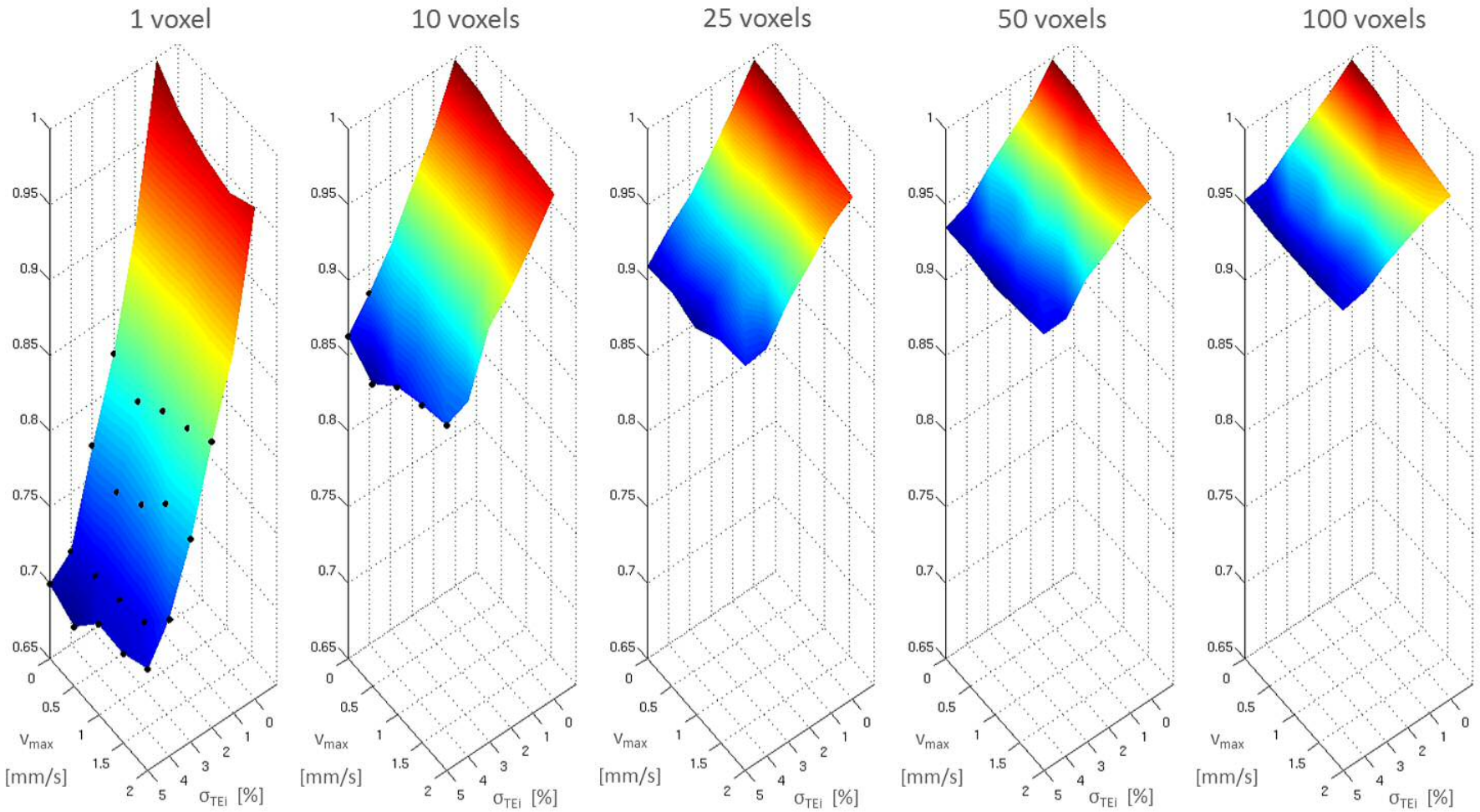

Figure 6-7: SSF values calculated from the synthetic data modelling signal from a subject, as function of the background and physiological noise for different ROI sizes. Black dots indicate SSF values for which SSF is lower than the median value calculated in grey matter for real data at each ROI size.

6.3.3 S_vO_2 estimates in acquired data

Results for the analysis run on data acquired on two subjects are displayed in Figure 6-8, Figure 6-9, Figure 6-10, Figure 6-11 and Figure 6-12.
Figure 6-8,A shows the grey matter regions of increasing size used for the analysis. These are localised in the frontal lobe of subject two. In Figure 6-8,B the logarithm of spectra at TE = TE_1 and the decay fitting of signal obtained from the grey matter regions shown, with the only venous side of the spectrum considered for the fitting. Spectra are similar to the one calculated for the synthetic data and reported in Figure 6-3, with a peak for the static component more than two orders of magnitude higher than the rest of the spectrum but no distinguishable lobes elsewhere.

Despite this, Figure 6-9 reports that the regularity of the fits of the tissue and venous component increase and estimates converge to 20.3 ms and 17.5 ms for higher numbers of voxels, this last corresponding to S_vO_2 = 0.57 (for assumed Hct = 0.44).

The regions considered for the analysis of the signal arising from the sSS are reported for both subjects in Figure 6-10, while in Figure 6-11 and Figure 6-12 the relative results.

In Figure 6-11 spectra of the signal are reported for subject 1 and 2 both at rest and stimulus condition. A peak is present in correspondence to null velocity in all cases, as well as pronounced spectral lobes found for negative velocities, with minimum values of about -3 cm/s and -4 cm/s stable across conditions for subject 1 and 2 respectively. The effect of noise is spread across all the velocity components, but it is more evident in the portions of spectra where no signal seems to be detected. In both subjects a couple of secondary lobes are highlighted symmetrically at negative and positive velocities (about ±15 cm/s and ±9 cm/s), with values about one order of magnitude lower compared to the main lobes.

Figure 6-12 shows the spectral decays and the relative estimates of for each subject and condition. For the first subject, is found to increase from 19.4 ms at baseline to 25.4 ms after stimulus, which in turns corresponds to an increase in S_vO_2 from 0.6 to 0.71. Similarly for the first subject, increases from 21.9 ms to 26.4 ms after stimulation, which corresponds to an increase in S_vO_2 form 0.65 to 0.72.

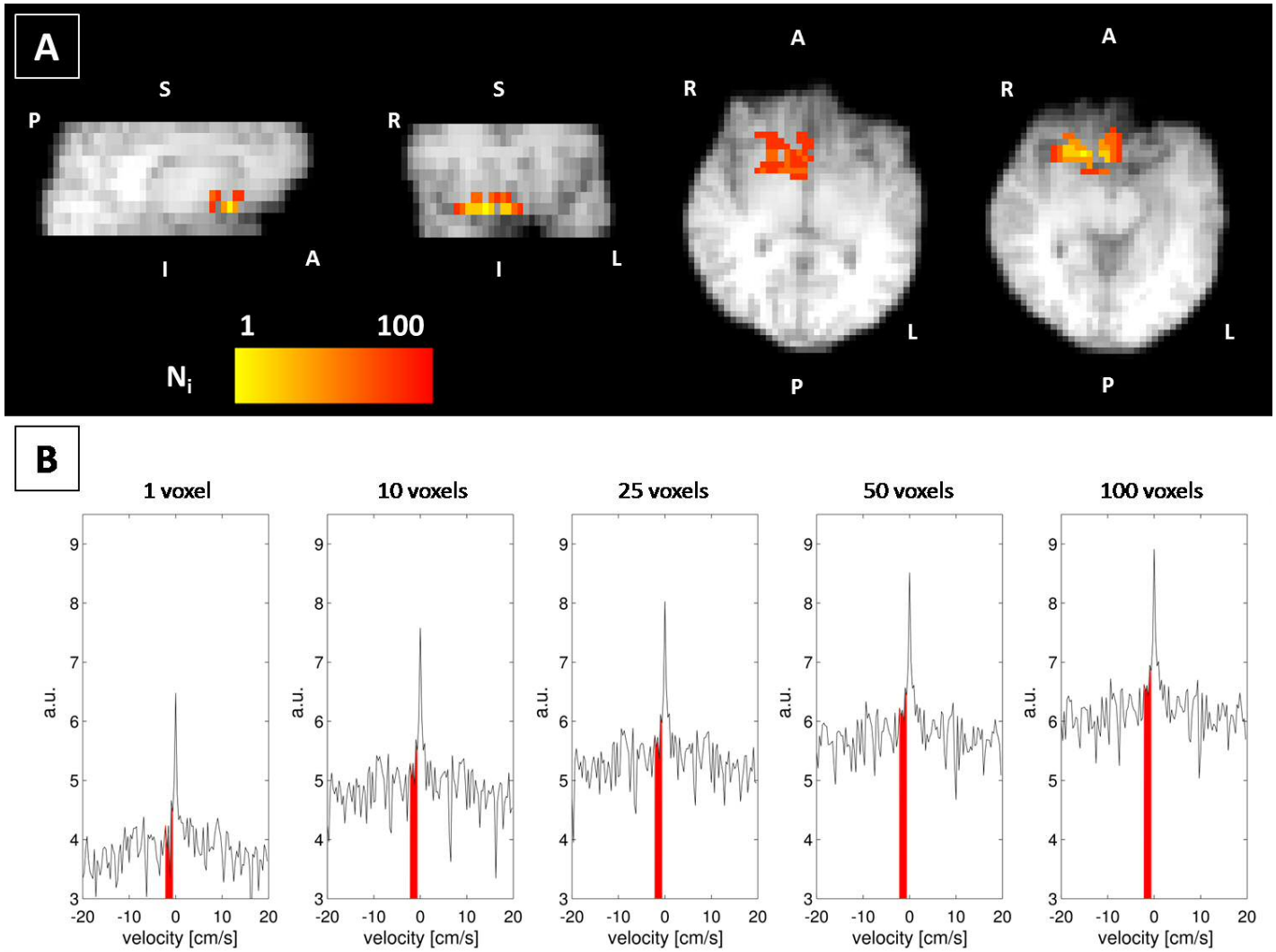

Figure 6-8: A - Anatomical position of the voxels considered for the spectral analysis. Colours code for the size of the region considered (with each region of size N_i being a subset of the region with size N_{i+1}). B – Spectra calculated at rest condition. Highlighted in red the portion considered for calculating the decay relative to the venous component.

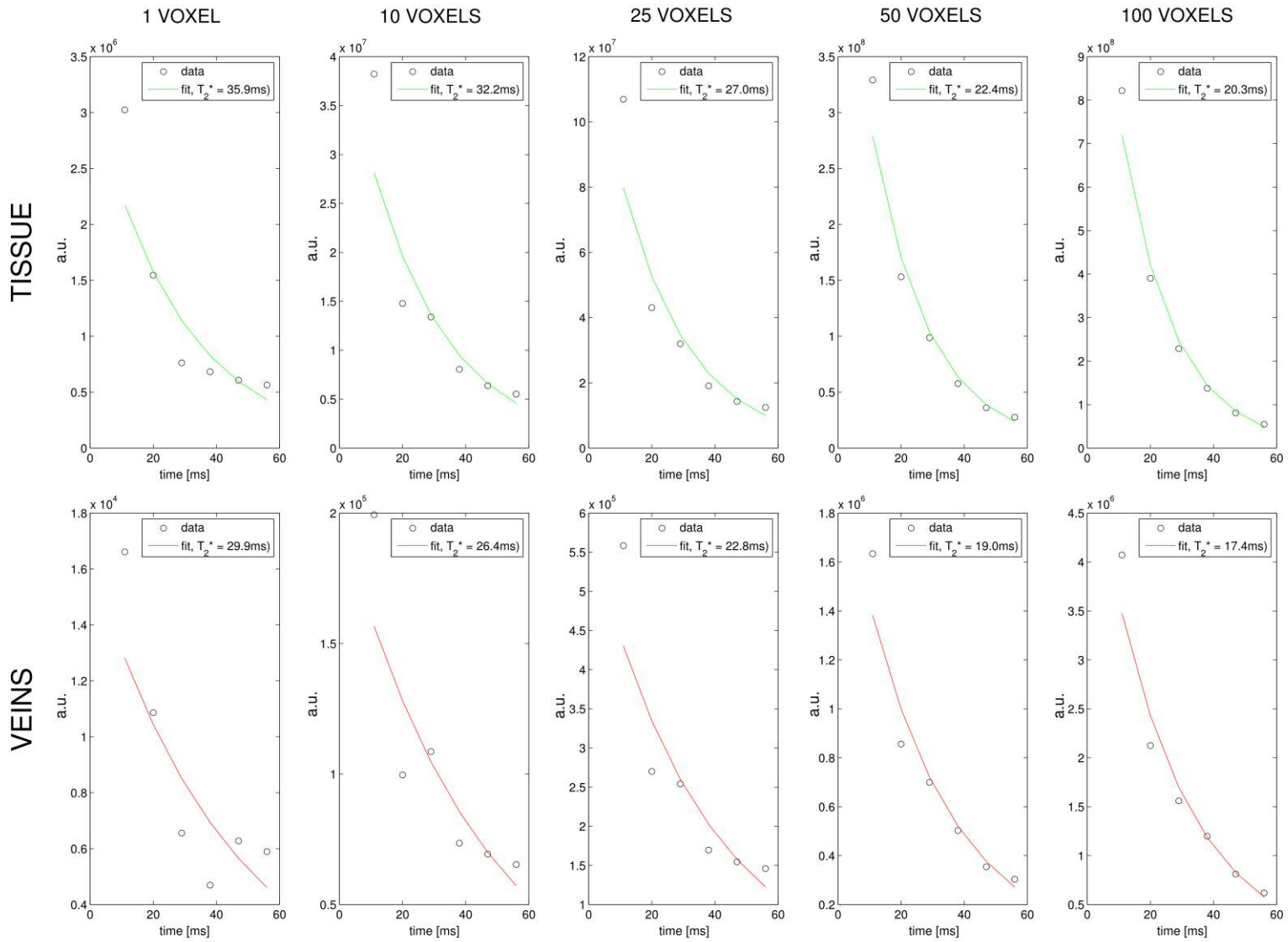

Figure 6-9: Decay fitting of signal obtained from sum of increasing numbers of grey matter voxels at rest. In the top panel results for the tissue component, in the bottom results for the venous component.

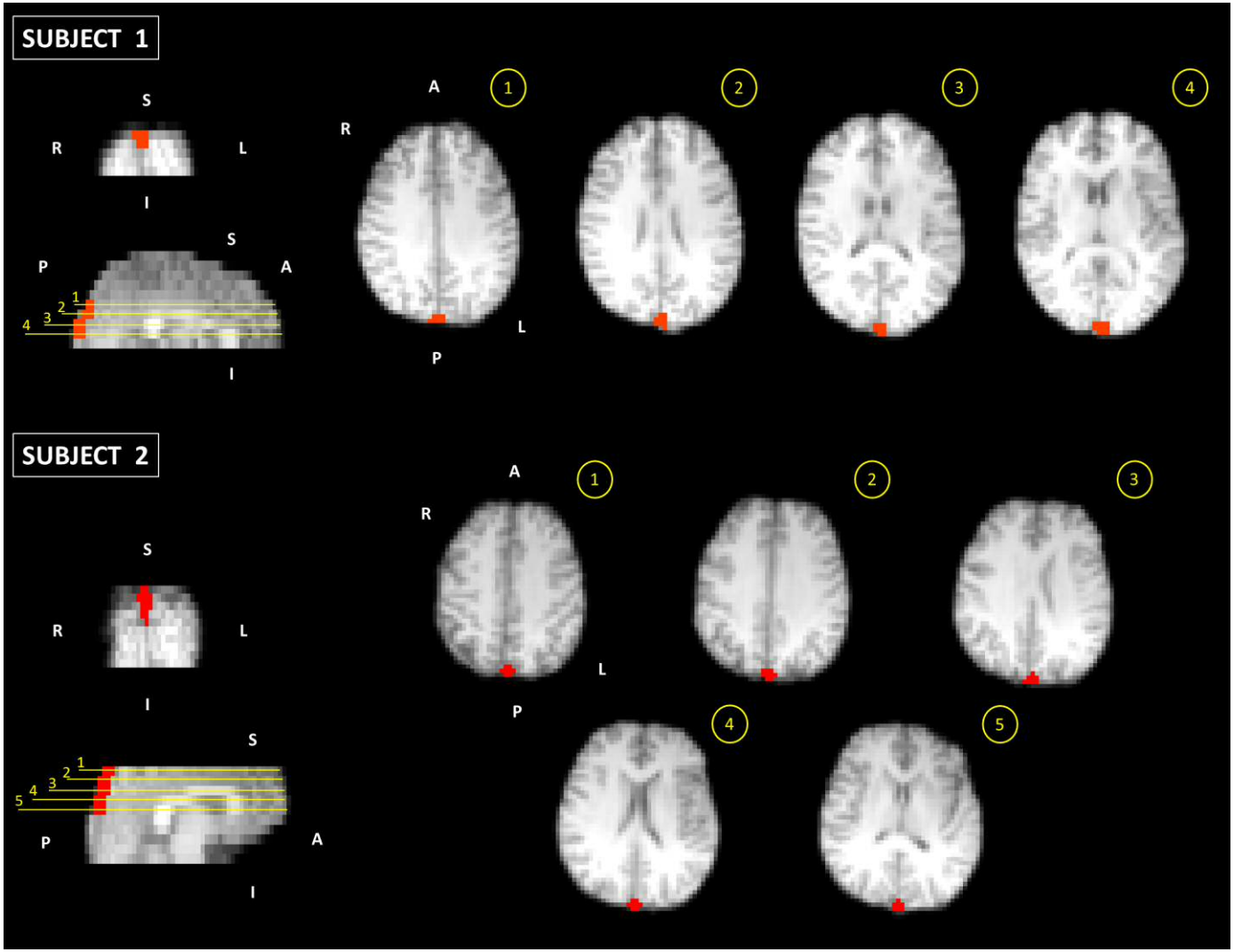

Figure 6-10: low-resolution anatomical images for subjects 1 and 2. In red the position of the regions considered for the analysis of sSS signal.

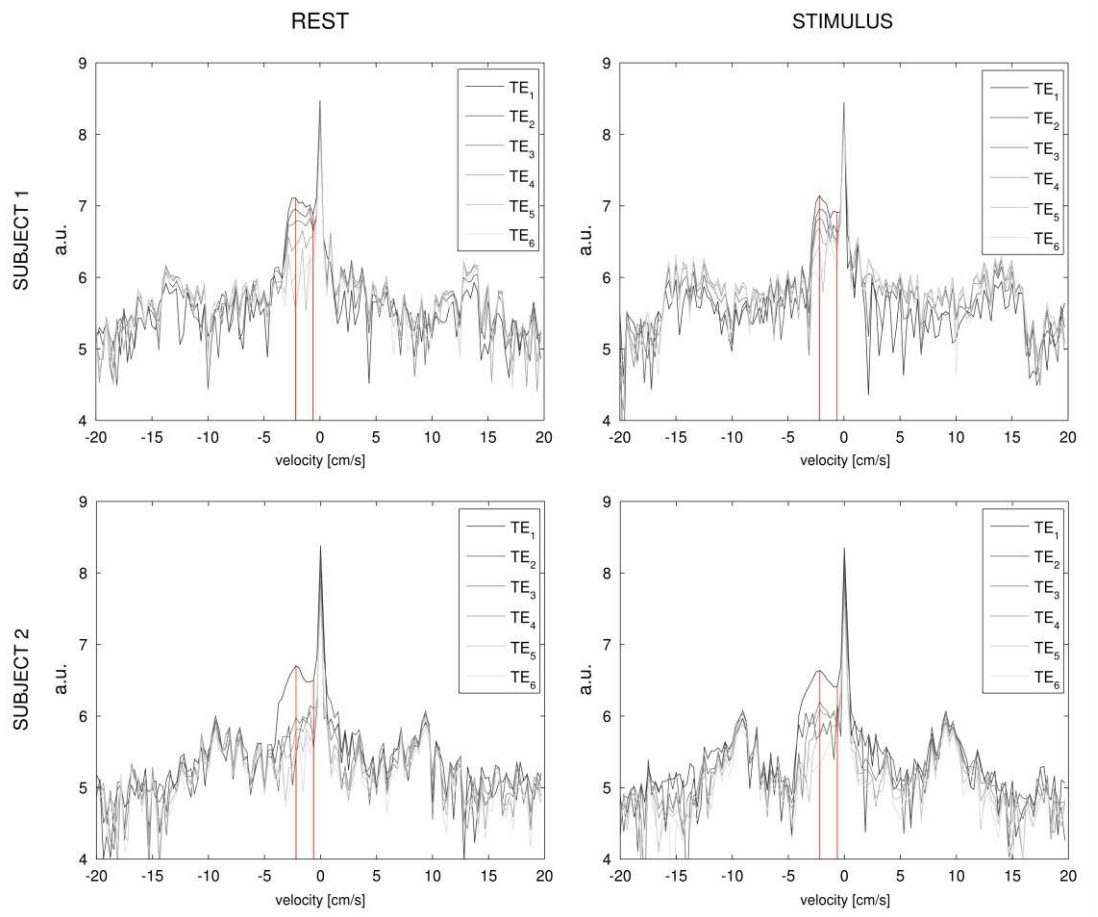

Figure 6-11: Spectra of the signal arising from the sSS of the two subjects in both rest and stimulus condition. Delimited in red the portion of the spectra considered for fitting.

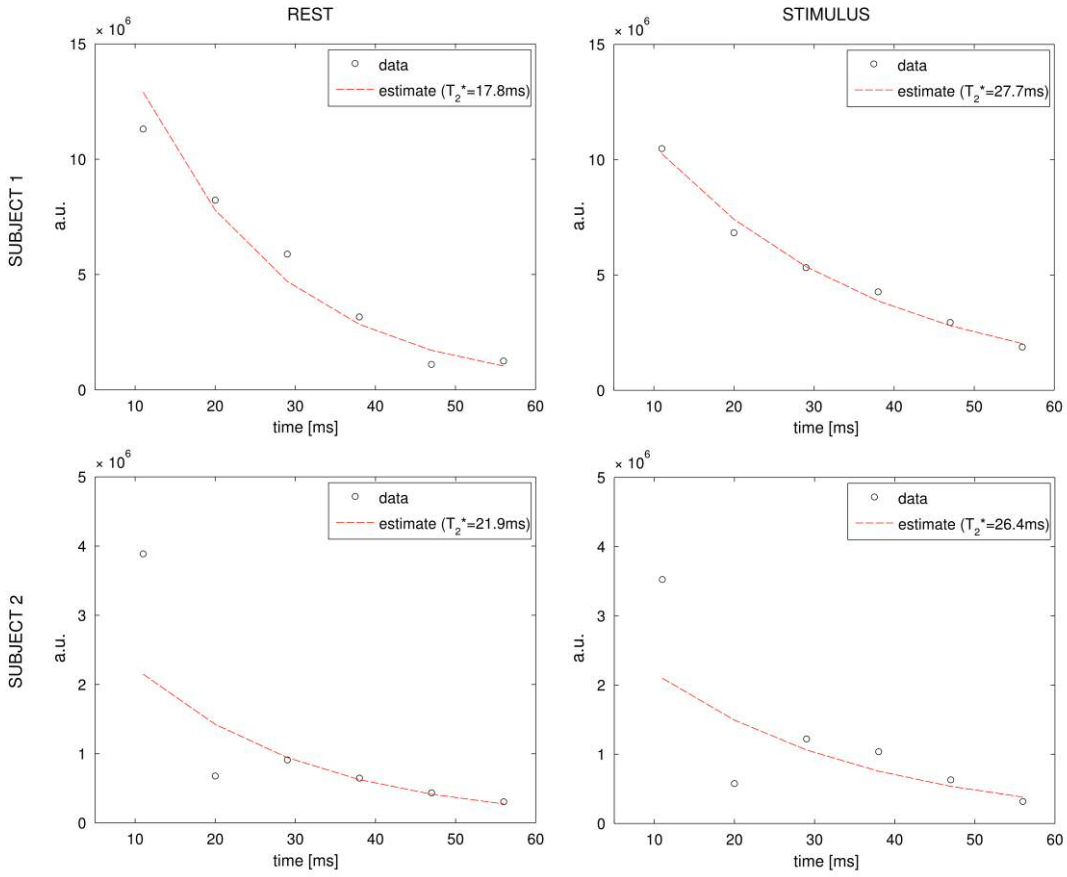

Figure 6-12: fit of the spectral decay for subject 1 and 2 (top, bottom) at resting state and during visual stimulus (left, right).

6.4 Discussion

6.4.1 Synthetic dataset

Spectra for synthetic signals reported in Figure 6-3 and the relative decay fit in Figure 6-4 exemplify the effect of the modelled sources of noise on the signal.

In particular, Figure 6-3-A reports the plot of the ideal noiseless condition, where the peak corresponding to the static signal and the lobes due to the moving components are clearly distinguishable, with the venous higher than the arterial (due to the different volume contribution of the two) and both with magnitude between two and three times lower than the static peak. The main effect of introducing physiological noise is spreading the peak in the signal due to the static component, so that both the signals from arterial and venous compartment are affected (Figure 6-3-B). Moreover, the synthetic signal shows characteristic oscillations, due to the way the physiological noise has been modelled. In fact it has been created as a sampling of velocities from a cycle with a sine function behaviour. The discrete distribution of a sine function can be approximated by *rectangular* functions, whose Fourier transformed equivalent (*sinc* function) cause the oscillations. Although very disruptive looking, this artefact has small magnitudes and reduces its effect when mixed with other confounding effects. The effect of background noise is instead less structured, with a widespread irregular component added across the entire spectrum (Figure 6-3-C). Finally from the other spectra (Figure 6-3-D,E,F) we can visualise what signal is expected from grey matter with physiological and morphological characteristics similar to those specified in our model. The comparison with the noiseless condition highlights how the spectral components due to the different compartments are no longer distinguishable by eye.

The consequences of the sources of nuisance on the estimates of T_2* are disruptive in both cases, with no particular differences in accuracy highlighted. On the other hand, while in both cases considering more voxels improves the regularity of the decays, values of seem to converge towards an overestimate. The main reason for this is that the noise in the data can only be positive,

representing an ever increasing proportion of the signal for longer TE and therefore altering the exponential decay.

6.4.2 Noise characterization

In distributions of SSF calculated for data from real case acquisitions values are generally higher for the phantom, due to the most of the spectral energy being concentrated in the static component (Figure 6-5). In the case of the subjects considered, estimates tend to be not only lower, but also more spread around their median values, denoting variability partially influenced by the effect of the contribution from physiological noise and partially related to variation in static signal through the brain.

The SSF values calculated allow us to compare the level of noise introduced in the modelling with values typically found in reality. The quantification of background noise given by simulations of the signal arising from a phantom (Figure 6-6) shows that the magnitude of σ_{TEi} in order to match values estimated in a real case scenario increases when considering increased number of voxels.

The quantification of the contribution of both sources of nuisance (Figure 6-7) firstly shows that the role of background noise is dominant compared to the physiological one. In fact for lower values of σ_{TEi} (< 1%) the SSF is maintained above realistic values even for the maximum value of v_{max} considered. Secondly, as previously seen for the phantom, the simulated effect of summing signal from more voxels seems to overestimate the noise attenuation observed in real data. This could have different explanations concerning the validity of the model we used for simulating the data, such as a shortcoming in accounting for additive effects of thermal noise, the presence – in the real data - of other more complex sources of noise, or finally the simplifications introduced in the physiology underlying the simulated signal.

The simulations also highlight the different behaviour of background and physiological noise for increasing voxels considered. In fact, while the contribution of the first is greatly decreased, the second only undergoes a slight

decrease. This can be explained by the nature of the noise, which is randomly distributed for the former, while is structured for the latter.

6.4.3 Acquired data

The data reported in Figure 6-8, Figure 6-9, Figure 6-10, Figure 6-11 and Figure 6-12 is representative of the signals that can be obtained with the proposed pipeline.

Figure 6-8,B and Figure 6-9 shows exempla of spectra and decay fit for signals originated from regions with increasing number of voxels in the grey matter. Results show that the information contained in a single voxel is not sufficient to accurately estimate S_tO_2 or S_vO_2 due to the effect of noise. This is consistent with what found in simulation for levels of noise comparable to reality (σ_{TEi} = 1% and v_{max} = 1 mm/s), leading to the conclusion that the methods – as is – is not suitable for voxel-wise estimates. Despite this and the fact that both positive and negative velocity contributions in the spectra are not immediately recognizable, the spectral decay appears already informative after about 25 voxels considered, therefore suggesting that the technique is suitable for ROI analysis. While the measurements of S_vO_2 are consistent with what expected, tissue values of are underestimated compared to the literature value of 47 ms (Zhao et al., 2007), suggesting a bias in the estimates. The reason for this is not immediately identifiable, but, considering the position of the region, it might be due to susceptibility induced signal drop-out. Still, our method enables to distinguish between the contributions from the two compartments considered.

The results of the sSS analysis are representative of such approach. Differently from the simulations previously discussed, in these cases the signal considered originates mostly from venous blood flowing with a negative velocity along the z axis. In fact, thanks to the high venous partial volume in the chosen ROI, the signal from the venous compartment is about one order of magnitude higher than in grey matter, making it clearly distinguishable in the spectra and allowing the fitting of the exponential decay. Estimated values of , and subsequently

S_vO_2, show in both cases an increase following stimulus, consistently with the expected enhanced venous oxygenation due to functional hyperaemia.

Notably, the quality of the fitting and the changes detected are lower in case of subject 2. This might be due to the fact that portion of sSS considered for the analysis might not be low enough in the z direction to drain the venous blood coming from the visual cortex interested in the stimulus.

In both subjects the spectra also show spurious lobes of increased signal in both negative and positive velocity. Due to the symmetry it is reasonable to assume that these are due to an artefact, whose nature has not been identified, but it is reasonable to speculate that they arise from aliasing of velocity components or ghosting phaenomena due to motion. Although, given that they are about one order of magnitude smaller than the signal of interest and they are clearly distinguishable in the spectra, they seem not to be of much concern for the analysis.

The number or subjects considered does not allow us to make conclusive statements about the effectiveness of the novel method, although it supplies a proof-of-principle of the proposed pipeline that, together with the modelling work, constitutes the basis for further development of the technique.

6.5 Limits and future developments

Due to the exploratory nature of the work presented, with a simulation study followed by a pilot data acquisition, some of the conclusions to be drawn are only partial or speculative. In this paragraph we want to highlight the main issues of the technique so far not discussed, along with the limits of our work. The aim is to further inform on the feasibility of the proposed method and on the major challenges to be addressed for its potential application.

The three main issues have been identified as: problems related to the effects of undesired motion, venous blood targeting and eddy current artefacts.

6.5.1 Motion-related issues

6.5.1.1 Motion and velocity encoding imaging

As discussed, velocity encoded imaging is designed to be sensitive to coherent movement of water molecules in the brain. This means, however, that the images also become sensitive to other sorts of movement. Image artefacts can therefore occur as a result both of motion of the subject, pulsatile motion of the brain itself as a result of the heart's activity.

While motion correction is performed for the real-case data from subjects, our model just took into account the second source of nuisance, showing its significant detrimental effect on SSF of the data and therefore estimates of SvO_2. Literature findings show that this is a complex phaenomenon due to its space and time dependency. The highest velocities have been found in the inferior and medial areas of the brain, while the superior tissue (roughly above the ventricles) is the less affected (Greitz et al., 1992). The motion evolves over time, peaking in correspondence to the systole, which usually represent about 20% in time of cardiac cycle, and is almost absent during diastole.

6.5.1.2 Local gradient fields

Two sources of nuisance in the data might result from alteration of local gradient fields, as commonly found in other techniques focused on the phase of the signal.

Firstly a major phase error might arise from the bulk motion of the brain in the presence of spatial imaging gradients, which would affect the dependency of the signal generated on moving blood. This results in erratic velocity phase encoding with the signal relative to tissue having a spectral component different from v=0 cm/s.

A second minor issue is the presence of susceptibility differences due to local gradient fields originated by surfaces of interface between tissue and air. This has been partially addressed through phase unwrapping and 3D spatial phase filtering. Nevertheless throughout the cardiac cycle nonlinear brain motion occurs such that the relative distances between different brain structures varies along time. It is therefore possible that such susceptibility-induced gradients contribute to additional dephasing and therefore to increased signal loss due to cardiac pulsation (Nunes et al., 2005), particularly in lower regions of the brain where both susceptibility differences and pulsatile brain motion are most significant.

6.5.1.3 CSF

CSF represents a nuisance source mainly because of its contribution in partial volume effects when moving due to cardiac activity. Specifically its signal partially adds to that of venous blood, altering the specificity of the measured as the relaxation time for CSF is typically one order of magnitude higher than blood (Perkins and Wehrli, 1986; Zhao et al., 2007).

Although the motion problem can be faced in the same way as discussed for the static component – given that the pressure waves originated during the systolic phase cause motion of both static tissue and CSF – the partial volume effect is inherited. Nevertheless, considering peak velocities of CSF below 2 mm/s (as found by Greitz and colleagues (Greitz et al., 1992, 1991)), the resolution of

velocities adopted in our implementation is enough to allow us to isolate pure venous blood signal, once motion correction techniques have been adopted.

Several solutions have been designed to address the problem of undesired motion. One is the gating of data acquisition, i.e. synchronizing the acquisition with the cardiac cycle. In this way it is possible to acquire data only in the diastolic period, when induced motions are minimal. The main drawback of this approach is the lengthening of acquisition time, which might represent a problem when combined with such an information dense approach as the Fourier velocity imaging.

Another similar solution may be the approach proposed by Nunes et al. (Nunes et al., 2005) for diffusion imaging, where acquisition has been synchronized to the cardiac cycle such that during systole only slices of superior brain are acquired (because they are less affected by movement), while the others are acquired during diastole. This allows the shortening of the acquisition time avoiding major motion artefacts.

6.5.2 Venous blood targeting

Our analysis has focused on a simplified description of vascular structure in a voxel, with arteries supposedly having a positive velocity, whilst veins negative along the longitudinal axis. This might roughly be the case for particular regions or specific direction of the motion encoding gradient considered, for instance in the cortex or in large vessels.

Nevertheless the vasculature in brain parenchyma is typically more complex, with arterioles and venules branching in various directions, in both healthy and especially pathologic conditions (Cassot et al., 2010). This affects the method in discussion as with arterial and venous blood possibly having common velocity components, there distinguishing between the two based on the velocity spectrum becomes more problematic. Estimates of a single would therefore express an apparent relaxation time arising from the two components.

The analysis shown is inherently limited in detecting the venous blood signal, mainly due to the small contribution of this to the spectra. In particular the amount of information present in a single voxel has been shown not to be enough to overcome the effect of noise.

Nevertheless, this approach presents a major improvement compared to methods exploiting velocity selective pulses. In fact all the signal of interest is targeted through phase encoding, avoiding signal loss. In particular it is possible to overcome some of the technical difficulties related to venous blood signal targeting, such as accuracy of the selected velocity of cut-off (v_{cutoff}, see Wu and Wong (Wu and Wong, 2007)) and inflow (Guo and Wong, 2012; Wong et al., 2006; Wu and Wong, 2006) or outflow (Bolar and Rosen, 2011) timings.

Targeting venous blood is one of the major problems puzzling all methods aiming at assessing oxygen consumption through $-S_vO_2$ calibration curves. In our case it's possible to imagine a development of the technique towards an approach with gradients applied in multiple directions, as for diffusion tensor imaging methods. This could maximize the difference between venous and arterial side of the spectrum the main drawback being represented by the lengthening of the acquisition time.

Another limitation of our implementation is the choice of measuring , which is suboptimal when compared to for two main reasons. Firstly because of the lower specificity to signal arising from blood due to the sensitivity to macroscale field inhomogeneities. Secondly, as relaxation is typically longer than , the same choice for TE values would result in better estimates of the exponential decays, especially considering the positive nature of the noise. The reason for the choice of this implementation has been practical, as the scanner in use only allowed a multi-echo gradient echo sequence and not spin echo. Nevertheless the principles of the technique discussed so far and the proof of concept hold true for an eventual implementation exploiting a spin echo acquisition.

An alternative solution to the same issue would be to have faster readout, allowing us to have TEs more closely spaced and therefore to characterise the evolution of the signal even for . One such approach is given by acquiring

images with reduced field of view (FOV), so that fewer line of k-space are needed to achieve the same spatial resolution in a shorter time. The FOV reduction is typically coupled to spatially-selective RF excitation pulses, in order to suppress the signal arising from the tissue outside the FOV which would appear as aliasing artefact otherwise (Zhao, 2005). In our specific case the image acquisition could be restricted to specific areas of interest, such as the superior sagittal sinus.

6.5.3 Eddy currents

Eddy currents are induced by time-varying magnetic fields from gradients in MRI pulse sequences. They generate unwanted magnetic fields that contrast the ones produced by the gradients and are therefore deleterious for images, giving phase artefacts. Their characteristics depend on magnitude and slew rate of the gradients delivered and on the structure of the scanner itself. For our purposes, given that the gradients involved are quite high, it is particularly important to consider their effects on the k-space navigation and on the phase encoding.

As regards the first, it is known that eddy currents may cause inaccuracy in the k-space acquisition trajectory and this especially a problem for spiral acquisitions, where the longer readout time worsen the effect, as k-space deviations can accumulate, leading to more deviation at the k-space periphery (Tan and Meyer, 2009).

The effects on phase encoding are more specifically linked with the technique we are discussing. A first inaccuracy introduced affects the dependency of the signal generated on moving spins. In fact, if the gradient imposed along a particular direction deviates from the ideal one, the value of its 0-th moment M_0 might be different from 0, leading to a phase which is dependent also on the static signal (see Paragraph 2.1.6). Then, because the phase errors due to eddy currents resulting from different velocity-encoding waveforms could be generally different, a dependency of the phase error on is possible. This adds up with the spatial dependency of the error which is determined by the direction of the velocity-encoding gradient (Bernstein et al., 2004).

A few approaches can be exploited to minimize eddy currents artefacts. They are based on characterization of their effect, either through acquisition of field maps (as proposed for diffusion MRI by Jezzard and colleagues (Jezzard et al., 1998)) or with acquisition of phantom images (Bastin and Armitage, 2000), or again recording the acquisition trajectory in the specific case of k-space readout (Tan and Meyer, 2009).

6.6 Conclusions

In this work we have explored a new method for estimating venous oxygen saturation based on phase encoding. A mathematical model has been designed, allowing a simulated implementation of the method. This model is able to effectively describe different aspects related to the generation of the signal, in particular the physiology and morphology of the underlying tissue (described with three compartments), the effect of two sources of noise (background and physiological) and the phase encoding operated by the Fourier velocity imaging approach.

Noise characterization is performed comparing acquired and simulated datasets, supplying an insight on the inherent limitations of the method and detrimental effect of noise in a real case scenario. As a proof of principle, provisional ROI and bulk S_vO_2 estimates are reported, showing respectively the feasibility of the method and effectiveness in detecting changes due to activation.

Other technical difficulties encountered in the application to real data are discussed, along with possible solutions and future directions of research. The results supply an initial evaluation of the potential and limits of the newly proposed technique as a tool for estimating brain S_vO_2.

Chapter 7

Final discussion and conclusions

Brain activity is inherently reliant on energy metabolism and oxygen consumption. Based on this assumption, from the earliest applications fMRI techniques inferred about brain activity from measurements of changes in magnetic signal due to blood oxygen content perturbations following hyperaemia triggered by tasks or particular conditions. More recently, studies on the complex relationship between the vascular and neural mechanisms regulating tissue physiology highlighted the limits of this approach (Ekstrom, 2010). For this reason new methods have been developed to directly assess oxygen metabolism, first in relative and finally in absolute terms. This would lead to a better understanding of brain functioning, potentially offering a marker of the (patho)physiological state of brain tissue (Lin et al., 2010), in applications like tumour (Brown and Wilson, 2004), stroke (Derdeyn et al., 2002), neurological (Santens et al., 1997) and neurodegenerative disorders (Ishii et al., 1996).

Current techniques for assessing oxygen metabolism (reviewed in Chapter 2) show limitations, both in terms of accuracy, precision and spatial resolution. Maps obtained with PET scans are often still regarded as gold standard. In this thesis we therefore aimed to develop a means for assessing oxygen metabolism with MRI firstly improving dual calibrated fMRI (dcFMRI) approaches and then exploring a new alternative method.

In **Chapter 3** the mathematical physiological models adopted by dcFMRI methods to estimate venous deoxyhaemoglobin concentration and thus OEF_0 and absolute $CMRO_2$ are analysed. In fact, optimising the integration of information carried by BOLD and CBF signals, modulated through hypercapnic and hyperoxic respiratory challenges, would provide better estimates of OEF_0 and therefore

absolute $CMRO_2$. The aim was to improve previous models relating the BOLD signal to the underlying physiology based on the bias in OEF_0 estimates and we focused in particular on the *original calibration model* proposed in our centre by Wise and colleagues (Wise et al., 2013). We performed a simulation study analysing a set of synthetic BOLD signals generated with a *detailed BOLD signal model* proposed by Griffeth and Buxton (Griffeth and Buxton, 2011) in the ideal noiseless condition, across a range of potential underlying physiological states. Our approach was similar to others recently adopted (Blockley et al., 2015; Griffeth et al., 2013) by linearizing the relationship between BOLD signal and changes in deoxyhaemoglobin. The novelty is the subsequent process of optimization aimed at improved performance in estimating OEF_0. Furthermore, an analysis on the effects of input errors was also carried out for a first evaluation of the behaviour of the model when dealing with errors in measurements and a further understanding of its limits.

The main result of the analysis was the characterisation of the bias present in the literature models, which led to the proposal of a new model: the *simplified calibration model*. This has fewer parameters, shows higher accuracy in estimating OEF_0 and also improved resilience to input errors. In conclusion, we showed that the proposed *simplified calibration model* is a potentially valuable tool for the unbiased evaluation of OEF_0 and therefore absolute $CMRO_2$ in studies using respiratory challenges. In particular, we would recommend it not only by virtue of its accurate results and reduced complexity, but also because of the enhanced flexibility with respect to the respiratory design of the experiment.

Besides these considerations, the model shares certain physiological assumptions with the previous ones (for instance the hypothesis of isometabolism during hypercapnia and hyperoxia), suggesting similar limits in its application. In particular it has been found to be affected by errors in measurements for high values of OEF_0, so that its accuracy for absolute estimates of $CMRO_2$ may not be optimal if applied to those pathological conditions where extreme values of OEF_0 might be expected (e.g. tumours).

Moreover, a caveat in our approach is that the optimization was carried out on synthetic data. The *detailed BOLD signal model* was chosen for generating the datasets in virtue of its comprehensive description of the signal, taking into account a multitude of biophysical parameters and intra- as well as extra-vascular contributions. While being a limitation in terms of signal authenticity, this enabled us to explore a wide range of physiological conditions and to have a quantification of the bias in the estimates based on the knowledge of the true underlying values.

In **Chapter 4** we wanted to assess the repeatability of the estimates of brain haemodynamics and metabolism obtained from dcFMRI experiments analysed with a novel forward model developed in our lab. This describes analytically the contributions of BOLD signal, ASL signal and of the measured end-tidal partial pressures of CO_2 and O_2 to the measured dual echo GRE signal in a dual calibrated BOLD experiment, where the physiological model adopted in the estimation framework included the *simplified calibration model* proposed in Chapter 3**.** Data from a test-retest repeatability experiment on ten healthy volunteers in the resting state were analysed with a Bayesian approach, supplying voxel-wise parametric maps of five physiological parameters: OEF_0, CBF, CVR, CBV and $CMRO_2$.

We evaluated the precision and reliability of the estimates and collected reference data in order to determine the viability of the estimation framework adopted for future studies. For this purpose, measures of correlations and metrics indices like coefficient of variation (CV) and intra-class correlation (ICC) were calculated at different levels of spatial resolution.

Results showed an overall consistency of the estimated parameters with literature reports and a good level of repeatability compared to recent similar repeatability studies on brain metabolism with PET (Bremmer et al., 2011) and MRI (Barhoum et al., 2014; Liu et al., 2013) techniques. The performance has been found to depend on the specific parameter under analysis and on the spatial resolution considered. In particular estimates of OEF_0 and CBF typically show a

higher degree of repeatability, while $CMRO_2$ is affected by the variability from both. The information supplied by grey matter maps is of extreme interest for the detail of the spatial distribution of brain physiology, despite some reliability limitations when compared to methods supplying bulk measurements.

The major limitations of the study are discussed, indicating that more work has to be done to further explore the possibilities of this method, such as to test its effectiveness in detecting physiological changes between different subjects and conditions. In fact, despite the good repeatability, the results highlighted a not negligible level of intra-subjects variability in the estimates. Moreover, sample size (N) calculations showed that for typical levels of statistical accuracy and effect size, the method is only suitable with small cohorts ($N<20$) for experimental designs with reduced subjects variability.

Therefore it is suggested that the method should be used with optimised experimental designs aimed at reducing the variability in the measurements (e.g. longitudinal, repeated measurements, crossover studies) for groups rather than single subject analyses.

The feasibility of this method was further investigated in the study presented in **Chapter 5**, where results from a randomised, double-blind, placebo-controlled drug study analysed with the same estimation framework are presented. In particular, with this work we aimed to quantify the acute effects of caffeine ingestion on oxygen metabolism and blood haemodynamics across grey matter.

Caffeine is known for increasing of the neuronal firing rate (Fredholm et al., 1999) and reducing CBF via vasoconstriction (Pelligrino et al., 2012). Due to the parallel effect on both neural and vascular systems, caffeine can alter the coupling between CBF and $CMRO_2$ and has therefore been extensively studied in fMRI studies. While converging evidence has been found indicating a reduction in baseline CBF (Cameron et al., 1990; Field et al., 2003), there is an insufficient body of research to support any specific direction of the effect on $CMRO_2$, with both increase (Griffeth et al., 2011), a tendency to decrease (Yang et al., 2015)

and no change (Xu et al., 2015) in $CMRO_2$ being reported. Crucially, to our knowledge no MR study has been published supplying grey matter maps of OEF_0 and absolute value $CMRO_2$ after caffeine assumption, motivating the application of our approach for providing a more detailed description of the acute effects on brain metabolism and haemodynamics.

The results of our experiment were consistent with the hypothesis of decrease in energetic demand due to an overall inhibitory effect of caffeine, supported by previous electrophysiology studies. While CBF, CBV and $CMRO_2$ changes seemed widespread, high resolution maps showed the effects on OEF_0 to be mostly localized in putamen, nucleus caudatus and thalamus. The results led to the assessment of the estimate framework based on our novel forward model with a dual calibrated BOLD experiment as the first viable MRI method to assess the effects of caffeine on brain metabolism and haemodynamics with a voxel-wise resolution. This, together with the results in Chapter 4, positively informs future applications of the method on drug studies and – more generally – brain patho-physiology.

Overall, the results presented in **Chapter 4** and **5** are representative of some of the most recent developments in the field of dcFMRI methods. These enable one to obtain estimates of absolute oxygen consumption with similar accuracy but lower invasiveness and cost than the gold standard PET. Besides, with the implementation reported we were able to supply maps of a wide range of physiological parameters across grey matter with good repeatability and efficacy in detecting changes due to drug manipulation.

Despite the developments presented, some caveats and limits of the original implementations are still present and need to be considered and addressed in future applications. The hypothesis of isometabolism during mild hypercapnia and hyperoxia is of major interest and has therefore been repeatedly discussed. Considering the disagreeing conclusions of studies aimed at testing it and the successful body of calibrated fMRI studies despite the highly detrimental effects of its violation (characterised in Chapter 3), it is reasonable to assume its validity.

Besides, a known change in oxygen metabolism due to a specific gas task could be accounted for by including it in the model.

One of the major limiting factors for the technique is represented by SNR, with about 18 minutes of acquisition needed for the estimates in our study. A better quality signal, or alternatively shorter scanning times, could be achieved firstly with hardware improvements, for instance using head coils with a higher number of channels, or with alternative imaging sequences, for example exploiting background suppression for acquiring the ASL signal. A more comprehensive physiological model with a dynamic description of the relationship between BOLD signal and $CMRO_2$ could also improve our estimates. Nevertheless, the estimation framework adopted is already an improvement of the original dcFMRI approach. In fact by accounting for multiple contributions to the signal, using a one-stage calculation (as opposed to two-stage approaches in literature (Bulte et al., 2012; Gauthier and Hoge, 2013) and adopting a Bayesian regularization, it supplies stable estimates of a larger number of physiological parameters then previous methods.

An SNR limitation also constrains the measurements to grey matter, where the signal is higher mainly due to the higher cerebral blood flow. With a better SNR the estimation framework could also be applied to white matter, but it would need some modifications; for example the physiological model relating BOLD and ASL signals to oxygen metabolism would need to be optimised in the context of white matter. Moreover, potential improvements could be introduced using higher magnetic fields, with the decrease in the signal due to longer arrival time partially counteracted by a longer longitudinal relaxation time.

Furthermore, the outliers in the results from **Chapter 4** and then from **Chapter 5** suggest that caution must be taken in considering individual results, especially at a voxel-wise level. Nevertheless it is shown that the technique is repeatable and suitable for group analysis, making it possible to detect areas of significant effects due to drug manipulation both in a voxel-wise or ROI-wise calculation.

Finally, the use of gas inhalation through masks, while far less invasive than the radiotracers used in PET, may represent a discomfort for the participants and

even lead to the exclusion of subjects with respiratory conditions of particular susceptibility to CO_2. Other calibration techniques could be further developed for establishing approaches with a minor impact of gas administration, for example exploiting ASE calibration.

dcFMRI is therefore shown as a valid alternative to PET for research applications with the potential to be eventually applied in a clinical environment. However, improved assessment of oxygen consumption could also be achieved by adopting different methods. An alternative novel approach has been explored in **Chapter 6** for the quantification of venous oxygen saturation, which can be used for estimating oxygen metabolism once joint with measurements of CBF. This is similar to other techniques estimating S_vO_2 through -S_vO_2 calibration curves (Bolar and Rosen, 2011; Guo and Wong, 2012) and does not require the use of respiratory tasks for calibration. The main novelties of our methods are the approach used for isolating the signal from venous vessels, based on Fourier velocity imaging encoding the MR signal from moving blood, and the use of - rather than -S_vO_2 calibration curves.

The aim was to explore the feasibility of the proposed method by analysing data from a simulation model of the signal and then running pilot acquisitions. From the datasets of synthetic MR signals we are able to characterize the expected signal and the detrimental effects of sources of nuisance in both simulated and acquired data, giving a quantitative indication on the feasibility of the novel technique. Then the effectiveness of the method was tested in the real case scenario in grey matter regions and by estimating the changes in S_vO_2 triggered by a visual stimulus in the superior sagittal sinus (sSS).

Results from the simulations showed that our three-compartment model is able to describe different aspects related to the generation of the signal, in particular the physiology and morphology of the underlying tissue, the effect of two main sources of noise (background and physiological) and the phase encoding operated by the Fourier velocity imaging approach. Noise characterization was performed comparing acquired and simulated datasets, supplying an insight on

the inherent limitations of the method and detrimental effect of noise in a real case scenario. As a proof of principle, grey matter ROI and bulk S_vO_2 estimates were calculated, showing the feasibility of the method and effectiveness in detecting changes due to activation.

The main difficulties encountered in the application to real data are discussed. These are firstly issues related to bulk movement of the static tissue which affects the encoding operated, determining spurious spectral components and CSF confounding. Possible solutions to these include more sophisticated acquisition schemes capable of minimizing motion, such as cardiac gating. The challenge of targeting venous blood in grey matter was also analysed, leading to the conclusion that further developments with gradients applied in multiple directions and a SE acquisition would be highly beneficial. Nevertheless, the results supply an initial evaluation of the potential and limits of the newly proposed technique as a tool for estimating brain S_vO_2 and ultimately $CMRO_2$.

In conclusion, the results shown in this thesis represent innovations in the research and assessment of MRI methods for absolute measurement of oxygen consumption in brain, both looking at current approaches and hinting at new research directions in this field. In particular, the results from the novel estimation framework for dual calibrated fMRI experiments recently developed in our lab help establishing this technique as a potentially viable method for assessing brain oxygen metabolism in a research environment and a promising alternative to current techniques.

References

Addicott, M. a, Yang, L.L., Peiffer, A.M., Laurienti, P.J., 2009. Methodological considerations for the quantification of self-reported caffeine use. Psychopharmacology (Berl). 203, 571–8. doi:10.1007/s00213-008-1403-5

Alsop, D.C., Detre, J. a., Golay, X., Günther, M., Hendrikse, J., Hernandez-Garcia, L., Lu, H., Macintosh, B.J., Parkes, L.M., Smits, M., van Osch, M.J.P., Wang, D.J.J., Wong, E.C., Zaharchuk, G., 2014. Recommended implementation of arterial spin-labeled perfusion MRI for clinical applications: A consensus of the ISMRM perfusion study group and the european consortium for ASL in dementia. Magn Reson Med 116, 102–116. doi:10.1002/mrm.25197

An, H., Lin, W., 2000. Quantitative measurements of cerebral blood oxygen saturation using magnetic resonance imaging. J. Cereb. Blood Flow Metab. 20, 1225–1236. doi:10.1097/00004647-200008000-00008

An, H., Lin, W., 2002. Cerebral venous and arterial blood volumes can be estimated separately in humans using magnetic resonance imaging. Magn. Reson. Med. 48, 583–588. doi:10.1002/mrm.10257

Ances, B., Liang, C., Leontiev, O., 2009. Effects of aging on cerebral blood flow, oxygen metabolism, and blood oxygenation level dependent responses to visual stimulation. Hum. Brain Mapp. 30, 1120–1132. doi:10.1002/hbm.20574.Effects

Andersson, J.L.R., Jenkinson, M., Smith, S.M., 2007. Non-linear registration aka Spatial normalisation FMRIB Technial Report TR07JA2. In Pract. 22.

Attwell, D., Iadecola, C., 2002. The neural basis of functional brain imaging signals. Trends Neurosci. 25, 621–625. doi:10.1016/S0166-2236(02)02264-6

Barhoum, S., Rodgers, Z.B., Langham, M., Magland, J.F., Li, C., Wehrli, F.W., 2014. Comparison of MRI methods for measuring whole-brain venous oxygen saturation. Magn. Reson. Med. 2128, 2122–2128. doi:10.1002/mrm.25336

Barzilay, Z., Britten, a G., Koehler, R.C., Dean, J.M., Traystman, R.J., 1985. Interaction of CO2 and ammonia on cerebral blood flow and O2 consumption in dogs. Am. J. Physiol. 248, H500–H507.

Bastin, M.E., Armitage, P. a, 2000. On the use of water phantom images to calibrate and correct eddy current induced artefacts in MR diffusion tensor imaging. Magn. Reson. Imaging 18, 681–7.

Benallal, H., Denis, C., Prieur, F., Busso, T., 2002. Modeling of end-tidal and arterial PCO2 gradient: comparison with experimental data. Med. Sci. Sports Exerc. 34, 622–9.

Berne, R., Winn, H.R., Knabb, R., Ely, S., Rubio, R., 1983. Blood Flow Regulation by Adenosine in Heart, Brain, and Skeletal Muscle, in: Berne, R., Rall, T., Rubio,

R. (Eds.), Regulatory Function of Adenosine, Developments in Pharmacology. Springer US, pp. 293–317. doi:10.1007/978-1-4613-3909-0_19

Bernstein, M.A., King, K.F., Zhou, X.J., 2004. Handbook of MRI Pulse Sequences, Chemistry & ….

Bilgic, B., Fan, A.P., Polimeni, J.R., Cauley, S.F., Bianciardi, M., Adalsteinsson, E., Wald, L.L., Setsompop, K., 2014. Fast quantitative susceptibility mapping with L1-regularization and automatic parameter selection. Magn. Reson. Med. 72, 1444–59. doi:10.1002/mrm.25029

Blockley, N.P., Griffeth, V.E.M., Buxton, R.B., 2012a. A general analysis of calibrated BOLD methodology for measuring CMRO2 responses: comparison of a new approach with existing methods. Neuroimage 60, 279–89. doi:10.1016/j.neuroimage.2011.11.081

Blockley, N.P., Griffeth, V.E.M., Germuska, M. a, Bulte, D.P., Buxton, R.B., 2013. An analysis of the use of hyperoxia for measuring venous cerebral blood volume: comparison of the existing method with a new analysis approach. Neuroimage 72, 33–40. doi:10.1016/j.neuroimage.2013.01.039

Blockley, N.P., Griffeth, V.E.M., Simonsen, C.Z., Buxton, R.B., 2012b. A review of calibrated blood oxygenation level-dependent (BOLD) methods for the measurement of task-induced changes in brain oxygen metabolism. NMR Biomed. doi:10.1002/nbm.2847

Blockley, N.P., Griffeth, V.E.M., Stone, A.J., Hare, H. V., Bulte, D.P., 2015. Sources of systematic error in calibrated BOLD based mapping of baseline oxygen extraction fraction. Neuroimage 122, 105–113. doi:10.1016/j.neuroimage.2015.07.059

Blockley, N.P., Jiang, L., Gardener, a G., Ludman, C.N., Francis, S.T., Gowland, P. a, 2008. Field strength dependence of R1 and R2* relaxivities of human whole blood to ProHance, Vasovist, and deoxyhemoglobin. Magn. Reson. Med. 60, 1313–20. doi:10.1002/mrm.21792

Boas, D. a., Strangman, G., Culver, J.P., Hoge, R.D., Jasdzewski, G., Poldrack, R. a, Rosen, B.R., Mandeville, J.B., 2003. Can the cerebral metabolic rate of oxygen be estimated with near-infrared spectroscopy? Phys. Med. Biol. 48, 2405–2418. doi:10.1088/0031-9155/48/15/311

Bolar, D.S., Rosen, B.R., 2011. QUantitative Imaging of eXtraction of oxygen and TIssue consumption (QUIXOTIC) using venular-targeted velocity-selective spin labeling. Magn. … 66, 1550–62. doi:10.1002/mrm.22946

Boxerman, J.L., Bandettini, P. a, Kwong, K.K., Baker, J.R., Davis, T.L., Rosen, B.R., Weisskoff, R.M., 1995a. The intravascular contribution to fMRI signal change: Monte Carlo modeling and diffusion-weighted studies in vivo. Magn. Reson. Med. 34, 4–10.

Boxerman, J.L., Hamberg, L.M., Rosen, B.R., Weisskoff, R.M., 1995b. MR contrast due to intravascular magnetic susceptibility perturbations. Magn. Reson. Med. 34, 555–566.

Bremmer, J.P., Van Berckel, B.N.M., Persoon, S., Kappelle, L.J., Lammertsma, A. a.,

Kloet, R., Luurtsema, G., Rijbroek, A., Klijn, C.J.M., Boellaard, R., 2011. Day-to-day test-retest variability of CBF, CMRO2, and OEF measurements using dynamic 15O PET studies. Mol. Imaging Biol. 13, 759–768. doi:10.1007/s11307-010-0382-1

Bright, M.G., Murphy, K., 2013. Reliable quantification of BOLD fMRI cerebrovascular reactivity despite poor breath-hold performance. Neuroimage. doi:10.1016/j.neuroimage.2013.07.007

Brown, G.G., Eyler Zorrilla, L.T., Georgy, B., Kindermann, S.S., Wong, E.C., Buxton, R.B., 2003. BOLD and perfusion response to finger-thumb apposition after acetazolamide administration: differential relationship to global perfusion. J. Cereb. Blood Flow Metab. 23, 829–837. doi:10.1097/01.WCB.0000071887.63724.B2

Bulte, D.P., Chiarelli, P. a, Wise, R.G., Jezzard, P., 2007. Cerebral perfusion response to hyperoxia. J. Cereb. Blood Flow Metab. 27, 69–75. doi:10.1038/sj.jcbfm.9600319

Bulte, D.P., Drescher, K., Jezzard, P., 2009. Comparison of hypercapnia-based calibration techniques for measurement of cerebral oxygen metabolism with MRI. Magn. Reson. Med. 61, 391–398. doi:10.1002/mrm.21862

Bulte, D.P., Kelly, M., Germuska, M. a, Xie, J., Chappell, M. a, Okell, T.W., Bright, M.G., Jezzard, P., 2012. Quantitative measurement of cerebral physiology using respiratory-calibrated MRI. Neuroimage 60, 582–91. doi:10.1016/j.neuroimage.2011.12.017

Buxton, R.B., 2009. Introduction to Funtional Magnetic Resonance Imaging, Second edi. ed. Cambridge University Press, New York.

Buxton, R.B., Frank, L.R., Wong, E.C., Siewert, B., Warach, S., Edelman, R.R., 1998. A general kinetic model for quantitative perfusion imaging with arterial spin labeling. Magn. Reson. Med. 40, 383–96.

Buxton, R.B., Uludağ, K., Dubowitz, D.J., Liu, T.T., 2004. Modeling the hemodynamic response to brain activation. Neuroimage 23 Suppl 1, S220–33. doi:10.1016/j.neuroimage.2004.07.013

Cameron, O.G.., Modell, J.G.., Hariharan, 1990. CAFFEINE AND HUMAN CEREBRAL BLOOD FLOW : A POSITRON EMISSION TOMOGRAPHY STUDY 47, 1141–1146.

Cassot, F., Lauwers, F., Lorthois, S., Puwanarajah, P., Cances-Lauwers, V., Duvernoy, H., 2010. Branching patterns for arterioles and venules of the human cerebral cortex. Brain Res. 1313, 62–78. doi:10.1016/j.brainres.2009.12.007

Çavuşoğlu, M., Pfeuffer, J., Uğurbil, K., Uludağ, K., 2009. Comparison of pulsed arterial spin labeling encoding schemes and absolute perfusion quantification. Magn. Reson. Imaging 27, 1039–1045. doi:10.1016/j.mri.2009.04.002

Chappell, M. a, MacIntosh, B.J., Donahue, M.J., Günther, M., Jezzard, P., Woolrich, M.W., 2010. Separation of macrovascular signal in multi-inversion time

arterial spin labelling MRI. Magn. Reson. Med. 63, 1357–65. doi:10.1002/mrm.22320

Chen, Y., Parrish, T.B., 2009a. Caffeine's effects on cerebrovascular reactivity and coupling between cerebral blood flow and oxygen metabolism. Neuroimage 44, 647–52. doi:10.1016/j.neuroimage.2008.09.057

Chen, Y., Parrish, T.B., 2009b. Caffeine dose effect on activation-induced BOLD and CBF responses. Neuroimage 46, 577–83. doi:10.1016/j.neuroimage.2009.03.012

Chiarelli, P. a, Bulte, D.P., Wise, R.G., Gallichan, D., Jezzard, P., 2007. A calibration method for quantitative BOLD fMRI based on hyperoxia. Neuroimage 37, 808–20. doi:10.1016/j.neuroimage.2007.05.033

Cicchetti, D. V, 2001. The precision of reliability and validity estimates re-visited: distinguishing between clinical and statistical significance of sample size requirements. J. Clin. Exp. Neuropsychol. 23, 695–700. doi:10.1076/jcen.23.5.695.1249

Clare, S., Francis, S., Morris, P.G., Bowtell, R., 2001. Single-shot T2(*) measurement to establish optimum echo time for fMRI: studies of the visual, motor, and auditory cortices at 3.0 T. Magn. Reson. Med. 45, 930–3. doi:10.1002/mrm.1124

Coles, J.P., Fryer, T.D., Bradley, P.G., Nortje, J., Smielewski, P., Rice, K., Clark, J.C., Pickard, J.D., Menon, D.K., 2006. Intersubject variability and reproducibility of 15O PET studies. J. Cereb. Blood Flow Metab. 26, 48–57. doi:10.1038/sj.jcbfm.9600179

Coles, J.P., Fryer, T.D., Smielewski, P., Chatfield, D.A., Steiner, L.A., Johnston, A.J., Downey, S.P.M.J., Williams, G.B., Aigbirhio, F., Hutchinson, P.J., Rice, K., Carpenter, T.A., Clark, J.C., Pickard, J.D., Menon, D.K., 2004. Incidence and Mechanisms of Cerebral Ischemia in Early Clinical Head Injury. J. Cereb. Blood Flow Metab. 202–211. doi:10.1097/01.WCB.0000103022.98348.24

Cox, R.W., 1996. AFNI: software for analysis and visualization of functional magnetic resonance neuroimages. Comput. Biomed. Res. 29, 162–173.

Croal, P.L., Hall, E.L., Driver, I.D., Brookes, M.J., Gowland, P. a., Francis, S.T., 2015. NeuroImage The effect of isocapnic hyperoxia on neurophysiology as measured with MRI and MEG. Neuroimage 105, 323–331. doi:10.1016/j.neuroimage.2014.10.036

Daunizeau, J., Adam, V., Rigoux, L., 2014. VBA: a probabilistic treatment of nonlinear models for neurobiological and behavioural data. PLoS Comput. Biol. 10, e1003441. doi:10.1371/journal.pcbi.1003441

Davis, T.L., Kwong, K.K., Weisskoff, R.M., Rosen, B.R., 1998. Calibrated functional MRI: Mapping the dynamics of oxidative metabolism. Proc. Natl. Acad. Sci. U. S. A. 95, 1834–1839.

Dean, J.B., Mulkey, D.K., Henderson, R. a, Potter, S.J., Putnam, R.W., 2004. Hyperoxia, reactive oxygen species, and hyperventilation: oxygen sensitivity of brain stem neurons. J. Appl. Physiol. 96, 784–791.

doi:10.1152/japplphysiol.00892.2003

Dimpfel, W., Schober, F., Spiller, M., 1993. The influence of caffeine on human EEG under resting conditions and during mental loads. Clin. Investig. 71, 197–207.

Diringer, M.N., Aiyagari, V., Zazulia, A.R., Videen, T.O., Powers, W.J., 2007. Effect of hyperoxia on cerebral metabolic rate for oxygen measured using positron emission tomography in patients with acute severe head injury. J. Neurosurg. 106, 526–529. doi:10.3171/jns.2007.106.4.526

Diringer, M.N., Yundt, K., Videen, T.O., Adams, R.E., Zazulia, A.R., Deibert, E., Aiyagari, V., Dacey, R.G., Grubb, R.L., Powers, W.J., 2000. No reduction in cerebral metabolism as a result of early moderate hyperventilation following severe traumatic brain injury. J. Neurosurg. 92, 7–13. doi:10.3171/jns.2000.92.1.0007

Dubois, A.B., 1952. Alveolar CO2 and O2 during breath holding, expiration, and inspiration. J. Appl. Physiol. 5, 1–12. doi:10.1016/S0140-6736(52)90957-4

Edelman, R.R., Siewert, B., Darby, D.G., Thangaraj, V., Nobre, a C., Mesulam, M.M., Warach, S., 1994. Qualitative mapping of cerebral blood flow and functional localization with echo-planar MR imaging and signal targeting with alternating radio frequency. Radiology 192, 513–520. doi:10.1148/radiology.192.2.8029425

Edelman, R.R., Chen, Q., 1998. EPISTAR MRI: multislice mapping of cerebral blood flow. Magn. Reson. Med. 40, 800–805. 10.1002/mrm.1910400603

Einöther, S.J.L., Giesbrecht, T., 2013. Caffeine as an attention enhancer: Reviewing existing assumptions. Psychopharmacology (Berl). 225, 251–274. doi:10.1007/s00213-012-2917-4

Fan, A.P., Benner, T., Bolar, D.S., Rosen, B.R., Adalsteinsson, E., 2012. Phase-based regional oxygen metabolism (PROM) using MRI. Magn. Reson. Med. 67, 669–78. doi:10.1002/mrm.23050

Ferrari, M., Quaresima, V., 2012. A brief review on the history of human functional near-infrared spectroscopy (fNIRS) development and fields of application. Neuroimage 63, 921–935. doi:10.1016/j.neuroimage.2012.03.049

Field, A.S., Laurienti, P.J., Yen, Y., Burdette, J.H., Moody, D.M., 2003. Radiology and Withdrawal : Confounding Variables in Quantitative Cerebral Perfusion Studies ? 1 129–135.

Floyd, T.F., Clark, J.M., Gelfand, R., Detre, J. a, Ratcliffe, S., Guvakov, D., Lambertsen, C.J., Eckenhoff, R.G., 2003. Independent cerebral vasoconstrictive effects of hyperoxia and accompanying arterial hypocapnia at 1 ATA. J. Appl. Physiol. 95, 2453–61. doi:10.1152/japplphysiol.00303.2003

Fox, P.T., Raichle, M.E., 1986. Focal physiological uncoupling of cerebral blood flow and oxidative metabolism during somatosensory stimulation in human subjects. Proc. Natl. Acad. Sci. U. S. A. 83, 1140–4.

Fox, P.T., Raichle, M.E., Mintun, M.A., Dence, C., 1988. Nonoxidative glucose

consumption during focal physiologic neural activity. Science 241, 462–464. doi:10.1126/science.3260686

Fredholm, B.B., Bättig, K., Holmén, J., Nehlig, A., Zvartau, E.E., 1999. Actions of caffeine in the brain with special reference to factors that contribute to its widespread use. Pharmacol. Rev. 51, 83–133. doi:0031-6997/99/5101-0083$03.00/0

Fukumitsu, N., Ishii, K., Kimura, Y., Oda, K., Sasaki, T., Mori, Y., Ishiwata, K., 2003. Imaging of adenosine A1 receptors in the human brain by positron emission tomography with [11C]MPDX. Ann. Nucl. Med. 17, 511–515. doi:10.1007/BF03006445

Gauthier, C.J., Hoge, R.D., 2012. Magnetic resonance imaging of resting OEF and $CMRO_2$ using a generalized calibration model for hypercapnia and hyperoxia. Neuroimage 60, 1212–25. doi:10.1016/j.neuroimage.2011.12.056

Ge, Y., Zhang, Z., Lu, H., Tang, L., Jaggi, H., Herbert, J., Babb, J.S., Rusinek, H., Grossman, R.I., 2012. Characterizing brain oxygen metabolism in patients with multiple sclerosis with T2-relaxation-under-spin-tagging MRI. J. Cereb. Blood Flow Metab. 32, 403–412. doi:10.1038/jcbfm.2011.191

Germuska, M. a, Merola, A., Stone, A.J., Murphy, K., Wise, R.G., 2015. A Bayesian framework for the estimation of OEF by calibrated MRI. Proc. Intl. Soc. Mag. Reson. Med.

Glover, G, Li, T., Ress, D., 2000. Image-Based Method for Retrospective Correction of Physiological Motion Effects in fMRI : RETROICOR. Magn. Reson. Med. 167, 162-167.

Greitz, D., Nordell, B., Ericsson, A., Ståhlberg, F., Thomsen, C., 1991. Notes on the driving forces of the CSF circulation with special emphasis on the piston action of the brain, in: du Boulay, G., Molyneux, A., Moseley, I. (Eds.), Proceedings of the XIV Symposium Neuroradiologicum SE - 59. Springer Berlin Heidelberg, pp. 178–181. doi:10.1007/978-3-642-49329-4_59

Greitz, D., Wirestam, R., Franck, A., Nordell, B., Thomsen, C., Stfihlberg, F., 1992. Diagnostic Neuroradiology radiology Pulsatile brain movement and associated hydrodynamics studied by magnetic resonance phase imaging The Monro-Kellie doctrine revisited 370–380.

Griffeth, V.E.M., Blockley, N.P., Simonsen, C.Z., Buxton, R.B., 2013. A New Functional MRI Approach for Investigating Modulations of Brain Oxygen Metabolism. PLoS One 8, e68122. doi:10.1371/journal.pone.0068122

Griffeth, V.E.M., Buxton, R.B., 2011. A theoretical framework for estimating cerebral oxygen metabolism changes using the calibrated-BOLD method: modeling the effects of blood volume distribution, hematocrit, oxygen extraction fraction, and tissue signal properties on the BOLD signal. Neuroimage 58, 198–212. doi:10.1016/j.neuroimage.2011.05.077

Griffeth, V.E.M., Perthen, J.E., Buxton, R.B., 2011. Prospects for quantitative fMRI: investigating the effects of caffeine on baseline oxygen metabolism and the response to a visual stimulus in humans. Neuroimage 57, 809–16.

doi:10.1016/j.neuroimage.2011.04.064

Grubb, R.L., Raichle, M.E., Eichling, J.O., Ter-Pogossian, M.M., 1974. The Effects of Changes in PaCO2 Cerebral Blood Volume, Blood Flow, and Vascular Mean Transit Time. Stroke 5, 630–639. doi:10.1161/01.STR.5.5.630

Guo, J., Wong, E.C., 2012. Venous oxygenation mapping using velocity-selective excitation and arterial nulling. Magn. Reson. Med. 68, 1458–71. doi:10.1002/mrm.24145

Haacke, E.M., Lai, S., Reichenbach, J.R., Kuppusamy, K., Hoogenraad, F.G., Takeichi, H., Lin, W., 1997. In vivo measurement of blood oxygen saturation using magnetic resonance imaging: a direct validation of the blood oxygen level-dependent concept in functional brain imaging. Hum. Brain Mapp. 5, 341–346. doi:10.1002/(SICI)1097-0193(1997)5:5<341::AID-HBM2>3.0.CO;2-3

He, X., Yablonskiy, D. a, 2007. Quantitative BOLD: mapping of human cerebral deoxygenated blood volume and oxygen extraction fraction: default state. Magn. Reson. Med. 57, 115–26. doi:10.1002/mrm.21108

Heijtel, D.F.R., Mutsaerts, H.J.M.M., Bakker, E., Schober, P., Stevens, M.F., Petersen, E.T., van Berckel, B.N.M., Majoie, C.B.L.M., Booij, J., Van Osch, M.J.P., Vanbavel, E., Boellaard, R., Lammertsma, A. a., Nederveen, a J., 2014. Accuracy and precision of pseudo-continuous arterial spin labeling perfusion during baseline and hypercapnia: A head-to-head comparison with (15)O H2O positron emission tomography. Neuroimage 92, 182–92. doi:10.1016/j.neuroimage.2014.02.011

Heiss, W.D., Herholz, K., 1994. Assessment of pathophysiology of stroke by positron emission tomography. Eur. J. Nucl. Med. 21, 455–465.

Hoge, R.D., Atkinson, J., Gill, B., Crelier, G.R., Marrett, S., Pike, G.B., 1999a. Investigation of BOLD signal dependence on cerebral blood flow and oxygen consumption: the deoxyhemoglobin dilution model. Magn. Reson. Med. 42, 849–863.

Hoge, R.D., Atkinson, J., Gill, B., Crelier, G.R., Marrett, S., Pike, G.B., 1999b. Linear coupling between cerebral blood flow and oxygen consumption in activated human cortex. Proc. Natl. Acad. Sci. U. S. A. 96, 9403–8.

Hoge, R.D., Franceschini, M. a., Covolan, R.J.M., Huppert, T., Mandeville, J.B., Boas, D. a., 2005. Simultaneous recording of task-induced changes in blood oxygenation, volume, and flow using diffuse optical imaging and arterial spin-labeling MRI. Neuroimage 25, 701–707. doi:10.1016/j.neuroimage.2004.12.032

Horvath, I., Sandor, N.T., Ruttner, Z., McLaughlin, a C., 1994. Role of nitric oxide in regulating cerebrocortical oxygen consumption and blood flow during hypercapnia. J. Cereb. Blood Flow Metab. 14, 503–509. doi:10.1038/jcbfm.1994.62

Ibaraki, M., Shinohara, Y., Nakamura, K., Miura, S., Kinoshita, F., Kinoshita, T., 2010. Interindividual variations of cerebral blood flow, oxygen delivery, and metabolism in relation to hemoglobin concentration measured by positron emission tomography in humans. J. Cereb. Blood Flow Metab. 30, 1296–

1305. doi:10.1038/jcbfm.2010.13

Ishii, K., Kitagaki, H., Kono, M., Mori, E., 1996. Decreased medial temporal oxygen metabolism in Alzheimer's disease shown by PET. J Nucl Med 37, 1159–1165.

Ishiwata, K., Mishina, M., Kimura, Y., Oda, K., Sasaki, T., Ishii, K., 2005. First visualization of adenosine A(2A) receptors in the human brain by positron emission tomography with [11C]TMSX. Synapse 55, 133–6. doi:10.1002/syn.20099

Ito, H., Ibaraki, M., Kanno, I., Fukuda, H., Miura, S., 2005. Changes in cerebral blood flow and cerebral oxygen metabolism during neural activation measured by positron emission tomography: comparison with blood oxygenation level-dependent contrast measured by functional magnetic resonance imaging. J. Cereb. Blood Flow Metab. 25, 371–377. doi:10.1038/sj.jcbfm.9600030

Ito, H., Kanno, I., Kato, C., Sasaki, T., Ishii, K., Ouchi, Y., Iida, A., Okazawa, H., Hayashida, K., Tsuyuguchi, N., Ishii, K., Kuwabara, Y., Senda, M., 2004. Database of normal human cerebral blood flow, cerebral blood volume, cerebral oxygen extraction fraction and cerebral metabolic rate of oxygen measured by positron emission tomography with 15O-labelled carbon dioxide or water, carbon monoxide and oxygen: . Eur. J. Nucl. Med. Mol. Imaging 31, 635–43. doi:10.1007/s00259-003-1430-8

Jain, V., Langham, M.C., Floyd, T.F., Magland, J.F., Wehrli, F.W., 2011. Rapid magnetic resonance measurement of global cerebral metabolic rate of oxygen consumption in humans during rest and hypercapnia. J. Cereb. Blood Flow Metab. 31, 1504–12. doi:10.1038/jcbfm.2011.34

James, W., 1890. Principles of Psychology, Henry Holt, New York. New York. doi:10.1073/pnas.95.3.765

Jenkinson, M., Bannister, P., Brady, M., Smith, S.M., 2002. Improved optimization for the robust and accurate linear registration and motion correction of brain images. Neuroimage 17, 825–841. doi:10.1016/S1053-8119(02)91132-8

Jensen, F.B., 2004. Red blood cell pH, the Bohr effect, and other oxygenation-linked phenomena in blood O2 and CO2 transport. Acta Physiol. Scand. 182, 215–27. doi:10.1111/j.1365-201X.2004.01361.x

Jezzard, P., Barnett, a S., Pierpaoli, C., 1998. Characterization of and correction for eddy current artifacts in echo planar diffusion imaging. Magn. Reson. Med. 39, 801–12.

Jones, M., Berwick, J., Hewson-Stoate, N., Gias, C., Mayhew, J., 2005. The effect of hypercapnia on the neural and hemodynamic responses to somatosensory stimulation. Neuroimage 27, 609–623. doi:10.1016/j.neuroimage.2005.04.036

Jones, N.L., Robertson, D.G., Kane, J.W., 1979. Difference between end-tidal and arterial PCO2 in exercise. J. Appl. Physiol. 47, 954–960.

Kety, S.S., Schmidt, C.F., 1948. The effects of altered arterial tensions of carbon dioxide and oxygen on cerebral blood flow and cerebral oxygen consumption of normal young men. J. Clin. Invest. 27, 484–492. doi:10.1172/JCI101995

Kim, S.-G., 1995. Quantification of relative cerebral blood flow change by flow-sensitive alternating inversion recovery (FAIR) technique: application to functional mapping. Magn. Reson. Med. 34, 293–301.

Kobari, M., Gotoh, F., Fukuuchi, Y., Tanaka, K., Suzuki, N., Uematsu, D., 1984. Blood flow velocity in the pial arteries of cats, with particular reference to the vessel diameter. J. Cereb. Blood Flow Metab. 4, 110–4. doi:10.1038/jcbfm.1984.15

Kruger, G., Glover, G.H., 2001. Physiological Noise in Oxygenation-Sensitive Magnetic 637, 631–637.

Langham, M.C., Magland, J.F., Floyd, T.F., Wehrli, F.W., 2009. Retrospective correction for induced magnetic field inhomogeneity in measurements of large-vessel hemoglobin oxygen saturation by MR susceptometry. Magn. Reson. Med. 61, 626–33. doi:10.1002/mrm.21499

Laughlin, S.B., Sejnowski, T.J., 2003. Communication in Neuronal Networks. Science (80-.). 301, 1870–1874. doi:10.1126/science.1089662

Laurienti, P.J., Field, A.S., Burdette, J.H., Maldjian, J. a., 2003. Relationship between Caffeine-Induced Changes in Resting Cerebral Perfusion and Blood Oxygenation Level – Dependent Signal 1607–1611.

Lauritzen, M., 2005. Reading vascular changes in brain imaging: is dendritic calcium the key? Nat. Rev. Neurosci. 6, 77–85. doi:10.1038/sj.jcbfm.9591524.0684

Lecrux, C., Hamel, E., 2011. The neurovascular unit in brain function and disease. Acta Physiol. 203, 47–59. doi:10.1111/j.1748-1716.2011.02256.x

Leenders, K.L., 1994. PET: Blood flow and oxygen consumption in brain tumors. J. Neurooncol. 22, 269–273. doi:10.1007/BF01052932

Lin, A.-L., Fox, P.T., Hardies, J., Duong, T.Q., Gao, J.-H., 2010. Nonlinear coupling between cerebral blood flow, oxygen consumption, and ATP production in human visual cortex. Proc. Natl. Acad. Sci. U. S. A. 107, 8446–51. doi:10.1073/pnas.0909711107

Lipp, I., Murphy, K., Caseras, X., Wise, R.G., 2015. Agreement and repeatability of vascular reactivity estimates based on a breath-hold task and a resting state scan. Neuroimage 113, 387–396. doi:10.1016/j.neuroimage.2015.03.004

Lipp, I., Murphy, K., Wise, R.G., Caseras, X., 2014. Understanding the contribution of neural and physiological signal variation to the low repeatability of emotion-induced BOLD responses. Neuroimage 86, 335–42. doi:10.1016/j.neuroimage.2013.10.015

Liu, P., Xu, F., Lu, H., 2013. Test-retest reproducibility of a rapid method to measure brain oxygen metabolism. Magn. Reson. Med. 69, 675–681. doi:10.1002/mrm.24295

Liu, T.T., Frank, L.R., Wong, E.C., Buxton, R.B., 2001. Detection power, estimation efficiency, and predictability in event-related fMRI. Neuroimage 13, 759–73. doi:10.1006/nimg.2000.0728

Liu, T.T., Wong, E.C., 2005. A signal processing model for arterial spin labeling functional MRI. Neuroimage 24, 207–15. doi:10.1016/j.neuroimage.2004.09.047

Lloyd-Fox, S., Blasi, A., Elwell, C.E., 2010. Illuminating the developing brain: The past, present and future of functional near infrared spectroscopy. Neurosci. Biobehav. Rev. 34, 269–284. doi:10.1016/j.neubiorev.2009.07.008

Lu, H., Clingman, C., Golay, X., Van Zijl, P.C.M., 2004. Determining the longitudinal relaxation time (T1) of blood at 3.0 tesla. Magn. Reson. Med. 52, 679–682. doi:10.1002/mrm.20178

Lu, H., Ge, Y., 2008. Quantitative evaluation of oxygenation in venous vessels using T2-Relaxation-Under-Spin-Tagging MRI. Magn. Reson. Med. 60, 357–63. doi:10.1002/mrm.21627

Lu, H., Van Zijl, P.C.M., 2005. Experimental measurement of extravascular parenchymal BOLD effects and tissue oxygen extraction fractions using multi-echo VASO fMRI at 1.5 and 3.0 T. Magn. Reson. Med. 53, 808–816. doi:10.1002/mrm.20379

Ma, Y., Berman, A.J.L., Pike, G.B., 2014. The Effect of Dissolved Oxygen on Relaxation Rates of Blood Plasma. Proc. Intl. Soc. Mag. Reson. Med.

Magkos, F., Kavouras, S.A., 2005. Caffeine use in sports, pharmacokinetics in man, and cellular mechanisms of action. Crit. Rev. Food Sci. Nutr. 45, 535–562. doi:10.1080/1040-830491379245

Marchal, G., Furlan, M., Beaudouin, V., Rioux, P., Hauttement, J.L., Serrati, C., de la Sayette, V., Le Doze, F., Viader, F., Derlon, J.M., Baron, J.C., 1996. Early spontaneous hyperperfusion after stroke. A marker of favourable tissue outcome? Brain 119 (Pt 2, 409–19. doi:10.1093/brain/119.2.409

Mark, C.I., Slessarev, M., Ito, S., Han, J., Fisher, J. a, Pike, G.B., 2010. Precise control of end-tidal carbon dioxide and oxygen improves BOLD and ASL cerebrovascular reactivity measures. Magn. Reson. Med. 64, 749–56. doi:10.1002/mrm.22405

McGraw, K.O., Wong, E.C., 1996. Forming inferences about some intraclass correlations coefficients. Psychol. Methods 1, 390–390. doi:10.1037/1082-989X.1.4.390

Mintun MA, Raichle ME, Martin WR, H.P., 1984. Brain oxygen utilization measured with O-15 radiotracers and positron emission tomography. J. Nucl. Med. 25, 177–187.

Novack, B.P., Shenkin, H. a, Bortin, L., Batson, P., Golden, D., 1953. Cerebral Blood Flow and Cerebral Oxygen Consumption in Vascular Disease1.

Nunes, R.G., Jezzard, P., Clare, S., 2005. Investigations on the efficiency of cardiac-gated methods for the acquisition of diffusion-weighted images. J. Magn. Reson. 177, 102–10. doi:10.1016/j.jmr.2005.07.005

Obata, T., Liu, T.T., Miller, K.L., Luh, W.-M., Wong, E.C., Frank, L.R., Buxton, R.B., 2004. Discrepancies between BOLD and flow dynamics in primary and supplementary motor areas: application of the balloon model to the interpretation of BOLD transients. Neuroimage 21, 144–153. doi:10.1016/j.neuroimage.2003.08.040

Ogawa, S., Menon, R.S., Tank, D.W., Kim, S.G., Merkle, H., Ellermann, J.M., Uğurbil, K., 1993. Functional brain mapping by blood oxygenation level-dependent contrast magnetic resonance imaging. A comparison of signal characteristics with a biophysical model. Biophys. J. 64, 803–12. doi:10.1016/S0006-3495(93)81441-3

Parkes, L.M., Tofts, P.S., 2002. Improved accuracy of human cerebral blood perfusion measurements using arterial spin labeling: Accounting for capillary water permeability. Magn. Reson. Med. 48, 27–41. doi:10.1002/mrm.10180

Pauling, L., Coryell, C.D., 1936. The Magnetic Properties and Structure of Hemoglobin, Oxyhemoglobin and Carbonmonoxyhemoglobin. Proc. Natl. Acad. Sci. U. S. A. 22, 210–216. doi:10.1073/pnas.22.4.210

Pellerin, L., Magistretti, P.J., 2004. Neuroenergetics: Calling Upon Astrocytes to Satisfy Hungry Neurons. Neurosci. 10, 53–62. doi:10.1177/1073858403260159

Pelligrino, D.A., Xu, H.-L., Vetri, F., 2012. Caffeine and the Control of Cerebral Hemodynamics. J Alzheimers Dis 29, 997–1003. doi:10.1016/j.biotechadv.2011.08.021.Secreted

Perkins, T.G., Wehrli, F.W., 1986. CSF signal enhancement in short TR gradient echo images. Magn. Reson. Imaging 4, 465–467. doi:10.1016/0730-725X(86)90023-8

Perthen, J.E., Lansing, A.E., Liau, J., Liu, T.T., Buxton, R.B., 2008. Caffeine-induced uncoupling of cerebral blood flow and oxygen metabolism: a calibrated BOLD fMRI study. Neuroimage 40, 237–47. doi:10.1016/j.neuroimage.2007.10.049

Poulin, M.J., Liang, P.J., Robbins, P.A., 1996. Dynamics of the cerebral blood flow response to step changes in end-tidal PCO2 and PO2 in humans. J. Appl. Physiol. 81, 1084–1095.

Ragan, D.K., McKinstry, R., Benzinger, T., Leonard, J., Pineda, J. a, 2012. Depression of whole-brain oxygen extraction fraction is associated with poor outcome in pediatric traumatic brain injury. Pediatr. Res. 71, 199–204. doi:10.1038/pr.2011.31

Raichle, M.E., Gusnard, D. a, 2002. Appraising the brain's energy budget. Proc. Natl. Acad. Sci. U. S. A. 99, 10237–10239. doi:10.1073/pnas.172399499

Raichle, M.E., Martin, W.R.W., Herscovltch, P., Mintun, M.A., Markham, J., 1983. Brain Blood Flow Measured with Intravenous H2O15 II . Implementation. J. Nucl. Med. 790–798.

Raichle, M.E., Mintun, M.A., 2006. BRAIN WORK AND BRAIN IMAGING. Annu. Rev.

Neurosci. 29, 449–476. doi:10.1146/annurev.neuro.29.051605.112819

Raichle, M.E., Posner, J.B., Plum, F., 1970. Cerebral blood flow during and after hyperventilation. Arch. Neurol. 23, 394–403.

Reivich, M., 1964. Arterial Pco2 and Cerebral Hemodynamics. Am. J. Physiol. 206, 25–35. doi:10.1097/00132586-196506000-00002

Richards, E.M., Fiskum, G., Rosenthal, R.E., Hopkins, I., McKenna, M.C., 2007. Hyperoxic reperfusion after global ischemia decreases hippocampal energy metabolism. Stroke 38, 1578–1584. doi:10.1161/STROKEAHA.106.473967

Robbins, P.A., Conway, J., Cunningham, D.A., Khamnei, S., Paterson, D.J., 1990. A comparison of indirect methods for continuous estimation of arterial PCO2 in men. J. Appl. Physiol. 68, 1727–31.

Rockswold, S.B., Rockswold, G.L., Zaun, D. a, Zhang, X., Cerra, C.E., Bergman, T. a, Liu, J., 2010. A prospective, randomized clinical trial to compare the effect of hyperbaric to normobaric hyperoxia on cerebral metabolism, intracranial pressure, and oxygen toxicity in severe traumatic brain injury. J. Neurosurg. 112, 1080–1094. doi:10.3171/2009.7.JNS09363

Rogers, P.J., Hohoff, C., Heatherley, S. V., Mullings, E.L., Maxfield, P.J., Evershed, R.P., Deckert, J., Nutt, D.J., 2010. Association of the anxiogenic and alerting effects of caffeine with ADORA2A and ADORA1 polymorphisms and habitual level of caffeine consumption. Neuropsychopharmacology 35, 1973–1983. doi:10.1038/npp.2010.71

Roland, P.E., Eriksson, L., Stone-Elander, S., Widen, L., 1987. Does mental activity change the oxidative metabolism of the brain? J. Neurosci. 7, 2373–2389.

Rostrup, E., Knudsen, G.M., Law, I., Holm, S., Larsson, H.B.W., Paulson, O.B., 2005. The relationship between cerebral blood flow and volume in humans. Neuroimage 24, 1–11. doi:10.1016/j.neuroimage.2004.09.043

Sakadžić, S., Mandeville, E.T., Gagnon, L., Musacchia, J.J., Yaseen, M.A., Yucel, M.A., Lefebvre, J., Lesage, F., Anders, M., Eikermann-haerter, K., Ayata, C., Srinivasan, V.J., Lo, E.H., Devor, A., Boas, D.A., 2015. margin of oxygen supply to cerebral tissue. doi:10.1038/ncomms6734.Large

Shrout, P.E., Fleiss, J.L., 1979. Intraclass correlations: Uses in assessing rater reliability. Psychol. Bull. doi:10.1037/0033-2909.86.2.420

Sicard, K.M., Duong, T.Q., 2005. Effects of hypoxia, hyperoxia, and hypercapnia on baseline and stimulus-evoked BOLD, CBF, and CMRO2 in spontaneously breathing animals. Neuroimage 25, 850–858. doi:10.1016/j.neuroimage.2004.12.010

Siesjo, B.K., Plum, F., 1971. Cerebral energy metabolism in normoxia and in hypoxia. Acta Anaesthesiol. Scand. Suppl. 45, 81–101.

Silvennoinen, M.J., Clingman, C.S., Golay, X., Kauppinen, R. a, van Zijl, P.C.M., 2003. Comparison of the dependence of blood R2 and R2* on oxygen saturation at 1.5 and 4.7 Tesla. Magn. Reson. Med. 49, 47–60. doi:10.1002/mrm.10355

Smith, a, 2002. Effects of caffeine on human behavior. Food Chem. Toxicol. 40,

1243–1255. doi:10.1016/S0278-6915(02)00096-0

Smith, J.E., Lawrence, A.D., Diukova, A., Wise, R.G., Rogers, P.J., 2012. Storm in a coffee cup: Caffeine modifies brain activation to social signals of threat. Soc. Cogn. Affect. Neurosci. 7, 831–840. doi:10.1093/scan/nsr058

Smith, S.M., 2002. Fast robust automated brain extraction. Hum. Brain Mapp. 17, 143–155. doi:10.1002/hbm.10062

Smith, S.M., Brady, J., 1997. SUSAN - a new approach to low level image processing.

Sokoloff, L., 1981. Localization of functional activity in the central nervous system by measurement of glucose utilization with radioactive deoxyglucose. J. Cereb. Blood Flow Metab. 1, 7–36. doi:10.1038/jcbfm.1981.4

Stanisz, Greg J, Odrobina, Ewa E, Pun, Joseph, Escaravage, Michael, Graham, Simon J, Bronskill, Michael J, Henkelman, R Mark, 2005. Magn Reson Med, 54: 507-512. doi: 10.1002/mrm.20605

Wansapura, Janaka P, Holland, Scott K, Dunn, R Scott, Ball, William S, 1999. NMR Relaxation Times in the Human Brain at 3.0 Tesla. Journal of Magnetic Resonance Imaging, 9: 531-538.

Svenningsson, P., Hall, H., Sedvall, G., Fredholm, B.B., 1997. Distribution of adenosine receptors in the postmortem human brain: an extended autoradiographic study. Synapse 27, 322–35. doi:10.1002/(SICI)1098-2396(199712)27:4<322::AID-SYN6>3.0.CO;2-E

Tal, O., Diwakar, M., Wong, C.-W., Olafsson, V., Lee, R., Huang, M.-X., Liu, T.T., 2013. Caffeine-Induced Global Reductions in Resting-State BOLD Connectivity Reflect Widespread Decreases in MEG Connectivity. Front. Hum. Neurosci. 7, 63. doi:10.3389/fnhum.2013.00063

Tan, H., Meyer, C.H., 2009. Estimation of k-space trajectories in spiral MRI. Magn. Reson. Med. 61, 1396–404. doi:10.1002/mrm.21813

Tancredi, F.B., Hoge, R.D., 2013. Comparison of cerebral vascular reactivity measures obtained using breath-holding and CO2 inhalation. J. Cereb. Blood Flow Metab. 33, 1066–74. doi:10.1038/jcbfm.2013.48

Tancredi, F.B., Lajoie, I., Hoge, R.D., 2014. A simple breathing circuit allowing precise control of inspiratory gases for experimental respiratory manipulations. BMC Res. Notes 7, 235. doi:10.1186/1756-0500-7-235

Tohgi, H., Yonezawa, H., Takahashi, S., Sato, N., Kato, E., Kudo, M., Hatano, K., Sasaki, T., 1998. Cerebral blood flow and oxygen metabolism in senile dementia of Alzheimer's type and vascular dementia with deep white matter changes. Neuroradiology 40, 131–137. doi:10.1007/s002340050553

Uludağ, K., Müller-Bierl, B., Uğurbil, K., 2009. An integrative model for neuronal activity-induced signal changes for gradient and spin echo functional imaging. Neuroimage 48, 150–65. doi:10.1016/j.neuroimage.2009.05.051

Van Osch, M.J.P., Hendrikse, J., Van Der Grond, J., 2007. Sensitivity comparison of multiple vs. single inversion time pulsed arterial spin labeling fMRI. J. Magn.

Reson. Imaging 25, 215–221. doi:10.1002/jmri.20823

Vidyasagar, R., Greyling, A., Draijer, R., Corfield, D.R., Parkes, L.M., 2013. The effect of black tea and caffeine on regional cerebral blood flow measured with arterial spin labeling. J. Cereb. Blood Flow Metab. 33, 963–8. doi:10.1038/jcbfm.2013.40

Vlassenko, A.G., McConathy, J., Couture, L.E., Su, Y., Massoumzadeh, P., Leeds, H.S., Chicoine, M.R., Tran, D.D., Huang, J., Dahiya, S., Marcus, D.S., Fouke, S.J., Rich, K.M., Raichle, M.E., Benzinger, T.L.S., 2015. Aerobic Glycolysis as a Marker of Tumor Aggressiveness: Preliminary Data in High Grade Human Brain Tumors. Dis. Markers 2015, 1–11. doi:10.1155/2015/874904

Weisskoff, R.M., Kiihne, S., 1992. MRI Susceptometry: Image-Based Measurement 383, 375–383.

Weisskoff, R.M., Zuo, C.S., Boxerman, J.L., Rosen, B.R., 1994. Microscopic Susceptibility Variation and Transverse Relaxation : Theory and Experiment. Magn. Reson. Med. 601–610.

Wise, R.G., Harris, A.D., Stone, A.J., Murphy, K., 2013. Measurement of OEF and absolute CMRO 2 : MRI-based methods using interleaved and combined hypercapnia and hyperoxia. Neuroimage 83, 135–147. doi:10.1016/j.neuroimage.2013.06.008

Wise, R.G., Pattinson, K.T.S., Bulte, D.P., Chiarelli, P. a, Mayhew, S.D., Balanos, G.M., O'Connor, D.F., Pragnell, T.R., Robbins, P. a, Tracey, I., Jezzard, P., 2007. Dynamic forcing of end-tidal carbon dioxide and oxygen applied to functional magnetic resonance imaging. J. Cereb. Blood Flow Metab. 27, 1521–1532. doi:10.1038/sj.jcbfm.9600465

Wise, R.G., Pattinson, K.T.S., Bulte, D.P., Rogers, R., Tracey, I., Matthews, P.M., Jezzard, P., 2010. Measurement of relative cerebral blood volume using BOLD contrast and mild hypoxic hypoxia. Magn. Reson. Imaging 28, 1129–34. doi:10.1016/j.mri.2010.06.002

Wong, E.C., Buxton, R.B., Frank, L.R., 1997. Implementation of quantitative perfusion imaging techniques for functional brain mapping using pulsed arterial spin labeling. NMR Biomed. 10, 237–49.

Wong, E.C., Buxton, R.B., Frank, L.R., 1998a. A theoretical and experimental comparison of continuous and pulsed arterial spin labeling techniques for quantitative perfusion imaging. Magn. Reson. Med. 40, 348–55.

Wong, E.C., Buxton, R.B., Frank, L.R., 1998b. Quantitative imaging of perfusion using a single subtraction (QUIPSS and QUIPSS II). Magn. Reson. Med. 39, 702–8.

Wong, E.C., Cronin, M., Wu, W.-C., Inglis, B., Frank, L.R., Liu, T.T., 2006. Velocity-selective arterial spin labeling. Magn. Reson. Med. 55, 1334–41. doi:10.1002/mrm.20906

Woolrich, M.W., Chiarelli, P. a, Gallichan, D., Perthen, J.E., Liu, T.T., 2006. Bayesian inference of hemodynamic changes in functional arterial spin labeling data. Magn. Reson. Med. 56, 891–906. doi:10.1002/mrm.21039

Wu, W.-C., Jiang, S.F., Yang, S.C., Lien, S.H., 2011. Pseudocontinuous arterial spin labeling perfusion magnetic resonance imaging-A normative study of reproducibility in the human brain. Neuroimage 56, 1244–1250. doi:10.1016/j.neuroimage.2011.02.080

Wu, W.-C., Wong, E.C., 2006. Intravascular effect in velocity-selective arterial spin labeling: the choice of inflow time and cutoff velocity. Neuroimage 32, 122–8. doi:10.1016/j.neuroimage.2006.03.001

Wu, W.-C., Wong, E.C., 2007. Feasibility of velocity selective arterial spin labeling in functional MRI. J. Cereb. Blood Flow Metab. 27, 831–8. doi:10.1038/sj.jcbfm.9600386

Xu, F., Liu, P., Pascual, J.M., Xiao, G., Lu, H., 2012. Effect of hypoxia and hyperoxia on cerebral blood flow, blood oxygenation, and oxidative metabolism. J. Cereb. Blood Flow Metab. 32, 1909–1918. doi:10.1038/jcbfm.2012.93

Xu, F., Liu, P., Pekar, J.J., Lu, H., 2015. Does acute caffeine ingestion alter brain metabolism in young adults? Neuroimage 110C, 39–47. doi:10.1016/j.neuroimage.2015.01.046

Xu, F., Uh, J., Brier, M.R., Hart, J.J.R., Yezhuvath, U.S., Gu, H., Yang, Y., Lu, H., 2011. The influence of carbon dioxide on brain activity and metabolism in conscious humans. J. Cereb. Blood Flow Metab. 31, 58–67. doi:10.1038/jcbfm.2010.153

Yablonskiy, D. a., Haacke, E.M., 1994. Theory of NMR signal behavior in magnetically inhomogeneous tissues: The static dephasing regime. Magn. Reson. Med. 32, 749–763. doi:10.1002/mrm.1910320610

Yang, L.L., Brugniaux, J., Dhaliwal, H., Beaudin, a. E., Eliasziw, M., Poulin, M.J., Dunn, J.F., 2015. Studying cerebral hemodynamics and metabolism using simultaneous near-infrared spectroscopy and transcranial Doppler ultrasound: a hyperventilation and caffeine study. Physiol. Rep. 3, e12378–e12378. doi:10.14814/phy2.12378

Yang, S.P., Krasney, J. a, 1995. Cerebral blood flow and metabolic responses to sustained hypercapnia in awake sheep. J. Cereb. Blood Flow Metab. 15, 115–123. doi:10.1038/jcbfm.1995.13

Yongbi, M.N., Fera, F., Mattay, V.S., Frank, J. a., Duyn, J.H., 2001. Simultaneous BOLD/perfusion measurement using dual-echo FAIR and UNFAIR: Sequence comparison at 1.5T and 3.0T. Magn. Reson. Imaging 19, 1159–1165. doi:10.1016/S0730-725X(01)00436-2

Young, W.L., Prohovnik, I., Ornstein, E., Ostapkovich, N., Matteo, R.S., 1991. Cerebral blood flow reactivity to changes in carbon dioxide calculated using end-tidal versus arterial tensions. J. Cereb. Blood Flow Metab. 11, 1031–1035. doi:10.1038/jcbfm.1991.171

Zhao, J.M., Clingman, C.S., Närväinen, M.J., Kauppinen, R. a, van Zijl, P.C.M., 2007. Oxygenation and hematocrit dependence of transverse relaxation rates of blood at 3T. Magn. Reson. Med. 58, 592–7. doi:10.1002/mrm.21342

Zhao, Lei, Madore, Bruno, Panych, Lawrence P., 2005. Reduced field-of-view MRI

with two-dimensional spatially-selective RF excitation and UNFOLD. Magn. Reson. Med. 5, 1118–25. 10.1002/mrm.20458

Zhao, J.M., Clingman, C.S., Närväinen, M.J., Kauppinen, R. a, van Zijl, P.C.M., 2007. Oxygenation and hematocrit dependence of transverse relaxation rates of blood at 3T. Magn. Reson. Med. 58, 592–7. doi:10.1002/mrm.21342